Advanced Fluid Models of ExB Discharges Applied to Hall Effect Thrusters

by

Davide Poli

A dissertation submitted in partial fulfilment of the requirements for the degree of Doctor of Philosophy in

Aerospace Engineering

Universidad Carlos III de Madrid

Advisors:

Eduardo Ahedo
Pablo Fajardo Peña

Tutor:

Pablo Fajardo Peña

2026

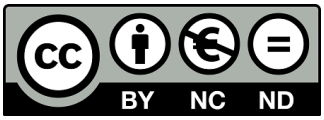

To my parents, Cristina and Fabrizio.

Acknowledgements

First of all, I would like to thank my tutor and thesis director, Pablo Fajardo and my thesis director, Eduardo Ahedo, for having given me the chance to do this PhD back in 2021. Eduardo, thank you for your constant patience and support, regardless of my stubbornness.

I would like to thank Gerjan Hagelaar for welcoming me for my research stay at the LAPLACE laboratory in Toulouse. It has been an insightful experience, and I hope to work together again in the future. I would also like to thank the team at LAPLACE, with special mention to Laurent and François, who contributed to making my stay a better experience.

On a more personal note, I cannot thank enough my parents, Fabrizio and Cristina, and my brother Stefano, for having always believed in me, supported and pushed me to do better. I feel extremely lucky to have a family like ours. Thanks to Matteo, Leonardo, Giusti and Lorenzo, it does not matter how many months have passed; seeing each other will always feel like home. Thanks to Matteo G. and Diego, companions of countless adventures up the mountains, you really made this journey much easier, and Diego, thank you for teaching me all the trivia about Spain. Matteo, thank you for all the conversations we had, about work and about life. I am glad to have shared an office with you. Thanks to Guillermo for all the good moments and the climbing tips. Thanks to Alberto for his constant advice and to Enrique for all the help at the beginning of my PhD. Thanks to Matteo R., the guru of instabilities, for all the help and all the time I invited myself to the Matteodero. Thanks to Marco, Simone, Davide, Qi, Scherezade, Borja, Andrés, Hugo, Iñaki and Alberto M. for all the good times we've spent together, inside and outside the office.

Finally, I would like to thank Tatiana, with whom I share my job, my passion, but most importantly, my life. I could have never done this without you by my side, and I am nothing but thrilled for what awaits us, because whatever it is, I know we will be together.

Published and submitted content

The following list reports the articles published (and submitted) to *peer-reviewed* journals, as well as conference proceedings.

Journal Publications

- **D. Poli**, E. Bello-Benítez, P. Fajardo, E. Ahedo. Time-dependent axial fluid model of the Hall thruster discharge and its plume, *Journal of Physics D: Applied Physics*, 56, 415203 (2023), DOI: 10.1088/1361-6463/ace2d0
  D. Poli developed the code, ran the simulations, performed the post-processing and wrote the manuscript. E. Bello-Benítez provided his stationary code for benchmarking and contributed with comments and revisions. P. Fajardo and E. Ahedo contributed with comments and revisions. The article has been published in the peer-reviewed journal *Journal of Physics D: Applied Physics* and it is wholly included in Chapter 2. Whenever material from this source is included in this thesis, it is singled out with typographic means and an explicit reference.

- **D. Poli**, P. Fajardo, E. Ahedo. A Non-neutral 1D Fluid Model of Hall Thruster Discharges: Full Electron Inertia and Anode Sheath Reversal, *Plasma Sources Science and Technology*, 33, 075014 (2024), DOI: 10.1088/1361-6595/ad6500
  D. Poli developed the code, ran the simulations, performed the post-processing and wrote the manuscript. P. Fajardo and E. Ahedo contributed with comments and revisions. The article has been published in the peer-reviewed journal *Plasma Sources Science and Technology* and it is wholly included in Chapter 3. Whenever material from this source is included in this thesis, it is singled out with typographic means and an explicit reference.

- **D. Poli**, E. Ahedo. Full-fluid Modelling of Rotating Plasma Instabilities in Penning-like Configurations, submitted to *Plasma Sources Science and Technology*.

D. Poli developed the code, ran the simulations, performed the post-processing and wrote the manuscript. E. Ahedo contributed with comments and revisions. The article has been wholly included in Chapter 5. Whenever material from this source is included in this thesis, it is singled out with typographic means and an explicit reference.

Conference Proceedings

- **D. Poli**, E. Bello-Benítez, P. Fajardo, E. Ahedo. Non Stationary Fluid Modelling of Plasma Discharge in Hall Thrusters, *Space Propulsion Conference 2022*, 116 (2022).
  D. Poli developed the code, ran the simulations, performed the post-processing and wrote the manuscript. E. Bello-Benítez provided his stationary code for benchmarking and contributed with comments and revisions. P. Fajardo and E. Ahedo contributed with comments and revisions. The paper has been presented with an oral presentation at the *Space Propulsion Conference 2022, Estoril, Portugal, 09-14 May 2022* and got awarded *Best PhD Paper Award in Space Transportation*.

- **D. Poli**, P. Fajardo, E. Ahedo, G. Hagelaar. Comparison of two fluid codes for modelling 2D instabilities in ExB plasmas, *38th International Electric Propulsion Conference*, 328 (2024).
  D. Poli developed the code, ran the simulations, performed the post-processing and wrote the manuscript. Gerjan Hagelaar provided the code MAGNIS to be used in the comparison and supervised the work carried out at the Laplace laboratory, Toulouse, France. P. Fajardo, E. Ahedo contributed with comments and revisions. The paper has been presented with an oral presentation at the *38th International Electric Propulsion Conference, Toulouse, France, 23-28 June 2024*.

- **D. Poli**, E. Ahedo. Towards Full-fluid Modelling of the Axial-azimuthal Hall Thruster Discharge, *39th International Electric Propulsion Conference*, 341 (2025).
  D. Poli developed the code, ran the simulations, performed the post-processing and wrote the manuscript. E. Ahedo contributed with comments and revisions. The paper has been presented with an oral presentation at the *39th International Electric Propulsion Conference, London, United Kingdom, 14-19 September 2025* and it is wholly included in Chapter 6. Whenever material from this source is included in this thesis, it is singled out with typographic means and an explicit reference.

Other research merits

- **D. Poli**, E. Bello-Benítez, L. Garrigues, P. Fajardo, E. Ahedo. Fluid vs kinetic simulation of the Penning discharge, *35th International Conference on Phenomena in Ionised Gases*, (2023).
  Oral presentation delivered by D. Poli at the *35th International Conference on Phenomena in Ionised Gases, Egmond Aan-Zee, The Netherlands, 9-4 July 2023.*

- **D. Poli**, P. Fajardo, E. Ahedo. Fluid Modelling of a Hall-effect Plasma Thruster, *3rd Spanish Fluid Mechanics Conference*, (2025).
  Oral presentation performed by D. Poli at the *3rdSpanish Fluid Mechanics Conference, Malaga, Spain, 24-27 June 2025.*

Abstract

Amongst the various technologies for in-space electric propulsion, Hall Effect Thrusters (HETs) dominate the market due to their scalability, reliability and efficiency. Nevertheless, the design process of HETs lacks the fundamental support of predictive numerical tools and relies on empirical scaling laws, making the development of new devices time-consuming. In this Thesis, the application of fluid modelling to Hall Effect Thruster discharges is advanced, demonstrating their potential and suitability in $E \times B$ plasmas simulations.

In the first part of this Thesis, a set of time-dependent quasi-neutral and non-neutral 1D models of the HET discharge is presented. The models provide a fast tool capable of capturing the main features of the HET plasma, enabling parametric analyses and preliminary performance assessments. The quasi-neutral drift-diffusion model extends the standard 1D description of Hall Effect Thrusters by expanding the computational domain in the far plume and by including additional physical effects, such as azimuthal electron inertia and characterisation of heavy species. Detailed analysis demonstrated their non-negligible impact on the stationary and dynamic response of the discharge, highlighting the high susceptibility of the breathing mode instability to the physical model and the simulation parameters. The extension to non-neutrality and full electron inertia confirmed the suitability of the quasi-neutral drift-diffusion formulation to describe the normal operating regime of HETs. However, in extreme conditions, a complete detachment of the plasma discharge from the anode is observed with the formation of a reversed, electron-attracting sheath, the modelling of which requires electron inertia. Even though a stable operation in this regime is not found, the onset of strong breathing mode oscillations can trigger periodic sheath transitions.

Although the 1D models proved to be an extremely versatile and powerful tool, they lack the aforementioned predictivity by relying on an empirical closure of the anomalous transport. The physics of this phenomenon is still poorly understood, and the formulation

of a simple, predictive model has been hindered by the complexity of the problem and the scarce interpretability of kinetic simulations, typically employed for its investigation.

In the second part of the Thesis, this problem is tackled with the fluid formalism, and the development of a 2D fluid model of $E \times B$ discharges is described. The model is first applied to simplified $E \times B$ geometries. The capability of the model to resolve rotating instabilities and their mode transitions is demonstrated by predicting the onset of dioctoron modes and rotating spokes in Penning discharges. The code is then used to perform the first full-fluid self-consistent simulation of the axial-azimuthal HET discharge. Here, it showed the ability to correctly capture the axial structure of the discharge, which is self-sustained without any empirical anomalous transport. The discharge develops instability-induced cross-field transport, which dominates over the collisional processes in the near-anode region. Differences and analogies with respect to similar kinetic simulations are commented on.

Contents

List of Figures

List of Tables

CHAPTER 1

Introduction

For almost a century, $E \times B$ devices have been utilised in both industrial and space applications due to their ability to sustain plasma discharges at low pressures: the perpendicular electric and magnetic fields confine the electrons, increasing the residence time in the device and allowing for efficient impact ionisation of the neutral gas [1]–[3]. The first observations of the effects of an applied magnetic field on plasma discharges date back to the end of the 19th century with the experiments of Phillips on afterglow discharges [4]. Phillips' observation of the trapping of electrons in the $E \times B$ motion was further analysed by Strutt [5] and Wehrli [6], but the first application to exploit such an effect appeared only in the 1930s with the work of Penning [7]. Penning demonstrated that the $E \times B$ device could be used as a pressure gauge, commercialised as the Penning Ionisation Gauge (PIG), where the discharge current is proportional to the pressure of the neutral gas. From this point on, Penning and reflex discharges have received a great deal of attention due to their many variations and broad range of operation [8]. The intensive investigation of such devices came along with the observation of a plethora of instabilities [9], deemed responsible for non-linearities in the pressure-current curve, and for the deterioration of the magnetic confinement of the electrons: the first theories on the "anomalous" enhanced cross-field transport, much larger than the classic collisional predictions, were formulated [10]. The problem of the turbulent cross-field transport remains poorly understood and characterised, affecting all the $E \times B$ devices that followed from the archetypal work of Penning.

Concurrently with the experiments on $E \times B$ plasmas, the concept of in-space electric propulsion was formulated, long before the first man-made object had been sent to space [11]. The justification for electric propulsion, which inspired visionaries such as

Goddard and Oberth [12], lies in the fundamental rocket equation of Tsiolkovsky:

$$\Delta v = v_e \ln \frac{m_0}{m_f}. \tag{1.1}$$

The equation relates the maximum change of velocity Δv to the initial m_0 and final m_f mass of the vehicle with the exhaust velocity v_e: the larger the exhaust velocity, the smaller the propellant mass needed to acquire the same Δv. Already at the beginning of the 20th century, it was clear that the ejection velocities attainable by accelerating charged particles were significantly larger than those of classic chemical rockets. However, contrary to chemical rockets, electric thrusters require an external energy source in the form of an electric power supply, whose mass usually increases with v_e and remains constant throughout the mission. As a result, there exists an optimal value of the exhaust velocity for a specific requirement of Δv. Nevertheless, despite this penalty, the 1950s and 1960s were characterised by the development of many prototypes of electric thrusters, such as arc-jets, ion-thrusters, and magnetoplasmadynamic thrusters [13], [14]. While the USA focused on ion-thrusters, eventually leading to the first flight in 1964 on board the SERT-1 spacecraft, the USSR, under the guidance of Morozov, led the development of another type of device called closed drift thruster (or stationary plasma thruster, SPT), nowadays commonly known as Hall Effect Thruster (HET) [15].

The basic working principle of HETs [16] relies on the confinement of electrons by an externally imposed magnetic field, perpendicular to the device axis, along which a moderate potential difference is applied. The magnetised electrons are thus trapped and forced to drift along their $E \times B$ motion, increasing the plasma resistivity and allowing the sustainment of a strong axial electric field E_z. On the other hand, the non-magnetised ions are not affected by the magnetic field and can be axially accelerated electrostatically. The increased residence time of electrons in the thruster channel not only permits the sustainment of strong electric fields, but also allows for efficient ion production via impact ionisation of the neutral propellant, typically consisting of a noble gas. A schematic representation of a Hall effect thruster is shown in figure 1.1.

Today, Hall Effect Thrusters dominate the in-space propulsion market, from small satellites to mega-constellations. In the last decade, HETs have been successfully designed in a large variety of powers, ranging from a hundred watts to tens of kilowatts, while maintaining high efficiency and specific impulse [18]. The technological advancements of HETs are the result of extensive experimental and numerical [19] research focused on the characterisation of magnetic topologies and erosion assessment. Nevertheless, despite the decades of research, the more fundamental physics of HETs remains poorly understood, hindering the use of accurate predictive models to design and optimise the thruster efficiently. In particular, just like the Penning discharges, magnetrons and other $E \times B$ devices, HETs are rich in instabilities [20] and their dynamics is strongly dominated by the anomalous cross-field transport of electrons. Particle in cell (PIC) simulations have confirmed [21]–[23] the role of instabilities (observed and theorised in other $E \times B$ devices as well) in the enhancement of electron mobility. Particular emphasis has

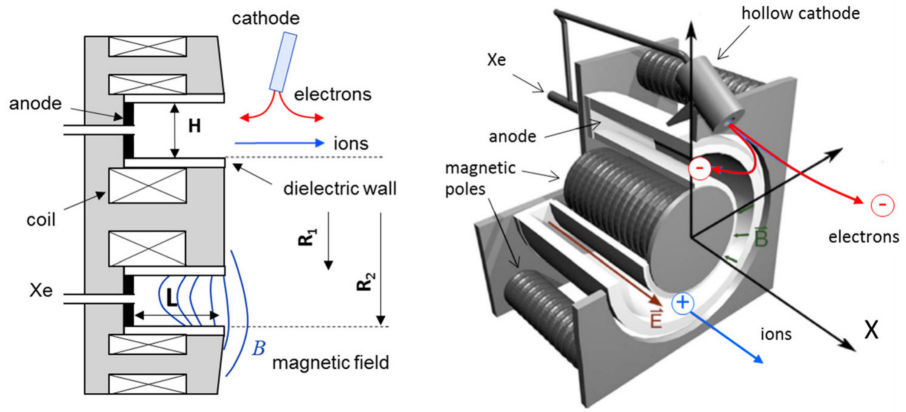

Figure 1.1: Schematic representation of a Hall Effect Thruster. Image reproduced from [17].

been given to the so-called electron cyclotron drift instability (ECDI), although without managing to obtain a simple (but predictive) description of it, partially due to the difficulty in interpreting the microscopic nature of the kinetic approach. On the other hand, fluid models deal directly with more tangible macroscopic quantities, at the expense of relying on stronger assumptions than the kinetic formulation. In particular, fluid models are limited to quasi-Maxwellian velocity distribution functions (VDFs), they lack finite Larmor radius effects, and they assume approximate closures of the set of equations. However, the ability to resolve a wide range of instabilities [24], [25], the possibility for ad hoc simplifications of the physical model and the higher computational speed (especially in quasi-neutral models), make the fluid approach an essential tool to analyse these devices.

In this Thesis, the application of fluid modelling to Hall Effect Thruster discharges is advanced, further demonstrating their potential and suitability in $E \times B$ plasmas simulations.

1.1. Thesis Objectives and Outline

This Thesis aims to extend the use of fluid modelling applied to Hall effect thrusters and other $E \times B$ devices to address both practical and theoretical aspects of the discharge. The know-how acquired throughout the Thesis and the set of numerical tools that have been developed will serve as a foundation for future studies of HETs and $E \times B$ plasmas in general, offering a different, more flexible formulation than kinetic approaches. Ultimately, the combined use of fluid and kinetic modelling aims to better characterise the plasma processes governing the dynamics of $E \times B$ devices. The Thesis objectives and the adopted methodology can be divided into two macro-categories. The first one, addressing a more applied use of numerical modelling, consists of:

1. The development of a fast quasi-neutral 1D time-dependent drift-diffusion axial model of the HET discharge to be used as a first approach to assess the macro-

scopic behaviour of the discharge [26]. The time-dependency extends the stationary models developed by Ahedo and Bello-Benitez [27], [28], enabling the capability of capturing axial instabilities in the $10^3 - 10^5$Hz range and non-stationary operation of the thruster in general. The low dimensionality and simpler physics allow for large parametric studies to understand the influence of free parameters and the level of modelled physics on the structure of the discharge and on the onset of axial oscillations.

2. The extension of the 1D model to account for non-neutrality and full-electron inertia [29], surpassing the limit of validity of the quasi-neutral drift-diffusion formulation and enabling the analysis of extreme regimes of discharge detachment and anode sheath reversal during axial oscillations.

These two objectives are covered in Chapters 2 and Chapter 3, respectively. The Chapters reproduce entirely the contents of the *peer-reviewed* journal articles published in *Journal of Physics D: Applied Physics* [26] and *Plasma Sources Science and Technology* [29].

The second part of the objectives, on the other hand, aims to answer more fundamental questions on the plasma dynamics. In particular, the objectives focus on the development of tools to characterise plasma instabilities and their contribution to anomalous transport in $E \times B$ discharges in general and in Hall Effect Thrusters as the ultimate goal. This is inherently a multidimensional problem; hence, the second part of the objectives deals with:

3. The development of a 2D three-fluid model of $E \times B$ discharges capable of resolving plasma instabilities. The model aims to be robust and general enough to be applied to a variety of problems for a wide spectrum study of partially magnetised plasmas and their dynamics. The large spatio-temporal scale separation in these devices poses strict conditions on the simulation parameters, hence the resulting numerical code requires parallelisation and optimisation.

4. The application of the aforementioned code to simplified $E \times B$ discharges to evaluate the capabilities of the fluid formulation of resolving plasma instabilities, their onset and the non-linear saturated regime.

5. The application of the model to the study of a self-consistent 3-fluid axial-azimuthal Hall Effect Thruster discharge. Given the novelty of the problem, the main objective is to address whether the fluid formulation can capture anomalous transport and whether the HET discharge is self-sustained.

A detailed description of the physical derivation and numerical schemes of the 2D model is reported in Chapter 4, whereas the last two objectives are addressed in Chapter 5 and Chapter 6, respectively. These last two Chapters reproduce the contents of the submitted

article to the *peer-reviewed* journal *Plasma Sources Science and Technology* and of the conference article presented at the *39th International Electric Propulsion Conference*.

All together, the objectives provide a comprehensive application of fluid modelling to $E \times B$ discharges, with specific application to Hall Effect thrusters.

As a final note, except for Chapter 4, the Thesis represents a compendium of published or submitted articles reproduced without modifications. For this reason, Chapters 2, 3, 5 and 6 are self-contained, including an abstract, an introduction, explaining the context and importance of the corresponding objective, the conclusions and the appendices. The author apologises for possible repetitions across the Chapters.

CHAPTER 2

Time-dependent Axial Fluid Model of the Hall Thruster Discharge and its Plume

This chapter reproduces the contents published by the author in the peer-reviewed journal Journal of Physics D: Applied Physics [26]. The typography has been adapted to the style of this thesis.

Abstract

One-dimensional axial models of a Hall thruster give a good qualitative picture of the main physical phenomena in the discharge with small computational effort. Time-dependent models, in particular, are widely used for the analysis of low-frequency axial oscillations (i.e. the breathing mode). The standard time-dependent three-fluid model found in the literature is here enhanced by extending the physical domain beyond the cathodic surface into the far plume and improving the modelling of some physical phenomena. A suite of five models is presented in this work with an increasing complexity of added physics; the most complete version accounts for ion and neutral energy evolution equations along with the partial inclusion of electron inertia. The added physics has a non-negligible impact on both the dynamics of the breathing mode and the time-averaged response of the plasma. In particular, it is found that the onset of the instability is sensitive to both the level of modelled physics and the operational parameters. In some cases, the strong breathing mode oscillations can result in a weak plasma attachment to the anode, leading to the collapse of the normal anode sheath and to the subsequent failure of the model.

2.1. Introduction

Nowadays, Hall-effect thrusters (HETs) are the most commonly used technology for solar electric propulsion. In fact, HETs are currently being used on a large variety of missions, from CubeSats to large geostationary satellites, being able to operate from a few hundred watts to several kilowatts for the largest devices. The versatility of HETs, coupled with the long flight heritage dating back to the 70's, makes them a reliable and mature technology for in-space propulsion. Despite the well-consolidated position of the HET technology, there are still several open questions from the physical point of view, such as plasma-wall interaction, plume physics, closure of fluid equations, or plasma oscillations. Addressing those questions is vitally important to achieve predictive fast numerical codes, which would push the design of HETs to the next level. The efforts of the HET community in answering those questions, from a theoretical point of view, have been translated into the development of kinetic, fluid and hybrid models [17], [19], [30] of different types depending on the problem to be analysed. The model presented in this paper belongs to the family of 1D axial fluid models. Such models give a good qualitative picture of the discharge physics and the interplay of different phenomena, at a cheap computational cost. They are, thus, well-suited for fast analysis on the effect of different parameters and to evaluate the impact of modelling additional physics. On the other hand, these models suffer from oversimplifying azimuthal physics, turbulent transport, plasma-wall interaction and magnetic topology. A complete stationary axial model of a HET discharge, from anode to cathode, was developed by Ahedo et al. [31] with later inclusion of the heat conduction [27] and plasma-wall interaction effects [32]. Recently, Bello-Benítez and Ahedo [33] extended that model by (a) introducing a volumetric cathode, which allows expanding the computational domain into the far plume, and (b) characterising the electron inertia by retaining its contribution in the azimuthal momentum equation. Some of the conclusions included the relevance of electron azimuthal inertia in smoothing gradients in the plume and close to the anode and cathode regions, and the apparent decoupling of the solution inside the chamber from the far plume one. Stationary models [27], [31]–[33] are also well suited to provide equilibrium solutions and to perform global linear stability analyses on longitudinal and azimuthal waves [34]–[36]. However, they are unable to provide information on the saturated behaviour of oscillations arising in the plasma discharge. In contrast, the intrinsic time-resolving capabilities of an axial transient model allow for the study of the non-linear evolution of instabilities. With this regard, axial-time dependent models have been extensively used to study the longitudinal, low-frequency oscillations of the discharge current caused by ionisation instabilities [37]–[42], usually called the breathing mode. An added complexity of the stationary formulation is to ensure the regular crossing of several internal sonic points, requiring special care for numerical convergence and internal regularising conditions. In order to reduce the number of sonic points, energy equations for the heavy species have so far been neglected in these models, thus assuming quasi-cold ions and neutrals. If the time derivative is retained in the fluid equations, time-dependent models are obtained. Such models require a different integra-

tion procedure where an initial solution is advanced in time by means of a time-marching algorithm. The mathematical nature of the time-dependent problem is completely different from the stationary one. Sonic points pose few and minor issues to the integration procedure of the time-dependent solution (e.g. the so-called 'sonic glitch' in some flux splitting finite volume schemes), allowing for a robust and more systematic inclusion of thermal effects on heavy species and other added physics to the model. This paper extends the recent stationary model of Bello-Benítez and Ahedo [33] in several aspects, proposing five models with an increasing complexity in the physics. While ion and neutral fluid equations are usually closed at the momentum equation, the most complete model includes energy equations for ions [41] and, for the first time, neutrals. Time derivatives are taken into account in every case, which allows us to analyse how additional physics of the present (ion and neutral energy equations) and previous [32], [33] (neutral momentum equation and electron inertia) works impact the breathing mode. Finally, the electron azimuthal inertia is retained and the plume past the cathode is included in the domain, which was done for the stationary case [33] but has never been done in previous time-dependent axial models [37]–[43]. In this article, both fully-stationary and breathing-mode types of solutions will be discussed, highlighting how both the physics considered and the model parameters affect the triggering of the ionisation instability. The failure of the model due to a lack of plasma attachment at the anode will be discussed too.

The paper is organised as follows. The complete model is presented in section 2.2, including the computation of the discharge current accounting for a finite-thickness cathode and electron azimuthal inertia. In section 2.3, the results are presented for steady state operation of the model, focusing on the effects of the newly introduced physics and the failure mechanism of the model. Finally, in section 2.4, the dynamic behaviour of the model is analysed and a preliminary study on the onset of the ionisation instability is presented. In this work, an SPT-100-type HET is considered as the reference thruster for all the simulations.

2.2. Model Formulation and solution method

2.2.1. Fluid equations

The model considers electrons, singly-charged ions, and neutrals (indices e, i, n, respectively) as three different fluids and a set of continuity, momentum, and energy equations for each of them. The model describes an axisymmetric plasma discharge by averaging the plasma properties along the radial direction. The divergence operator is thus expressed as:

$$\nabla \cdot \boldsymbol{g} = \frac{1}{A_c}\frac{d}{dz}\left(A_c g_z\right) + g'_w \tag{2.1}$$

where $\boldsymbol{g}$ is an arbitrary flux vector, z the axial coordinate, A_c the discharge cross section, and g'_w accounts for differential fluxes to lateral walls. A schematic of the computational

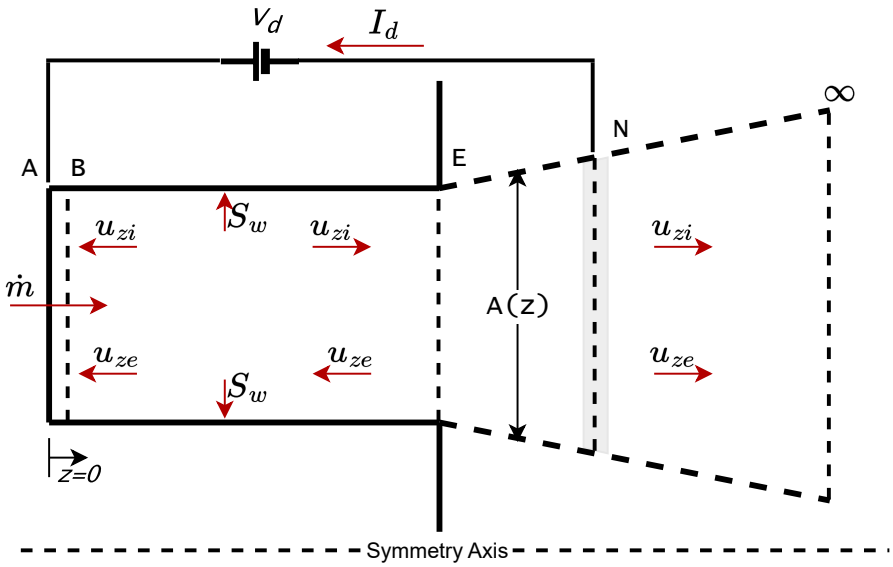

Figure 2.1: The figure represents the Hall thruster model used in this work. *A* represents the location of the anode, *B* is the location of the sheath edge, which is used as boundary of the quasi-neutral domain. The Debye sheath is a discontinuity surface in the quasinuetral model, i.e. $z_B \simeq z_A = 0$. Point *E* indicates the channel exit and *N* the centre of the electron emission layer (i.e. cathode or neutraliser).

domain and main features is shown in Fig. 2.1. Except for the anode sheath AB, the discharge is assumed quasi-neutral both in the annular thruster channel BE and the divergent plume E∞. The cathode emission and the plasma plume expansion make the problem 2D or 3D, so strong assumptions are needed to treat the external region as a 1D plasma beam [33]. First, the localised electron-injection neutraliser is here represented as an emission layer centred at N with a thickness ℓ_c, extending across the whole ion beam. Second, the effective cross-section area of the plasma beam $A_c(z)$ is assumed to contain most of the expanding plasma beam. The plume can be distinguished between the current-driving near-plume EN, and the current-free far-plume N∞. Using standard notation, the full set of fluid equations, three for species, in their conservative form is expressed as:

$$\frac{\partial n_e}{\partial t} + \frac{1}{A_c}\frac{\partial}{\partial z}(A_c n_e u_{ze}) = S_p - S_w + S_c, \tag{2.2}$$

$$\frac{\partial n_i}{\partial t} + \frac{1}{A_c}\frac{\partial}{\partial z}(A_c n_i u_{zi}) = S_p - S_w, \tag{2.3}$$

$$\frac{\partial n_n}{\partial t} + \frac{1}{A_c}\frac{\partial}{\partial z}(A_c n_n u_{zn}) = -S_p + S_w, \tag{2.4}$$

$$0 = en_e\frac{\partial \phi}{\partial z} - \frac{\partial p_e}{\partial z} + m_e n_e(u_{ye}\omega_{ce} - u_{ze}\nu_e), \tag{2.5}$$

$$\frac{\partial}{\partial t}(n_e u_{ye}) + \frac{1}{A_c}\frac{\partial}{\partial z}(A_c n_e u_{ye} u_{ze}) = -n_e(u_{ze}\omega_{ce} + u_{ye}\nu_e), \tag{2.6}$$

$$\frac{\partial}{\partial t}(n_i u_{zi}) + \frac{1}{A_c}\frac{\partial}{\partial z}\left(A_c n_i u_{zi}^2\right) = -\frac{en_i}{m_i}\frac{\partial \phi}{\partial z} - \frac{1}{m_i}\frac{\partial p_i}{\partial z} - S_w u_{zi} + S_p u_{zn}, \tag{2.7}$$

$$\frac{\partial}{\partial t}\left(n_n u_{zn}\right)+\frac{1}{A_c}\frac{\partial}{\partial z}\left(A_c n_n u_{zn}^2\right)=-\frac{1}{m_i}\frac{\partial p_n}{\partial z}-S_p u_{zn}+S_w u_{znw}, \tag{2.8}$$

$$\frac{\partial}{\partial t}\left(\frac{3}{2}p_e\right)+\frac{1}{A_c}\frac{\partial}{\partial z}\left(A_c\frac{5}{2}p_e u_{ze}+A_c q_{ze}\right)=u_{ze}\frac{\partial p_e}{\partial z}-S_p\mathscr{E}_{inel}-S_w\mathscr{E}_{ew}+S_c\mathscr{E}_c + \left(n_e\nu_e+\frac{1}{2}\left(S_p-S_w+S_c\right)\right)m_e u_e^2, \tag{2.9}$$

$$\frac{\partial}{\partial t}\left(\frac{3}{2}p_i\right)+\frac{1}{A_c}\frac{\partial}{\partial z}\left(A_c\frac{5}{2}p_i u_{zi}\right)=u_{zi}\frac{\partial p_i}{\partial z}+S_p\left(\frac{3}{2}T_n+\frac{m_i}{2}\left(u_{zi}-u_{zn}\right)^2\right)-S_w\frac{3}{2}T_i, \tag{2.10}$$

$$\frac{\partial}{\partial t}\left(\frac{3}{2}p_n\right)+\frac{1}{A_c}\frac{\partial}{\partial z}\left(A_c\frac{5}{2}p_n u_{zn}\right)=u_{zn}\frac{\partial p_n}{\partial z}-S_p\frac{3}{2}T_n+S_w\left(\mathscr{E}_{nw}+\frac{m_i}{2}\left(u_{zn}-u_{znw}\right)^2\right). \tag{2.11}$$

The quasineutral condition, $n_e = n_i$, is added to these equations except in the anode sheath AB; this is considered infinitely thin in the quasineutral scale (i.e. $z_B \simeq z_A = 0$) and is solved analytically to provide jump conditions between A and B.

In the continuity equations (2.2)-(2.4), $S_p = n_e\nu_p$, $S_w = n_e\nu_w$, and S_c represent, respectively, volumetric plasma production, plasma recombination at lateral dielectric walls, and electron injection at the cathode. Expressions for the ionisation frequency ν_p and the wall collision frequency ν_w are reported in appendix 2.A. The axial electric current in the quasineutral domain is

$$I_z = e n_e A_c (u_{zi} - u_{ze}). \tag{2.12}$$

The combination of the ion and electron equations yields its axial evolution as

$$\partial I_z/\partial z = -eA_c S_c. \tag{2.13}$$

The integration of this equation across the cathode layer will give a current-free plume (i.e. $I_z = 0$) downstream of the cathode and the discharge current ($I_z = I_d$) in the thruster channel. Notice that in addition to I_z, there is the azimuthal electric current $I_y(z) \simeq -en_e A_c u_{ye}$, responsible for the magnetic thrust.

In the momentum equations of the 3 species, the pressure tensors are reduced to isotropic scalar pressures $p_s \equiv n_s T_s, (s = e, i, n)$; ions are treated as unmagnetised, and charge-exchange collisions have been omitted. The electron momentum equations (2.5) and (2.6) are dominated (except in the far plume) by the magnetic force, with $\omega_{ce} = eB/m_e$ the gyrofrequency based on the effective radial magnetic field B. They also include a resistive force based on the electron total collision frequency ν_e, which is made up of four contributions:

$$\nu_e = \nu_{ei} + \nu_{en} + \nu_{wm} + \nu_t, \tag{2.14}$$

where ν_{ei} and ν_{en} correspond to collisions with ions and neutrals, ν_{wm} to wall collisionality, and ν_t to turbulent transport. Then, in the axial momentum equation (2.5) the inertial terms are negligible compared to the pressure gradient (i.e. the drift diffusion approximation $u_{ze} \ll c_e = \sqrt{T_e/m_e}$ applies), while in the azimuthal momentum equation (2.6), the

inertial terms must be kept [33], [36]. The empirical frequency for turbulent transport is hereby modelled as $\nu_t = \alpha_t \omega_{ce}$ with α_t a constant; since a study on the effects of ν_t on the discharge is out of the scope of this work, $\alpha_t = 0.01$ is kept fixed in all the simulations and will not be discussed any further.

The three equations (2.9)-(2.11) for the thermal energies include contributions from the same sources as the three continuity equations. Besides, the electron energy equation includes the (conductive) axial heat flux,

$$q_{ze} = -\frac{5p_e}{2m_e}\frac{\nu_e}{\nu_e^2+\omega_{ce}^2}\frac{\partial T_e}{\partial z}, \tag{2.15}$$

which is known to be important [27] to avoid unphysical heating of electrons and to guarantee a smooth transition between the ionisation and the ion reversed-flow regions. The introduction of the heat flux gives a parabolic character to that equation.

The magnetic field used in this axial model is radial and must be understood as a radial average value. It is modelled as [33]

$$\boldsymbol{B}(z) = \mathbf{1}_r\, B_m \exp\left[-(z-z_m)^2/\ell_m^2\right], \tag{2.16}$$

where B_m is its maximum value, z_m is the location of the maximum, and ℓ_m the characteristic length of magnetic decay. In general different values of ℓ_m are used in the interior (ℓ_{m1}) and exterior (ℓ_{m2}) regions. In this work, the plume cross-section is modelled as a hyperbolic expansion:

$$A_c(z) = 2\pi R d(z), \quad d(z) = \sqrt{d_{c0}^2 + 4\,(z-z_E)^2\tan^2\theta}, \text{ for } z > z_E \tag{2.17}$$

where R is the chamber mid-radius, $d(z)$ the plume width, with d_{c0} the chamber width and θ the plume divergence half-angle. Appendix 2.A compiles the expressions for the source terms and the collision frequencies. Most of them have been used in previous works. The addition of the neutral energy equation (2.11) has required the definition of a neutral energy per recombination event $\mathscr{E}_{nw}$ (reported in the appendix). Given the low dimensionality of the model, a proper description of ion-wall recombination processes cannot be formulated. Instead, a phenomenological model is used, based on the ion energy accommodation parameter α_w'.

2.2.2. Boundary Conditions and discharge current

The boundary conditions must be consistent with the hyperbolic nature of the quasineutral system, exception made for the electron energy equation, which is parabolic due to the diffusion term. For what concerns the heavy species, the outflow at the far plume is supersonic, so that all the characteristic lines are exiting the domain; as a result, outflow boundary conditions are used. At the anode, a sonic condition is considered for ions while neutrals are injected supersonically, allowing for the imposition of three boundary conditions. At the far plume, the only imposed condition is the electron temperature,

$T_{e\infty}$, as suggested by [33]. Moving to the anode, conditions are imposed at the anode sheath edge B. The boundary conditions at B are: the Bohm condition on the ion velocity ($u_{ziB} = -\sqrt{T_{eB}/m_i}$); the electron heat flux [27]

$$q_{zeB} = n_B u_{zeB} T_{eB} \left(\frac{e\phi_{AB}}{T_{eB}} - \frac{1}{2} \right); \tag{2.18}$$

and for neutrals, values of its mass flow rate (accounting for ion recombination at the anode A), temperature, and (supersonic) axial velocity, which are the same as at A.

The present model only supports normal, electron-repelling sheaths with a positive sheath potential drop, $\phi_{AB} = \phi_B - \phi_A > 0$, satisfying [31]

$$\phi_{AB} = \frac{T_{eB}}{e} \ln \frac{\bar{c}_{eB}}{4|u_{zeB}|}, \tag{2.19}$$

with $\bar{c}_{eB} = \sqrt{8T_e/\pi m_e}$ the electron mean thermal velocity. Notice that at the low oscillation frequencies considered here, the sheath behaves as quasi-stationary. Both ϕ_{AB} and q_{zeB} are updated at each time step according to the above equations.

The model formulation considers the discharge current, I_d, as an input parameter, and the discharge potential, $V_d \equiv \phi_A - \phi_N$, as an output. Nonetheless, both the practical operation of a Hall thruster (where dI_d/dV_d is very small) and the convergence of the numerical model prefer to take V_d as input and I_d as output. In a stationary model, I_d is simply an unknown to solve for in the system of equations [33]. In a time-dependent model, a relation $I_d(V_d)$ must be added to the set of differential equations. The common way to do it is by integrating equation (2.5) from N to A [37], [38], [40]. First, that equation is rewritten as

$$\frac{\partial \phi}{\partial z} = \frac{1}{en_e}\frac{\partial p_e}{\partial z} - u'_{ye}B + \frac{u_{zi}}{\mu_{\perp e}} - \frac{I_d}{A_c n_e e \mu_{\perp e}} \iota_z, \tag{2.20}$$

with $\iota_z = I_z/I_d$ the normalized axial electric current, $\chi = eB/\nu_e m_e$ the Hall parameter, $\mu_{\perp e} = (1+\chi^2)^{-1}(e/m_e\nu_e)$ the perpendicular electron mobility, and, calling $u_{ye} = -u_{ze}\chi + u'_{ye}$, u'_{ye} is the contribution of azimuthal electron inertia to u_{ye}. Integrating equation (2.20) between A and N yields

$$I_d(V_d) = \frac{V_d + \phi_{AB} + \int_0^{z_N} \left(\frac{1}{en_e}\frac{\partial p_e}{\partial z} - u'_{ye}B + \frac{u_{zi}}{\mu_{\perp e}} \right) dz}{\int_0^{z_N} \frac{\iota_z \, dz}{A_c e n_e \mu_{\perp e}}}. \tag{2.21}$$

Models neglecting azimuthal inertia have $u'_{ye} = 0$ and those ending the discharge at N with a surface cathode, have $\iota_z = 1$ [37], [40]. Equation (2.21) is added to the set of differential equations in the numerical integration scheme.

2.2.3. Numerical Integration Scheme

The spatial discretisation is performed using a finite volume scheme with second-order Kurganov-Tadmor [44] fluxes for the convective terms. The diffusion term in the electron

energy equation is discretised with central differencing. The hyperbolic equations are advanced in time using an explicit second-order Runge–Kutta scheme where each species is treated as a coupled system. The electron energy equation is integrated with a semi-implicit Crank–Nicolson scheme, where all the nonlinear terms are treated explicitly. To avoid oscillations at the ion stagnation point, the electron pressure coupled method introduced by Hara [43] has been used. The stationary solution from the model of [33] is used as the initial condition. In each time step the following integration procedure is used:

1. The neutral fluid is advanced.
2. The ion fluid is advanced considering the newly calculated neutral state.
3. All collision frequencies are updated with the new densities.
4. The electron energy equation is advanced.
5. The new discharge current is computed.
6. The electron axial velocity is updated.
7. The electron azimuthal velocity is advanced.

The integration scheme is solved with a newly developed parallel MPI code written in Fortran 90. The CFL condition for the electron azimuthal momentum equation constrains the time-step to relatively small values. A typical simulation with 2000 cells, 2 ms of physical integration time, and a timestep 1×10^{-9} s takes roughly 5 minutes on an AMD Ryzen 5 2600X with 5 cores. This computational time still has room for improvement since the code has not been aggressively optimised.

2.3. Fully steady-state solutions

The model introduced in section 2.2 includes a number of effects that can have a strong impact on the solution. In order to evaluate the effects of the new equations, five model configurations have been defined with increasing physics complexity:

- Model 1: Heavy species temperatures are constant and uniform, electrons are inertialess, and neutrals have constant velocity.
- Model 2: Neutral momentum equation is introduced.
- Model 3: Azimuthal electron inertia is introduced.
- Model 4: Neutral energy equation is introduced.
- Model 5: Ion energy equation is introduced.

Table 2.1: Relevant simulation parameters for the nominal case. These parameters have been used in all the simulations unless specified otherwise.

Parameter	Value	Parameter	Value
$\dot{m}$	$4.75\,\mathrm{mg\,s^{-1}}$	V_d	300 V
T_n	0.06 eV	$T_{e\infty}$	1 eV
u_{zn}	$300\,\mathrm{m\,s^{-1}}$	$\mathscr{E}_c$	5 eV
T_i	0 eV	z_∞	8.35 cm
B_m	266 G	z_m	2.5 cm
ℓ_{m1}	1.30 cm	ℓ_{m2}	1 cm
z_E	2.5 cm	z_N	3.35 cm
A_c	$40\,\mathrm{cm^2}$	R	4.25 cm
d_{c0}	1.5 cm	ℓ_c	0.5 cm
α_t	0.01	$\tilde{\nu}_w$	0.17
α'	0 %	θ	16 deg

In particular, Model 1 represents the commonly adopted model where heavy species pressure effects and neutral dynamics are neglected. The number of differential equations to solve goes from 6 in Model 1 to 10 in Model 5.

The use of a time-dependent model, apart from the possibility of resolving the dynamics of the discharge, is advantageous from the numerical solution point of view when additional physics is considered. For instance, stationary models have to deal with the imposition of regularising conditions at the sonic points, of which the position is unknown a *priori*. Introducing a finite neutral temperature would bring the number of sonic points in the system from 2 to 3 [33], while the introduction of ion temperature and heavy species energy equations would simply modify the existing points. Time dependency removes the issue of the sonic points, being the system of conservation laws hyperbolic (exception made for the electron energy equation), thus allowing for a straightforward time integration.

2.3.1. Comparison with the Stationary Model

First, the time-dependent model has been verified against the stationary model of [33] for a set of parameters yielding a fully-stationary solution. This last one includes electron azimuthal inertia and neutral momentum; the latter one has been considered with perfect accommodation for the wall-born neutrals, resulting in a constant neutral velocity in the whole domain. Concerning the time-dependent model, the azimuthal inertia has been included but not the neutral momentum, because, due to the different definition of the wall accommodation, it would not be possible to obtain a constant velocity solution. Finally, the coefficient $\tilde{\nu}_w$ for the wall-loss frequency has been kept constant, to be consistent with Bello-Benítez and Ahedo.

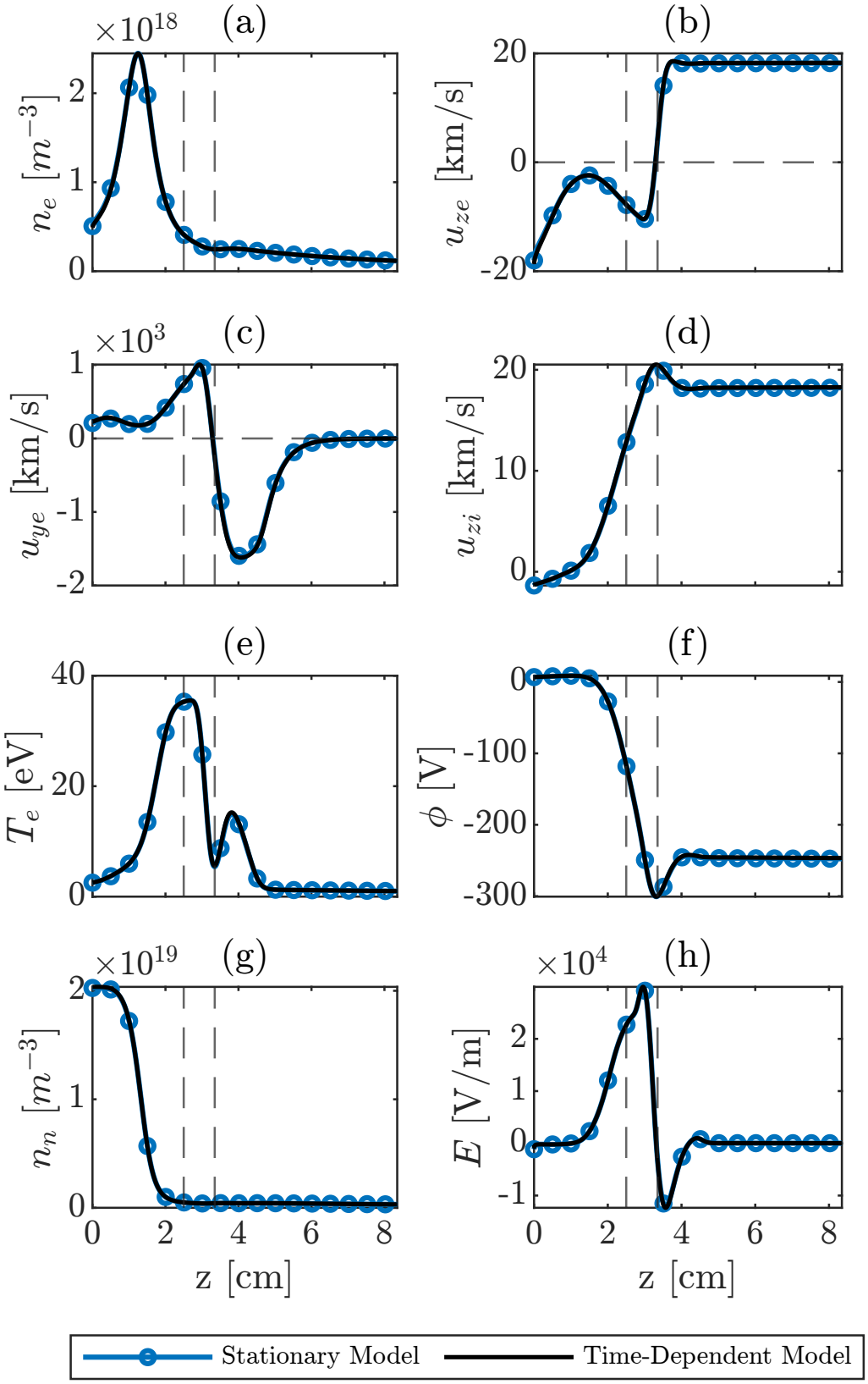

Figure 2.2: Comparison of the steady-state solution of the time-dependent model at 2 ms with the stationary model of Bello-Benítez and Ahedo [33]. Starting from the left, the two vertical dashed lines represent the points E and N respectively.

The main simulation parameters are reported in Tab. 2.1 and are kept constant for all simulations, if not explicitly specified. It must be noted that even though the neutral injection temperature T_n in Tab. 2.1 is larger than zero, whereas in [33] heavy species are cold, this has no effect in this case, having neglected the neutral momentum equation. The steady-state solutions from the time-dependent model at 2 ms and the stationary model are compared in Fig. 2.2. For the comparison, the neutral velocity and the wall-recombination parameter have been considered constant and equal to u_{zn} =300 m s^{-1} and $\tilde{\nu}_w = 0.17$. As it can be seen, there is an excellent agreement between the two solutions. Thanks to the second-order scheme of the present model, the numerical diffusion is minimal, which otherwise would result in a smoothing of the plasma density peak [in subplot (a)]. After the cathode, where the plasma starts to become demagnetised, the supersonic expansion of the plume results in the acceleration of the ions. The conservation of ion flux requires a decay of the plasma density, as it can be seen in Fig. 2.2(a).

2.3.2. Effects of modelling additional Physics

The effects of including additional physics in the time-dependent model are evaluated here. The analysis is performed by keeping all the parameters in Tab. 2.1 fixed while varying the configurations from Model 1 to Model 5. With the five models, fully stationary solutions are reached, and they are depicted in Fig. 2.3; in particular, the solutions for Model 1 to Model 3 coincide with those of [33]. The main changes introduced by each new model with respect to Model 1 are highlighted next.

Model 2. The introduction of the neutral momentum equation strongly affects the neutral and plasma density profiles. The neutral velocity, reported in Fig. 2.3(h), presents an important increase followed by a local minimum after the channel exit, from where it starts increasing again downstream. The non-monotonic behaviour can be explained by looking at equation (2.8), where u_{znw} is zero due to the perfect accommodation assumption ($\alpha'_w = 0\%$) and the pressure gradient is the sole term accelerating the neutrals. In the proximity of the channel exit, where neutrals are mostly depleted, the wall source term is responsible for the aforementioned minimum in their velocity, even in the case of perfect accommodation, as it can be derived from the neutral velocity equation [33]. The strong increase of the neutral velocity in the channel leads to a steeper decrease of the neutral density due to continuity, which results in a sensibly altered plasma density profile, featuring a smaller peak and a shift towards the anode. To satisfy ion continuity with a smaller density, a larger ion velocity can be observed in Fig. 2.3(d).

Model 3. The effects of including azimuthal inertia are appreciated mainly in the profiles of u_{ye} and T_e downstream the cathode, figures 2.3(c) and (e). The lower $|u_{ye}|$ in the case with inertia is responsible for a lower collisional heating and thus a lower electron temperature. In accordance with [33], the azimuthal velocity decays differently in the demagnetised far plume, where the inertial force, instead of the magnetic one, counteracts the collisional force. In case of low electron mobility at the anode (either

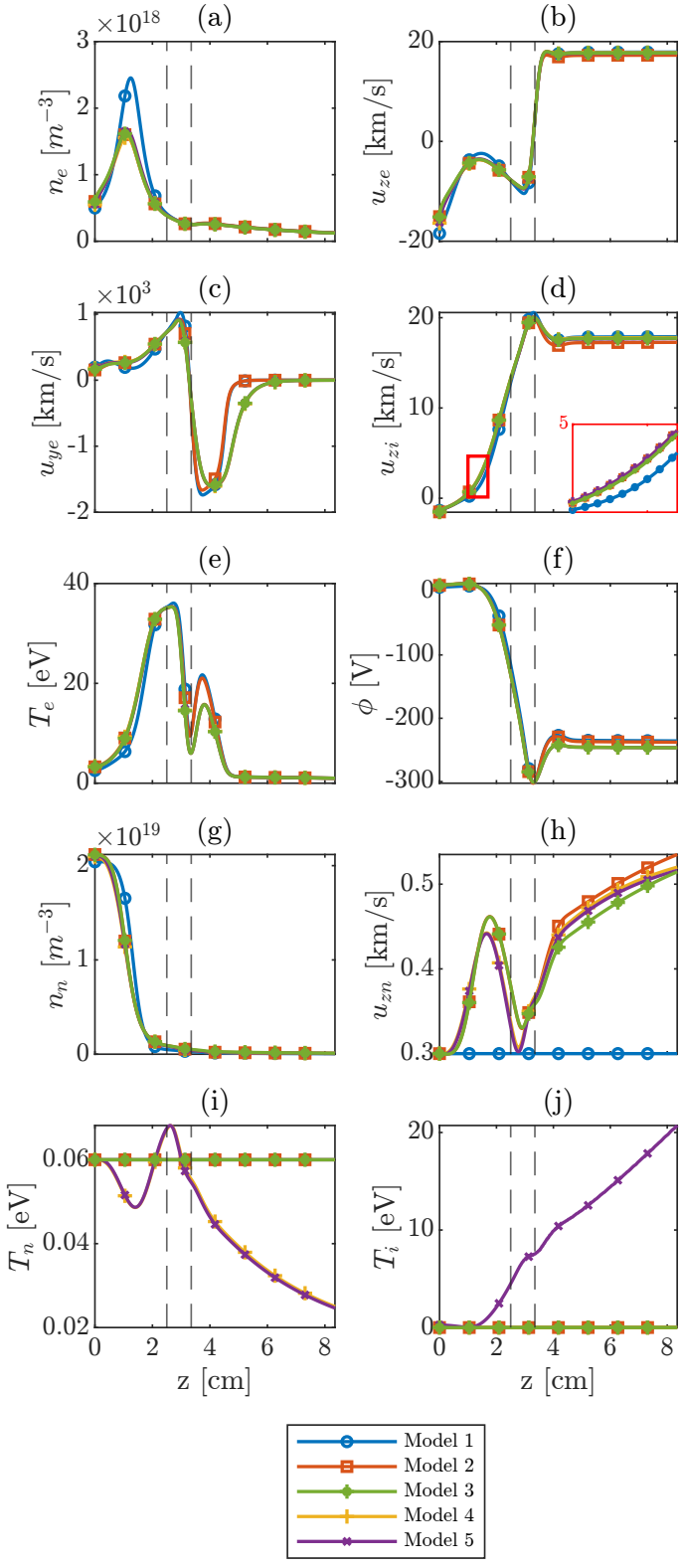

Figure 2.3: Steady state for different configurations of the time-dependent model. Perfect accommodation for neutral wall interactions is considered. Starting from the left, the two vertical dashed lines represent the point E and N respectively.

for a large magnetic field or small anomalous transport), it will be shown later that the azimuthal inertia bounds u_{ye} in that region[33] [this is not observed in Fig. 2.3, being the electron mobility at the anode large enough.]

Model 4. The introduction of the neutral energy equation has little effect on the steady state solution, exception made for T_n. By observing equation (2.11) a cooling of the neutrals is to be expected since $\mathscr{E}_w, u_{znw} = 0$ and the contribution of $S_w m_i u_{zn}^2/2$ is about one order of magnitude smaller than the ionisation loss.

Model 5. Similarly to Model 4, the introduction of the ion energy equation affects little the stationary solution. The large increase of the ion temperature, observed in Fig. 2.3(j), is due to the spatially extended production of slow ions along the discharge, and is materialised in the term $S_p m_i (u_{zi} - u_{zn})^2/2$. From a kinetic point of view, the high T_i represents the broadening of the velocity distribution function resulting from the inclusion of slow ions.

To summarise the comparison among models, the biggest effects on the stationary solution are introduced by the neutral momentum equation and the electron azimuthal inertia. For what concerns the introduction of energy equations for the two heavy species, the effects are limited to ion and neutral properties, without sensibly influencing the overall plasma discharge.

In terms of performances, such as the discharge current I_d and the thrust F, defined as

$$F = \sum_{s=i,n,e} \left[(m_s u_{zs}^2 + T_s) n_s A \right]_\infty , \tag{2.22}$$

the variations among the models are small, the maximum being 5.6% and 4.6% for the discharge current and the thrust, respectively, and will not be discussed further.

2.3.3. Effects of Neutral Interaction with lateral walls

The interaction of heavy particles with walls is a very complex phenomenon, seldom studied in the frame of Hall thrusters. A detailed modelling of such interactions is out of the scope of this work, but a limited study based on a single parameter yields interesting results. Figure 2.4 shows fully stationary solutions for the case of Tab. 2.1, except for $\ell_{m,1}$ =1.42 cm, and different values of the wall accommodation factor. (The influence of $\ell_{m,1}$ on the onset of oscillating solutions will be discussed in the next section.) Evident in Fig. 2.4 are the effects of the increased neutral energy input on the neutral magnitudes (plots (g)-(i)) and T_i (plot (j)). Regarding this last one, there is no direct influence of α'_w in equation (2.10), but its effects are accounted for in the energy sources due to ionisation of slow neutrals; in particular, the term $(u_{zn} - u_{zi})^2$ is responsible for mitigating T_i in the plume, due to a smaller velocity difference between the two heavy species for larger α'_w. While these effects are predominant in the near plume and around the cathode, it is possible to appreciate small variations of n_e and T_e (plots (a) and (e)) inside the channel too, in particular a higher mean plasma density is observed for higher energy inputs to

neutrals (i.e. for larger α'_w), which is again associated to a lower u_{zi} (plot (d)) inside the channel as shown in the zoom-in.

The effects of the wall-born neutral velocity, $u_{znw} = u_{zi}\sqrt{\alpha'_w}$, are expected to have a smaller impact on the discharge, especially before the ion acceleration region, because of the relatively small u_{zi}. Nevertheless, it has been seen that the dynamic behaviour of the discharge is influenced not only by the energy input but also by u_{znw}.

A noteworthy observation is the behaviour of n_n (plot (g)) at the anode, which presents a steep increase resembling a shock, more evident at larger α'_w. A preliminary analysis of this phenomenon suggests that the supersonic neutral flow becomes quickly thermally-choked due to the wall energy input, which can be large compared to the average energy of the neutral fluid, resembling the behaviour of a Rayleigh flow model [45]. This behaviour represents a limitation of the 1-D fluid formulation, which considers a single and simple population per heavy species.

2.3.4. Attachment of the discharge to the anode

Since only neutrals are injected in the chamber, an ion backstreaming region must exist for the plasma discharge to be quasineutral at the back of the thruster channel, i.e. for the discharge to be 'attached' to the anode. At the same time, since an ion backwards current means a penalty in performance, it is also paramount to limit that current. In practice, this is done by adjusting the magnetic field strength in the near-anode region [16], [46]. In the present study, the anode magnetic field is controlled, $B_A \equiv B(z_A)$, by acting on the gradient length ℓ_{m1}, Eq. (2.16). As ℓ_{m1} increases, B_A increases, and the ion current at the anode $|I_{iA}|$ [with $|I_{iA}| = |I_{iB}| \ll I_d$] decreases [31], as illustrated in Tab. 2.2. This in turn reduces the sheath potential ϕ_{AB}, and eventually the normal (electron-repelling) sheath vanishes and a reverse (electron-attracting) sheath forms.

That transition was well characterised by Ahedo et al. [47], [48]. Beyond $|I_{iA}|$, the magnitudes of interest near the anode are the plasma densities and velocities:

$$\begin{aligned} &u_{ziB} = c_{sB} \equiv \sqrt{T_{eB}/m_i}, \\ &n_{eB} = |I_{iA}|/(eA_c c_{sB}), \\ &|u_{zeB}| \simeq I_d/(eA_c n_{eB}) \equiv c_{sB} I_d/|I_{iA}|, \\ &u_{yeB} \approx \chi_B |u_{zeB}| = \chi_B c_{sB} I_d/|I_{iA}|. \end{aligned} \tag{2.23}$$

For $|I_{iA}|/I_d \gg O(\chi_B\sqrt{m_e/m_i})$, the standard situation of Model 1 applies. For $|I_{iA}|/I_d = O(\chi_B\sqrt{m_e/m_i})$, it is $u_{yeB} = O(\bar{c}_{eB})$ and azimuthal inertia is already important near the anode. When $|I_{iA}|/I_d$ further decreases and becomes $O(\sqrt{m_e/m_i})$ it is $|u_{zeB}| = O(\bar{c}_{eB})$: axial electron inertia becomes relevant too and the normal sheath collapses (i.e. $|u_{zeB}| = \bar{c}_{eB}/4$ and $\phi_{AB} = 0$) when $|I_{iA}|/I_d = \sqrt{2\pi m_e/m_i}$ [$\simeq 0.5\%$ for xenon]. The present model, which neglects axial electron inertia, cannot analyse solutions with reverse anode sheaths, where the very small ion back current is no longer sonic at the sheath edge [48].

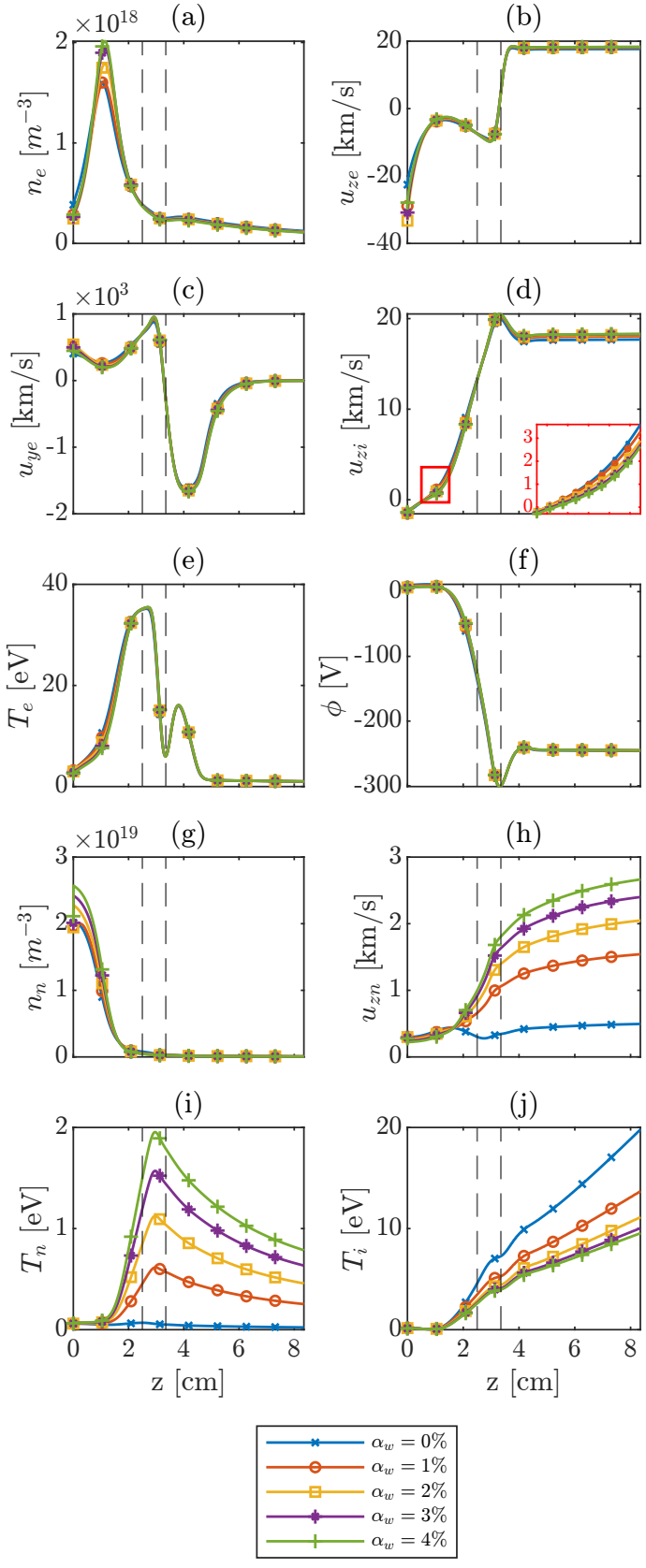

Figure 2.4: Plasma discharge parameters for Model 5 at different α'_w. Starting from the left, the two vertical dashed lines represent the point E and N respectively.

The last column of Tab. 2.2 measures the relevance of the azimuthal inertia at the anode. For a fully stationary solution and assuming $\nu_e \gg (S_p - S_w + S_c)/n_e$, Eq. (2.6) yields

$$\frac{u_{ye}}{\chi |u_{ze}|} \simeq 1 + \frac{1}{\omega_{ce}} \frac{\partial u_{ye}}{\partial z}, \tag{2.24}$$

the last term being the azimuthal inertia effect. This is non negligible when either ω_{ce} becomes small (i.e. in the far plume always, or near the anode if B_A is small enough) or $\partial u_{ye}/\partial z$ becomes large (i.e. around the cathode always, or near the anode if B_A is large enough). Table 2.2 illustrates the two situations at the anode. Indeed, while inertia bounds u_{yeB} for large B_A, it enhances it for small B_A, thanks to the change of sign of $\partial u_{ye}/\partial z$. This phenomenon is evident in Fig. 2.5 where u_{ye} in the near anode region is reported for different B_A, corresponding to the cases of Tab. 2.2. For the convergence of the model, the inclusion of the azimuthal inertia is important in limiting u_{yeB} at large B_A where the vanishing sheath condition is eventually reached.

The limit of validity of the model, which results in the failure of the numerical code, is represented in Fig. 2.6. Plot (a) shows a well behaved simulation where the model is far enough from the sheath vanishing condition $4|u_{zeB}|/\bar{c}_{eB} = 1$; it must be noted that plot (a) shows only part of the initial transient of the simulation, which would eventually converge to the values reported in the last row of Tab. 2.2. However, if the magnetic field is increased, the simulation soon reaches the sheath vanishing condition, as shown in plot (b). As soon as the sheath vanishes, the solution becomes nonphysical, leading to the failure of the numerical code after a few timesteps. (In general, all the results beyond the sheath collapse should not be considered and are hereby retained for the sake of showing how the numerical code fails.) To solve correctly the vanishing of the normal sheath and the transition to an inverse sheath, full electron inertia (i.e. on the axial and azimuthal directions) must be accounted for, which imposes a stronger constraint on the timestep. This regime is not treated in this work.

In a dynamic scenario, sheath vanishing can occur when strong oscillations are present, yielding small minima of $|I_{iA}|/I_d$. This can be the consequence of either the onset of a strong ionisation instability or the discharge transient if the initial condition is too far from the new set of simulation parameters. This last situation is avoided by using the model of Bello-Benítez and Ahedo to generate new initial profiles for this model when the simulation parameters are changed appreciably.

2.4. Breathing Mode Solutions

In the previous section, all solutions were fully-stationary, or there was a failure of the simulation due to the sheath collapsing. Here, solutions in which the ionisation instability develops are analysed, leading to 'breathing mode' solutions, where at long times (in the order of 10^{-3}s), and for V_d constant, I_d oscillates with a constant oscillation amplitude $\pm\Delta I_d$ and frequency f_d. Naturally, other plasma magnitudes oscillate too.

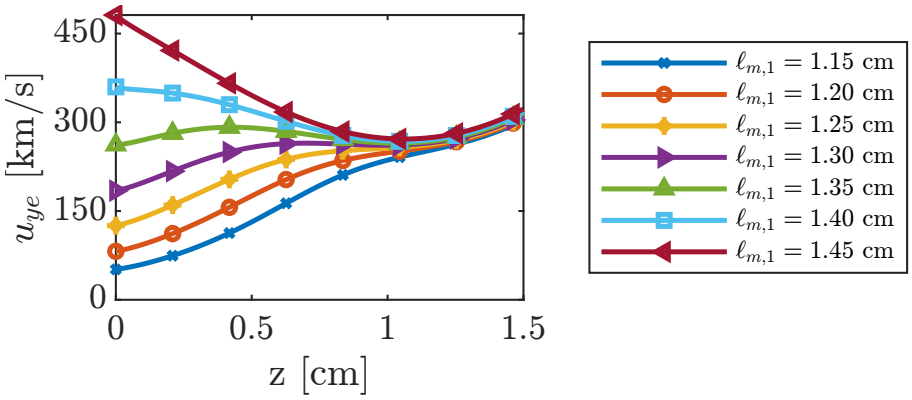

Figure 2.5: Model 5. Azimuthal electron velocity in the near anode region for the cases of Tab. 2.2.

Table 2.2: Model 5. Relevant plasma parameters at the anode for different values of the magnetic field at the anode.

ℓ_{m1}	B_A	$\lvert I_{iA}\rvert$	$\lvert I_{iA}\rvert/I_d$	n_{eB}	$\frac{4\lvert u_{zeB}\rvert}{\bar{c}_{eB}}$	$\frac{u_{yeB}}{\chi_B\lvert u_{zeB}\rvert}$
[cm]	[G]	[A]	[%]	$[10^{17}m^{-3}]$	[-]	[-]
1.15	2.4	0.77	14.5	7.61	0.040	1.15
1.20	3.5	0.70	13.2	6.95	0.044	1.13
1.25	4.9	0.63	11.9	6.27	0.048	1.11
1.30	6.6	0.55	10.6	5.57	0.053	1.08
1.35	8.7	0.48	9.2	4.86	0.060	1.03
1.40	11.0	0.41	7.9	4.12	0.069	0.95
1.45	13.7	0.34	6.6	3.39	0.082	0.86

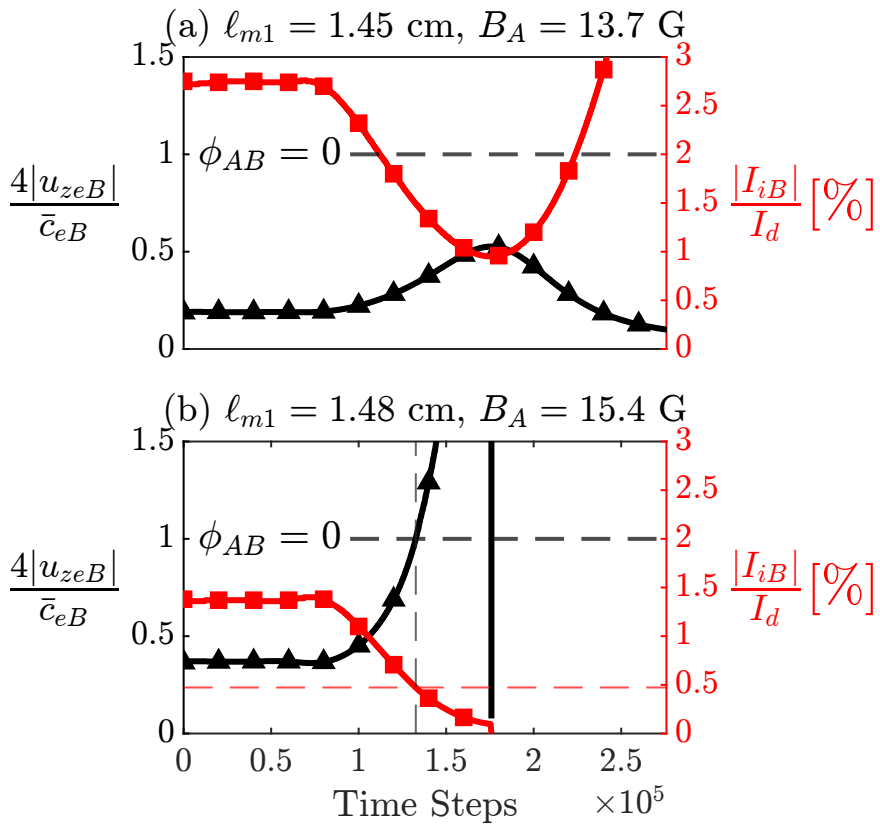

Figure 2.6: Anode sheath collapse in Model 5. Plot (a) represents a well-behaved simulation in nominal conditions, where a negative sheath is present, being $4|u_{zeB}|/\bar{c}_{eB} < 1$. Plot (b) represents a condition in which the sheath transition occurs, followed by the failure of the simulation, with M_e rapidly increasing over unity and the ion current fraction reaching 0.5%. The horizontal dashed line indicates the no sheath condition.

The development of the breathing mode is found to depend on both the physical model used and the values of several parameters. The analysis that follows is by no means exhaustive, but it clearly shows the difficulties in predicting the onset of the ionisation instability and its large sensitivity to the modelled physics and operating parameters.

2.4.1. Cases with total wall accommodation

As for most similar models in the literature, a breathing mode solution is particularly easy to recover in Model 1, where $u_{zn} = \text{const}$. To illustrate this, simulations with Model 1 are shown for the parameters of Table 2.1, except for ℓ_{m1}, which is varied. Figure 2.7 (top) states that the discharge is stationary for $\ell_{m1} \leq 1.376$ cm; it develops a breathing mode for 1.378 cm $\leq \ell_{m1} \leq 1.388$ cm; and there is a sheath collapse for larger values of ℓ_{m1}, corresponding to $B_A \geq 10.53$G.

Figure 2.7 (bottom) shows the oscillation range of both I_d and $|I_{iA}|$ in the transition from the 'stationary' to the 'breathing mode' regime. Once the breathing mode is triggered, the amplitudes of the oscillations grow with larger anode magnetic strength, eventually leading to model failure for $\ell_{m,1} \geq 1.388$. As an example, for $\ell_{m,1} = 1.383$, the mean value of I_d is 5.4 A, the oscillation amplitude and frequency are ± 0.23 A and 15.8 kHz, and the lower bound of $|I_{iA}|/\bar{I}_d$ is 0.0415.

When more physics is accounted for, it has been observed [40], [41] that the ionisation instability is more easily damped. This is also observed with our models: going from Model 1 to 5, with $\alpha'_w = 0$, Fig. 2.8 shows the time evolution of I_d for different models at $\ell_{m1} = 1.383$ cm, all of them launched with the same initial conditions. While Model 1 shows the commented breathing mode solution, initial oscillations of I_d are damped within 1 ms for Models 3 to 5, leading to a fully stationary solution. Model 2 is a particular case since initial oscillations decay very slowly. In fact, it takes about 80 ms for the current oscillations to damp completely for Model 2 and $\ell_{m1} = 1.383$ cm. For Model 2, the transition to a breathing mode solution takes place at $\ell_{m1} \simeq 1.39$ cm, and it is more drastic, as shown in Fig. 2.9. This is consistent with [41], which reported that when the neutral momentum is accounted for, the triggering of the ionisation instability requires a lower electron mobility.

2.4.2. Model 5 with partial wall accommodation

The previous subsection has discussed cases with perfect wall accommodation, i.e. $\alpha'_w = 0$. The parametric investigation of the onset of the breathing mode is here extended to $\alpha'_w > 0$ but focused on Model 5, which is the most affected by wall accommodation.

Figure 2.10(top) shows the regions in the parametric plane (ℓ_{m1}, α'_w), corresponding to the three types of solutions (stationary one, breathing mode, and sheath collapse). The solutions are considered stationary when the residual oscillations of I_d are smaller than

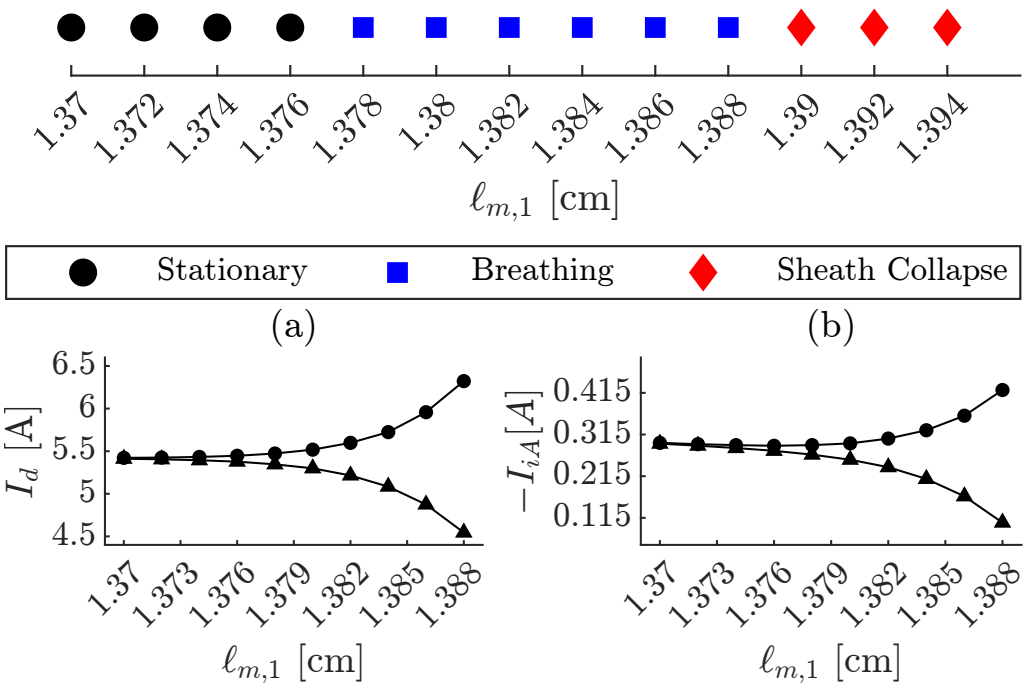

Figure 2.7: Model 1. (top) Classification of the discharge solutions for different ℓ_{m1} and the parameters of Tab. 2.1. (bottom) Lower and upper bounds of I_d and $-I_{iA}$ oscillations within the breathing mode interval.

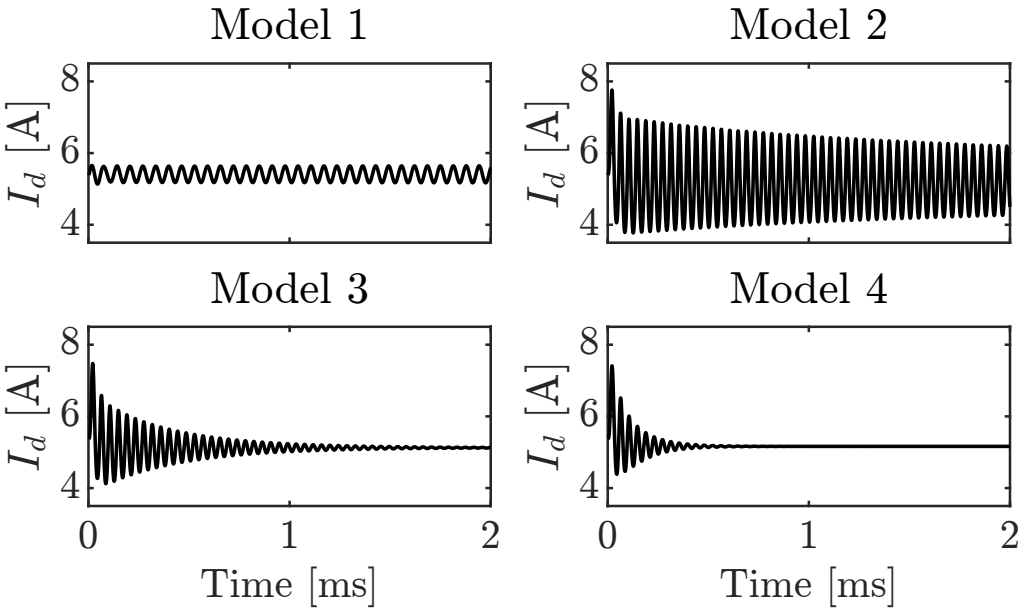

Figure 2.8: Time evolution of the discharge current for Models 1 to 4 for the first 2 ms. Model 5 behaves as Model 4. Simulation parameters correspond to table 2.1 exception made of $\ell_{m,1}$ =1.383 cm.

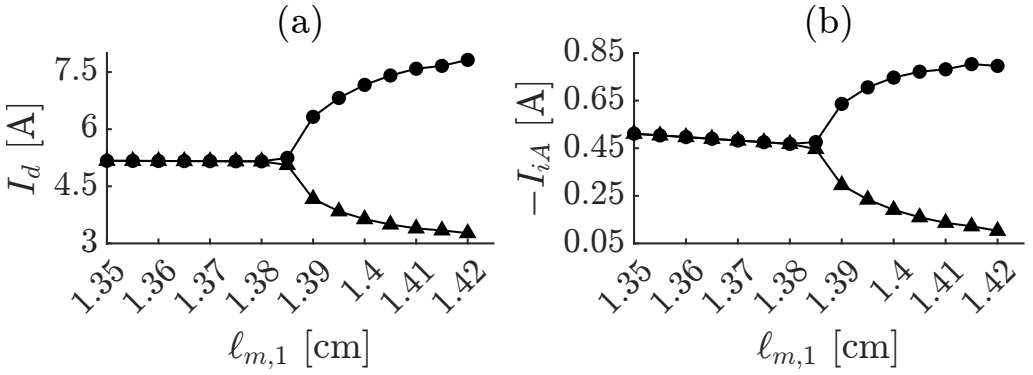

Figure 2.9: Lower and upper bounds of I_d and $-I_{iA}$ oscillations at 80 ms for values of $\ell_{m,1}$ within the stationary-breathing mode transition interval of Model 2.

2% after 4 ms of simulation time. The grey region at the bottom-right corner of the figure corresponds to stationary solutions requiring a smaller timestep for numerical convergence. For instance, the case ($\ell_{m,1} = 1.48$ cm, $\alpha'_w = 0$) requires a timestep of 5×10^{-11} s, ten times smaller than the one used in the rest of the simulations. This parametric plot shows that for ℓ_{m1} within the range considered, as α'_w increases, there is a transition from a stationary solution to a breathing mode case and finally to sheath collapse. The higher ℓ_{m1} is, the larger is the range of α'_w yielding stationary solutions.

Figure 2.10(bottom) quantifies for $\ell_{m1} = 1.40$ cm, the oscillations of I_d and $-I_{iA}$ as α'_w increases. The breathing mode appears for $\alpha'_w \approx 3.5\%$ and the normal-sheath model fails for $\alpha'_w > 8.5\%$. The amplitude of the oscillations increases with α'_w increasing. Very relevant for the failure of the simulations is the lower boundary of $-I_{iA}$, reaching 48 mA for $\alpha'_w = 8.5\%$; as a reference, $-I_{iA}$ =410 mA for $\alpha'_w = 0\%$.

A natural point arising from the results presented so far is the comparison between the breathing mode developing in Model 1, with total wall-accommodation, and the one in Model 5, with partial wall-accommodation. Figure 2.11 provides a partial response by considering two cases: Model 1 with ($\ell_{m,1} = 1.383$ cm, $\alpha'_w = 0$), and Model 5 with ($\ell_{m,1} = 1.383$ cm, $\alpha'_w = 3.9\%$). The resulting oscillation frequency and amplitude of I_d are 15.8 kHz and ± 0.23 A for Model 1 and 20.7 kHz and ± 0.49 A for Model 5; thus there is a non-negligible difference in the frequency. The behaviour of the two breathing modes has been assessed in the figure by comparing the phase and amplitude of the oscillations of $I_{i\infty}$, $\tilde{n}_e$, $\tilde{n}_n$, and $\tilde{T}_e$ with those of I_d; $I_{i\infty}$ is the ion current at the downstream boundary, and the other three magnitudes are average values over the whole domain of the corresponding magnitudes. The phase correlation with I_d of a variable X with oscillation $\pm\Delta X$ is computed as

$$R = \left(\int_0^T \Delta X \Delta I_d dt \right) \left(\int_0^T (\Delta X)^2 dt \int_0^T (\Delta I_d)^2 dt \right)^{-1/2} \tag{2.25}$$

and the time interval T is adjusted to several cycles of the breathing mode.

Figure 2.11 suggests that the two breathing modes have the same nature. Phase corre-

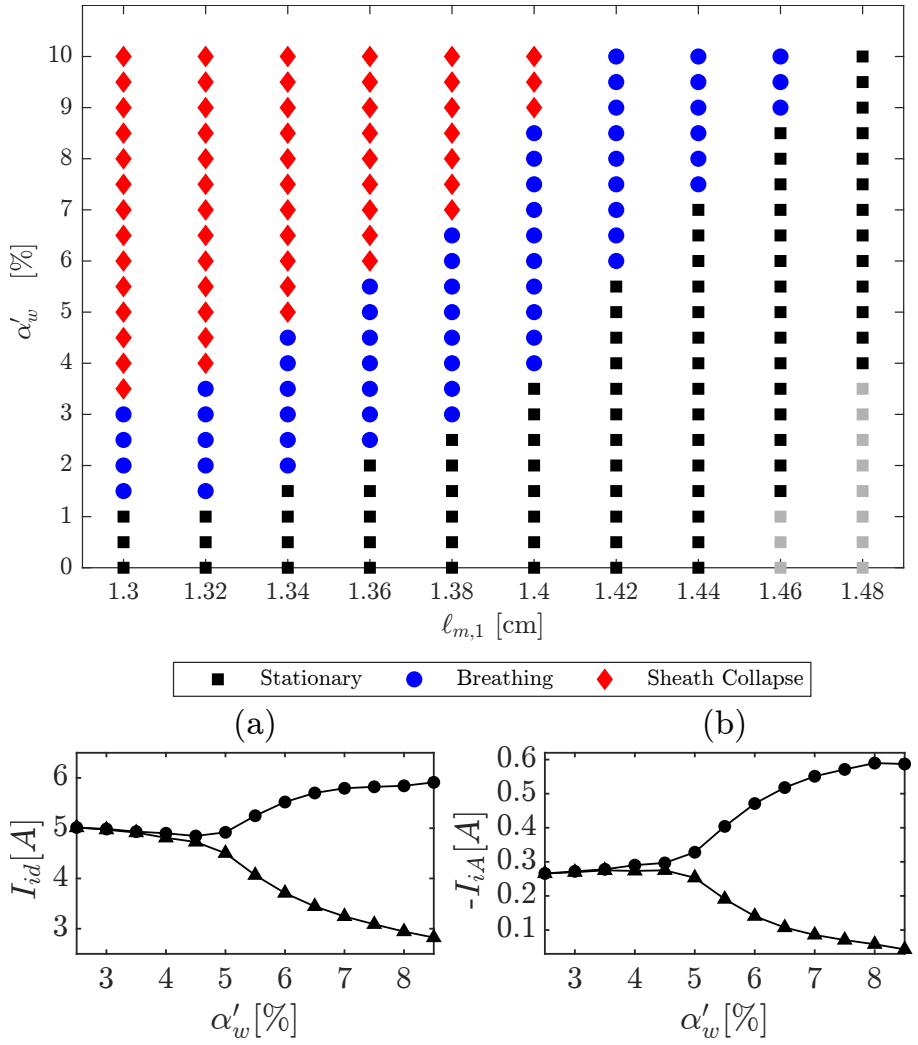

Figure 2.10: (Top) Domain of existence of different solution types for Model 5 for different α'_w and $\ell_{m,1}$ (i.e. B_A). Points in grey require a smaller timestep for numerical convergence (Bottom). Lower and upper bounds of I_d (a) and $-I_{iA}$ (b) for $\ell_{m1} = 1.40\,\text{cm}$ and different values of α'_w. For $\alpha'_w > 8.5\%$ the sheath collapse condition is reached.

lations and relative amplitudes are very similar with some differences only on the phase correlation of $\tilde{T}_e$ and the relative amplitudes of $I_{i\infty}$ and I_{iA}. The two breathing modes present a quasi perfect phase correlation of $I_{i\infty}$ and $\tilde{n}_e$ with I_d, a phase difference with I_d of 90° for I_{iA}, and $90 \pm 20°$ for $\tilde{T}_e$, and a phase difference of $\approx 65°$ between $\tilde{n}_e$ and $\tilde{n}_n$. Regarding the relative amplitudes of the oscillations of the different variables it is noteworthy: the near perfect match between $\tilde{n}_e$ and I_d (i.e. $\Delta\tilde{n}_e/\bar{n}_e \approx \Delta I_d/\bar{I}_d$, with overbars indicating mean-values); the limited oscillations of n_n and T_e; and the 4-times amplified oscillations of I_{iA}. Since $|I_{iA}| \ll I_d$, the electron current $|I_{eA}|$ oscillates approximately as I_d. These results for the breathing mode are well aligned with existing semianalytical theories [38], [49].

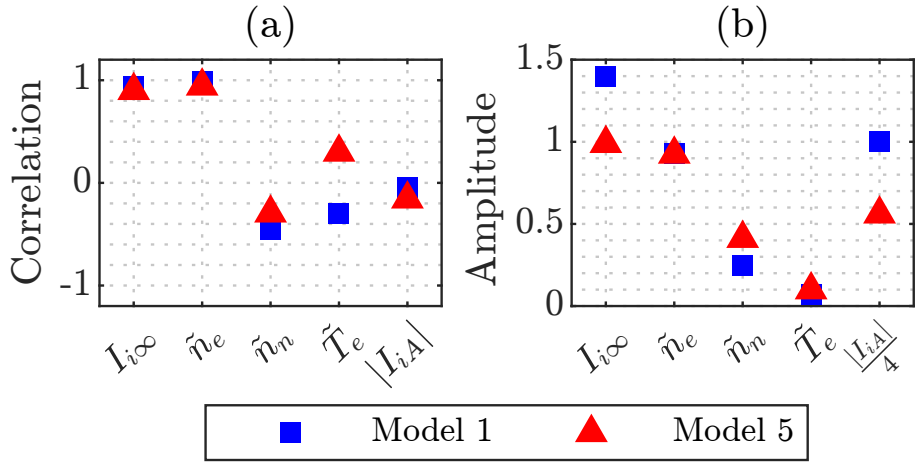

Figure 2.11: Comparison between the ionisation instability of Model 1 and Model 5 at $\alpha'_w = 3.9\%$. Subplot (a) shows the cross correlation of relative quantities, averaged in the whole domain, with respect to I_d. Subplot (b) shows the relative amplitude of the same quantities with respect to I_d. A factor of 1/4 has been included to plot the oscillation amplitude of I_{iA}.

2.5. Conclusions

A set of 1D time-dependent quasi-neutral models for HET discharges, with different treatments of several physical phenomena, has been presented. From Model 1 to 5, the neutral momentum equation, azimuthal electron inertia, neutral energy equation, and ion energy equations have been added. The plasma domain extends from the anode to the far downstream plume and includes a thick cathode neutraliser external to the thruster channel. These time-dependent models are generalisations of the 1D stationary model of Bello-Benítez and Ahedo, which already includes azimuthal electron inertia but considers only cold ions and neutrals.

The model, being 1D axially, includes the interaction of the plasma species with the lateral dielectric walls of the annular channel through empirical models for ion recombination and accommodation, and secondary-electron emission. On the other hand, the plasma attachment to the metallic anode (and gas injector) is assumed to generate a normal (i.e. electron-repelling) Debye sheath.

The numerical techniques used for the numerical integration in the stationary and time-dependent models are totally different. The experience has shown that numerical convergence is much better achieved by taking V_d as known and I_d as the output parameter, than vice versa. In the time-dependent model, this requires adding an integral relation for $I_d(V_d)$. The novelty here has been in including electron inertia and cathode effects in equation (2.21).

Simulations have been run for the five time-dependent models and certain ranges of main parameters. Three types of results have been found: fully-stationary solutions, breathing-mode-type solutions, and failure of the simulation due to the collapse of the

anode normal sheath.

Fully-stationary solutions have been benchmarked satisfactorily against those of Bello-Benítez and Ahedo [33], but they have also shown that the variations of T_i and T_n emanating from the respective energy equations affect the plasma response.

For the breathing mode, clear trends are found in the evolution of the oscillation of I_d, and other plasma currents, with the parameter triggering the breathing mode (for instance, the wall accommodation factor). While the oscillations of I_d are relevant for the anode-to-cathode power source, those of the ion current backstreaming to the anode, I_{iA}, are crucial for the plasma attachment. The failure of the time-dependent models presented here is due to very low values of $-I_{iA}$ and the collapse of the normal anode sheath. The solution to this numerical issue is to include full electron inertia and inverse anode sheaths within the model.

Apart from this, it is necessary to better fit wall-related source terms of this 1D axial model with the solutions obtained from 2D(z,r) models. Beyond gaining in accuracy, this is suspected to affect also the parametric regions for the breathing mode. Nonetheless, a systematic analysis of the breathing mode was out of the scope of this work. Here, an attempt was made to show that the breathing mode depends as much on the physics involved in the model as on the partially empirical parameters representing some effects (wall accommodation, neutral velocity,...). In our opinion, this reinforces a suggestion already implicit in the abundant literature on the subject: it seems extremely challenging to derive laws determining the parametric threshold of the breathing mode even in the simplified 1D configuration considered here.

Acknowledgments

This research was initiated in the frame of the project SIMTURB-CM, funded by Comunidad de Madrid, and was completed under the project ESPEOS, funded by Agencia Estatal de Investigación with Grant Number PID2019-108034RB-I00. A preliminary study [50] was first presented at the Space Propulsion Conference 2022, Estoril, Portugal, and received The Best PhD Paper Award in Space Transportation.

Appendices

2.A. Source terms and collision frequencies

This appendix summarises the formulas for the source terms and collision frequencies used in equations (2.3)-(2.11). Most of the expressions come from previous works on the axial fluid model [31]–[33], [51]. Xenon is used in the simulations here, and some constants below correspond to it exclusively.

Plasma production is given by $S_p = n_e \nu_p$, with the ionisation (or production) frequency is expressed as

$$\nu_p = n_n \bar{c}_e \sigma_{ion0} \left[1 + \frac{T_e E_{ion}}{(T_e + E_{ion})^2}\right] \exp\left(-\frac{E_{ion}}{T_e}\right), \tag{2.26}$$

with $E_{ion} = 12.1\text{eV}$ the first ionisation energy and $\sigma_{ion0} = 5 \times 10^{-20}$ m^2. In Eq. (2.9), the effective energy loss due to ionisation and excitation, satisfies

$$\mathscr{E}_{inel} = \left(2 + \frac{1}{4} \exp \frac{2E_{ion}}{3T_e}\right) E_{ion}. \tag{2.27}$$

The electron injection at the cathode, centred at z_N and with effective thickness $2\ell_c$, is assumed to follow [33]

$$S_c(z) = \frac{I_d}{eA\sqrt{\pi}\ell_c} \exp \frac{-(z - z_N)^2}{\ell_c^2}. \tag{2.28}$$

Applying this to Eq. (2.13) and integrating, the normalized current function $\imath_z = I_z/I_d$ satisfies

$$\imath_z = \frac{1}{2} \text{erfc} \frac{z - z_N}{\ell_c}. \tag{2.29}$$

The elastic electron-neutral collision frequency is modelled crudely as $\nu_{en} = n_n \bar{c}_e \sigma_{en}$ with

$\sigma_{en} = 27 \times 10^{-20} \mathrm{m}^2$. The elastic electron-ion collision frequency is modelled as

$$\nu_{ei} = n_i R_{ei}, \quad \frac{R_{ei}}{10^{-12} m^3/s} = 2.9 \cdot \left(\frac{1eV}{T_e}\right)^{3/2} \ln\Lambda,$$
$$\ln\Lambda \approx 9 + \frac{1}{2}\ln\left[\left(\frac{10^{18} m^{-3}}{n_e}\right)\left(\frac{T_e}{1eV}\right)^3\right]. \quad (2.30)$$

Finally, the parameters related to plasma interaction with the lateral dielectric walls are presented. The sheath potential fall in a dielectric wall satisfies

$$\Delta\phi_w = \frac{T_e}{e}\ln\left(\sqrt{\frac{m_i}{2\pi m_e}}(1-\delta_s)\right). \quad (2.31)$$

Here, δ_s is the effective SEE yield, modelled as

$$\delta_s = \begin{cases} \sqrt{T_e/T_1} & \text{if } T_e < T_1 \delta_s^{\star 2}, \\ \delta_s^\star & \text{if } T_e \geq T_1 \delta_s^{\star 2}, \end{cases} \quad (2.32)$$

with T_1 material-dependent and $\delta_s^\star$ the emission yield corresponding to the space-charge saturation limit. This one follows

$$\delta_s^\star = 1 - 3.32\sqrt{2\pi m_e/m_i}, \quad (2.33)$$

and represents the classical Hobbs-Wesson result [52]. In this work T_1 =36.77 eV. The wall-loss term in the continuity equations is expressed as $S_w = n_e \nu_w$, with

$$\nu_w = \tilde{\nu}_w \sqrt{T_e/m_i} \quad (2.34)$$

$\tilde{\nu}_w$ a fitting parameter, constant inside the source and decreasing to zero downstream the cathode. The wall-collisionality for electron momentum follows

$$\nu_{wm} = \nu_w \delta_s/(1-\delta_s) \quad (2.35)$$

and the effective energy loss per electron is

$$\mathscr{E}_{ew} = \left(5.62 + \frac{1.65}{1-\delta_s}\right) T_e \quad (2.36)$$

for Xenon.

An "average" ion impacts the lateral wall with an energy

$$\frac{m_i u_{zi}^2}{2} + \frac{5}{2}T_i + \frac{T_e}{2} + e\Delta\phi_w.$$

Most of this ion energy is accommodated at the wall, and the rest is re-injected by the new neutral from ion recombination. The understanding of this process continues to be under investigation [53], [54]. Here, a parameter α_w' measuring the 'non-accommodated energy' fraction is defined, and the resultant neutral energy is equi-distributed into the following thermal and (axial) mechanical parts:

$$\mathscr{E}_{nw} = \left(\frac{5}{2}T_i + \frac{T_e}{2} + e\Delta\phi_w\right)\alpha_w', \quad (2.37)$$

$$m_i u_{znw}^2/2 = \alpha_w' \, m_i u_{zi}^2/2. \quad (2.38)$$

CHAPTER 3

A Non-neutral 1D Fluid Model of Hall Thruster Discharges: Full Electron Inertia and Anode Sheath Reversal

This chapter reproduces the contents published by the author in the peer-reviewed journal Plasma Sources Science and Technology [29]. The typography has been adapted to the style of this thesis.

Abstract

A non-neutral model of the axial plasma discharge in a Hall thruster, including full electron inertia, is presented. In the finite-volume formulation, two types of sheath boundary conditions previously used in the literature are tested and proven to behave practically identically in this model. Both normal and reversed (i.e. electron repelling and attracting, respectively) anode sheaths are admitted. This model is compared with the quasineutral model developed in a previous work, which includes only azimuthal electron inertia and normal anode sheaths. Both models agree excellently within the parametric region where steady-state solutions with a normal anode sheath exist. The non-neutral model shows the absence of steady-state solutions with a reversed anode sheath. Nonetheless, a reversed sheath can appear during the transient to a steady-state solution with a normal sheath, and the periodic transition from a normal to a reversed sheath can be observed in the presence of breathing-mode oscillations. In other cases, the reversed sheath leads to the discharge shut-off. Full electron inertia is always important in the presence of a reversed sheath. The parametric threshold of the wall accommodation parameter from a stationary solution to a breathing mode one differs slightly between the non-neutral and the quasi-neutral model.

3.1. Introduction

Despite the decades of research on Hall Effect Thrusters (HETs), there is an incomplete understanding of the plasma structure in the near-anode region. Today, it is commonly accepted the existence of a plasma sheath (or anode fall), of the thickness of a few Debye lengths, such that the anode is at a lower or higher potential than the near-anode plasma. The difficulties in accurately measuring the plasma properties in the near-anode region led to a limited amount of experimental evidence. Zhurin *et al.* [16], who transcribed the vast knowledge of Russian literature, states that during normal operation, the electron thermal flux is sufficient to sustain the discharge and thus an electron-repelling sheath, hereafter called normal, forms at the anode. However, in case of low discharge voltage or propellant flow, the thermal flux is not sufficient, and an electron-attracting, or reversed, sheath is necessary; in this condition, the discharge is easily extinguished.

The presence of a normal electron-repelling sheath is indirectly associated with a backflow of ions, which has been experimentally observed by Bishaev and Kim [55] and Kim [46]. By measuring the plasma potential a few millimetres downstream of the anode, Dorf *et al.*[56], [57] obtained insight into the nature of the anode fall in HETs. The experimental evidence suggests that both a normal and reversed sheath can form, depending on the thruster operating parameters and the dielectric coating of the anode during the experiments. In clean anode conditions, the anode sheath is normally electron-repelling, with the potential drop decreasing at lower discharge voltages, while the appearance of dielectric deposition in the anode is associated with an electron-attracting anode fall. The formation of a normal sheath has been numerically observed in the models of Fife [58], Ahedo *et al.* [27], [31], and Barral *et al.* [59] in which the ion backflow is recovered. A reduction of the ion current to the anode is associated with a decrease in the anode potential fall, which eventually collapses, reaching the no-sheath condition. A similar sheath structure transition has been observed around the hollow anode of an Anode-layer type HET by Yokota et al.[60] with 2D particle-in-cell (PIC) simulations.

The no-sheath condition has been further investigated numerically by Ahedo and Rus [47], who suggested that when approaching the vanishing of the sheath, the azimuthal electron inertia becomes important, thus violating the drift-diffusion assumption. Recently Poli *et al.* [26] developed a time-dependent 1D quasi-neutral model which includes electron azimuthal inertia, where it has been shown how during strong 'breathing mode' oscillations the ion backflow to the anode can be greatly reduced, approaching the no-sheath condition and exiting the validity of the axial drift-diffusion regime for electrons: the model, which assumes the classical sheath formulation, cannot correctly capture the no-sheath condition and the simulation fails. A two-region asymptotic model of the plasma on a conducting electrode, capable of smoothly capturing the vanishing sheath, has been developed by Ahedo and Escobar [48] to characterise the near anode region of HETs. However, the model completely neglects the plasma discharge, thus the mutual influence of the sheath and bulk plasma during the HET operation, for which a

full model coupling the two regions is needed.

While the computational cost of 2D PIC codes makes them unsuited for simulating the neutral timescales and anode sheath physics, and 1D PIC codes are seldom used[61], the literature is populated with 1D fluid models of HET discharges [37], [38], [40]–[42]. However, the vast majority of them assume quasi-neutrality, the electron drift-diffusion approximation, and a normal anode sheath. An exception is Sahu et al. [39], who analysed a non-neutral model with full electron inertia. However, their analysis is focused on the comparison with quasi-neutral models and the relevance of electron inertia on anomalous electron transport.

In this work, the quasineutral model of Poli *et al.* is revisited to account for non-neutrality and self-consistent resolution of the anode sheath through Poisson's equation. The two-fluid description of the plasma sheath requires the imposition of specific boundary conditions for the ion and electron fluids; the two common approaches found in the literature, introduced by Cagas et al.[62] and Sahu et al.[39], are here analysed and compared both in the stationary and dynamic regimes. The non-neutral model is capable of resolving the smooth transition from a normal to a reversed anode sheath and demonstrates how this can occur during strong breathing mode oscillations, as suggested by Poli *et al.*.

The paper is organised as follows. The revisited model is presented in section 3.2 and the sheath boundary conditions in section 3.3.1. The comparison with the quasi-neutral model is presented in section 3.4 for a normal sheath condition. The transition to a reversed sheath is detailed in section 3.5 and finally, the ionisation instability is analysed in section 3.6.

3.2. Model Formulation

The model considers electrons, singly-charged ions, and neutrals (indexes *e, i, n*, respectively) as three different fluids and solves for the continuity, momentum, and energy equations. The model describes an axisymmetric plasma discharge by averaging the plasma properties along the radial direction. The full system of the three fluid plasma equations, written with standard notation, reads:

$$\frac{\partial n_e}{\partial t} + \frac{1}{A_c}\frac{\partial}{\partial z}\left(A_c n_e u_{ze}\right) = S_p - S_w, \tag{3.1}$$

$$\frac{\partial n_i}{\partial t} + \frac{1}{A_c}\frac{\partial}{\partial z}\left(A_c n_i u_{zi}\right) = S_p - S_w, \tag{3.2}$$

$$\frac{\partial n_n}{\partial t} + \frac{1}{A_c}\frac{\partial}{\partial z}\left(A_c n_n u_{zn}\right) = -S_p + S_w, \tag{3.3}$$

$$\frac{\partial}{\partial t}\left(n_e u_{ze}\right) + \frac{1}{A_c}\frac{\partial}{\partial z}\left(A_c n_e u_{ze}^2\right) = \frac{1}{m_e}\left(e n_e \frac{\partial \phi}{\partial z} - \frac{\partial p_e}{\partial z}\right) + n_e\left(u_{ye}\omega_{ce} - u_{ze}\nu_e\right), \tag{3.4}$$

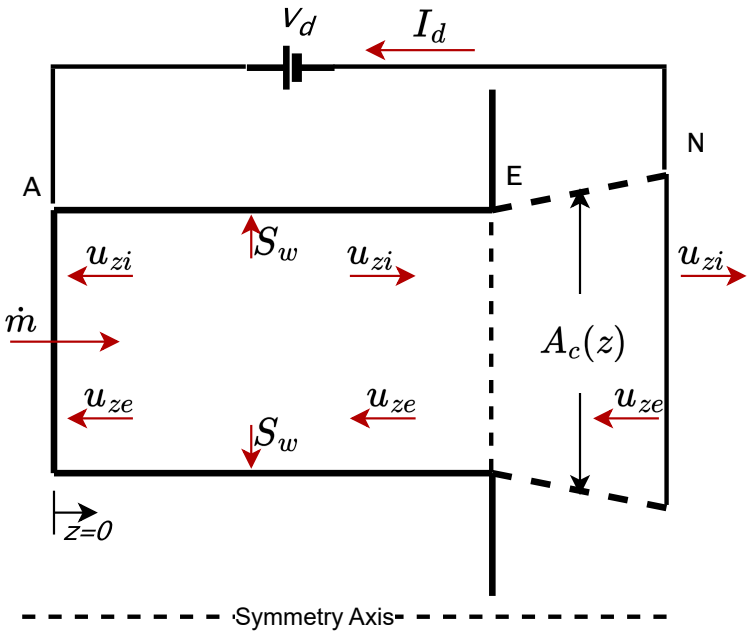

Figure 3.1: The figure represents the Hall thruster model used in this work. *A* represents the location of the anode, point *E* indicates the channel exit and *N* is the planar cathode boundary.

$$\frac{\partial}{\partial t}\left(n_e u_{ye}\right)+\frac{1}{A_c}\frac{\partial}{\partial z}\left(A_c n_e u_{ye} u_{ze}\right)=-n_e\left(u_{ze}\omega_{ce}+u_{ye}\nu_e\right), \tag{3.5}$$

$$\frac{\partial}{\partial t}\left(n_i u_{zi}\right)+\frac{1}{A_c}\frac{\partial}{\partial z}\left(A_c n_i u_{zi}^2\right)=-\frac{e n_i}{m_i}\frac{\partial \phi}{\partial z}-\frac{1}{m_i}\frac{\partial p_i}{\partial z}-S_w u_{zi}+S_p u_{zn}, \tag{3.6}$$

$$\frac{\partial}{\partial t}\left(n_n u_{zn}\right)+\frac{1}{A_c}\frac{\partial}{\partial z}\left(A_c n_n u_{zn}^2\right)=-\frac{1}{m_i}\frac{\partial p_n}{\partial z}-S_p u_{zn}+S_w u_{znw}, \tag{3.7}$$

$$\frac{\partial}{\partial t}\left(\frac{3}{2}p_e\right)+\frac{1}{A_c}\frac{\partial}{\partial z}\left[A_c\left(\frac{5}{2}p_e u_{ze}+q_{ze}\right)\right]=u_{ze}\frac{\partial p_e}{\partial z} - S_p\mathscr{E}_{inel}-S_w\mathscr{E}_{ew}+\left(n_e\nu_e+\frac{1}{2}\left(S_p-S_w\right)\right)m_e u_e^2, \tag{3.8}$$

$$\frac{\partial}{\partial t}\left(\frac{3}{2}p_i\right)+\frac{1}{A_c}\frac{\partial}{\partial z}\left(A_c\frac{5}{2}p_i u_{zi}\right)=u_{zi}\frac{\partial p_i}{\partial z}+S_p\left(\frac{3}{2}T_n+\frac{m_i}{2}\left(u_{zi}-u_{zn}\right)^2\right)-S_w\frac{3}{2}T_i, \tag{3.9}$$

$$\frac{\partial}{\partial t}\left(\frac{3}{2}p_n\right)+\frac{1}{A_c}\frac{\partial}{\partial z}\left(A_c\frac{5}{2}p_n u_{zn}\right)=u_{zn}\frac{\partial p_n}{\partial z}-S_p\frac{3}{2}T_n+S_w\left(\mathscr{E}_{nw}+\frac{m_i}{2}\left(u_{zn}-u_{znw}\right)^2\right), \tag{3.10}$$

$$q_{ze}=-\frac{5p_e}{2m_e}\frac{\nu_e}{\nu_e^2+\omega_{ce}^2}\frac{\partial T_e}{\partial z}. \tag{3.11}$$

In addition, the potential is computed from Poisson's equation

$$\frac{d^2\phi}{dz^2}=\frac{e}{\varepsilon}\left(n_e-n_i\right), \tag{3.12}$$

with ε the plasma permittivity.

Analogously to Poli *et al.*, the continuity equations (3.1)-(3.3) include the volumetric plasma production $S_p = n_e \nu_p$ and recombination at the lateral walls $S_w = n_e \nu_w$, for which the collision frequencies can be found in [26]. Isotropic scalar pressure $p_s \equiv n_s T_s, (s = e, i, n)$ is assumed for the momentum equations, and ions are considered unmagnetised; in the electron momentum equations, $\omega_{ce} = eB/m_e$ is the gyrofrequency and ν_e the total electron collision frequency, which is used to define a resistive force. Four contributions are included in the collision frequency

$$\nu_e = \nu_{ei} + \nu_{en} + \nu_{wm} + \alpha_t \omega_{ce}, \tag{3.13}$$

namely: the electron-ion, electron-neutral, wall collision frequency and a model for the anomalous transport; the latter is hereby defined with an empirical parameter $\alpha_t = 0.01$, which is kept constant throughout the paper. A detailed description of the collision frequencies and the expansion of the plume cross-section can be found in [26]. Ion-neutral charge exchange collisions are not considered in this model.

The momentum and energy equations of neutrals include terms proportional to u_{znw} and $\mathscr{E}_{nw}$, accounting for the energy of neutrals coming from ion recombination at the lateral walls. Following [26], $\mathscr{E}_{nw}$ and $m_i u_{znw}^2/2$ are considered proportional to a wall accommodation parameter α'_w, with α'_w=0 corresponding to total wall accommodation (i.e. no energy of the recombined ion is retained). This empirical parameter is difficult to fit from existing experimental and theoretical evidence. Laser-induced fluorescence measurements in a HET coupled with hybrid simulations was used by Mazouffre et al.[63] to find $\alpha'_w \approx 10\%$ as the best fit. On the other hand, α'_w=0 was used by Hofer et al.[64] based on the analysis of gas interactions with general surfaces (not specific for HET) by Bird[65]. Thus, the range $\alpha'_w = 0 - 10\%$ has been considered in [26] and the present paper.

The electron energy equation (3.8) includes the axial heat flux, reported in Eq. (3.11), which is important to avoid nonphysical electron temperatures[27]. Nonetheless, this heat flux is modelled with the conductive law (3.11) and uses the same effective collisionality ν_e as for particle diffusion. This Fourier's law must thus be considered as a simple quasistatic closure of the fluid equations. Further works could consider the temporal-spatial evolution of the heat flux and a higher-order moment closure of the electron fluid model.

Finally, the magnetic field profile used for this 1D model is [28]

$$\boldsymbol{B}(z) = \mathbf{1}_r \, B_m \exp\left[-(z - z_m)^2 / \ell_m^2\right], \tag{3.14}$$

where B_m is its maximum value, z_m is the location of the maximum and $\ell_{m1,2}$ the characteristic lengths of magnetic decay inside and outside the channel.

The system of equations is integrated in time using a second-order total variation diminishing Runge-Kutta scheme[66] and discretised in space with the Kurganov-Tadmor [44] second-order finite volume scheme. Each species is treated individually as a separate hyperbolic system. As for the electrons, the energy equation is a convection-diffusion PDE, which is solved explicitly in time with the continuity and momentum equations. Poisson's equation is discretised using finite differences, and the resulting tridiagonal matrix

is solved using the Thomas algorithm. In the nominal case, the domain is discretised in 1000 cells and advanced in time with a time-step $\Delta t = 1$ ps, thus resolving both the Debye length and the plasma frequency constraints.

The present non-neutral model (NNM) and the quasi-neutral model (QNM) of Poli *et al.* [26] differ, of course, on the treatment of Poisson's equation and the resultant boundary conditions at the ends of the plasma domain. In addition, the NNM includes both the azimuthal and axial inertia of electrons, while the QNM only includes the azimuthal electron inertia. There are no changes in the treatment of the heavy species. Additionally, the plasma domain in Ref. [26] extended across a volumetric cathode, into the far plume, while here it goes from the anode to a surface (infinitely thin) cathode that decouples the far plume. This is justified by the much higher computational cost here and the delicate numerical convergence of the fluid equations coupled with Poisson's one in the rarefied far plume with the volumetric cathode. The effects of collapsing the volumetric cathode to a surface one are briefly discussed in appendix 3.A.

3.3. Boundary Conditions

The system of 11 equations requires the specification of boundary conditions. Anode boundary conditions for ions and electrons will be discussed separately in section 3.3.1 since the formation of the anode sheath requires particular care.

The neutral fluid is injected supersonically, allowing for the imposition of temperature, velocity, and mass flow rate, accounting for ion recombination at the anode. At the cathode, outflow boundary conditions are imposed. Electrons are injected at the cathode with a current $I_{eN} = I_d - I_{iN}$ and a given energy $\mathscr{E}_{ec}$; the azimuthal velocity at injection is set to zero. Ions leave the domain supersonically at the cathode, so that an outflow condition is used. Finally, Dirichlet conditions specify the discharge potential between the anode and cathode in Poisson's equation.

3.3.1. Anode boundary conditions

In the literature, two main kinds of fluid boundary conditions allow the resolution of the Debye sheaths, which hereby will be referred to as the *vacuum* and *kinetic* conditions. A third type of boundary condition is used by [67], [68], which however can be reconducted to a simplified version of the kinetic boundary condition, as shown later.

The *vacuum boundary condition* (VBC), proposed by Cagas et al. [62], relies on the assumption that no plasma exists outside of the computational domain, i.e. in the absorbing wall on which the sheath will form. If a ghost-cell approach is used in the formulation of the boundary conditions, coupled with a Riemann solver-based discretisation algorithm, such a condition can be easily imposed by setting to zero all the plasma properties in the ghost-cell. The strong discontinuity with the domain's interior can be resolved with

an exact or approximate Riemann solver, which will compute the correct fluxes across the wall interface. Applying such conditions to both the ion and electron fluids will result in the formation of a sheath, even though no physical constraint on the plasma sheath is directly taken into account, thanks to the information on the wave speeds (much larger for electrons, being based on the species sound-speed) intrinsically used by the Riemann solver. Since dealing with zero density is impractical in the Fortran numerical code, a particle number density of 1 m^{-3} is used to avoid division by zero. For what concerns the electron energy equation, the inclusion of the diffusion term requires the imposition of two boundary conditions, one for the anode and one at the cathode. Setting $T_e = 0$ in the ghost cell would result in zero temperature at the wall, leading to problems in the numerical code; to avoid this, the temperature is computed from the first cell with a zero-order extrapolation (note that in the ghost cell, $p_e \approx 0$ is still valid, being $n_e \approx 0$). Finally, if an approximate Riemann solver is used, care must be taken to ensure the positivity of density and energy, which can be violated in near vacuum conditions for non positive-preserving schemes [69].

The *kinetic boundary condition* (KBC) is based on the assumption that the plasma at the anode follows a drifted Maxwellian velocity distribution function (VDF), and no particle is re-emitted into the plasma from the wall (the secondary electron emission yield of metals is generally very low, thus it is usually neglected at the anode). First introduced by Sahu et al. [39] as a sheath boundary condition, it is derived from the classic theory of molecular flow impinging on a surface [70]. While the assumption of a Maxwellian VDF at the anode is in general arguable [71], a more appropriate description would be obtained with a half-Maxwellian VDF, being the wall a physical boundary after which no plasma exists. In this assumption, the fluid velocity is a result of the asymmetry of the truncated VDF, showing good agreement with the kinetic theory[72]. However, by definition, the fluid formulation assumes a full Maxwellian VDF at every point of the domain, so an inconsistency would arise if the thus computed $n_\alpha, T_\alpha, \bar{u}_\alpha$ are used to define a half-Maxwellian VDF of the species $\alpha = i, e$. By carrying out the integration for the different moments of the velocity distribution function, we obtain the following fluxes of particles, axial and azimuthal momentum, and energy, respectively:

$$\Gamma_{1\alpha} = \pm n_\alpha \frac{\bar{c}_\alpha}{4} \left[\exp(-\tilde{u}_{z\alpha}^2) + \sqrt{\pi}\tilde{u}_{z\alpha}\left(\operatorname{erf}\tilde{u}_{z\alpha} \pm 1\right)\right], \tag{3.15}$$

$$\Gamma_{2\alpha} = \pm \frac{n_\alpha T_\alpha}{m_\alpha} \left[\frac{\tilde{u}_{z\alpha}}{\sqrt{\pi}}\exp(-\tilde{u}_{z\alpha}^2) + \left(\frac{1}{2} + \tilde{u}_{z\alpha}^2\right)\left(\operatorname{erf}\tilde{u}_{z\alpha} \pm 1\right)\right], \tag{3.16}$$

$$\Gamma_{3\alpha} = u_{y\alpha}\Gamma_{1\alpha}, \tag{3.17}$$

$$\Gamma_{4\alpha} = \pm n_\alpha \frac{\bar{c}_\alpha}{4} T_\alpha \left[2\exp(-\tilde{u}_{z\alpha}^2) + \frac{5}{2}\sqrt{\pi}\tilde{u}_{z\alpha}\left(\operatorname{erf}\tilde{u}_{z\alpha} \pm 1\right)\right], \tag{3.18}$$

where $\tilde{u}_{z\alpha} = u_{z\alpha}(2T_\alpha/m_\alpha)^{-0.5}$ is the normalized axial velocity and $\bar{c}_\alpha = (8T_\alpha/\pi m_\alpha)^{0.5}$ the thermal speed; the $\pm$ depends on the direction of the cell face normal, the minus here applying to the anode face . The fluxes, computed from the plasma properties at the anode, can be readily used as boundary conditions in the finite volume scheme for both ions

Table 3.1: Relevant simulation parameters for the nominal case.

Parameter	Value	Parameter	Value
$\dot{m}$	$4.75\,\mathrm{mg\,s^{-1}}$	V_d	300 V
T_n	0.06 eV	$\mathscr{E}_{ec}$	5 eV
u_{zn}	$300\,\mathrm{m\,s^{-1}}$	θ	16 deg
B_m	266 G	z_m	2.5 cm
ℓ_{m1}	1.30 cm	ℓ_{m2}	1 cm
z_E	2.5 cm	z_N	3.35 cm
A_c	$40\,\mathrm{cm^2}$	R	4.25 cm
d_{c0}	1.5 cm	α'_w	0 %
α_t	0.01	$\tilde{\nu}_w$	0.17
ε	$8.85\times10^{-11}\,\mathrm{F\,m^{-1}}$		

and electrons by replacing the numerical flux computed at the boundary interface. This boundary condition naturally adapts to both normal and reversed sheaths. For instance, from Eq. (3.15) the two limits

$$\lim_{\tilde{u}_{z\alpha}\to 0}\Gamma_{1\alpha} = \pm n_\alpha\frac{\bar{c}_\alpha}{4}, \qquad \lim_{\tilde{u}_{z\alpha}\to\infty}\Gamma_{1\alpha} = n_\alpha u_{z\alpha}, \tag{3.19}$$

represent the extreme cases of density flux in the case of no bulk velocity and hypersonic flow directed towards the wall, which in the case of an electron fluid would result in a normal and reversed sheath, respectively.

The third kind of boundary condition that is commonly found is based on the integration of a Maxwellian VDF with zero drift velocity. The resulting mass flux is equivalent to the first limit case of Eqs. (3.19) and the boundary condition is obtained by the simple summation of the convection flux and the thermal flux:

$$\Gamma_{1\alpha} = n_\alpha\left(u_{z\alpha}\pm\frac{\bar{c}_\alpha}{4}\right). \tag{3.20}$$

While formally, the limits of this boundary condition are equivalent to Eqs. (3.19), the simple summation of the fluxes will result in inaccurate predictions for $u_{z\alpha} = O(\bar{c}_\alpha)$.

3.4. Steady State Solutions with Normal anode sheath

The relevant parameters used for the simulation are reported in Tab. 3.1 and correspond to the nominal steady-state simulation of [26]; it must be noted that in this work the volumetric cathode and plume have been dropped, reducing the domain to the one of Fig. 3.1. The surface cathode has been chosen to better compare with the non-neutral model, for

which the extended domain means much larger computational times and convergence issues related to the solution of Poisson's equation. The QNM and NNM are compared in Fig. 3.2, accounting for the different boundary conditions in the latter one. The comparison shows excellent agreement between the models, exceptions made for the axial velocities and densities at the anode, which will differ due to the self-consistent resolution of the sheath. The anode currents and the sheath potential are reported in Tab. 3.2, where the models converge to the same discharge current with a maximum error of 0.5%. It has been observed that in general, the quasi-neutral model predicts a lower $|I_{iA}|$, which in extreme cases can lead to the failure of the classic sheath model. The sheath potential is hereon indicated by ϕ_{AB} for both the QNM and NNM, where the point B corresponds to the location where the Bohm criterion is met, either for ions or electrons in normal and reversed sheath, respectively.

The steady-state comparison shows how the two sheath boundary conditions lead to negligible differences in the discharge profiles. The zoom-in of plot (h) of Fig. 3.2 shows the self-consistent plasma sheath compared with the infinitely thin sheath model in the QNM [26], for which the potential drop satisfies

$$\phi_{AB} = \frac{T_{eB}}{e} \ln \frac{\bar{c}_{eB}}{4|u_{zeB}|} \tag{3.21}$$

with $\bar{c}_{eB} = \sqrt{8T_e/\pi m_e}$ the electron mean thermal velocity. It can be seen that the sheath potential is slightly overestimated with respect to the thin sheath model, and the VBC produces a larger drop than the KBC; nevertheless, the differences are marginal and can safely be neglected.

The comparison between the QNM and NNM has been performed for different values of ℓ_{m1} (and thus of B_A); a maximum value of $\ell_{m1} \approx 1.34$ cm exists for the QNM, above which the sheath collapses during the transient phase and leads to the failure of the simulation. However, up to this value, the steady-state solution of the QNM reproduces very well that of the NNM, demonstrating the validity of the QNM assumptions as long as the no-sheath condition is not reached. An upper limit on the magnetic field also exists for the NNM, for which the plasma discharge can detach from the anode as shown in section 3.5.

The boundary conditions for the NNM are analysed here. In a normal sheath regime, the sheath formation implies the satisfaction of the Bohm criterion for ions, which are required to cross the sheath boundary with $u_{zi} \geq c_s$, where $c_s = [(T_e + T_i)/m_i]^{0.5}$ is both the Bohm's and the ion-sound speed in this fluid model. The fulfilment of the Bohm criterion is reported in Fig. 3.3 (top), where for both boundary conditions the ions enter the sheath (identified as the region where charge separation becomes large) supersonically. In the case of the VBC condition, the ion sonic point is slightly closer to the anode than with the KBC; nonetheless, it still enforces the Bohm criterion, as opposed to what Joncquieres *et al.* [67] observed. The differences with respect to Joncquieres et al. extend to the momentum balance in the near anode region, wherein the current implementation of the VBC and KBC show the same behaviour, as shown in Fig. 3.3 (bottom). For both conditions, the dominant terms are the pressure and the electrostatic forces, which do not

Table 3.2: Nominal case. Anode currents and sheath potential at steady-state for the case of Tab. 3.1.

	NNM + KBC	NNM + VBC	QNM
I_d [A]	5.1159	5.0880	5.1118
$\lvert I_{iA}\rvert$ [A]	0.4726	0.4796	0.4124
ϕ_{AB} [V]	10.17	10.8	9.05

vanish at the wall; this is in contrast with [67] in which the vacuum condition results in zero pressure and electrostatic force at the wall. From the axial momentum balance, the axial inertial terms can be safely neglected, as expected in normal sheath operation, where the drift-diffusion approximation is in general justified.

Table 3.1 shows that the nominal simulation applies in Poisson's equation a permittivity ten times the vacuum one, ε_0, to relax the Debye length and the timestep. Fig. 3.4 plots n_e and ϕ for the nominal case but three different permittivities. The differences between the cases ε equal to ε_0 and $10\varepsilon_0$ are negligible except for the extension of the thin anode sheath, and thus $\varepsilon = 10\varepsilon_0$ is used throughout the paper. For $\varepsilon = 100\varepsilon_0$ there are mild differences in the electron density profile. The computational gain by multiplying the permittivity by 10 is 7 times.

3.5. Anode sheath reversal

Normal Hall thruster operation requires the presence of an ion back-flow at the back of the thruster channel to keep the plasma discharge 'attached' to the anode. The ratio of the ion backstreaming and the discharge currents $|I_{iA}|/I_d$, is an important parameter for the overall thruster efficiency. In usual operating conditions, the magnetic field is regulated so that the backstreaming current is $5-10\%$ of I_d, with the thruster efficiency degrading for larger percentages. This is associated with the formation of a normal sheath, which accelerates the ions, providing the necessary backflow. However, there might be conditions for which the anode sheath fall is reduced, such as at low mass-flow rate [16] or low discharge voltage [47], or more in general when the electron transport to the anode is smaller, either due to a large magnetic field (or a cusped topology [73]) or to dielectric coating deposited on the anode during the thruster operation [57]. When the electron transport becomes too small to sustain the discharge, the sheath collapses and a reversed sheath forms. The classic sheath formulation used in 1D HET models cannot capture the transition, being based on the hypothesis of $u_{ze} \ll c_e$, thus resulting in the failure of the simulation. Moreover, the drift-diffusion assumption for the electrons is no longer valid in a positive sheath, as shown later.

The non-neutral two-fluid formulation of the present model allows to resolve the transition to a reversed sheath. In this work, in line with [26], the transition is triggered by reducing the anode electron mobility by increasing the anode magnetic field. As with the quasi-neutral model, an increase of B_A results in a decrease of I_{iA}, which eventually

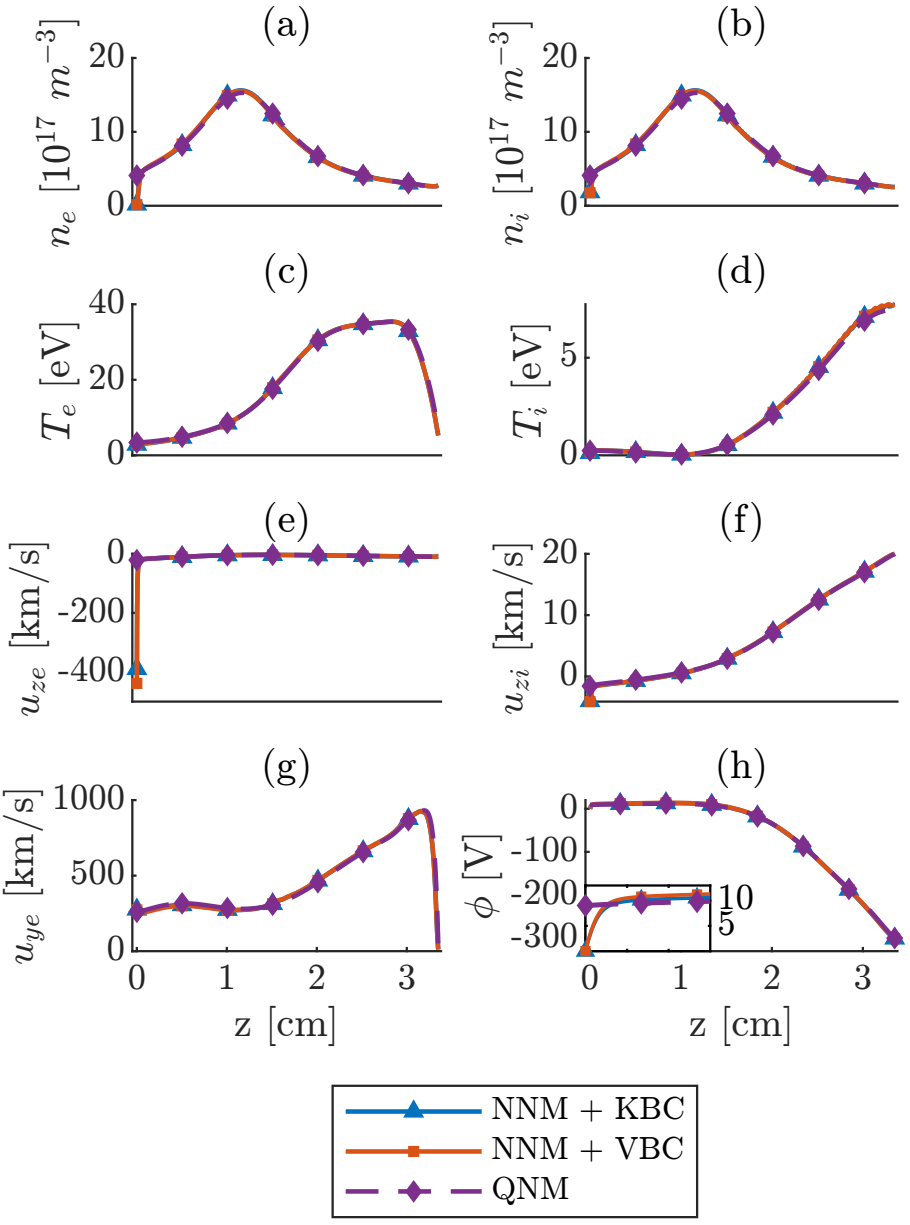

Figure 3.2: Nominal case, defined in Table II. Comparison of steady-state solutions for the NNM + KBC and NNM + VBC, with the QNM of [26].

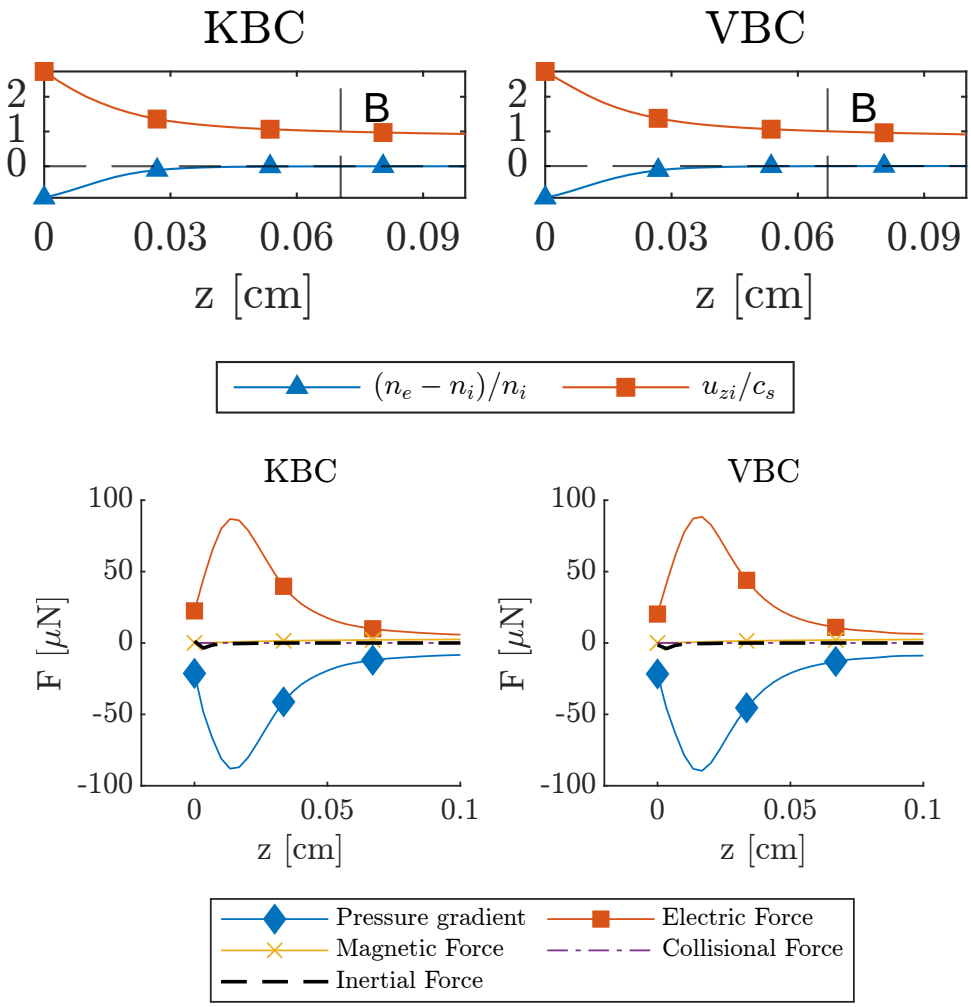

Figure 3.3: (Top) Comparison of the fulfilment of the Bohm criterion for the KBC and VBC for the nominal case at steady state. The vertical dashed lines identify the point where u_{zi} matches the Bohm velocity (point B). (Bottom) Steady-state comparison of the near anode electron axial momentum balance for the KBC and VBC.

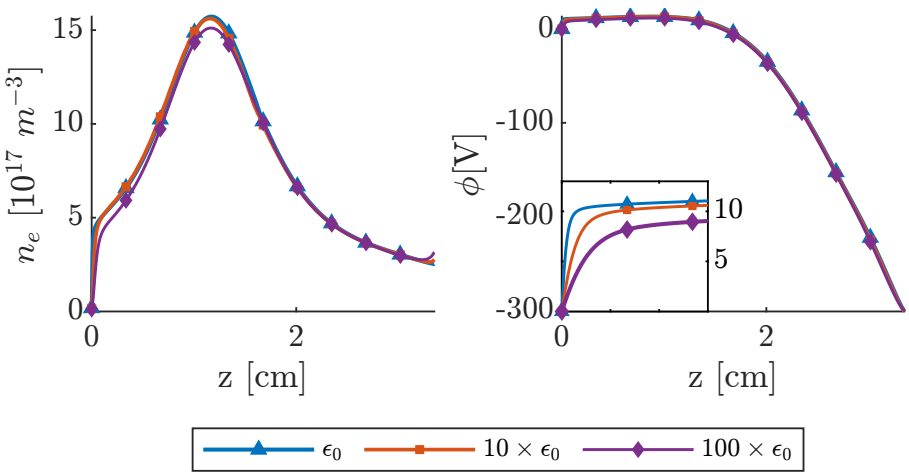

Figure 3.4: Steady state comparison for different values of permittivity for the case reported in Tab. 3.1.

leads to the collapse of the anode sheath and subsequently to the formation of a reversed sheath.

For moderate values of B_A, the transition to a reversed sheath, coincident with the depletion of ion density at the anode, is unstable, and the plasma discharge manages to re-attach itself to the electrode in a few µs, recovering the normal sheath condition. However, if B_A is further increased, the discharge completely detaches from the anode in the order of tens of µs, leading to the depletion of plasma density in the whole domain which eventually causes the failure of the simulation: for the parameters of Tab. 3.1, the limit is at ℓ_{m1} =1.42 cm (i.e $B_A = 12.04$ G), above which no solution is found. These different behaviours are reported in Fig. 3.5 where depending on B_A the discharge either recovers or shuts off at ~ 60 µs; in both cases, during the reversed sheath operation, $I_{iA} \approx 0$ A, as shown in Fig. 3.5 (bottom). The time evolution of the depletion of ion density is shown in Fig. 3.6 for the NNM+KBC at ℓ_{m1} =1.422 cm (i.e $B_A = 12.14$ G). As for the steady state solution, the increase in vacuum permittivity does not affect the overall behaviour of the anode sheath dynamics: using $\varepsilon = \varepsilon_0$, the discharge has the same behaviour as Fig. 3.5 but with a stronger electric field and a more abrupt transition. (Indeed, the same trend is found when going from $\varepsilon = \varepsilon_0$ to the quasineutral limit $\varepsilon = 0$.)

The instantaneous axial electron momentum balance in the reversed sheath condition is reported in Fig. 3.7 for both the vacuum and kinetic boundary conditions. In the electron-attracting sheath condition, the role of ions and electrons is exchanged, so that electrons satisfy the analogue of the Bohm criterion, entering the sheath supersonically. Pressure is no longer balancing the electric force, which is compensated by the inertial terms; consequently, the drift-diffusion approximation is not valid anymore.

A different mechanism which can trigger the transition to a reversed sheath is the reduction of the mass flow rate to small values, as observed by Zhurin *et al.* [16]. The present model behaves as expected, and for low values of $\dot{m}$ ($\sim 20\%$ of the nominal mass flow rate), the anode sheath is reversed and extends into a large fraction of the channel, being the plasma density extremely low. In this operating condition, the discharge gets easily extinguished and the plasma density is completely depleted in ~ 200 µs.

In general, the non-neutral model could not obtain a stationary reversed sheath operating point, but rather an unstable condition that either transitions to the normal sheath or results in the shut off of the discharge.

3.6. Breathing Mode and sheath reversal

In this section, the non-neutral model is used to show cases exhibiting "breathing-mode" (BM) oscillations with normal and reversed sheaths. As in [26] for Model 5 (the closest to the present nonneutral model), the nominal case of Table I does not develop the BM, even changing ℓ_{m1} (i.e. the magnetic field profile), and the accommodation parameter α'_w will be varied to obtain BM solutions and show the presence of reversed sheaths. Other parameters could have been used for this, but an analysis of the parametric regime for the

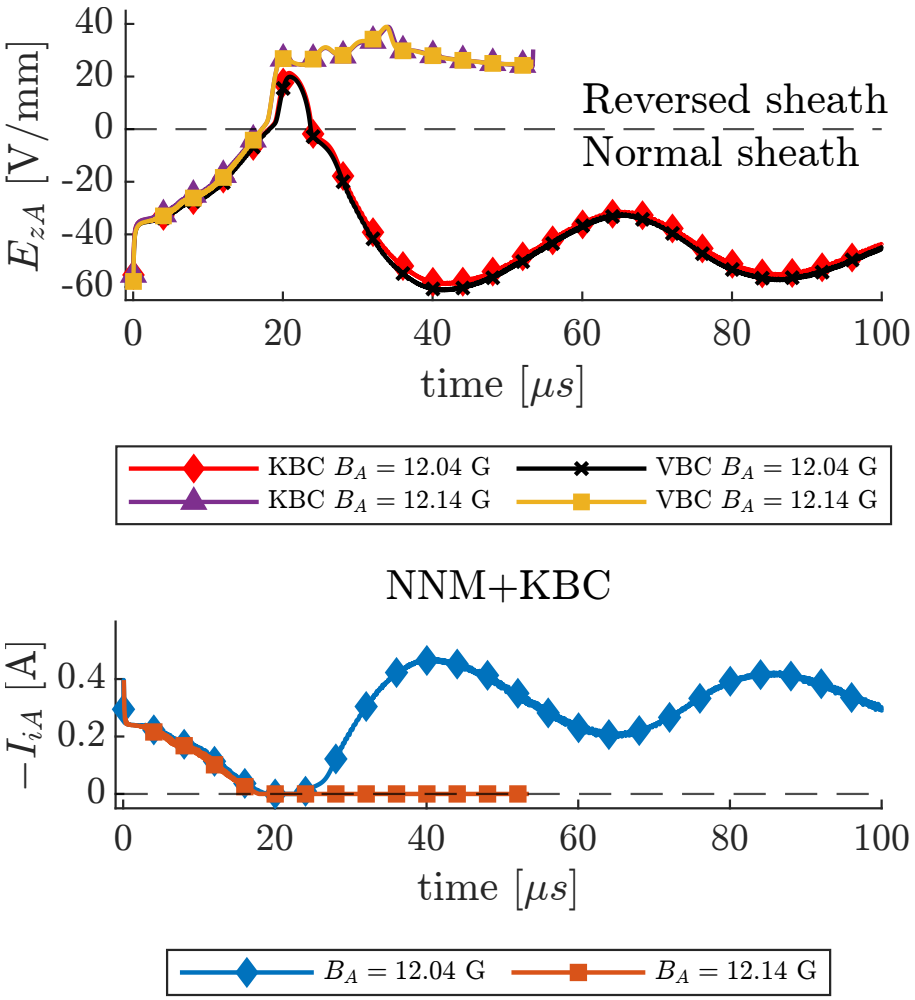

Figure 3.5: (Top) Anode electric field for the *vacuum* and *kinetic* conditions plotted over time. For the case at B_A =12.04 G the sheath experiences a temporary transition to electron-attracting before stabilizing on the normal sheath operating condition; whereas for the case at B_A =12.14 G the plasma discharge does not recover from the transition and eventually completely detaches from the anode leading to the shut off of the discharge. (Bottom) Detail of $-I_{iA}$ in the two aforementioned cases for the *kinetic* boundary condition.

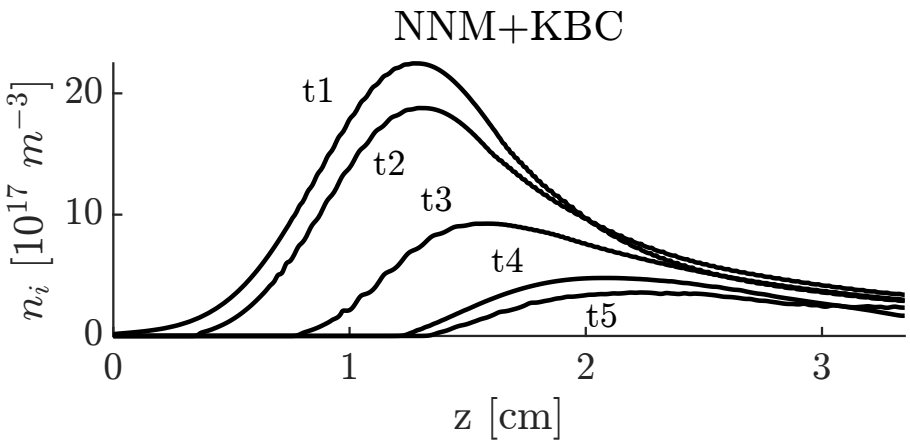

Figure 3.6: Time evolution of n_i for the case with B_A =12.14 G and KBC. The time evolution starts at the transition of the anode sheath from normal to reversed, associated with a strong depletion of the ion density which eventually extends to the whole domain, leading to the failure of the simulation and the shut off of the discharge. In the plot, $t1 \approx$ 25 µs and $t5 \approx$ 57 µs .

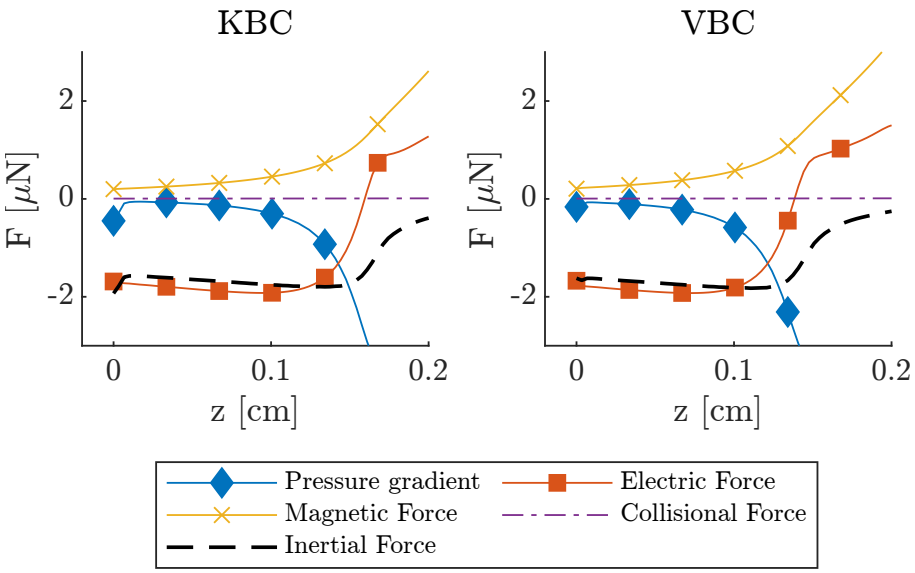

Figure 3.7: Instantaneous near anode electron axial momentum balance for the KBC and VBC in a reversed sheath. The plot refers to the timestep of maximum electric field in the reversed sheath shown in Fig. 3.5 (top) for B_A =12.04 G. The knee observable in the electric force roughly describes the extension of the reversed sheath in the thruster channel.

Table 3.3: Mean and oscillations of discharge current, sheath potential (at the Bohm crossing point) and breathing mode frequency for the kinetic and vacuum conditions. Nominal case except for ℓ_{m1} =1.30 cm, $\alpha'_w = 5.5\%$.

	NNM + KBC	NNM + VBC
I_d [A]	4.56 ± 2.12	4.55 ± 2.09
ϕ_{AB} [V]	6.72 ± 5.21	7.18 ± 5.20
f [kHz]	20	20

BM is out of the scope here.

While quasi-neutral 1D models have been extensively used in the literature to simulate the ionisation instability, to our knowledge, there is no analysis of such a phenomenon when non-neutral effects are accounted for. The major drawback of using the present model in the breathing-mode time scales is the much larger computational time compared to the QNM; for instance, the simulations presented in the following sections required a total of 2×10^9 iterations to reach 2 ms, for a simulation time of $\sim$ 2 days ($\sim$ 300 times more than the QNM).

3.6.1. Boundary Condition Comparison

The first analysis aims to compare the two types of sheath boundary conditions in the dynamic regime. The same simulation has been performed with both the KBC and VBC for the set of parameters reported in Tab. 3.1, with the sole exception of taking $\alpha'_w = 5.5\%$. The discharge current, sheath potential and oscillation frequency are reported in Tab. 3.3. Small discrepancies can be observed in the discharge current and sheath potential, which is overestimated by the VBC; besides this, the choice of the boundary condition does not affect the oscillation period or phase of the breathing mode. The time-averaged profiles over several oscillation cycles are shown in Fig. 3.8, where, as in the stationary case, the different boundary conditions yield almost perfectly matching results. In light of this, it is safe to assume that the choice of the sheath boundary condition has very little influence on the overall discharge, both in the stationary and dynamic scenarios.

3.6.2. Triggering the ionization instability

Figure 3.9 shows the evolution of main plasma variables near the anode when α'_w is varied from 0 to 10%, and the magnetic field profile is kept fixed (with ℓ_{m1} =1.3 cm). The solutions of the quasi-neutral model and the non-neutral one (with KBC) are compared. The figure shows the transition from a steady-state to a BM solution at a certain α'_w, and then plots the maximum and minimum values of ϕ_{AB}, $-I_{iA}$ and I_d at 2 ms. For the non-neutral model, ϕ_{AB} is computed as the potential fall between the anode and the sheath edge B, which, at each timestep, is identified as the Bohm condition point. For $\alpha'_w > 6\%$

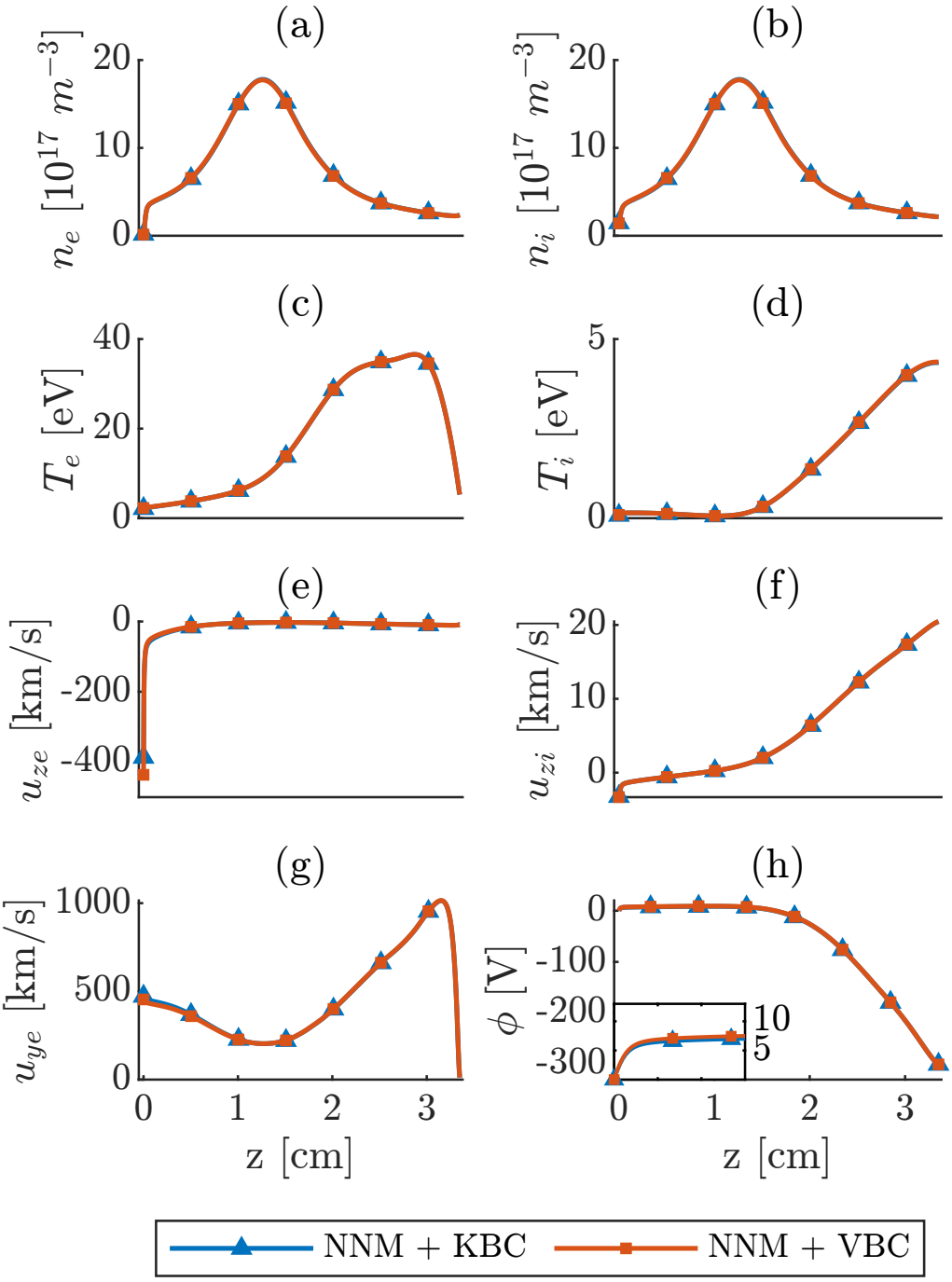

Figure 3.8: Nominal case except for ℓ_{m1} =1.30 cm, $\alpha'_w = 5.5\%$. Time-averaged discharge profiles over the breathing-mode cycles for the KBC and VBC.

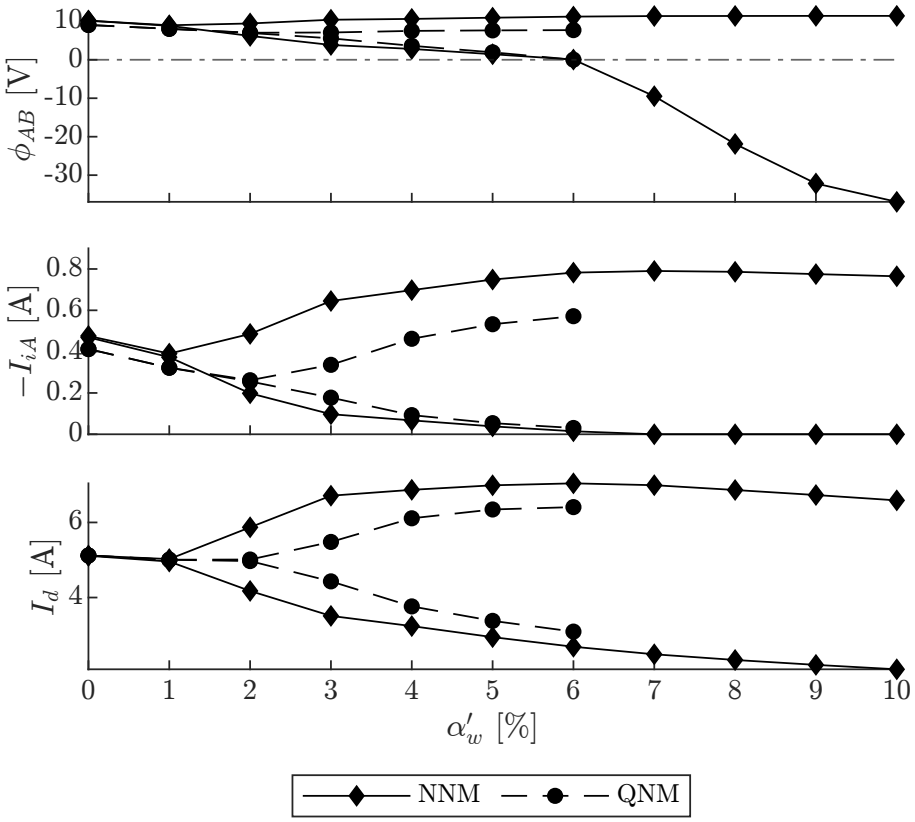

Figure 3.9: Lower and upper bounds of ϕ_{AB}, $-I_{iA}$ and I_d at 2 ms for different values of α'_w, for the QNM and NNM+KBC with $\ell_{m1} = 1.30$ cm.

(i.e. at large enough energy of neutrals), the non-neutral model predicts a transition to a reversed sheath at each breathing mode oscillation period, whereas the quasi-neutral model reaches the sheath vanishing condition and eventually the failure of the simulation. For $\alpha'_w \to 0$, the two models converge to the same stationary solution of Fig. 3.2.

It must be noted that compared to the results in [26], the quasi-neutral model fails at larger values of α'_w; such difference is found to be caused by the usage of a planar cathode and no downstream plume, as opposed to a volumetric cathode. A more detailed analysis of the effects of the volumetric cathode is presented in the Appendix.

3.6.3. Sheath reversal

As already observed by Poli *et al.* [26], during strong breathing mode oscillations $|I_{iA}|/I_d$ can reach very small values. As commented before in Section 3.5, in the quasi-neutral model, this results in the failure of the simulation, being the infinitely thin sheath model no longer valid. In Figure 9, this happens at $\alpha'_w \approx 6\%$. However, when the sheath is self-consistently resolved in the non-neutral model, the transition to an electron-attracting sheath is observed right before the peak of the discharge current in each breathing mode period. Figure 3.10 shows the BM solution for $\alpha'_w = 10\%$. When the discharge current increases, $n_{iA}, I_{iA} \to 0$, and the electron flux must provide the necessary current, an

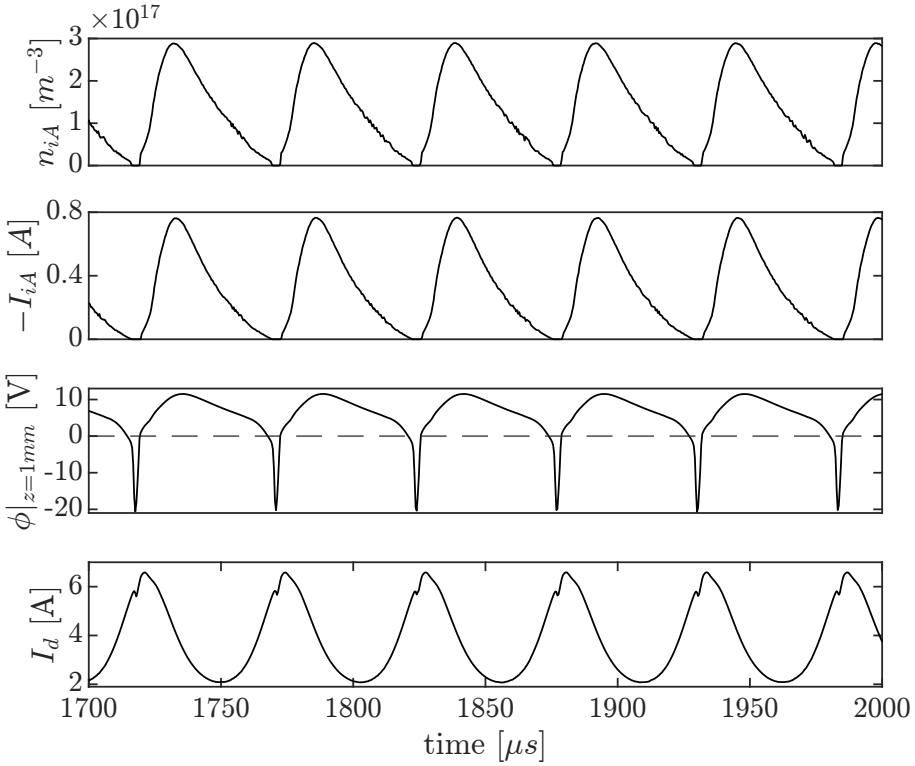

Figure 3.10: Ion density, ion current to the anode, potential and discharge current over various breathing mode cycles. The plots refer to the case with ℓ_{m1} =1.30 cm, $\alpha'_w = 10\%$.

electron-attracting sheath forms which sharply accelerates the electrons to supersonic velocities. The third plot of Fig. 3.10 shows the time evolution of the potential sampled at z =0.1 cm over multiple breathing mode cycles. It is clear the transition from normal to reversed sheath, which is associated with large negative values of the potential; the reversed sheath regime lasts for about 9% of the oscillation period before transitioning back to a normal sheath once the discharge reattaches to the anode. Even though a steady-state operation in the reversed sheath regime could not be found, Fig. 3.10 shows the existence of solutions with stable periodic transition to such a condition.

3.7. Conclusions

A 1D time-dependent non-neutral model of the HET discharge is presented. The model resolves self-consistently the plasma sheath according to the two-fluid formulation, and two different boundary conditions are analysed. The plasma domain extends from the anode to the planar cathode, including part of the plume expansion right after the channel exit. This model is the generalisation to account for the non-neutrality and full electron inertia of Model 5 presented in [26]. The model allows the resolution of the normal (electron-repelling) and reversed (electron-attracting) sheath and its smooth transition at the anode; this novelty extends the capabilities of classic 1D models aiming to analyse the approach of the no sheath condition commonly obtained when electron mobility is

reduced.

The comparison with the quasi-neutral model has shown very good agreement in predicting the discharge current and the most relevant properties of the plasma discharge, with only some differences in the anode sheath potential drop. Nonetheless, the comparison confirms the capability of quasi-neutral models to correctly capture the main discharge features, as long as the no-sheath condition is not reached, for which the model hypotheses fail and a non-neutral fully inertial treatment is required.

The integration of the equation involves the resolution of 3 (non-strictly) hyperbolic systems, one for each species, advanced explicitly in time and the solution of Poisson's equation for the potential. To relax the time-step and Debye length constraints, the vacuum permittivity has been increased by a factor of ten without observing major differences in the solution, apart from the Debye sheath thickness. The self-consistent modelling of the anode sheath is obtained by imposing appropriate boundary conditions; here, the *kinetic* and *vacuum* conditions are analysed. The model showed insensitivity to the choice of boundary conditions, with just minor differences in the predicted anode falls, both in the normal and reversed sheath. The analysis has been carried out for simulations reaching a stationary solution and for the ones exhibiting breathing mode, showing again almost perfect agreement between the two boundary conditions in the different regimes. As in [26], the triggering and amplitude of the breathing mode have been controlled by tuning the empirical wall accommodation parameter α'_w. First, with normal anode sheaths, the trends of the amplitude of discharge current oscillations with α'_w show good agreement with the quasi-neutral model. Second, the non-neutral model has allowed to analyse the anode fall transition from electron-repelling to electron-attracting. As expected, the transition is the result of reduced electron mobility at the anode, which in this work is mainly obtained through the regulation of the magnetic field decay in the channel or by the onset of strong ionisation instability; alternatively, an important reduction of the propellant mass-flow rate can effectively induce the transition, as observed experimentally during the extensive Russian testing of HETs. From the simulations, it appears that the reversed sheath condition is not a stable operating point, leading either to the transition to normal operating mode or the shut off of the discharge; the latter is associated with a strong depletion of ion density in the near anode region, corresponding to a detachment of the plasma bulk from the anode, which is eventually convected out of the thruster. Nonetheless, during strong ionisation instability, the periodic transition to the reversed sheath condition has been observed in each period of the oscillation. Throughout the different analysed simulation conditions, no stable reversed sheath operating point could be found, which can be the result of the low dimensionality of the model, which neglects important 2D effects (such as the localised formation of the reversed sheath, which does not involve the whole electrode). As suggested by the classic sheath theory, the electron dynamics inside the reversed sheath is dominated by the electric field, which is balanced by the electron axial inertia. The necessary contribution of inertia violates the drift-diffusion assumption, highlighting the limit of quasi-neutral drift-diffusion 1D HET models when strong reductions of the electron mobility are analysed.

Appendices

3.A. Influence of the cathode thickness

The major difference between the quasi-neutral model used in this work with respect to the one presented in Ref. [26], is the absence of the volumetric cathode and far plume, which is here substituted by a planar cathode. While the far plume has little influence on the discharge properties within the channel, Bello-Benítez and Ahedo [28] observed that the thickness of the volumetric cathode can mildly modify the stationary plasma discharge around the cathode region, and surprisingly, in the proximity of the anode. However, the volumetric source term has non-negligible effects on the thruster dynamics, as highlighted in Fig. 3.A.1, where the occurrence of breathing mode at 10 ms is evaluated for different thicknesses of the volumetric source term. Given the results of Ref. [28], where the cathode effects propagate to the anode, it is not surprising that the ionisation instability is affected as well, being extremely sensitive to the discharge equilibrium. In particular, a larger volumetric cathode length promotes the onset of the ionisation instability. However, for $\ell_c \to 0$ the steady state solution is identical to the one obtained with the surface cathode and no far plume, being the regions before and after the cathode decoupled; the comparison is reported in Fig 3.A.2. For this reason, the differences in the discharge stability of the QNM with respect to the model of Ref. [26] can be solely attributed to the choice of the cathode model.

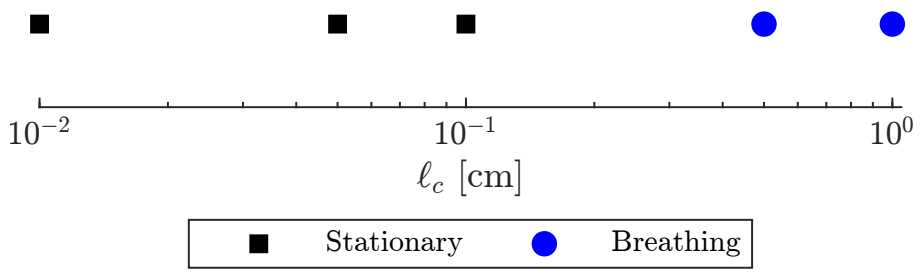

Figure 3.A.1: Ionisation instability at 10 ms for the Model 5 of [26] for different thicknesses of the cathode volumetric source term at ℓ_{m1} =1.34 cm, $\alpha'_w = 4\%$.

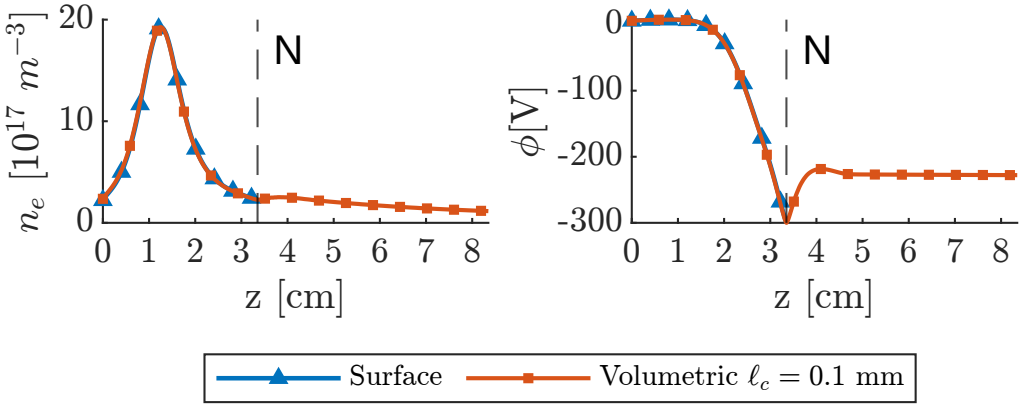

Figure 3.A.2: Comparison at 10 ms of the QNM presented in this paper with respect to the Model 5 of [26], considering a cathode thickness $\ell_c = 0.1$ mm, ℓ_{m1} =1.34 cm, $\alpha'_w = 4\%$.

CHAPTER 4

2D Fluid Code: Modelling Strategies and Numerical Implementation

This chapter describes the physical and numerical details of the 2D fluid model, together with the actual implementation and structure of the code. The current implementation of the model solves the 3-fluid (electrons, ions and neutrals) approximation of the plasma discharge with a Finite Volume Method. In the next sections, a brief derivation of the 5-moment model from the Boltzmann equation is reported, and the numerical techniques implemented in the code are detailed. In the last section, 1D and 2D validation test cases are shown.

4.1. Fluid description of a plasma

In general, plasma can be statistically described by the collisional Boltzmann equation:

$$\frac{\partial f_\alpha}{\partial t} + \boldsymbol{v}_\alpha \cdot \nabla_x f_\alpha + \frac{q_\alpha}{m_\alpha} [\boldsymbol{E} \times \boldsymbol{B}] \cdot \nabla_v f_\alpha = \left[\frac{\partial f_\alpha}{\partial t} \right]_{coll}, \tag{4.1}$$

where f_α is the velocity distribution function (VDF) of species $\alpha = e, i, n$, ∇_x and ∇_v are the derivatives in space and velocity, m_α is the mass, and the right-hand side represents the collisional processes. Given the complexity associated with directly solving the Boltzmann equation, it is customary to approximate it using either a kinetic or fluid approach. In general, high-order moment fluid models can be derived, although here only the transport equations of mass, momentum and energy are considered, yielding the so-called 5-moment description of a plasma. A possible derivation of the model starts by

taking moments of the velocity distribution function:

$$\begin{aligned} n_\alpha &= \iiint f_\alpha d^3\boldsymbol{v}, \quad n_\alpha \boldsymbol{u}_\alpha = \iiint \boldsymbol{v} f_\alpha d^3\boldsymbol{v}, \\ \overline{\overline{M}}_\alpha &= m_\alpha \iiint \boldsymbol{v}\boldsymbol{v} f_\alpha d^3\boldsymbol{v}, \quad \boldsymbol{P}''_\alpha = \frac{m_\alpha}{2} \iiint \boldsymbol{v} v^2 f_\alpha d^3\boldsymbol{v}, \end{aligned} \tag{4.2}$$

corresponding to the number density n_α, the particle flux vector $n_\alpha \boldsymbol{u}_\alpha$, the momentum flux tensor $\overline{\overline{M}}_\alpha$, and the energy flux vector $\boldsymbol{P}''_\alpha$ (note that formally $\boldsymbol{P}''_\alpha$ is not the complete third order moment of the VDF, which coincides with the energy flow triad) [71], [74]. The transport equations can be obtained by multiplying the Boltzmann equation for the moments and integrating over the velocity space, yielding a set of exact equations:

$$\frac{\partial n_\alpha}{\partial t} + \nabla \cdot (n_\alpha \boldsymbol{u}_\alpha) = S_\alpha, \tag{4.3}$$

$$m_\alpha \frac{\partial (n_\alpha \boldsymbol{u}_\alpha)}{\partial t} + \nabla \cdot \overline{\overline{\boldsymbol{M}}}_\alpha = q n_\alpha [\boldsymbol{u}_\alpha \times \boldsymbol{B} - \nabla \phi] + \boldsymbol{R}_\alpha, \tag{4.4}$$

$$\frac{1}{2} \frac{\partial \operatorname{tr}(\overline{\overline{M}}_\alpha)}{\partial t} + \nabla \cdot \boldsymbol{P}''_\alpha = q n_\alpha \boldsymbol{u}_\alpha \cdot \nabla \phi + E_\alpha, \tag{4.5}$$

where $\frac{1}{2}\operatorname{tr}(\overline{\overline{M}}_\alpha) = \frac{3}{2} p_\alpha + \frac{1}{2} m n_\alpha \boldsymbol{u}_\alpha \boldsymbol{u}_\alpha = \mathscr{E}_\alpha$ is the fluid total energy with p_α the fluid scalar pressure. The terms S_α, $\boldsymbol{R}_\alpha$ and E_α account for the effects of collisions (and more in general of external sources) on plasma production, momentum exchange, and loss (or gain) of energy, respectively. The above equations can be further expanded by decomposing the momentum flux tensor and the energy flux vector:

$$\overline{\overline{M}}_\alpha = \overline{\overline{p}}_\alpha + m_\alpha n_\alpha \boldsymbol{u}_\alpha \boldsymbol{u}_\alpha \tag{4.6}$$

$$\boldsymbol{P}''_\alpha = (m_\alpha u_\alpha^2/2) n_\alpha \boldsymbol{u}_\alpha + \boldsymbol{h}_\alpha + \overline{\overline{\tau}}_\alpha \cdot \boldsymbol{u}_\alpha + \boldsymbol{q}_\alpha \tag{4.7}$$

where $\overline{\overline{p}}_\alpha$ is the pressure tensor, $\boldsymbol{h}_\alpha = (5/2) T_\alpha n_\alpha \boldsymbol{u}_\alpha$ is the enthalpy flux, with T_α the average temperature, $\overline{\overline{\tau}}_\alpha = \overline{\overline{p}}_\alpha - n_\alpha T_\alpha \overline{\overline{I}}$ the gyrostress tensor and $\boldsymbol{q}_\alpha$ the heat flux vector. The system of equations (4.3-4.7), which up to this point is *exact*, is undetermined, as it has more unknowns than equations, and a closure must be imposed. The main assumption of the 5-moment fluid model is to assume the gas at thermal equilibrium, hence described by a Maxwellian velocity distribution function:

$$f_\alpha = n_\alpha \left(\frac{m_\alpha}{2\pi e T_\alpha} \right)^{3/2} \exp \left[- \frac{m_\alpha (\boldsymbol{v} - \boldsymbol{u}_\alpha)^2}{2 e T_\alpha} \right], \tag{4.8}$$

for which the distribution of the random velocity is isotropic. From this, it follows that the pressure tensor $\overline{\overline{p}}_\alpha$ is isotropic and $\nabla \cdot \overline{\overline{p}}_\alpha = \nabla p_\alpha$ with $p_\alpha = n_\alpha e T_\alpha$ for the equation of state of an ideal gas. For the same reason, for a Maxwellian VDF $\boldsymbol{q}_\alpha = 0$. Finally, by definition, also the gyrostress tensor $\overline{\overline{\tau}}_\alpha$ vanishes. With these three important assumptions:

$$\nabla \cdot \overline{\overline{p}}_\alpha = \nabla p_\alpha, \quad \boldsymbol{q}_\alpha = 0, \quad \overline{\overline{\tau}}_\alpha = 0, \tag{4.9}$$

the system of equations can be written in a closed formulation as:

$$\frac{\partial n_\alpha}{\partial t} + \nabla \cdot (n_\alpha \boldsymbol{u}_\alpha) = S_\alpha \tag{4.10}$$

$$\frac{\partial (n_\alpha \boldsymbol{u}_\alpha)}{\partial t} + \nabla \cdot (n_\alpha \boldsymbol{u}_\alpha \boldsymbol{u}_\alpha) = \frac{q n_\alpha}{m_\alpha} [\boldsymbol{u}_\alpha \times \boldsymbol{B} - \nabla \phi] - \frac{1}{m_\alpha} \nabla p_\alpha + \boldsymbol{R}_\alpha \tag{4.11}$$

$$\frac{\partial (\mathscr{E}_\alpha)}{\partial t} + \nabla \cdot ((\mathscr{E}_\alpha + p_\alpha) \boldsymbol{u}_\alpha) = q n_\alpha \boldsymbol{u}_\alpha \cdot \nabla \phi + E_\alpha \tag{4.12}$$

This system of equations represents the ideal 5-moment model, describing the time evolution of mass, momentum and energy, and it is the set of equations implemented in the 2D code. However, as already commented in chapter 2 [Eq. 2.15], it is customary for fluid models (of this type), especially applied to Hall effect thrusters [30], to include an approximate description of the heat flux vector $\boldsymbol{q}_\alpha$. The standard closure applies to collisional plasmas (yielding a conductive heat flux) and takes the form of a Fourier-like law:

$$\boldsymbol{q}_\alpha + \frac{\omega_{c\alpha}}{\nu_\alpha} (\boldsymbol{q}_\alpha \times \boldsymbol{B}) = -\frac{5 e n_\alpha T_\alpha}{2 m_\alpha \nu_\alpha} \nabla T_\alpha, \tag{4.13}$$

with ω_{ce} and ν_α, the cyclotron frequency and the total collision frequency, respectively. This closure is obtained by the stationary ($\boldsymbol{u}_\alpha = 0$), steady-state assumption of the complete heat flux transport equation with the Crook collision model to account for the collisional effects [74]. In this Thesis, the heat flux vector in the 2D code is always neglected (i.e. solving the ideal 5-moment system), mostly due to the unjustified assumption of a stationary flow in $E \times B$ devices, as it will be highlighted in the following chapters.

4.2. Numerical methods

To illustrate the numerical methods implemented by the code to solve the fluid equations (4.10-4.12), the system of conservation laws is written in its generic differential form for the two directions z and y:

$$\frac{\partial \boldsymbol{U}}{\partial t} + \frac{\partial \boldsymbol{F}}{\partial z} + \frac{\partial \boldsymbol{G}}{\partial y} = \boldsymbol{S}, \tag{4.14}$$

where

$$\begin{aligned} \boldsymbol{U} &= \begin{bmatrix} n \\ nu \\ nv \\ \mathscr{E} \end{bmatrix}, \quad \boldsymbol{F} = \begin{bmatrix} nu \\ nu^2 + p/m \\ nuv \\ (\mathscr{E} + p)u \end{bmatrix}, \\ \boldsymbol{G} &= \begin{bmatrix} nv \\ nvu \\ nv^2 + p/m \\ (\mathscr{E} + p)v \end{bmatrix}, \quad \boldsymbol{S} = \begin{bmatrix} S \\ \frac{qn}{m}\left[vB - \frac{\partial \phi}{\partial x}\right] + R_x \\ \frac{qn}{m}\left[-uB - \frac{\partial \phi}{\partial y}\right] + R_y \\ qn\boldsymbol{u} \cdot \nabla \phi + E \end{bmatrix} \end{aligned} \tag{4.15}$$

are the vectors of states, fluxes in the two directions and source terms, respectively. Note that the species subscript α has been dropped, but the charge q is kept, so that equation (4.14) applies to electrons, ions and neutrals. The system of equations is integrated with a Finite Volume Method (FVM) on a structured Cartesian mesh. The finite volume approach has been chosen due to its inherent property of ensuring conservation, which is derived from the integral formulation of the conservation laws [75]. The state vector $\boldsymbol{U}$ is considered at the cell centre and represents the cell average of the fluid variables. The current implementation of the FVM utilises a 1D approximate Riemann solver to treat the discontinuity arising at each cell interface; the use of genuinely 2D Riemann solvers is seldom done in practice, due to the significantly higher complexity. The numerical scheme is thus to be intended as applied component-wise in the two directions and without loss of generality, it is presented hereafter in the more concise 1D formulation along the z direction (the y direction is readily recovered considering the flux vector $\boldsymbol{G}$).

The numerical integration of equation (4.14) is composed of three basic blocks: cell face reconstruction of the variables, numerical fluxes evaluation and time integration; a brief description of the methods employed in each block is hereby reported.

4.2.1. Cell face reconstruction

As previously mentioned, the state vector $\boldsymbol{U}$ represents the cell average value of the macroscopic variables, and it is stored at the cell centre; as a result, the first step in the integration of the equations is to compute an appropriate estimation of the state vector at the cell interfaces with which the numerical fluxes can be evaluated. Even though the equations are solved in their conservative form, the cell face reconstruction is performed on the primitive variables $\boldsymbol{Q} = [n, u, v, p]^t$ to reduce the risk of internal energy and density positivity violations. A conversion between the conservative and primitive variables is performed before the reconstruction. In this section, as reported in Fig. 4.1, the cell interfaces are denoted by the subscripts $i-1/2$ and $i+1/2$ for the interfaces located left and right of the generic ith cell, respectively; in addition, the superscripts L and R are used to specify whether the reconstructed value at the interface is obtained from the left or right side of the interface itself (i.e whether it is obtained from the ith or ith+1 cell). The superscripts are used to introduce local coordinates at each cell interface, greatly simplifying the numerical flux expression.
Several schemes with different approximation orders are available in the code:

Piecewise-constant The most crude approximation implemented in the code relies on the assumption of piecewise-constant reconstruction of the variables inside the cells. Despite its robustness and simplicity, the method is only 1st order accurate, and it can lead to the introduction of large numerical diffusivity from the approximate Riemann solver due to the possibly large discontinuities across the cells.

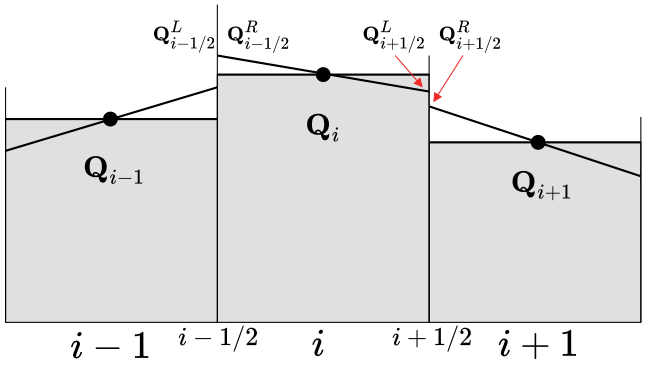

Figure 4.1: Schematic representation of the piecewise-linear reconstruction of the cell-averaged states $\boldsymbol{Q}_i$.

MUSCL 2nd order A more accurate approximation is obtained by considering a piecewise-linear reconstruction, adopting the Monotonic Upstream-centred Scheme for Conservation Laws (MUSCL) [76], [77]. The reconstructed values at the cell interface are obtained by evaluating the gradients between the cell i and its neighbours $(i+1, i-1)$, yielding a second-order accurate scheme. To avoid introducing new maxima and minima, and thus spurious oscillations in the solution, a Total Variation Diminishing (TVD) [78] nonlinear limiter is used. The current implementation uses the *minmod* slope limiter, although other choices are possible. The reconstructed primitive variables vector at the cell interfaces $i-1/2$, $i+1/2$ is computed as:

$$\boldsymbol{Q}^R_{i-1/2} = \boldsymbol{Q}_i - \frac{1}{2}\Delta_i, \quad \boldsymbol{Q}^L_{i+1/2} = \boldsymbol{Q}_i + \frac{1}{2}\Delta_i \tag{4.16}$$

with Δ_i the local slope of Q_i in the i-th cell computed with the *minmod* slope limiter

$$\Delta_i = \text{minmod}\left(\theta\frac{\boldsymbol{Q}_i - \boldsymbol{Q}_{i-1}}{\Delta z}, \frac{\boldsymbol{Q}_{i+1} - \boldsymbol{Q}_{i-1}}{2\Delta z}, \theta\frac{\boldsymbol{Q}_{i+1} - \boldsymbol{Q}_i}{\Delta z}\right), \quad 1 \leq \theta \leq 2, \tag{4.17}$$

$$\text{minmod}(x_1, x_2, \ldots x_j) = \begin{cases} \min_j\{x_j\}, & \text{if } x_j > 0 \;\forall j, \\ \max_j\{x_j\}, & \text{if } x_j < 0 \;\forall j, \\ 0, & \text{otherwise.} \end{cases} \tag{4.18}$$

with θ a free parameter: for $\theta = 1$ the usual *minmod* limiter is recovered, while for $\theta = 2$ a less diffusive version is obtained. In the vast majority of the cases, $\theta = 1$, yielding a slightly more diffusive but robust solution.

CWENO 3rd order The highest order reconstruction scheme available in the code is a 3rd-order Central Weighted Essentially Non Oscillatory (CWENO) scheme developed by Kurganov and Levy [79]. While the scheme performs well in smooth scenarios, it lacks robustness when the plasma becomes turbulent; thus, it is seldom used and it is here only cited for the sake of completeness.

Regardless of the reconstruction scheme, once the primitive variables at the cell interfaces are obtained, the conservative variables are recovered to be later used by the Riemann solver.

4.2.2. Approximate Riemann solvers

Table 4.1: Approximate Riemann solvers available in the code. For each solver, the number of waves and the capability of resolving contact discontinuities are reported.

Solver	Waves	Contact discontinuity	ref
Rusanov	1	No	[80]
HLLE	2	No	[81]
HLLEM	2	Yes	[82]
HLLC	3	Yes	[83]
Roe	4	Yes	[84]

The code contains a variety of approximate Riemann solvers that can be readily used with any of the reconstruction schemes described in the previous section. The available solvers are reported in table 4.1; for each solver, the number of resolved waves and the capability of capturing the contact discontinuity are reported. All of the implemented solvers can capture shock and expansion waves, however, with different levels of accuracy due to the different number of resolved waves. The Roe solver is seldom used due to the intrinsic flaw of entropy-violating expansion-shock waves; even with the inclusion of the entropy-fix [85], the HLLC remains the preferred choice in terms of accuracy and computational cost (in the current implementation).

For the sake of brevity, only the HLLC scheme is hereby explicitly reported, noting that the HLL-family and Rusanov can be reduced to the same formulation when suitable wave speeds are selected.

HLLC Solver Following the same notation of section 4.2.1, $\boldsymbol{Q}^L_{i+1/2}, \boldsymbol{Q}^R_{i+1/2}$ represent the left and right reconstructed states across the interface located at $i+1/2$; from now on the interface location subscript will be omitted without loss of generality, being the discussion applicable to every cell interface in the two directions of the Cartesian mesh. Across the interface, the reconstructed states are in general different, thus introducing a discontinuity: the approximate Riemann solvers provide a numerical flux to connect the two states without solving the complete Riemann problem. As before, the scheme is presented for one of the two spatial coordinates, to be intended as applied on the direction normal to the cell interface; application to the other coordinate is straightforward. The HLLC scheme, proposed by Toro [83], is based on the HLL solver, but it allows the exact resolution of contact discontinuities by including a third wave and thus four states. The general wave structure of the HLLC solver is reported in Fig. 4.2. The inclusion of

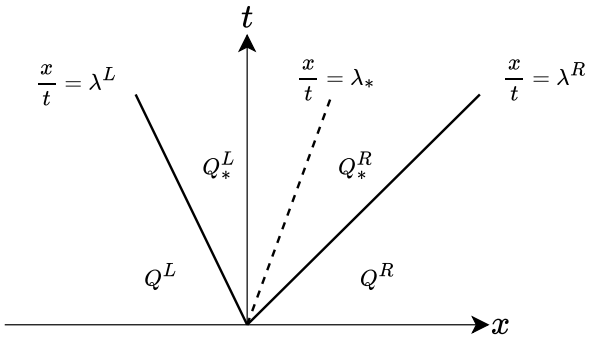

Figure 4.2: HLLC wave structure.

the contact discontinuity requires the estimation of a contact speed λ^*, generating two intermediate states composing the star region. The numerical flux is thus expressed as:

$$\boldsymbol{F} = \begin{cases} \boldsymbol{F}^L, & \text{if } 0 \leq \lambda^L, \\ \boldsymbol{F}_*^L, & \text{if } \lambda^L < 0 \leq \lambda_*, \\ \boldsymbol{F}_*^R, & \text{if } \lambda_* < 0 \leq \lambda^R, \\ \boldsymbol{F}^R, & \text{if } 0 > \lambda^R. \end{cases} \tag{4.19}$$

In case of supersonic flow, the scheme reverts to the classic upwind scheme, imposing the numerical flux to be F^L, F^R depending on the flow direction; in this condition, the numerical flux coincides with the physical flux evaluated at the cell interface. In the case of subsonic flow, a suitable expression for the star region flux must be provided. A possible formulation is:

$$\boldsymbol{F}_*^K = \frac{\lambda_* \left(\lambda^K \boldsymbol{Q}^K - \boldsymbol{F}^K\right) + \lambda^K p_* \boldsymbol{D}}{\lambda^K - \lambda_*}, \quad K = L, R, \quad \boldsymbol{D} = [0, 1/m, 0, \lambda_*]^T \tag{4.20}$$

where p^* is the contact pressure. The inclusion of the mass in $\boldsymbol{D}$ is necessary when the equations solve for the number density n instead of the density ρ. To compute the fluxes, the wave speeds $\lambda^L, \lambda^R, \lambda_*$ must be computed. Several approaches to estimate the wave speed (not necessarily coincident with the eigenvalues of the system) can be used; here, the expressions of Davis [86] are used, given their simplicity and robustness due to the more diffusive nature. Less diffusive wave speed estimates could be used [82], [87], at the cost of sacrificing robustness and computational speed. The wave speeds are computed as

$$\lambda^L = \min\left(u^L - a^L, u^R - a^R\right), \quad \lambda^R = \min\left(u^L + a^L, u^R + a^R\right). \tag{4.21}$$

where $a^{R,L} = \sqrt{\gamma e T / m}$ is the local sound speed. Once the left and right wave speeds are obtained, the contact speed can be computed as:

$$\lambda_* = \frac{p^R - p^L + n^L u^L \left(\lambda^L - u^L\right) - n^R u^R \left(\lambda^R - u^R\right)}{n^L \left(\lambda^L - u^L\right) - n^R \left(\lambda^R - u^R\right)}, \tag{4.22}$$

and finally, the contact pressure:

$$p^* = \frac{1}{2}\left[p^L + p^R + n^L\left(\lambda^L - u^L\right)\left(\lambda^* - u^L\right) + n^R\left(\lambda^R - u^R\right)\left(\lambda^* - u^R\right)\right]. \tag{4.23}$$

The numerical flux can now be calculated according to equation 4.19, with which the discrete flux divergence $\frac{\Delta \boldsymbol{F}}{\Delta z} = (\boldsymbol{F}_i - \boldsymbol{F}_{i-1})/\Delta z$ can be computed, and the homogeneous part of the system can be advanced in time.

4.2.3. Vacuum Tracking Scheme

A novelty of the code is the implementation of a vacuum tracking algorithm, which allows for the integration of the 5-moment model in the presence of vacuum regions. This scheme is based on the threshold-based algorithm of Subramaniam and Raja [88] and built over the HLLC solver. The implementation of the scheme is detailed in section 5.2.3, as part of the submitted article to the peer-reviewed journal *Plasma Sources Science and Technology*. To avoid repetitions, the algorithm is not reported here, and the reader is referred to Chapter 5.

4.2.4. Time Integration

Conservation laws can generally be integrated in an *unsplit* way, advancing in time the semi-discrete formulation of equation 4.14:

$$\frac{\partial \boldsymbol{U}}{\partial t} = -\frac{\Delta \boldsymbol{F}}{\Delta z} - \frac{\Delta \boldsymbol{G}}{\Delta y} + \boldsymbol{S} \tag{4.24}$$

where $\boldsymbol{S}$ is the generic source term vector and $\frac{\Delta \boldsymbol{F}}{\Delta z}, \frac{\Delta \boldsymbol{G}}{\Delta y}$ the discrete divergence of the numerical fluxes computed as shown in the previous section. In the code, time integration is treated explicitly, which makes the Euler-Poisson system unconditionally unstable as shown by Fabre [89]. This instability is stronger at larger plasma densities, and at the typical HET densities ($\approx 1 \times 10^{18}\,\mathrm{m}^{-3}$) the solution is destroyed in the order of microseconds; at lower densities the instability does not seem to appear in the time scales of interest ($\approx 1 \times 10^{-4}\,\mathrm{s}$). According to Fabre, the system of equations is unconditionally stable if the Poisson equation is solved implicitly in time (instead of appearing explicitly in the momentum equations), which would result in much larger computational complexity. Following Reboul et al. [90], fractional-step methods can be used to obtain a stable system without the computational cost of the full implicit treatment. In such methods, the system of equations is split into a hyperbolic homogeneous system

$$\frac{\partial \boldsymbol{U}}{\partial t} + \frac{\Delta \boldsymbol{F}}{\Delta z} + \frac{\Delta \boldsymbol{G}}{\Delta y} = 0, \tag{4.25}$$

and a system of ordinary differential equations

$$\frac{\partial \boldsymbol{U}}{\partial t} = \boldsymbol{S}. \tag{4.26}$$

The two systems are advanced in time one after the other, giving freedom to use different methods (e.g. in case of stiff source terms). Reboul et al. suggest computing the electrostatic potential with the Poisson equation between the convective (4.25) and source terms (4.26) steps. The code allows to use of the Strang splitting [91] or the simpler balanced splitting of Wu et al. [92]. While both splitting methods are second-order accurate in time, the latter one does not suffer from the famous steady state splitting error of the Strang splitting. Nevertheless, the integration algorithm is here explicitly reported for the more standard Strang splitting:

1. Advance the source terms sub-step of $\Delta t/2$
2. Advance the convection terms sub-step of Δt
3. Compute ϕ from the Poisson equation
4. Advance the source terms sub-step of $\Delta t/2$

Regardless of the splitting scheme, the equations are integrated using explicit time-stepping methods. Runge-Kutta (RK) methods of order 2, 3 and 4 can be selected, as well as the stabilised Runge-Kutta-Chebyshev (RKC) method. Usually, the Strong-Stability-Preserving third order Runge-Kutta (SSP-RK3) [93] provides a good compromise between stability, accuracy and computational speed. If the source terms are particularly stiff, the second-order, s-stage RKC method can be used to increase the stability region along the negative real axis [94].

In the code, all the integration subroutines (one for each method) share the same header structure. This allows for the selection of the integration scheme by simply assigning the appropriate procedural pointer to the desired method.

Time-step and cell size selection Besides the Euler-Poisson instability, the physics of the problem and the nature of the equations impose stringent requirements on the spatial and temporal scales. To correctly resolve non-neutral effects, the mesh size must be smaller than the Debye length λ_d, so that:

$$\Delta z, \Delta y < \lambda_d = \sqrt{\frac{\varepsilon_0 e T_e}{n_e e^2}}. \tag{4.27}$$

The size of the cells directly affects the integration time-step, since the Courant-Friedrichs-Lewy (CFL) condition is computed taking into account the fastest wave-speed in the system. Accounting for the two dimensions solved by the model, the time step must satisfy:

$$\Delta t_c = \mathrm{CFL} \times \min\left(\frac{\Delta z}{\max_\Omega(\rho_z)}, \frac{\Delta y}{\max_\Omega(\rho_y)}\right), \tag{4.28}$$

with Ω the computational domain, $\Delta z, \Delta y$ the mesh size and $\rho_{z,y} = \max\{|\lambda_1|, ..., |\lambda_n|\}$ the spectral radius of the flux Jacobian of the electron system in the two directions (in these

plasmas, ions timescales are usually much larger than the ones of electrons).

Moreover, the proper resolution of the plasma time-scales requires the time-step to be smaller than the plasma frequency ω_p and the electron cyclotron frequency ω_{ce}:

$$\omega_p = \sqrt{\frac{n_e e^2}{m_e \varepsilon_0}}, \quad \omega_{ce} = \frac{eB}{m_e} \tag{4.29}$$

with B the magnetic field. In certain magnetised plasmas, $\omega_p \approx \omega_{ce}$ and the time-step constraint is given by the upper-hybrid frequency $\omega_{uh} = \sqrt{\omega_p^2 + \omega_{ce}^2}$. The complete time-step criterion is thus given by:

$$\Delta t \leq \min\left(\Delta t_c, 0.2\frac{2\pi}{\omega_{uh}}\right) \tag{4.30}$$

where the factor 0.2 is introduced to ensure numerical stability, although usually the CFL condition for electrons is much more restrictive than the upper-hybrid frequency. When launching a simulation, the time-step can be kept fixed or updated explicitly at each iteration following equation (4.30); typically, the simulations are run with CFL=0.7.

4.3. Code structure

In this section, the main features of the code are presented. The finite volume code is written in Fortran, except for the input generation, which is handled by Python classes, and it is composed of a main program and 12 modules, which are hereby briefly described:

- **Main program**: It is the core of the code where the MPI environment is initialised.
- **DataType module**: It contains all the data structures, abstract interfaces and constants used by the code; it is accessed by every other module.
- **Math module**: It contains all the subroutines responsible for computing finite differences, interpolation and printing tools for debugging purposes.
- **Post module**: It contains all the subroutines linked to parallel HDF5, reading the SimState and creating and writing to the PostData output file.
- **Algorithm module**: It is called by the main module and encloses all the operations performed by the code and the actual algorithm to solve the equations.
- **Mesh module**: It is responsible for performing the MPI domain decomposition, computing the local and global computational and physical coordinates.
- **Boundary module**: Here, the MPI communications (HALO exchange) are performed, and the MPI-specific derived data types are defined. The module also contains subroutines for the imposition of appropriate boundary conditions on the external boundary of each local domain patch.

- **Initialisation module**: Here, all the data structures are allocated, the procedural pointers are assigned, and the sparse matrix for the Poisson equation is created.
- **Fluid BCs module**: This module contains all the boundary conditions for the fluid equations. Every subroutine shares the main header, so that different BCs can be selected by simply associating a pointer.
- **Collision module**: Here, the collision operators are calculated, as well as the timestep estimation.
- **Fluid Equation module**: This module contains the subroutines computing the semidiscrete version of the equations, fluxes and source terms.
- **Finite Volume module**: The module contains all the approximate Riemann solvers, reconstruction schemes and slope limiters.
- **Integration module**: The main Runge-Kutta integrators are contained in this module, as well as the Poisson resolution subroutines.

Additional external libraries are required, such as the direct solver MUMPS [95] and its dependencies and parallel HDF5; the code is compiled using Intel Fortran and uses the implementation of BLAS and SCALAPACK contained in Intel Math Kernel Library (MKL). To guarantee flexibility and modularity without sacrificing computational efficiency, the code relies heavily on procedural pointers for the selection of integrators, finite volume schemes, boundary conditions and fluid equations: at run time, the various pointers are associated at the beginning of the algorithm, thus avoiding excessive conditional statements in the main loops and the associated conditional branching. Moreover, the strict definition of abstract interfaces for the pointers forces consistency in the definition of subroutine headers, keeping the code easy to modify and expand.

4.3.1. MPI Domain-Decomposition

The code is parallelised using the Message Passing Interface (MPI) to implement 2D domain decomposition. At run-time, the number of MPI processes is specified, the processes are then organised in a 2D Cartesian topology, and the computational domain is divided into equal blocks to ensure load balancing. The integration of the fluid equations requires communication between the various blocks, which is performed by defining a *halo* region in each subdomain. The depth of the halo region can be selected at run-time based on the order of the FVM scheme (e.g for the 2nd order MUSCL scheme a depth of 2 cells is needed), and an appropriate MPI derived datatype is created based on the geometry, depth and number of equations (thus the number of variables per cell) using *subarrays*. The actual communication is performed using *send_recv* by populating a structure defining boundary cells for each side of the subdomain: in the case of an external boundary, no communication is performed, and the appropriate boundary conditions are imposed.

The boundary structure is then added to each subdomain as a halo region, regardless of the type of boundary (internal or external). Communication is performed at each stage of the Runge-Kutta integrator for the convection part of the equations, whereas it is usually not necessary for the source terms subsystem.

Future works include the optimisation of the *halo* exchange subroutines to further reduce the communication time, allowing for a better scalability of the code in high-performance computing (HPC) facilities.

4.3.2. Poisson integration

In each iteration, the electric potential ϕ is computed by solving the 2D Poisson equation. The elliptic equation is discretised using the classic finite-difference 5-point stencil:

$$\frac{\phi_{i+1,j} - 2\phi_{i,j} + \phi_{i-1,j}}{\Delta y^2} + \frac{\phi_{i,j+1} - 2\phi_{i,j} + \phi_{i,j-1}}{\Delta z^2} = \frac{e\left(n^e_{i,j} - n^i_{i,j}\right)}{\varepsilon_0}. \tag{4.31}$$

The matrix coefficients are computed in the initialisation module in a sparse formulation. Due to the 2D block domain decomposition, the coefficients are computed following a local indexing in each MPI process to guarantee optimal partitioning and reduce the communication traffic. The sparsity pattern of the matrix on a 4x4 matrix is reported in Fig. 4.3 along with the partitioning into 4 MPI processes. The sparse matrix is stored in the COO (coordinate) format and passed to the direct linear solver library MUMPS. Being the coefficients constant, the factorisation of the matrix is performed only once during the initialisation phase. In each iteration of the algorithm, the right-hand side of equation 4.31 is updated and the backsubstitution step is performed.

4.3.3. Input and Output handling

Here, the input generation and output file creation are briefly described. Before running any simulation, proper initialisation has to be performed. The input generation starts by appropriately modifying the *input_file.txt*, which contains all the parameters that can currently be set in the code. The input file is rather generic, allowing for the specification of numerical integration, boundary conditions and equations to solve for each one of the three populations (electrons, ions and neutrals), as well as volumetric source terms, collisional processes, initial conditions and parameters related to the fields (boundary conditions for Poisson and magnetic field profiles). By calling the *input_generation.py* script, the input text file is imported in Python, where a class is created and populated with all the specified parameters. The simulation folders are generated, and based on the specified flags, previous simulation results can be interpolated and set as initial conditions. The initial conditions, along with all the simulation parameters, are saved in an HDF5 file created by the Python class called *SimState.h5*.

Once the simulation has been launched, the Fortran code reads the *SimState.h5* with appropriate subroutines in the Post module used as wrappers for the functions of the

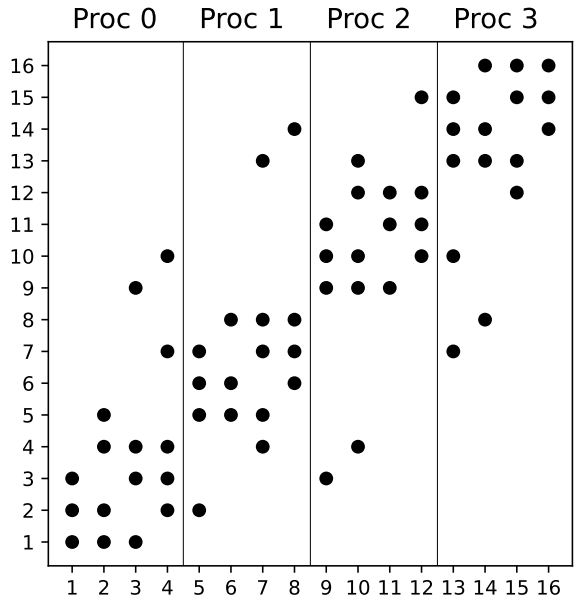

Figure 4.3: Sparsity pattern of the 5-point stencil on a 4x4 domain decomposed in 4 MPI processes.

parallel HDF5 library. The input parameters are stored in the *SimParams* data structure, and the output file *PostData.h5* is generated using parallel MPI access. The output file is created to be self-consistent, containing all the information necessary to run or re-initialise a simulation. At the beginning of the simulation, the whole PostData file is created following the same structure as the SimState. As the algorithm runs, the variables of interest are written in parallel at every time interval Δt_{save} specified in the input file.

4.4. Code validation

In this section, the finite volume solver of the code is validated with classic CFD test cases for the Euler equations. To evaluate the performance of the code, some of the cases reported by Liska and Wendroff [96] and Schulz-Rinne et al. [97] have been reproduced, both in 1D and 2D. The HLLC scheme with piecewise-linear MUSCL reconstruction and minmod limiter has been used in all the tests.

4.4.1. 1D Tests

Here, several 1D Riemann problems proposed originally by Toro [77] and reproduced by Liska and Wendroff [96] are presented. To perform these tests, the 2D code is used in quasi-1D mode by imposing periodic conditions and using a small number of cells in the y direction. The 2D code is directly compared with the exact solution of the Riemann problem using the *NUMERICA* exact Riemann solver developed by Toro [98]. The initial

Table 4.2: Initialisation parameters for the 1D Riemann problems. The initial states are divided into *left* and *right* semidomains, z_0 is the location of the interface at the initial time. The last column reports the time at which the solution is computed. Data taken from[96].

Test	Left			Right			z_0	Time
	p	n	u_z	p	n	u_z		
1	1.0	1.0	0.75	0.1	0.125	0.0	0.3	0.2
2	0.4	1.0	-2.0	0.4	1.0	2.0	0.5	0.15
3	1000	1.0	-19.59745	0.01	1.0	-19.59745	0.8	0.012
4	460.894	5.99924	19.5975	46.095	5.99924	-6.19633	0.4	0.035
5	1.0	1.4	0.0	1	1.0	0.0	0.5	2.0
6	1.0	1.4	0.1	1	1.0	0.1	0.5	2.0

Table 4.3: Relative L_1 errors in percentage with respect to the exact solution obtained with *NUMERICA*. For Test 2, the error refers to the internal energy. For all the other cases, the error is computed on the density.

Test	1	2	3	4	5	6
L_1 [%]	1.58	20.9	2.16	3.02	0.0	0.56

conditions for the problems are reported in Tab. 4.2; a computational domain of $z \in (0,1)$ and a polytropic index $\gamma = 1.4$ are used in all the tests. The domain is discretised in 100 cells in all cases, except for Test 3 and Test 4, for which 200 cells are used; the exact solution with *NUMERICA* is evaluated over 1000 points. The L_1 relative error of the solution with respect to the exact Riemann solver is computed for every testcase, considering the density n as variable of interest, except for Test 2, for which the internal energy $Te/(\gamma-1)$ is used; the results are reported in Tab. 4.3 as percentages. Compared with the results reported in [96], the code appears to be in line with the other numerical schemes. The two extremes are Test 3 (3a in Liska), which is resolved particularly well, and Test 2, which presents a significant error in the internal energy (although in line with other schemes). Test 5 demonstrates the capability of the HLLC to exactly resolve contact discontinuities (the accuracy is slightly degraded in slow-moving contacts, Test 6). The comparison of relevant magnitudes between the computed and exact solution (red markers and solid line, respectively) is shown in Fig. 4.4 for Test 2, Test 3 and Test 4. As mentioned before, the largest error is produced in the approximation of the internal energy in Test 2, which is renowned to be a difficult problem due to the formation of near-vacuum regions. On the other hand, the code resolves almost exactly the non-isolated contact discontinuity of Test 3 (located at $z = 0.8$), but excessively diffuses the slow-moving contact of Test 4 (located at $z = 0.7$). In general, the solutions of the various tests compare well with those reported by Toro [77], taking into account the 2nd order MUSCL reconstruction hereby implemented.

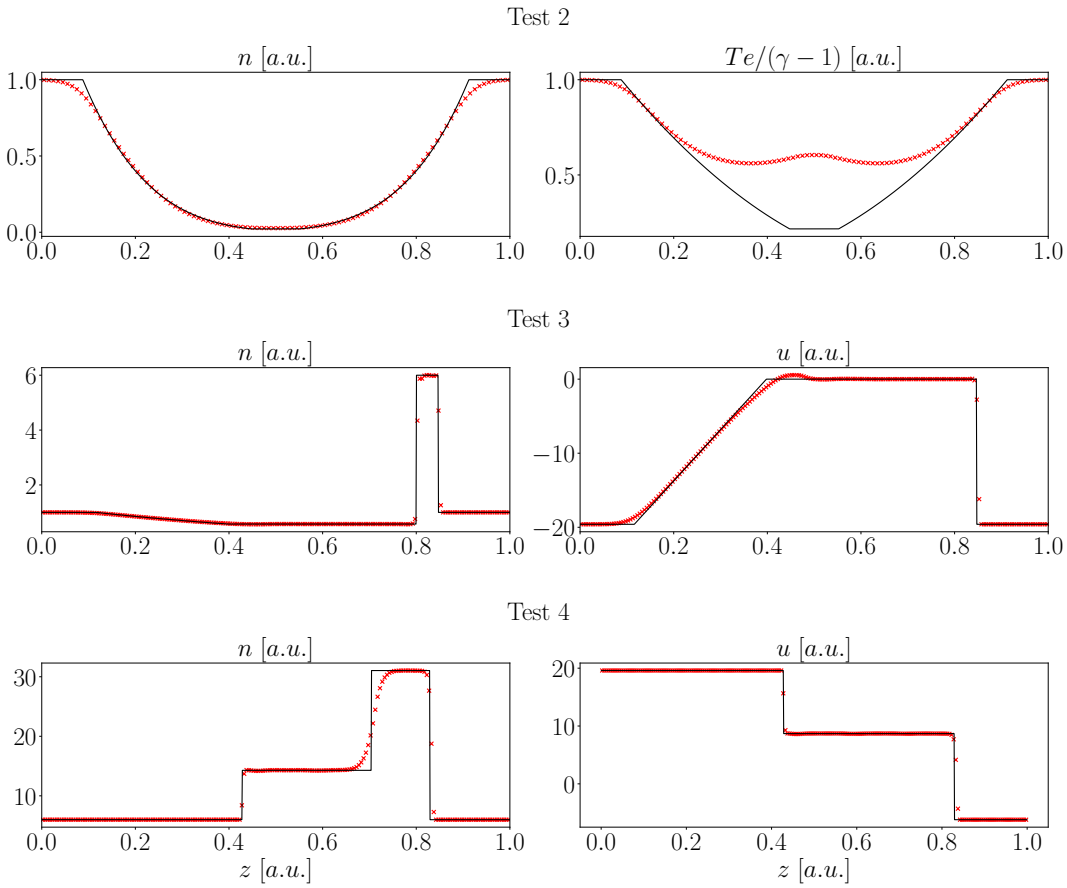

Figure 4.4: Computed (red markers) and exact solution (solid line) of some variables of interest for Test 2, Test 3 and Test 4.

4.4.2. 2D Tests

From the 2D tests described by Liska and Wendroff, four Riemann problems and the Noh implosion are here reproduced. The main parameters of the 2D Riemann problems are reported in Tab. 4.4, defining density, pressure and velocities of the initial state in the four left/right-upper/lower quadrants of the computational domain. Consistent with the review paper, the simulations are performed in a domain $(z,y) \in (0,1) \times (0,1)$ with 400×400 cells and a polytropic index of $\gamma = 1.4$. The results are presented in Fig. 4.5 as subplots corresponding to Cases 3, 4, 12, and 15, showing 2D contour plots of the density and velocity field overlaid on the pressure map. The number of contours for each specific case is reported in the caption of the figure. Precisely assessing the quality of the results is not possible, as the exact solution of these 2D Riemann problems is not known. However, visual comparison with the results reported in [96] and [97], obtained with the same contour levels, shows good agreement of the solutions.

Table 4.4: Initialisation parameters for the cases shown in Fig. 4.5. The initial states are divided into *left* and *right* quadrants, with the first and second rows corresponding to the *top* and *bottom* quadrants, respectively. The last column reports the time at which the plots are shown. Data taken from Liska and Wndroff [96].

Case	Left				Right				Time
	p	n	u_z	u_y	p	n	u_z	u_y	
3	0.3	0.5323	1.206	0.0	1.5	1.5	0.0	0.0	0.3
	0.029	0.138	1.206	1.206	0.3	0.5323	0.0	1.206	
4	0.35	0.5065	0.8939	0.0	1.1	1.1	0.0	0.0	0.25
	1.1	1.1	0.8939	0.8939	0.35	0.5065	0.0	0.8939	
12	1.0	1.0	0.7276	0.0	0.4	0.5313	0.0	0.0	0.25
	1.0	0.8	0.0	0.0	1.0	1.0	0.0	0.7276	
15	0.4	0.5197	-0.6259	-0.3	1.0	1.0	0.1	-0.3	0.2
	0.4	0.8	0.1	-0.3	0.4	0.5313	0.1	0.4276	

In addition to the 2D Riemann problems, the Noh implosion test case is shown in Fig. 4.6. This test case considers an ideal gas with $\gamma = 5/3$, for which it admits an analytical solution. The domain is initialised with a uniform density $n = 1$, a pressure of 1×10^{-6} and velocities directed towards the lower left corner with magnitude $u^2 + v^2 = 1$. The left and bottom boundaries are reflective (i.e. a frictionless wall), whereas on the other boundaries, the exact solution as a function of time is applied. The solution consists of a circular shock of infinite strength reflecting from the origin (i.e. lower left corner), propagating with a velocity of $1/3$. Behind the shock, the density is 16 and the velocity 0, whereas in front of the shock the density is $n = 1 + t(x^2 + y^2)^{-0.5}$, with t the time. The presence of the strong shock makes the Noh implosion a difficult test for numerical solvers (e.g half of the solvers in [96] fail the test). The numerical solution of the testcase at $t = 2$

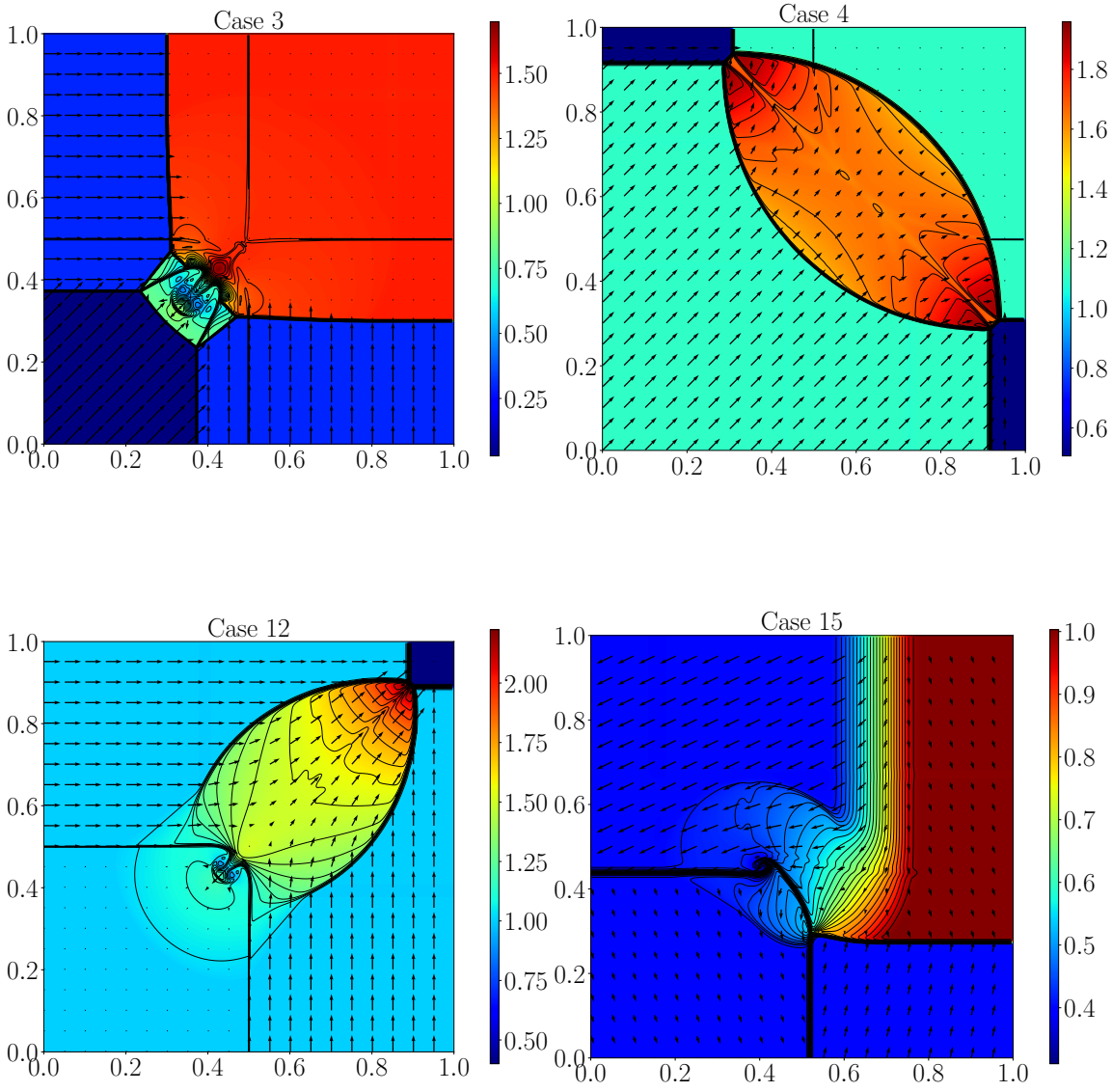

Figure 4.5: Numerical solution of the 2D Riemann problems of table 4.4. For each case, contour lines of the density and velocity (arrows) field are overlaid on the pressure map. The number of contour lines for each case is here reported as minimum, maximum and number of contours: Case 3 (0.16, 1.71, 32), Case 4 (0.52,1.92,29), Case 12 (0.51,1.7,30) and Case 15 (0.43, 0.99, 29).

is shown in Fig. 4.6. The finite volume solver successfully reproduces the test, capturing the correct shock position and the density behind it, although strong oscillations can be observed when the shock is aligned with the mesh. This phenomenon is consistent with the problem of the carbuncle instability, which is known to affect many solvers in the presence of strong shocks [99]. Several fixes have been proposed [100]–[102] to solve the carbuncle instability. However, in the present version of the code, no technique has been implemented yet, and it is left as a topic of future developments.

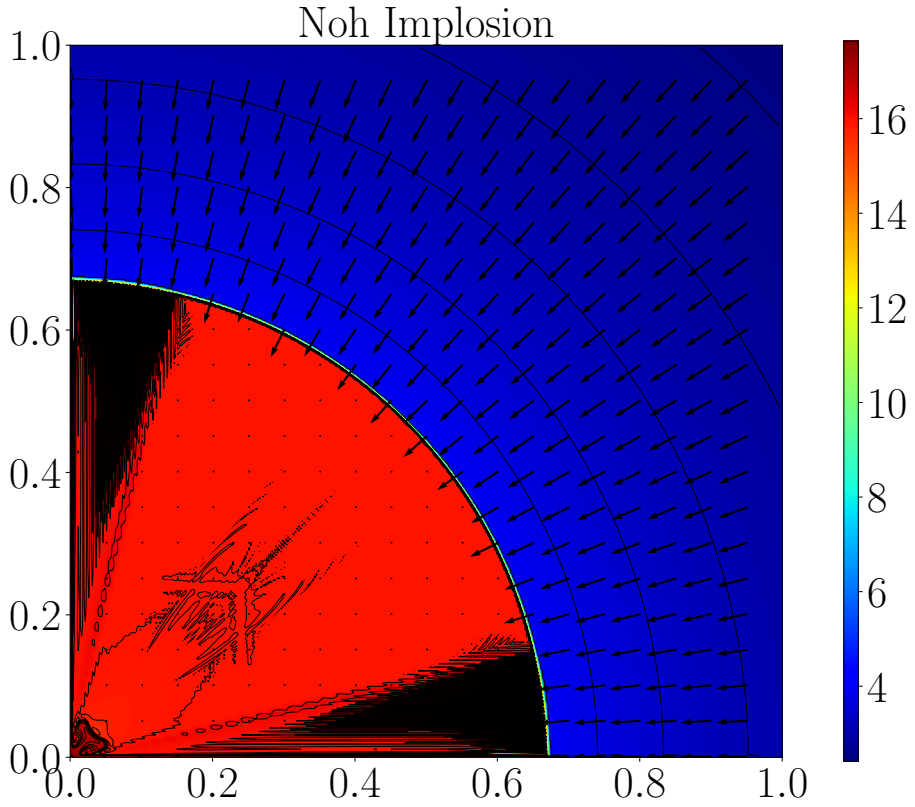

Figure 4.6: Density map of the Noh implosion at $t = 2$ overlaid by a total of 23 density contours (2.5 to 4 with step 0.25 and 14 to 17 with step 0.2), and by the velocity field arrows.

CHAPTER 5

Full-fluid Modelling of Rotating Plasma Instabilities in Penning-like Configurations

This chapter reproduces the contents submitted by the author to the peer-reviewed journal Plasma Sources Science and Technology. The typography has been adapted to the style of this thesis.

Abstract

A novel time-dependent full-fluid 2D model of $E \times B$ discharges is presented. The model is based on the finite volume method with the addition of a threshold-based vacuum tracking algorithm. These tracking capabilities enable unprecedented fluid simulations of $E \times B$ plasma instabilities with near-vacuum regions. Two test cases are presented: the plasma layer (a semi-periodic domain resembling a hollow beam) and a square cross-section Penning-like discharge. In the two cases, an electron beam is injected into a background of neutrals, and ions are solely produced by impact ionisation. In both geometries, the simulations are performed from the limit of a pure electron plasma to a quasineutral plasma by increasing the background neutral density, showing a distinct transition from diocotron modes at low pressures to rotating spokes at high pressures. In line with theoretical and experimental results, the saturated regime of the diocotron mode results in the formation of electron vortices. The structure of the discharge in the different regimes is analysed, and the main spoke characteristics are assessed. In the square Penning configuration, the discharge transitions from vortices to the long-wavelength $m = 1$ rotating spoke. Finally, a variation of the square configuration is used to demonstrate the onset of the short-wavelength spiral structure observed in particle-in-cell simulations.

5.1. Introduction

Since the last century, $E \times B$ devices have been widely used in industrial and space applications for their capability of sustaining plasma discharges at low pressures: the perpendicular electric and magnetic fields increase the residence time of electrons, allowing for efficient impact ionisation of the neutral gas [1]–[3]. The first observation of $E \times B$ discharges dates back to the end of the 19th century with the experiments of Philips [4] on the effects of magnetic fields on the afterglow of discharges. The phenomenon was further studied by Strutt [5] and Wehrli [6], but the first application of $E \times B$ devices was obtained in 1930's by Penning [7], showing how the discharge can be used as a pressure gauge, commercialised as Penning Ionisation Gauge (PIG), being the discharge current proportional to the pressure. From this point on, the Penning discharge (or reflex discharge) gained popularity, and many experiments have been conducted in a large variety of regimes [8], proving the capabilities of sustaining plasma discharges at extremely low pressures. The concept of $E \times B$ confinement was then extended to many types of devices, such as ion pumps, magnetrons (cylindrical and planar)[1], and Hall Effect thrusters (HETs) [103], covering a multitude of applications from material processing to in-space propulsion.

A usually undesirable feature of $E \times B$ plasmas is the inherent weakening of the magnetic confinement of electrons as a result of the onset of a wide range of instabilities [24], [25]. Plasma instabilities are deemed responsible for the enhanced cross-field transport of electrons, resulting in the loss of performance and efficiency of such devices. Abundant experimental evidence has demonstrated the onset of instabilities in the vast operational regimes of Penning discharges, spanning from high-frequency oscillations to low-frequency coherent structures [8]. While the first ones can be attributed to the growth of diocotron modes [9] in non-neutral plasmas at low pressure, the latter ones have been associated with the long-wavelength Simon-Hoh instability [104], [105]. In particular, Thomassen [10] suggested that the low-frequency modes are responsible for the observed anomalous cross-field diffusion in such regimes.

Improvements in computational capabilities have enabled more accurate simulations of $E \times B$ plasmas, and particular effort has been put by the low-temperature plasma community into the analysis of rotating instabilities in magnetrons [106]–[108], HETs [19] and Penning discharges, although the latter ones are limited to the high-pressure and low-magnetic-field regime. Penning discharges and magnetised plasma columns, in general, result in much simpler numerical models than HETs and magnetrons. They are usually approximated as a 2D slice of an infinitely long device, allowing to neglect of the (albeit important) dynamics along the magnetic field. Following the work of Carlsson et al. [109], which performed particle-in-cell (PIC) simulations of a simplified Penning discharge geometry, several authors simulated rotating structures with kinetic codes. Slight variations of the set-up of Carlsson et al. enabled to recover the $m = 1$ spoke [110], [111], as well as $m > 1$ structures [112], [113]. A recent work from Tyushev et al. [114] showed

the transition from one mode to the other as a function of the magnetic field and, for some parameters, the coexistence of both short and long wavelength instabilities. The onset of the long wavelength structures is commonly attributed, according to local linear fluid theory, to the modified, collisionless Simon-Hoh instability [115] (MSHI), for which the condition $\nabla n_e \cdot \boldsymbol{E} > 0$ with n_e the electron density and $\boldsymbol{E}$ the electric field, has to be met (resulting in an ion-confining potential). In contrast, the smaller-scale structures are associated with drift-resistive instabilities [112], [114].

In general, PIC simulations can accurately reproduce a large amount of physics, thanks to the resolution of kinetic effects and arbitrary velocity distribution functions (VDFs); however, the phenomenological extrapolation can be extremely complicated, due to the lack of intuitive physical meaning of what is being observed. On the other hand, fluid models deal directly with macroscopic quantities and transport equations, allowing for better quantification of the effects of the single terms, at the cost of being limited to quasi-Maxwellian VDFs and neglecting kinetic effects.

Fluid simulations of a Penning-type geometry have been performed by Mansour and Hara [116], in particular in a configuration conceptually similar to that of Lucken et al. [113], except for the absence of collisions. While their results show the development of rotating structures, the potential well necessary for the $m = 1$ spoke is not obtained, and the $m > 1$ structures appear to be less fine than the ones observed in PIC simulations, probably due to the lack of collisions and the use of a too diffusive numerical scheme. In general, fluid models struggle with the setup of Carlsson et al. due to the strongly negative potential, especially during the transient, resulting from the injection of a net current (i.e. more electrons than ions): the destabilisation of the column suddenly generates strong vacuum states while the ion density at the boundary reaches extremely low values due to the confining potential. As a result, to the authors' knowledge, there is currently no fluid model capable of simulating the setup of the Penning discharge in the long-wavelength regime.

In this article, a novel, 2D, non-neutral, full-fluid model of $E \times B$ discharges is presented and applied to two simplified geometries: the plasma layer and the standard configuration of the Penning discharge. The model relies on a threshold-based vacuum tracking algorithm to handle near-vacuum states and expand the electron and ion population in a perfect vacuum. In both geometries, the effect of background neutral pressure is explored, analysing the limit of extremely low pressure where the onset of diocotron modes is observed [9], [117], [118], consistent with experimental evidence, and the transition to a spoke regime at larger neutral densities. Moreover, in the Penning discharge, the $m = 1$ spoke satisfying the modified Simon-Hoh condition is obtained, and differences with the PIC results in the literature are commented on. Finally, the short-wavelength spiral structure observed in the Penning discharge is recovered for a slightly different configuration.

The rest of the article is organised as follows. Section 5.2 describes the test case geometry and the set of transport equations, with section 5.2.2 detailing the numerical scheme

and the vacuum tracking algorithm. The results are reported in sections 5.3 and 5.4 for the plasma layer and Penning discharge, respectively.

5.2. Discharge Model

In this section, the fluid model of the plasma discharge and the numerical techniques used for the solution are discussed. All the simulations in this work have been carried out with argon as the working gas.

5.2.1. Fluid Model

The plasma discharge is modelled with a 5-moment full-fluid approximation, using a non-neutral Finite Volume Method (FVM) 2D2V code. The macroscopic transport equations are solved for the electron and ion populations, whereas the neutrals are kept as a constant and uniform background of density n_n. Only the out-of-plane component of the magnetic field $\boldsymbol{B}$ is considered, and all the gradients in such direction are neglected. The effects of the magnetic field are considered for both ions and electrons, although only the latter ones are strongly magnetised, whereas the ions can be considered unmagnetised. The system of equations, expressed in the conservative formulation, reads:

$$\frac{\partial n_e}{\partial t} + \nabla \cdot (n_e \boldsymbol{u}_e) = S_p + S_B, \tag{5.1}$$

$$\frac{\partial n_e \boldsymbol{u}_e}{\partial t} + \nabla \cdot (n_e \boldsymbol{u}_e \boldsymbol{u}_e) = -\frac{\nabla p_e}{m_e} + \frac{e n_e}{m_e} (\nabla \phi - \boldsymbol{u}_e \times \boldsymbol{B}) - n_e \boldsymbol{u}_e n_n R_{en}, \tag{5.2}$$

$$\frac{\partial \mathscr{E}_e}{\partial t} + \nabla \cdot [(\mathscr{E}_e + p_e)\boldsymbol{u}_e] = e n_e \boldsymbol{u}_e \cdot \nabla \phi + \frac{3}{2} S_B T_{eB} - S_p \mathscr{E}_{inel}, \tag{5.3}$$

$$\frac{\partial n_i}{\partial t} + \nabla \cdot (n_i \boldsymbol{u}_i) = S_p, \tag{5.4}$$

$$\frac{\partial n_i \boldsymbol{u}_i}{\partial t} + \nabla \cdot (n_i \boldsymbol{u}_i \boldsymbol{u}_i) = -\frac{\nabla p_i}{m_i} - \frac{e n_i}{m_i} (\nabla \phi - \boldsymbol{u}_i \times \boldsymbol{B}) - n_i \boldsymbol{u}_i n_n R_{cex}, \tag{5.5}$$

$$\frac{\partial \mathscr{E}_i}{\partial t} + \nabla \cdot [(\mathscr{E}_i + p_i)\boldsymbol{u}_i] = -e n_i \boldsymbol{u}_i \cdot \nabla \phi + \frac{3}{2} S_p T_n - n_n R_{cex} (\mathscr{E}_i - \frac{3}{2} n_i T_n), \tag{5.6}$$

$$\nabla^2 \phi = \frac{e}{\varepsilon_0} (n_e - n_i), \tag{5.7}$$

where most symbols are standard for fluid magnitudes and $\mathscr{E} = \left(\frac{3}{2}T + \frac{1}{2}mu^2\right) n$ represents the total energy with adiabatic index $5/3$. In addition, $S_p = n_e n_n R_p(T_e)$ is the production rate due to ionisation and S_B the volumetric source term for the injected electron beam. The electron beam is injected with zero velocity, so that only the internal energy of the beam $\frac{3}{2} S_B T_{eB}$ contributes positively to the electron total energy, whereas inelastic losses, $S_p \mathscr{E}_{inel}$, represent a sink term. For both ions and electrons, only the scalar isotropic pressures, p_i and p_e, are considered, and the conductive heat flux is neglected. It is important

to note that by assuming an isotropic scalar pressure, the gyroviscosity, which can partially compensate inertial effects, is neglected. This assumption is a limitation of the 5-moment model. Ions are subject to charge exchange collisions with neutrals, while electrons perform both inelastic and elastic collisions. Coulomb collisions have not been included, as they are negligible compared to the electron-neutral ones. Collisional rates for ions and electrons R_{cex}, R_{en} and R_p are obtained from experimental cross-sections, assuming a Maxwellian distribution over a wide range of temperatures. The resulting collisional rates are supplied to the code as lookup tables and interpolated at each timestep. The cross-sections for ionisation and elastic collisions are obtained from LxCat [119] from the Hayashi and COP [120] databases, while the charge exchange cross-sections are from Sakabe and Izawa [121]. The effective inelastic energy loss $\mathscr{E}_{inel}$, accounting for both ionisation and excitation is expressed as a fit to the expression derived by Dugan et al. [122] and proposed by Fife[58]:

$$\mathscr{E}_{inel} = (1.75 + 0.188 \exp(0.624\ \mathscr{E}_i/T_e))\mathscr{E}_i, \tag{5.8}$$

with $\mathscr{E}_i$ =15.76 eV the ionisaition energy for argon. In this work, no artificial augmentation of the vacuum permittivity ε_0 has been used.

5.2.2. Code description

The system of hyperbolic equations is solved using a 2D Cartesian FVM. The spatial discretisation is performed with a 2nd order MUSCL scheme with minmod [76] slope limiter using primitive variable reconstruction, and the numerical flux is computed with the HLLC approximate Riemann solver [83]. The electron and ion systems are treated separately but coupled through the Poisson equation. To satisfy the stability criterion of the Euler-Poisson system[89], [90], the equations cannot be trivially advanced in time explicitly, as the system is unconditionally unstable. To overcome this issue, a fractional step method is used to advance separately the homogeneous and the source part of the balance laws. In particular, the second-order accurate Strang splitting scheme is used [91], computing the new potential between the convective and source term steps. The advancing algorithm for a time increment Δt is the following:

1. The collision frequencies are interpolated.
2. The source terms are advanced of $0.5\Delta t$.
3. The homogeneous system is advanced of Δt.
4. The Poisson equation is solved with the new densities.
5. The source terms are advanced of $0.5\Delta t$.

The temporal integration is performed with the 3rd order Strong-Stability-Preserving Runge-Kutta (SSP-RK3) [93] and the Poisson equation is solved using a 5-point finite-difference stencil with the direct solver MUMPS [95]. The algorithm uses an adaptive time-step, meaning that in every iteration, the time-step is computed to satisfy the convective CFL constraint dictated by the largest eigenvalue of the electron system

$$\Delta t_c = \mathrm{CFL} \times \min\left(\frac{\Delta z}{\max_\Omega(\rho_z)}, \frac{\Delta y}{\max_\Omega(\rho_y)}\right), \tag{5.9}$$

with Ω the computational domain, $\Delta z, \Delta y$ the mesh size and $\rho_{z,y} = \max\{|\lambda_1|, ..., |\lambda_n|\}$ the spectral radius of the flux Jacobian of the electron system in the two directions; a value of CFL=0.7 is typically used. Moreover, to ensure the plasma stability, the time-step must resolve the upper-hybrid frequency $\omega_{uh} = \sqrt{\omega_{pe}^2 + \omega_{ce}^2}$, with ω_{pe} and ω_{ce} the plasma and electron cyclotron frequency, respectively. The time-step is thus computed according to:

$$\Delta t \leq \min\left(\Delta t_c, 0.2\frac{2\pi}{\omega_{uh}}\right) \tag{5.10}$$

where the factor 0.2 has been introduced to ensure numerical stability. To further reduce the computational time, the code is parallelised using domain decomposition with the MPI standard.

5.2.3. Vacuum scheme

As mentioned in the introduction, Penning-like geometries are particularly difficult to solve with a standard FVM code: the strong magnetisation of the electrons, coupled with a negative potential well confining the ions and the onset of instabilities, generates near vacuum states (i.e. regions of very low density). In general, approximate Riemann solver algorithms do not handle well the sudden generation of vacuum, mostly due to a failure in the linearisation of the problem near such points (see page 327 of reference [LeVeque [76]]), resulting in the occurrence of negative density or pressure. Positive-pressure preserving [82] solvers ensure the positivity of density and pressure under certain conditions; however, when the equations are not homogeneous (thus including Lorentz force, ionisation, volumetric sources and sinks), such conditions no longer hold, and positivity is not always enforced. To circumvent the problem, the vacuum tracking algorithm has been implemented.

The first vacuum tracking algorithm was proposed by Munz [123] as a sub-cell resolution tracking of the interface of a single fluid with vacuum in 1D. The scheme has been developed to remove the need to assume a low background density to approximate the expansion in vacuum of the Euler equations, which is known to produce a strong unphysical shock. It can be demonstrated (see page 139 of reference [Toro [77]]) that the correct solution of the Riemann problem with vacuum consists of a contact discontinuity coincident with the tail of a rarefaction wave, and a shock wave is never admissible. The scheme uses the exact solution of the Riemann problem of a free expansion into vacuum

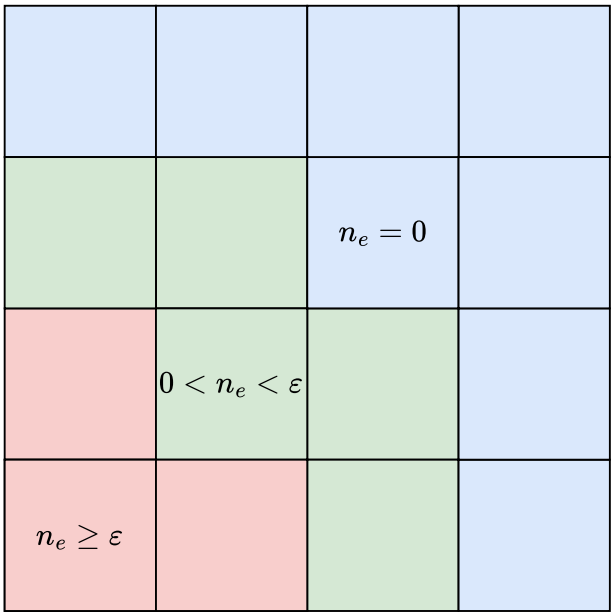

Figure 5.1: Representation of the threshold-based approach for the classification of the cells in the vacuum scheme. In this scheme, red corresponds to *filled* cells, green to *transition* and blue to *vacuum* ones.

for a generic gas with adiabatic index γ. In this case, the speed of the contact discontinuity, which coincides with the velocity of propagation of the fluid-vacuum front, is found to be

$$w_{vac} = u \pm \frac{2a}{\gamma - 1}, \tag{5.11}$$

with u the normal velocity just before the vacuum interface, a_{gas} the gas sound speed at the same location, and the $\pm$ depends on the location of the vacuum state (i.e, right or left). In this work, the fluid-vacuum front speed is computed *for both ions and electrons*.

While Munz used this information to track the movement of the front at the sub-cell level, this becomes very cumbersome in 2D, and the scheme of Subramaniam and Raja [88] has been used here. In their algorithm, a threshold-based approach is used where the domain is split into three types of cells, as shown in Fig. 5.1, based on the local value of the density n of each charged population (i.e. electrons and ions):

$$\text{cell state} = \begin{cases} \text{filled}, & \text{if } n \geq \varepsilon, \\ \text{transition}, & \text{if } 0 < n < \varepsilon, \\ \text{vacuum}, & \text{if } n = 0. \end{cases} \tag{5.12}$$

At every step, the local density is checked, and the cells are stored in the three states. When two or more *filled* cells are adjacent, the standard HLLC algorithm is applied, whereas when a *filled* cell communicates with a *vacuum* one, the numerical flux function is modified by using the vacuum front wave-speed w_{vac} in the approximate Riemann

solver. Once a cell starts getting filled, it moves to the *transition* category. The fluxes between *transition* and *filled* cells are again computed using the classic HLLC solver. To avoid positivity violations due to low densities, *transition* cells are not allowed to exchange fluxes with each other, thus limiting the expansion in very low-density regions. As for the sources, the injection terms are allowed in every state, whereas the application of forces and collisional processes is limited to filled cells. By doing this, the variables in the *transition* cells are effectively frozen to avoid failure due to low density and, at the same time, ensure global conservation.

The threshold value ε needs to be tuned to the specific scenario, and it should be chosen large enough to ensure positivity during the strong vacuum generations behind rotating structures and small enough not to severely affect the solution. Several values of ε have been tested, spanning various orders of magnitude and the one that has been found to ensure successful simulation of all the cases presented here is $\varepsilon = 2 \times 10^9\ \mathrm{m}^{-3}$.

A 1D test case highlighting the difference in solutions between standard methods and the vacuum scheme is reported in Appendix 5.A.

5.2.4. Wall boundary conditions

In all the geometries simulated in this work, the plasma is bounded by metallic walls where secondary electron emission has been neglected. Absorbing boundary conditions are known to be difficult for fluid models due to the kinetic nature of the plasma sheath [29], [39], [62], [90]. In this work, given the necessity of resolving both electron-attracting and electron-repelling sheaths, coupled with the possible formation of vacuum states at the walls, the vacuum sheath proposed by Cagas et al. [62] has been used. The condition is based on the assumption that all the plasma variables vanish inside the wall. When using the vacuum scheme, the condition is simplified even more to the mere imposition of empty ghost-cells

$$\begin{bmatrix} n \\ nu_z \\ nu_y \\ \mathscr{E} \end{bmatrix}^{\alpha}_{ghost} = \begin{bmatrix} 0 \\ 0 \\ 0 \\ 0 \end{bmatrix}, \quad \alpha = i, e. \tag{5.13}$$

To avoid overestimating the fluxes at the wall, at the boundaries, the standard wave-speeds $u \pm a$ are used instead of Eq. (5.11). For the Poisson equation, $\phi = 0$ is imposed at the grounded wall interface.

5.3. Plasma Layer Case

The first geometry analysed consists of a planar semi-periodic domain, along the y direction with two grounded walls on the z direction, as schematically shown in Fig. 5.2. A thin uniform electron beam of thickness h spanning the whole periodic direction is injected at

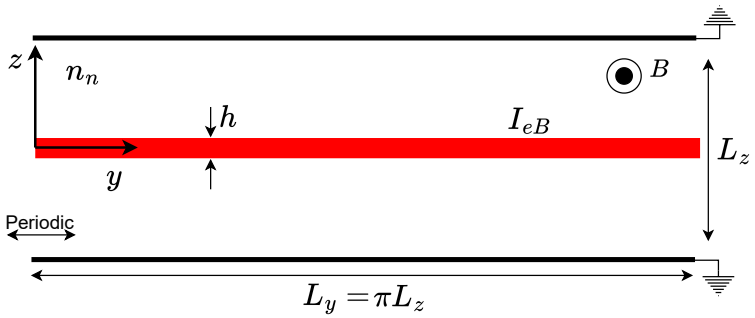

Figure 5.2: Plasma layer test case schematic. Electron beams are injected in the red regions with current I_{eB} and temperature T_{eB}. Ions are solely produced by ionisation of a uniform background of neutrals of density n_n by impacting electrons. At initialisation, the domain is empty. Walls are connected electrically to ground (i.e., $\phi_W = 0$).

the centre of the domain, and a perpendicular uniform magnetic field is considered. The injection is modelled as a volumetric source of electrons with a temperature T_{eB} and zero velocities, thus only contributing to the continuity and energy equations. Following the notation of a preliminary work [124], this geometry is referred to as the plasma layer. Even though the plasma layer does not directly represent a commonly used device, it possesses interesting features:

- The electric field is antisymmetric with respect to the centre of the injection ($z = 0$). As a result, the $E \times B$ velocity changes sign, creating a shear layer inside the thin electron beam.
- The $E \times B$ direction is aligned with the y axis and the grid, simplifying the analysis of the rotating structures.
- The absence of concave corners improves the numerical stability of the code.

Moreover, by choosing the periodic direction length $L_y = \pi L_z$, the plasma layer represents an opened version of a hollow beam between two coaxial walls, with the assumption of negligible radial effects. The main simulation parameters are reported in Table 5.1

The following sections report the simulation results for the plasma layer at different background density regimes

5.3.1. Low pressure regime - Electron vortices

Devices with $E \times B$ configurations can sustain plasma discharge at extremely low pressures. In these conditions, the electrons are usually strongly magnetised and their residence time is much larger than that of the few ions produced, which can easily escape along the magnetic field lines, so that the discharge tends to a pure electron plasma [8]. The model presented in section 5.2.1 is purely 2D, considering a slice of an infinitely long

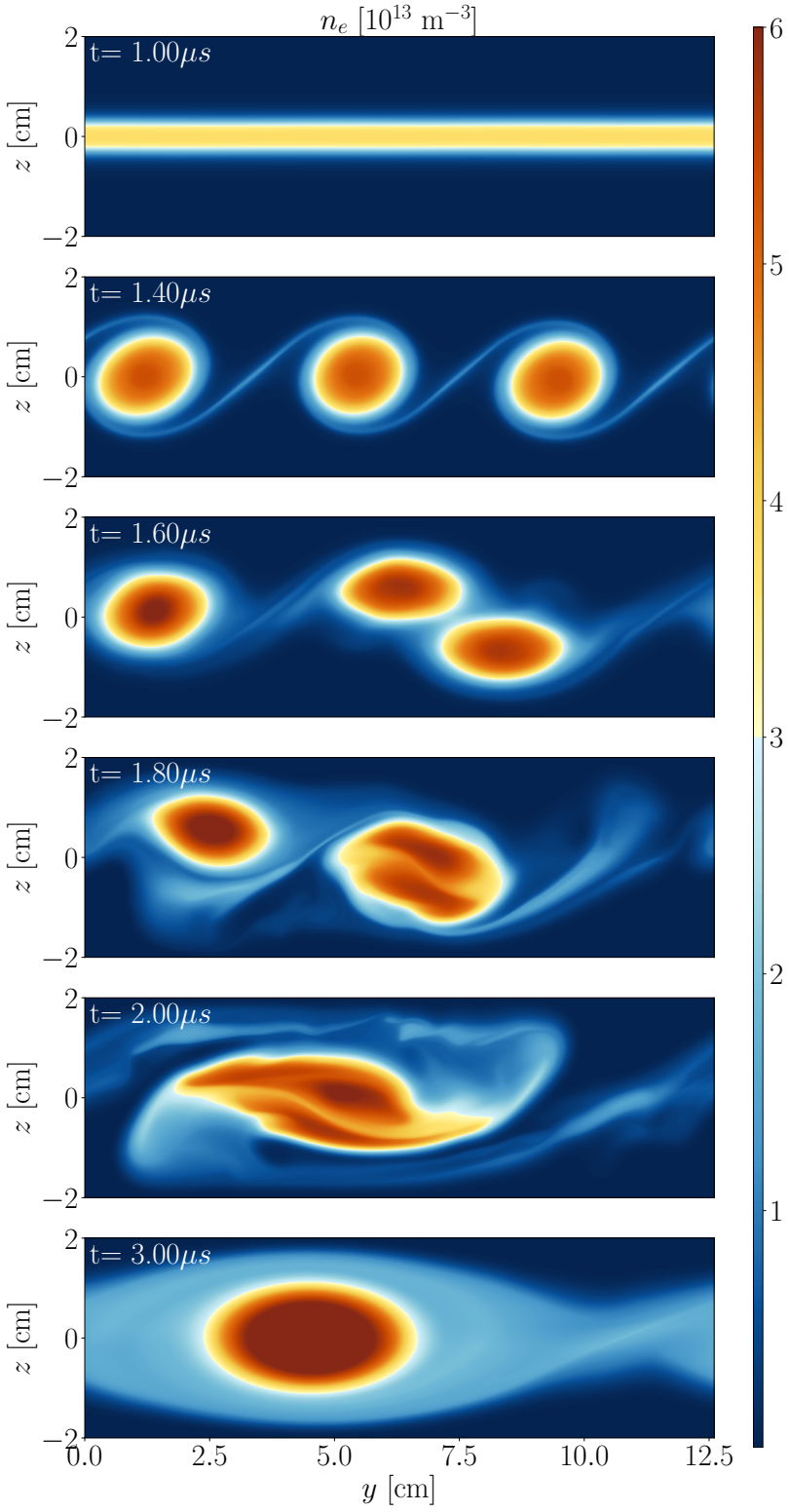

Figure 5.3: Temporal evolution of the electron density in the diocotron instability and vortex formation for a pure electron plasma for B=100 G, $n_n = 0$.

Table 5.1: Relevant simulation parameters for the plasma layer case.

Parameter	Value	Parameter	Value
L_y	12.6 cm	L_z	4 cm
h	4 mm	I_{eB}	5 mA
T_{eB}	15 eV	n_n	0 - 10^{21} m^{-3}
T_n	0.06 eV	B	100 G
Cells y	644	Cells z	255

device, and thus neglects the motion of ions (and electrons) parallel to $\boldsymbol{B}$. Nevertheless, reducing the background neutral density to a low value effectively reduces the ionisation source term S_p, and the ion population remains small compared to the electrons. In these conditions, the discharge is effectively non-neutral, and it represents a common operating point of Penning discharges. Due to the excess of electrons, the discharge develops a deep potential well and, because of the geometry, an antisymmetric electric field. The magnetised electrons are dominated by the strong $E \times B$ drift, which has opposite directions in the two half-domains along z, thus creating a strong azimuthal velocity shear. The configuration of a thin electron shear layer is known to be unstable, as many experiments have demonstrated [117], [118], [125]–[127], due to the onset of the diocotron instability[128]–[130]. The diocotron mode behaves similarly to the Kelvin-Helmholtz instability in fluids, where surface waves grow until they reach the non-linear regime and the subsequent wave breaking. In the non-linear regime, the diocotron instability is responsible for the formation of isolated electron vortices. Kervalishvili [131], [132] carried out extensive studies on the formation, dynamics, and interaction of electron vortices in pure electron plasmas and low-pressure gas discharges. In particular, electron vortices are associated with the periodic ejection of high-energy electrons to the cathode [132], parallel to the magnetic field lines. A limit of the model in the present work is the absence of the out-of-plane velocity necessary to observe such phenomena.

Figure 5.3 shows the time evolution for the limiting case $n_n = 0$, resulting in a pure electron plasma, at 100 G. In agreement with the theory of the diocotron instability, the thin plasma shear layer is unstable, and surface waves start propagating at the edges of the injected electron beam. The instability grows until the nonlinear phase is reached, characterised by the production of electron vortices. The breakdown of the electron beam in vortices is in perfect agreement with experimental observation of hollow and strip electron beams in axial magnetic fields, as it can be observed in Fig. 5.4 adapted from Cutler [118]: the photographs of the electron beam impinging on a phosphor screen show the formation of several electron vortices for different operating conditions. The number of vortices is associated with the mode of the diocotron instability, which, for a large aspect ratio injection, tends to be larger than 1. The multiple vortices are interconnected by spiral "arms", and they coalesce into larger structures, eventually decaying into a single large vortex. The mutual interaction is responsible for the formation of filamentary tails

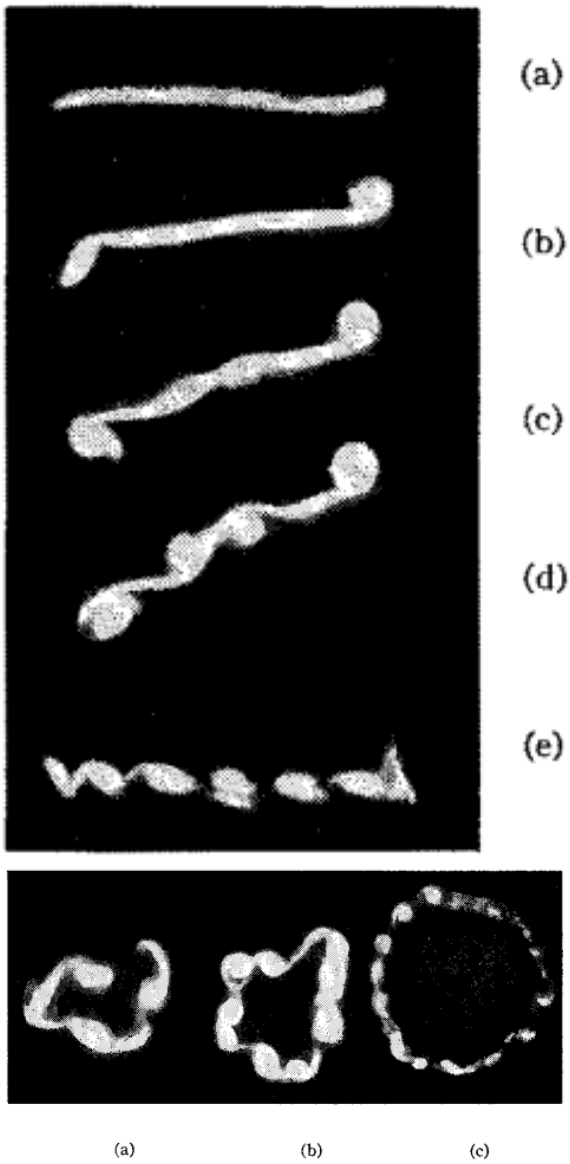

Figure 5.4: Experimental photographs obtained using phosphor screens from Cutler [118]. (Top) Formation of vortices due to instabilities in an electron strip beam. (Bottom) Breakup of a hollow electron beam into vortices. Each set of photographs does not represent a time sequence but different discharge conditions. Reproduced with permission of *Journal of Applied Physics*.

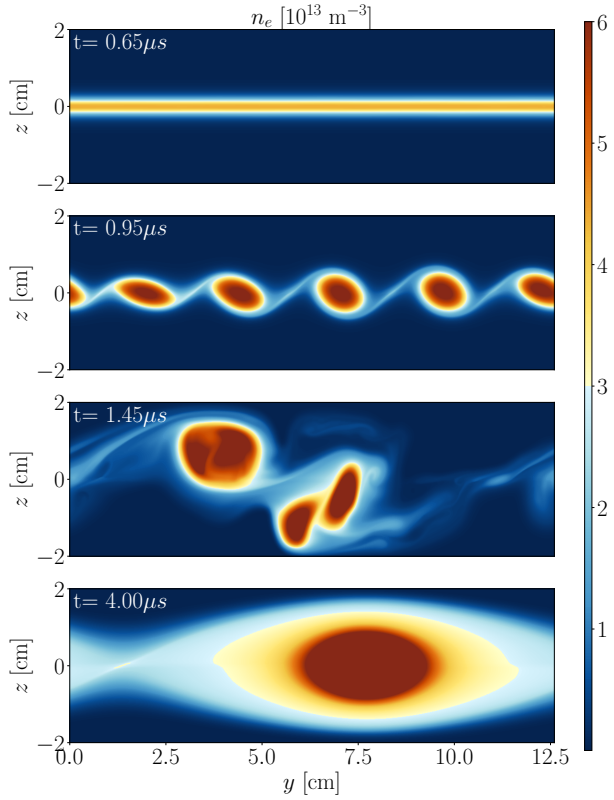

Figure 5.5: Temporal evolution of diocotron instability and vortex formation for a pure electron plasma at B=100 G with injection thickness h =1 mm.

as observed experimentally [133], which extend and form an electron background to the central structure.

According to theoretical and experimental observations [117], [129], the mode number, and thus the number of vortices in which the beam breaks up, is dependent on the aspect ratio of the beam, resulting in higher modes for smaller h/L_y. The increased mode number is correctly captured by the model as shown in Fig. 5.5, where h is reduced from 4 to 1 mm and the beam breaks up in 5 vortices. As for the case of Fig. 5.3, the vortices merge into a single large structure.

Finally, it is worth mentioning the analogy observed by Levy [134] between magnetised pure electron plasmas and inviscid fluids in 2D. The two sets of equations describing such systems are indeed isomorphic, where the fluid stream function maps to the Poisson equation, and thus, the fluid vorticity maps to the (rescaled) electron density, that is

$$\zeta = \nabla^2 \psi \quad \leftrightarrow \quad \frac{e n_e}{\varepsilon_0} = \nabla^2 \phi, \tag{5.14}$$

where ζ is the fluid vorticity and ψ the stream function. It is important to note that the analogy remains valid as long as the out-of-plane dynamics is neglected, ensuring that the electric field in that direction vanishes. Experimentally, vorticity in a fluid is not directly measurable, whereas density is a central and tangible quantity in plasmas. Hence, the mapping between ζ and n_e allows for an easier analysis of the Kelvin-Helmholtz

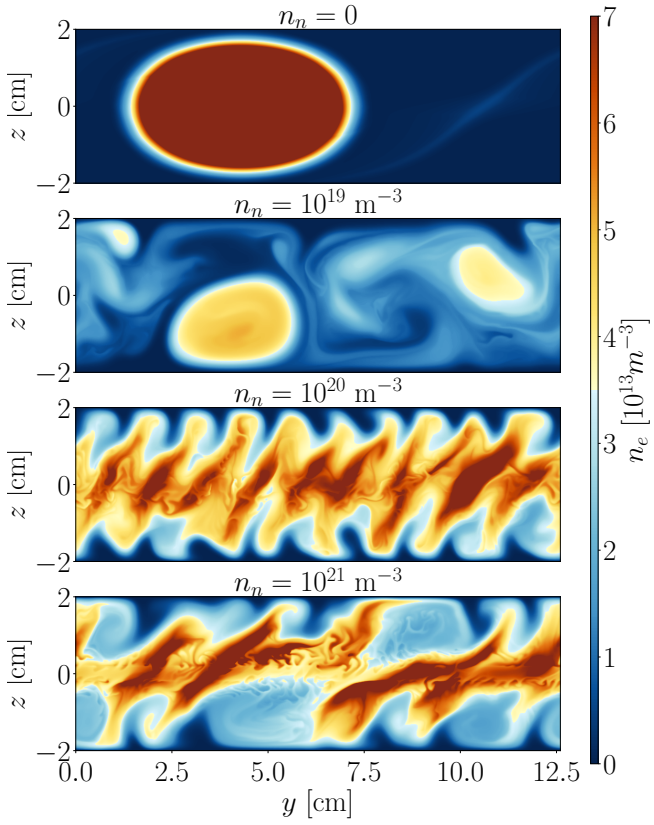

Figure 5.6: Instantaneous snapshots of n_e for different background neutral densities at B=100 G.

instability in 2D inviscid flows by the observation of the corresponding diocotron modes in pure electron plasmas [117]. Here, the analogy is mentioned in relation to the abundant numerical simulations [135], [136] of inviscid fluids, where the vorticity field behaves as the density maps reported in Figs. 5.3 and 5.5. In particular, the evolution of the non-linear phase of the diocotron modes can be explained by the theories of 2D turbulence decay in fluids [137], where small vortices quickly merge into larger structures, subjected to an inverse energy cascade.

5.3.2. High pressure regime - spoke transition

When the background neutral density is increased, ions are generated by impact ionisation of the neutrals by the confined electrons, and the discharge is no longer a pure electron plasma. A secondary, but no less important, effect of increasing the neutral density is the higher rate of elastic electron-neutral collisions, which allow the electrons to move across the magnetic field lines and trigger resistive instabilities. In particular, a distinct mode transition in the turbulent behaviour of the discharge has been observed at larger pressures, associated with the formation of rotating spokes. Figure 5.6 shows the instantaneous electron density distribution for different neutral densities at B =100 G.

At intermediate neutral densities in the range $0 < n_n \leq 10^{19}$ m^{-3}, the discharge retains the vortex structures of the pure electron plasma, but the number of electron vortices increases with the neutral density, and the discharge becomes more chaotic. In this regime, the multiple vortices interact with each other, and new vortices are continuously formed and dissipated. The structures move chaotically in both y and z directions, and the filamentary tails of the vortices result in a diffuse density distribution. A third regime can be observed for $n_n > 10^{19}$ m^{-3} where the discharge forms rotating spokes with $m > 1$ instead of the large vortices observed at lower densities. The spokes move along the y direction as rigid bodies with a velocity close to the ion sound-speed. Due to the antisymmetry of the setup, the structures drift in opposite directions in the two semidomains along z, preserving the shear layer around the electron injection.

The transition from vortices to spokes is also observed at 50 G, where the same general trends observed at 100 G are still valid. A similar mode transition triggered by the background pressure, from a vortex-dominated regime to coherent spokes, has been numerically observed by Boeuf [108] with a 2D PIC simulation of a cylindrical magnetron, showing a strong phenomenological consistency with the trends hereby described. Moreover, in the vast literature on Penning discharges of the past century, there is abundant experimental evidence of strong mode transitions based on the mode of operation [1], [8]. In particular, radio frequency oscillations are usually obtained at low pressures and have been associated with the formation of diocotron modes [9], which, as shown in section 5.3.1, lead to the formation of vortices. On the other hand, at higher pressures, there are conditions for which the discharge presents low-frequency coherent oscillations. Unfortunately, the simplified 2D geometry of the test case makes it difficult to compare directly with the experimental results, mostly due to the lack of an imposed electric field between anode and cathode which makes the dynamics aligned with $\boldsymbol{B}$ not negligible (in these devices, the cathode is usually perpendicular to the magnetic field lines).

Averaged 1D profiles. Figure 5.7 depicts the variation of some time and azimuthally averaged variables of interest at $B = 100$ G for different values of the neutral density. Only the positive half-domain is shown due to symmetry. Plot (a) depicts the distribution of the electron density, which reflects the existence of the three distinct regimes: the large vortex in the pure electron plasma ($n_n = 0$) results in the largest average electron density, whereas the diffuse distribution produced by the chaotic movement of the vortices for $n_n = 10^{19}$ m^{-3} yields the smallest one; the other cases with $n_n > 0$ m^{-3} converge to an average electron density $\bar{n}_e \sim 5 \times 10^{13}$ m^{-3}. The last point can be explained by observing that the electron temperature $\bar{T}_e$ [plot (b)] decreases monotonically with n_n due to the increase of inelastic losses for excitation and ionisation, thus greatly reducing the plasma production and preventing an increase of the plasma density in the domain. As expected, the increase of the ion population has a strong effect on the electric potential profile, as shown in plot (c), which goes from a deep potential well in the case of pure electron plasma to slightly positive values at larger densities. In particular, the on-axis value of

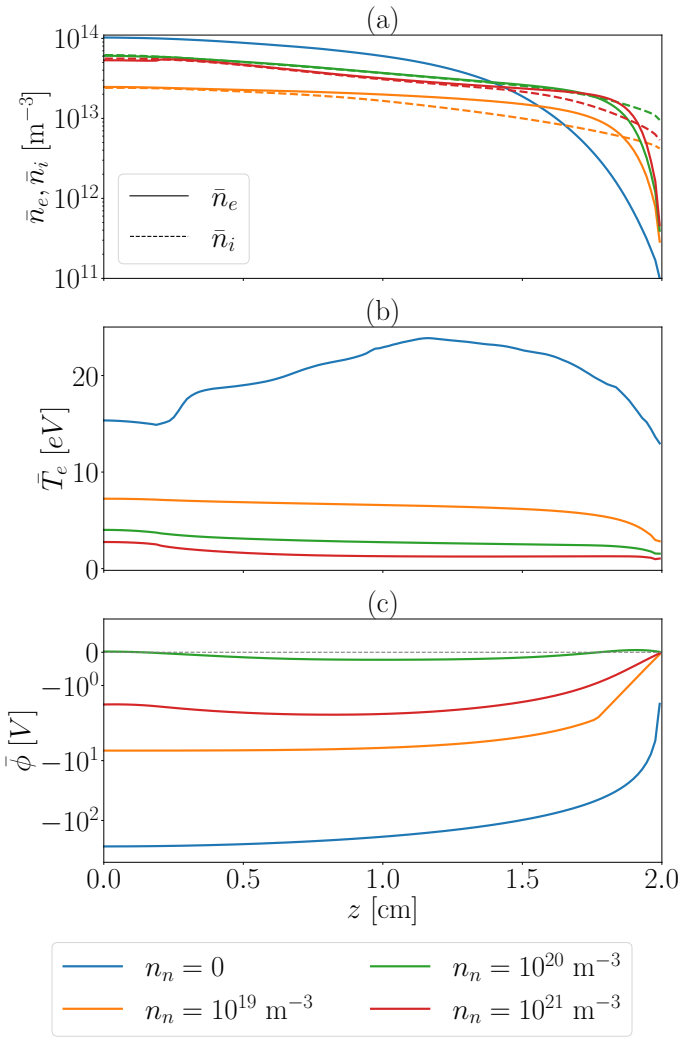

Figure 5.7: Azimuthally and time averaged profiles along z for different values of n_n at $B = 100$ G. In plot (a), $\bar{n}_e$ and $\bar{n}_i$ are represented by a solid and dashed line, respectively. Only the half-domain $z \geq 0$ is shown.

$\bar{\phi}$ shows a non-monotonic behaviour with the neutral density, reaching the maximum for $n_n \sim 10^{20}$ m^{-3}. The presence of the maximum can once again be related to the excessive cooling of electrons at larger neutral densities.

Momentum balance. The electron momentum balance is reported here to analyse the structure of the discharge in the different operating conditions. By averaging azimuthally and in time all terms and using an overbar for averaged variables, the momentum equation (5.2) can be expressed formally as the force balance

$$0 = \bar{F}_{pr} + \bar{F}_{el} + \bar{F}_{mg} + \bar{F}_{co} + \bar{F}_{in}, \tag{5.15}$$

with $\bar{F}_{pr}$, $\bar{F}_{el}$, $\bar{F}_{mg}$, $\bar{F}_{co}$ the pressure, electrostatic, magnetic, and collisional forces, respectively, and $\bar{F}_{in}$ the (minus) temporal and convective inertia terms. These forces are

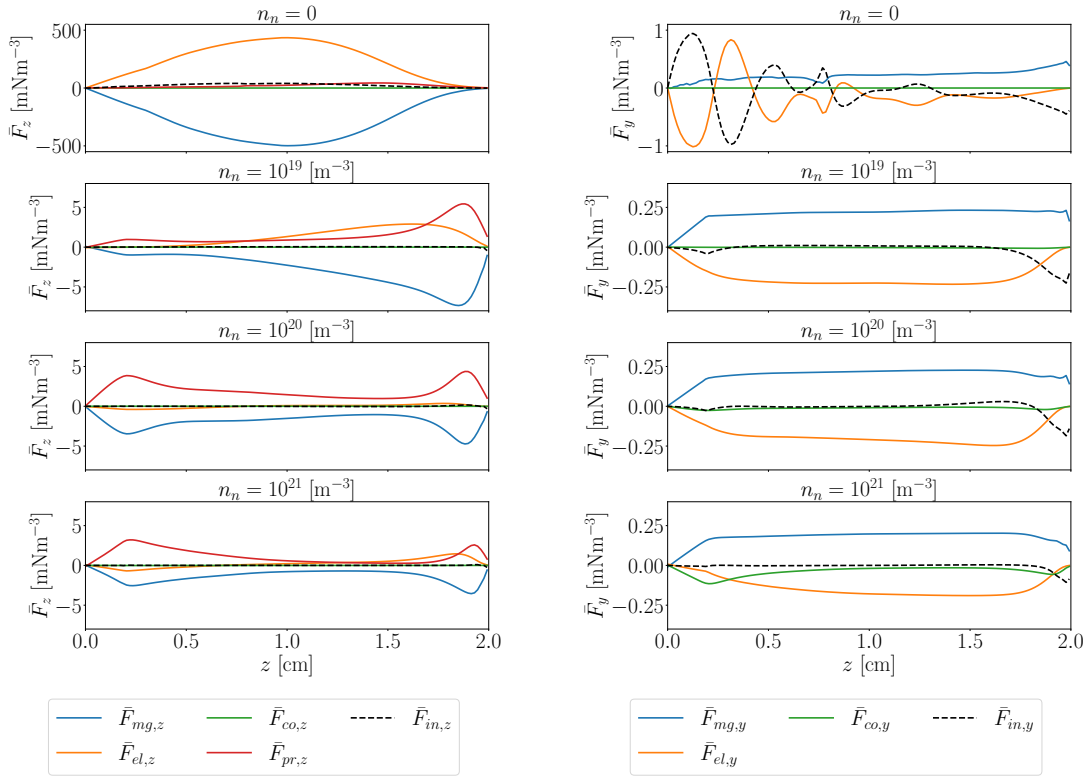

Figure 5.8: Axial (left) and azimuthal (right) momentum balances averaged in time and space (y direction) for the plasma layer at different background neutral densities. Note that for the first plots, a different scale is used and only the half-domain $z \geq 0$ is shown.

shown in Fig. 5.8 for different n_n (only one half domain is shown due to symmetry), for the z (left) and y (right) directions. By observing the force balance along z, the collisional and inertial forces are negligible for all the values of neutral density. On the other hand, it can be observed a distinct transition in the behaviour of the electric force $\bar{F}_{el}$, which completely balances the magnetic force for $n_n = 0$, becomes comparable to the pressure force for $n_n = 10^{19}$ m^{-3} and is negligible for $n_n = 10^{20}$ m^{-3}, where $\bar{F}_{pr}$ balances $\bar{F}_{mg}$. When the neutral density is further increased, the electrostatic force in the sheath

is comparable to the pressure force, consistent with the decrease of potential observed in Fig. 5.7. Due to the presence of an electron-attracting sheath (in most cases), $\bar{F}_{pr}$ and $\bar{F}_{el}$ have the same sign and are balanced by the magnetic force, even in the sheath, being the Debye length larger than the Larmor radius of electrons (i.e. these sheaths are magnetised). The azimuthal momentum balances [Fig. 5.8(right)] for $n_n \geq 10^{19}$ m^{-3} show a standard behaviour in $E \times B$ discharges, where the electrostatic force mostly balances the magnetic one. In the azimuthal momentum equation $\bar{F}_{el,y} = \overline{en_e \partial\phi/\partial y}$ is usually associated with the "anomalous" contribution to cross-field transport [138], and it is different from zero only when there is a correlation between the density and electric field fluctuations. Here, the electrostatic force dominates over the collisional one, with the exception made for the injection region of $n_n = 10^{21}$ m^{-3}, indicating the predominant contribution of instability-induced transport over classical mechanisms (i.e., collisions). On the other hand, in the magnetised sheath, where the electrostatic force vanishes, the contribution of inertia $\bar{F}_{in,y} \simeq -m_e \overline{\partial\left(n_e u_{ye} u_{ze}\right)/\partial z}$ is dominant and balances the magnetic force. The importance of inertia is highlighted even more by the case $n_n = 0$ where it almost completely balances the electrostatic force.

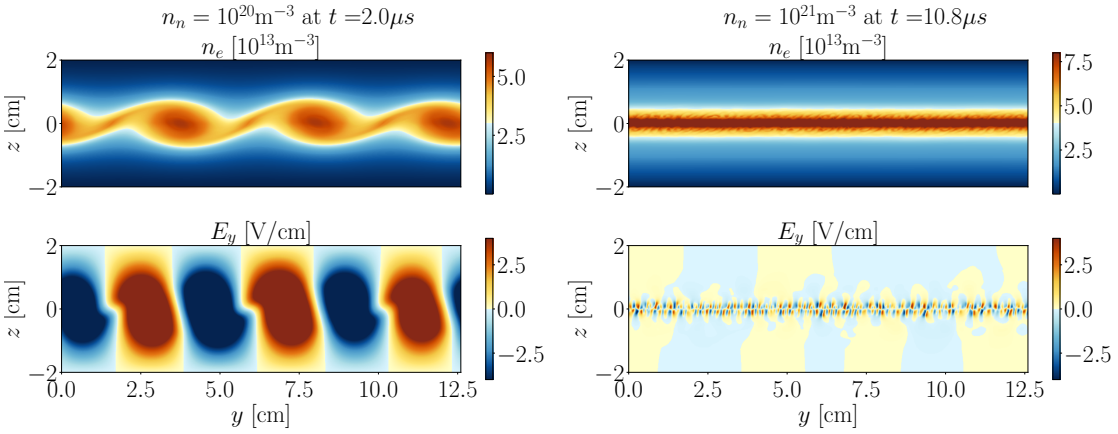

Figure 5.9: Electron density n_e and electric field E_y at the time of the onset of the instability for the cases at $n_n = 10^{20}$ m^{-3} (left) and $n_n = 10^{21}$ m^{-3} (right).

Instability onset. Even though the saturated regimes at $n_n = 10^{20}$ m^{-3} and $n_n = 10^{21}$ m^{-3} remain qualitatively the same, featuring large counter-streaming spokes, the onset of the instability at the beginning of the simulation presents non-negligible differences between the two cases. Figure 5.9 shows the instantaneous electron density and azimuthal electric field for the cases at $n_n = 10^{20}$ m^{-3} and $n_n = 10^{21}$ m^{-3}, along with the corresponding simulation time. In the first case, the destabilisation of the electron beam happens very soon in the simulation, with a behaviour analogous to the one presented in Sec. 5.3.1 for the diocotron instability, suggesting a scarcity of ions in the domain. At larger densities, the charge imbalance is reduced by the larger ionisation rate and by the higher losses of electrons to the lateral walls due to the increased electron mobility caused by electron-neutral collisions. The result is a very different transient characterised by the absence of the

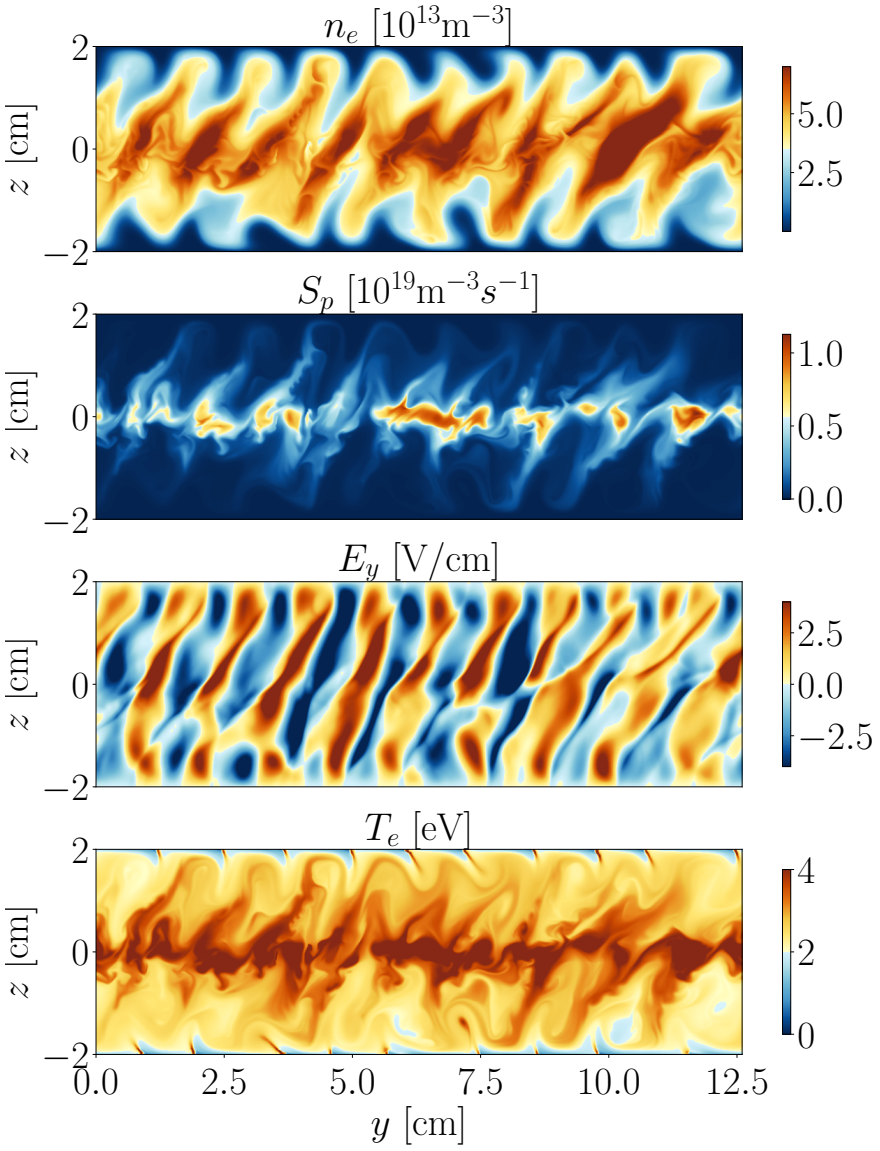

Figure 5.10: Instantaneous distribution (at 200 µs) of n_e, S_p, E_y and T_e for the case $n_n = 10^{20}$ m^{-3} and B =100 G.

large diocotron-like vortices and the appearance of a high-frequency instability localised around the beam injection area. The short-wavelength instability progressively extends towards the lateral walls while increasing in wavelength, until eventually the saturated regime of Fig. 5.6 is reached.

Spoke Analysis. Here, a preliminary analysis of the spoke regime is presented. Figure 5.10 shows the instantaneous profiles of n_e, S_p, E_y and T_e at 200 µs for the case B =100 G, $n_n = 10^{20}$ m^{-3}. In these conditions, the discharge presents several spokes, propagating azimuthally with opposite velocities in the two antisymmetric semi-domains. At the centre of the shear layer, the formation of fast-dynamics turbulent structures can be observed. The spokes are associated with sharp changes of the azimuthal electric field,

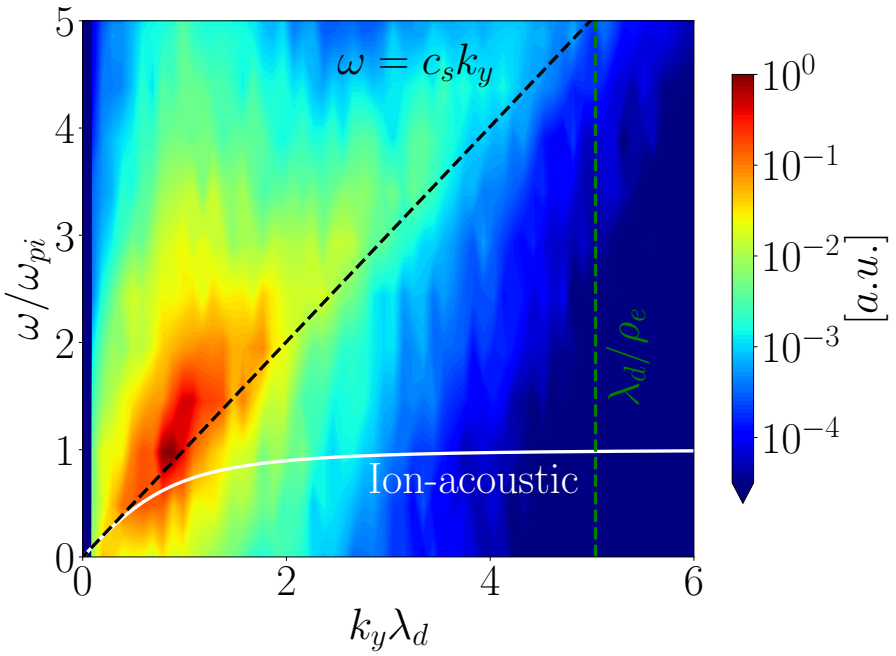

Figure 5.11: 2D FFT of the test case $B = 100$ G, $n_n = 10^{20}$ m^{-3} at $z = 1$ cm. The frequency and wavenumber axes have been normalised with the ion plasma frequency ω_{pi} and Debye length λ_d, respectively. The white dashed line represents $w = c_s k$, the white solid line the ion-acoustic wave dispersion relation, and the green vertical dashed line is the electron Larmor radius ρ_e.

as shown in the 2D map of E_y. The spokes move along the y direction with a velocity close to the ion-sound velocity $c_s = \sqrt{T_e/m_i}$. This seems to be in good agreement with the 2D Fast-Fourier-Transform (FFT) (performed on the y spatial coordinate and time) of the electric field E_y at $z = 1$ cm which closely follows $\omega \simeq c_s k_y$, as shown in Fig. 5.11.

To address whether the formation of the spokes can be associated with the Critical Ionisation Velocity (CIV), often cited as a possible reason for the spoke formation $E \times B$ devices, such as homopolar discharges [139], the distribution of the ionisation source term S_p is reported in Fig. 5.10. According to the CIV theory, if the relative motion of plasma and neutrals exceeds the critical ionisation velocity obtained as $v_{CIV} = \sqrt{2eE_{ion}/m_i}$, with E_{ion} the ionisation energy, a rapid ionisation of the gas by turbulent heating of the electrons is observed [140]. As shown in Fig. 5.10, the ionisation source term is predominantly localised in the central part of the discharge, in the injection region, and does not seem to originate from the rotating structures. Moreover, as commented before, the spokes rotate with a velocity close to $c_s \approx 3100\,\mathrm{m\,s^{-1}}$, which is lower than the critical ionisation velocity for argon $v_{CIV} \approx 8720\,\mathrm{m\,s^{-1}}$. Finally, the distribution of the electron temperature T_e highlights how the hottest part of the discharge corresponds to the injection region, suggesting that no relevant turbulent collisionless heating is taking place in the rotating structures, as suggested by the CIV theory. For these reasons, it appears that the origin of the spoke is of a different nature, and the critical ionisation velocity theory does not apply here.

5.4. Square domain

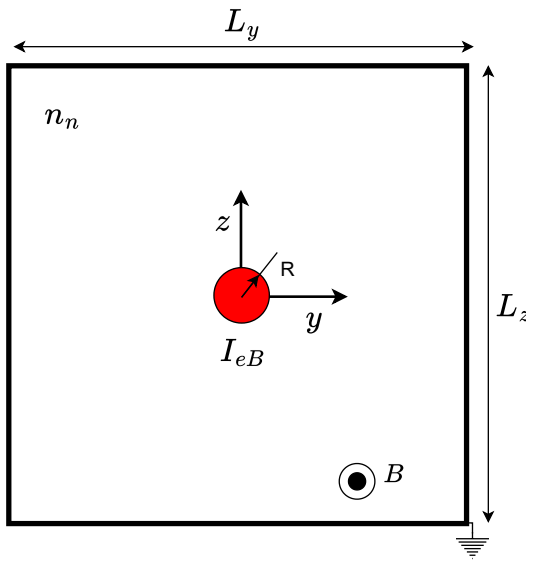

Figure 5.12: Geometry of the square cross-section Penning discharge. The electron beam is injected at the centre of the domain (red circle).

Table 5.2: Relevant simulation parameters for the square Penning discharge case.

Parameter	Value	Parameter	Value
L_y	6 cm	L_z	6 cm
R	4 mm	I_{eB}	2 mA
T_{eB}	10 eV	n_n	0 - 10^{21} m^{-3}
T_n	0.06 eV	B	50 G
Cells y	305	Cells z	305

In this section, a more standard setup is explored. The schematic reported in Fig. 5.12 shows the classic [109] representation of the cross section of a Penning discharge with a square domain. In the high-pressure regime (i.e. sufficiently large neutral background density), this configuration is usually used in PIC models to study the onset of rotating instabilities, with particular emphasis on the long-wavelength $m = 1$ rotating spoke [109]–[111], [114], [141]. However, high-frequency spiral structures have also been observed by Lucken et al. [112]. In a recent work from Tyushev et al. [114], both modes have been recovered for different magnetic field values, and the mode transition has been attributed to a change in the development mechanism of the instability. The $m = 1$ rotating spoke has often been associated with the onset of the drift-gradient instability known as modified Simon-Hoh instability [115], which requires the condition $\nabla n \cdot \boldsymbol{E} > 0$ and thus a potential

well at the centre of the domain. On the other hand, consistent with Lucken et al., the high-frequency spiral structure seems to be linked with a drift-resistive instability, generally occurring when the potential at the centre of the domain is positive (i.e. $\nabla n \cdot \boldsymbol{E} < 0$). The fluid local linear theory can generally explain both instability modes; however, to understand the extent of kinetic effects in PIC simulations, it is interesting to reproduce these rotating structures with a non-linear fluid model, especially in the saturated non-linear regime. Moreover, as mentioned in the Introduction, extensive experiments have been performed on Penning discharges in the low-pressure regime. In line with the plasma layer section, the numerical analysis of the Penning discharge at low neutral density is first presented in the following sections.

5.4.1. Low pressure regime

Here, the square geometry of the Penning discharge is analysed in the low-pressure regime. For all the simulations described here, the parameters in Table 5.2 are used. As for section 5.3.1, it is interesting to observe the behaviour of the discharge in the pure electron plasma limit, where $n_n = 0$ and only electrons are injected in an empty domain. As expected, the magnetised electrons remain trapped at the centre of the domain until the circular column destabilises into a $m = 4$ structure (possibly induced by the square geometry of the domain), from the vertices of which four clumps of density are formed, making the plasma blob non-uniform. The non-uniformity in the density distribution persists throughout the 800 µs simulation, contrary to the uniform vortex observed in section 5.3.1, resulting in fast-rotating fluctuations. Nevertheless, neither a defined rotating structure nor displacement of the column is observed, and the electrons reach the quasi-stationary distribution reported in Fig. 5.13(top). Figure 5.13(b),(c) shows the time-averaged profiles of n_e and ϕ at $z = 0$ cm, featuring the expected deep potential well at the centre of the domain.

However, when the neutral density is increased, a completely different behaviour is observed. In line with what was observed in the plasma layer, the discharge becomes more chaotic, and the plasma density does not remain confined at the centre of the domain. Instead, a strong periodic destabilisation is observed, which pushes the blob of plasma towards the lateral walls. While approaching the wall, the blob deforms into an ellipsoid, and it starts rotating along the domain perimeter, following the lateral boundaries as the circular structure of the vortex is restored. The vortex moves around the domain until it returns to the injection region, and the process repeats. This time evolution is shown in Fig. 5.14 for a background neutral density $n_n = 10^{18}\mathrm{m}^{-3}$. The periodic destabilisation is reflected in the collected current at the walls (i.e. the sum of the currents on the 4 lateral boundaries), which presents periodic bursts of current with a frequency $f \approx 65$ kHz. In this regime of the discharge, increasing the neutral density to $n_n = 10^{19}\mathrm{m}^{-3}$ does not alter the qualitative behaviour of the destabilisation except for a more chaotic evolution of the moving vortex and a higher frequency of the periodic bursts ($f \approx$133 kHz). As mentioned in the previous sections, drawing direct comparisons with experiments is challenging due

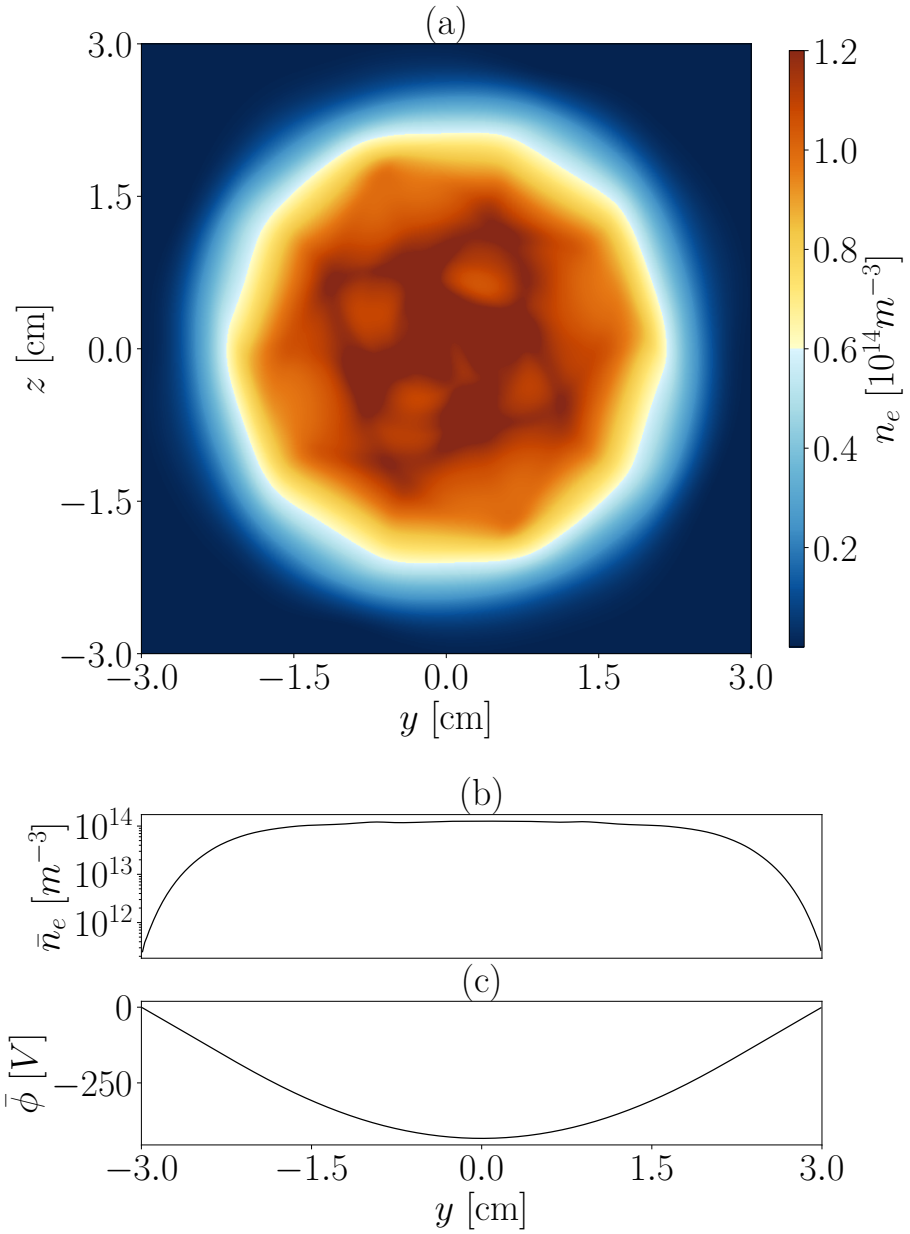

Figure 5.13: (a) Instantaneous distribution of n_e for the case $n_n = 0$ and B =50 G. (b)(c) Time-averaged profiles of electron density and potential, taken at z =0 cm.

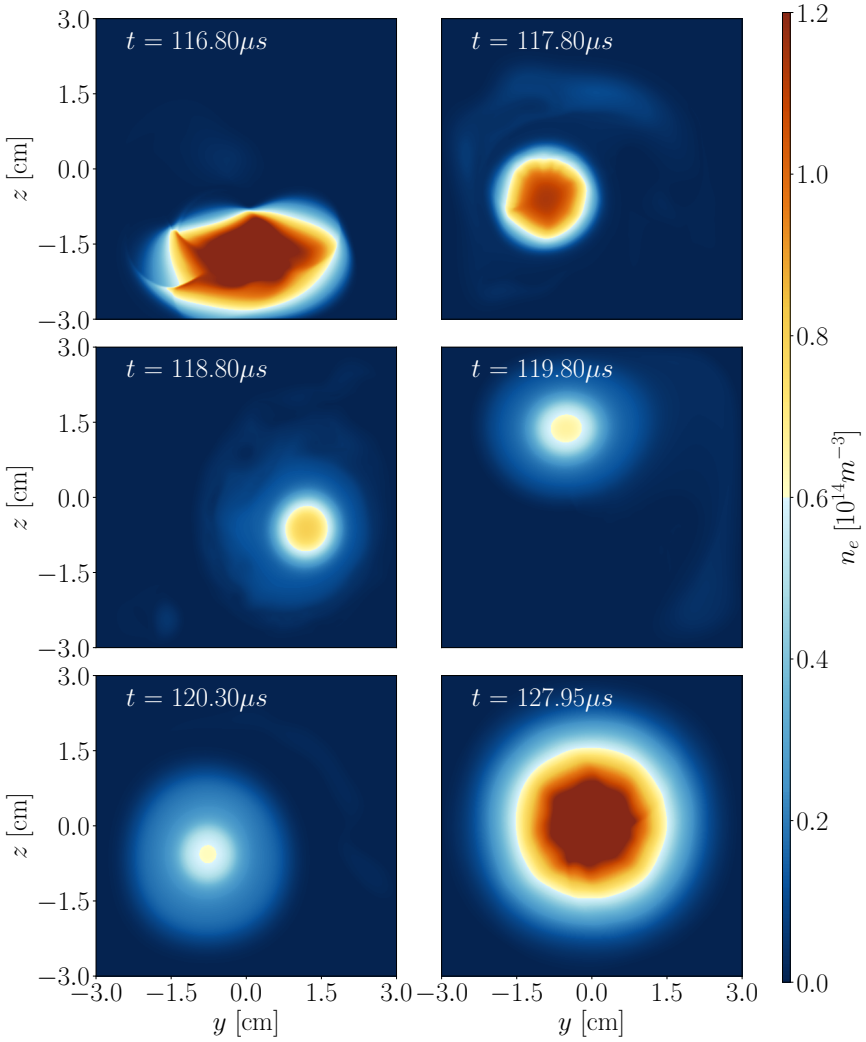

Figure 5.14: Time evolution of the electron density n_e during a period of destabilisation of the discharge for the case $n_n = 10^{18}\mathrm{m}^{-3}$ and B =50 G.

to the model's limited dimensionality. Nevertheless, for certain parameters, experiments have shown [1] a pressure dependency of the oscillation frequency of Penning discharges and other $E \times B$ devices.

5.4.2. Long-wavelength $m = 1$ spoke

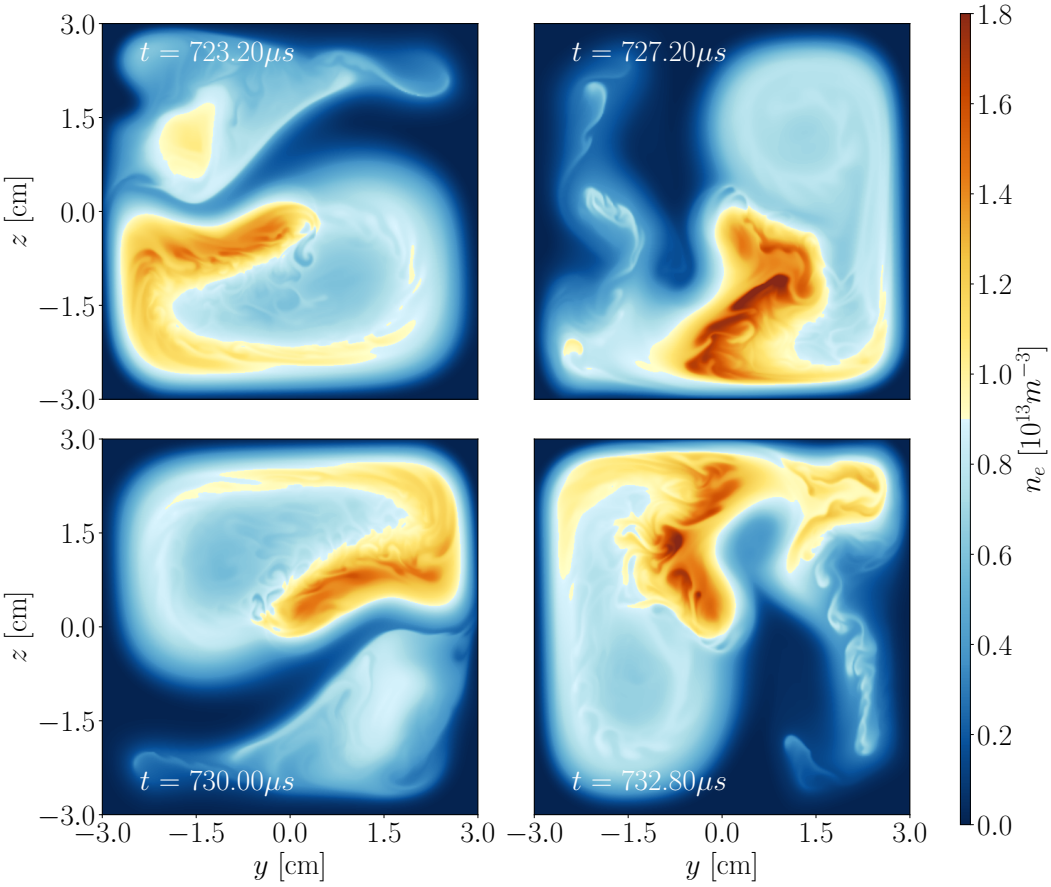

Figure 5.15: Time evolution of the electron density n_e for the rotating spoke at B =50 G and $n_n = 10^{20}$ m^{-3}.

Increasing the background neutral density to $n_n = 10^{20}$m^{-3} results in a mode transition of the discharge, where the periodic destabilisation is lost and a continuous $m = 1$ rotating spoke is observed. It is worth noting that the single-spoke configuration is complicated to obtain, on the one hand, due to the necessity of a potential well and the consequent generation of near-vacuum states, and on the other, due to the sensitivity of the discharge to the simulation parameters. Here, the first full fluid simulation of a single rotating spoke in the Penning discharge geometry is obtained. Figure 5.15 shows the time evolution of the electron density in a complete rotation of the $m = 1$ spoke: compared to PIC simulations, the spoke appears to be less defined, always preceded by a large current loop and followed by periodic separation of density blobs from the main structure. Nevertheless, even in PIC simulations, the spoke appearance seems to be strongly dependent

on the discharge parameters, some featuring the same loop, which however breaks down into smaller vortices. Moreover, the peak density of the spoke of Fig. 5.15 remains low and close to the background electrons; several numerical tests have shown that at larger densities, the spoke coherence is lost. It has been found that PIC simulation parameters are not directly applicable to these fluid simulations, mostly due to the different electron beam injection conditions (i.e. the lack of the perpendicular velocity and thus the kinetic energy in that direction) and due to the larger numerical diffusion characteristic of fluid simulations; in future works the off-plane velocity can be added, thus partially reducing the discrepancies. Besides the aforementioned differences, the simulation can reproduce a $m = 1$ spoke rotating at a frequency f =83.9 kHz. The spoke is characterised by the presence of finer structures, mostly localised in the leading edge of the spoke, where the density loop closes on itself. Figure 5.16 shows the time-averaged profiles of several

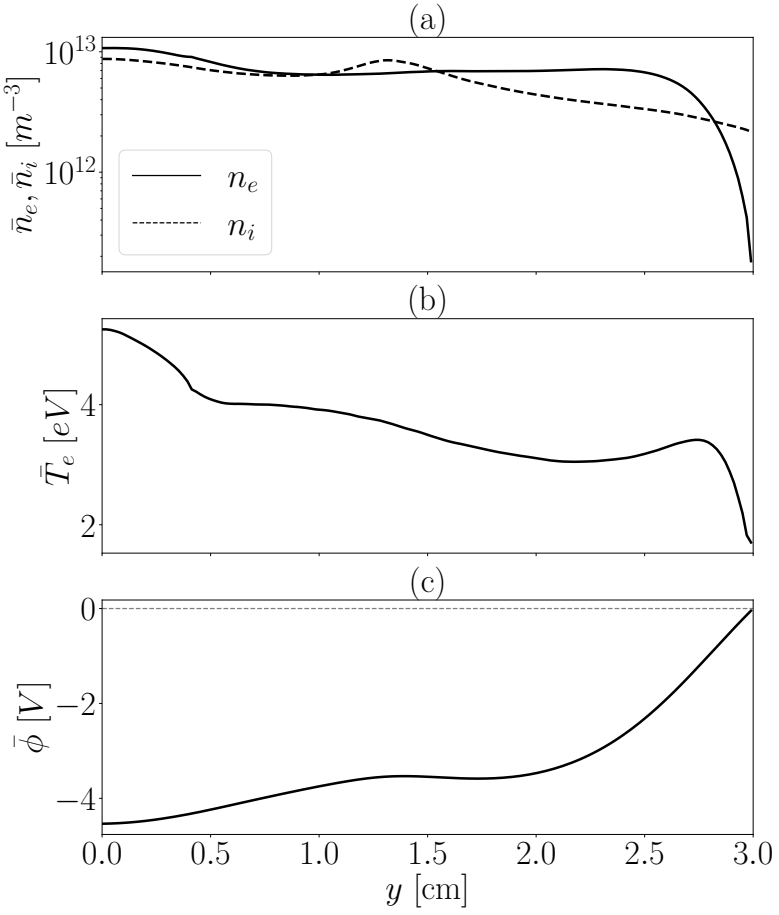

Figure 5.16: Time averaged properties of the rotating spoke at B =50 G and $n_n = 10^{20}$ m^{-3}, taken at $z = 0$ of Fig. 5.15. Only the half-domain $y \geq 0$ is shown.

quantities (evaluated at $z = 0$). As shown in plot (b), the potential is negative at the centre of the domain, in agreement with PIC simulations in the literature in the presence of the $m = 1$ spoke, as opposed to the case shown in Fig. 5.17. Even though looking at plots (a) and (b), it can be observed that the condition for the MSHI is present, it is not trivial to assess the origin of the rotating instability: the MSHI derivation is based on local linear

theory, thus not strictly applicable to the profiles of Fig. 5.16 where the saturated regime is shown; in general the presence of global or boundary effects cannot be excluded. Moreover, the coexistence of short and long-wavelength structures suggests a more complex scenario, where collision-driven drift-resistive modes play a non-negligible role. Increasing the neutral density to $n_n = 10^{21}$ m^{-3} results in a loss of the $m = 1$ mode in favour of higher mode numbers, usually $m = 2$ and $m = 3$, although in a much less coherent way: the rotating structure does not reach a stable operation in the 800 µs simulated, but it rather switches between $m = 2$ and 3 with the sporadic occurrence of the single spoke.

5.4.3. Short-wavelength spiral structure

As previously commented, recent works have shown how the Penning discharge can be subject to a mode transition from the long-wavelength $m = 1$ mode to the $m > 1$ short-wavelength spiral structure [114]. With the geometry and the parameters reported in section 5.4 (with reference to Fig. 5.12 and Table 5.2), the transition to the spiral spoke regime has not been recovered in the present work. The reasons behind the lack of such a transition are not clear, bearing in mind that the differences in the electron beam injection of this model with respect to 2D3V PIC codes (mentioned in the previous section) can play a role. Nevertheless, in general, the spiral spoke regime can be easily obtained with a 5-moment fluid model (or even an isothermal model [124]), showing qualitative agreement with kinetic results [112]. Here, a variation of the configuration used so far is presented, where the self-consistent ionisation has been removed, and the same amount of ion and electron current $I_e = I_i = I$ is injected at the centre of the domain following a Gaussian distribution, with L =10 cm and B =200 G. This setup simulates the conditions used by Lucken et al., which rely on RF power deposition to create a current-free plasma source. Moreover, the simulation domain is initialised with a uniform background density of electrons and ions, as the vacuum scheme is not necessary for this configuration. The instantaneous distribution of plasma density (the discharge is quasi-neutral except for the sheaths) is shown in Fig. 5.17, above the time-averaged profiles of plasma potential and electron density. In analogy with both Lucken et al. and Tyushev et al., the spiral spoke is obtained when the density and potential profile [plots (b) and (c)] follow the same decay towards the wall, as opposed to the MSHI condition observed in the $m = 1$ configuration [Fig. 5.16]. Similar results with a fluid model have been obtained by Mansour and Hara [116], although in their case the rotating structures are not as those obtained either by PIC codes [112], [114] or in this work, probably due to the lack of electron-neutral collisions and the excessive diffusivity of the numerical scheme used. Figure 5.17 shows the instantaneous electron density map and the averaged profiles of n_e and ϕ; it is interesting to observe that both this case and the plasma layer of Fig. 5.10 present spokes with $m > 1$ and the same averaged profiles of electron density and potential.

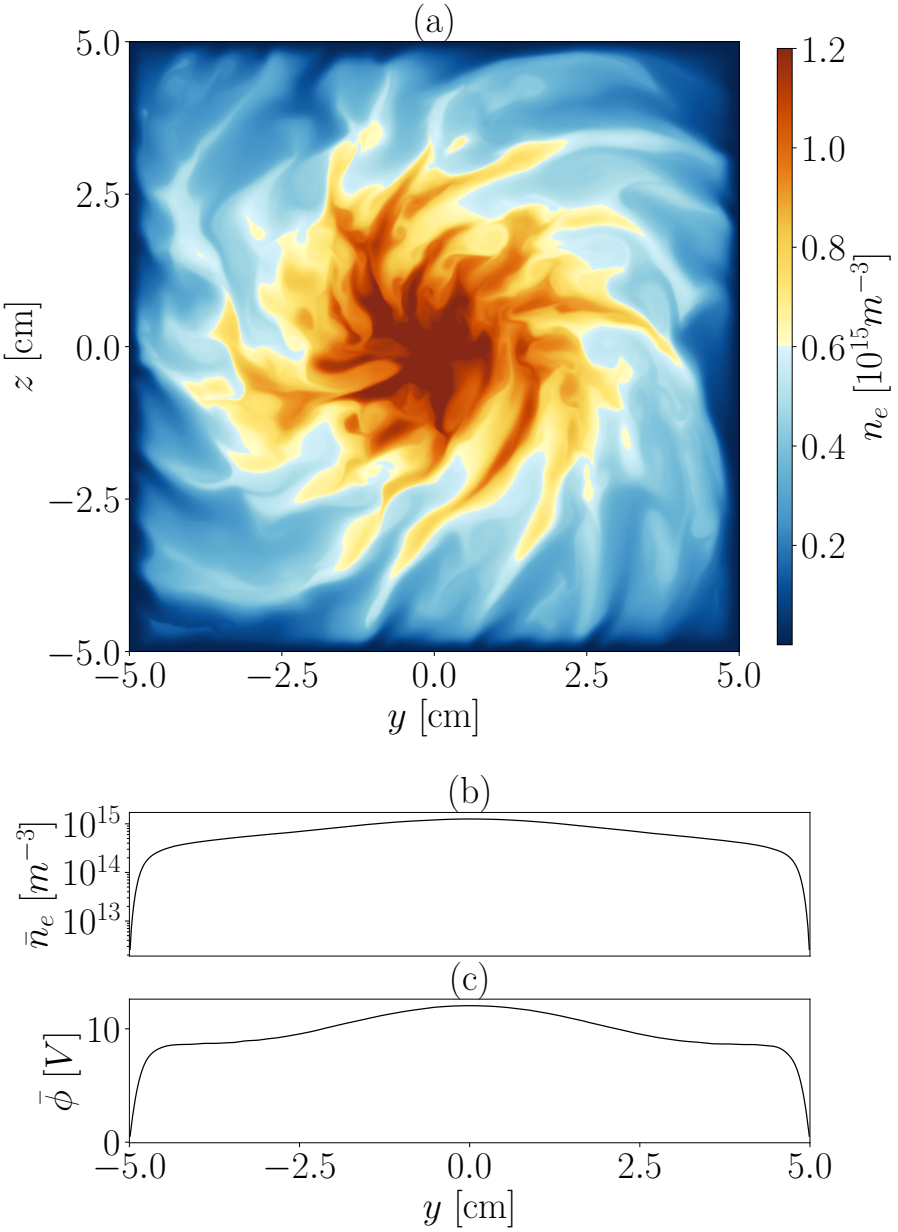

Figure 5.17: (Top) Spiral spoke with Gaussian injection of electrons and ions, with $I_e = I_i = 50$ mA at 200 G. (Bottom) Plots (a) and (b) show the time-averaged profiles of electron density and potential, taken at $z = 0$.

5.5. Summary and Conclusions

A novel 2D full-fluid code to model $E \times B$ discharges has been presented. The standard 5-moment two-fluid plasma model is introduced here with a new numerical approach to overcome the difficulties associated with simulating $E \times B$ plasmas. The *vacuum* scheme is used to expand plasma in regions of very low density while maintaining the classic Finite Volume Method scheme based on the use of approximate Riemann solvers. The scheme relies on a threshold-based approach [88] to subdivide the computational domain in *filled* cells, where the standard HLLC method is used, and *vacuum* or *transition*, at the interface of which the exact Riemann solution of a vacuum-gas expansion is used. The resulting scheme is capable of handling vacuum and near-vacuum states, including the possibility of initialising the discharge in a perfectly empty domain, as is usually done with PIC codes. The use of the vacuum sheath condition from Cagas et al. [62] for the absorbing metallic walls allows for the immediate resolution of both electron-attracting and electron-repelling sheaths.

The vacuum scheme has been used to simulate two different test cases, which can be partially related to the geometry and characteristics of the Penning discharge. The first test case, further from the classic geometry, consists of a thin electron beam injected between two parallel metallic plates, thus resembling a hollow electron beam or a strip beam. The background neutral density n_n has been varied from 0 to 10^{21} m^{-3} at magnetic fields between 50 and 100 G. The ions in the domain are solely produced by ionisation of the background neutral gas. In this configuration, a strong shear layer forms in the magnetised electrons, due to the opposite $E \times B$ drift arising from the antisymmetry of the electric field with respect to the beam injection. In the limit of $n_n = 0$ the discharge is composed of a pure electron plasma, a condition often found in the use of Penning discharges at very low pressures. As predicted by the theory and experimental results, the electron beam is subject to diocotron modes, which eventually break down the plasma beam in electron vortices: the vortices interact with each other, merging into larger structures. The formation of the vortex structure due to the diocotron instability is directly compared with photographs of phosphor screens in similar devices; the dependency of the diocotron mode number on the thickness-to-length ratio h/L_y is briefly commented.

At higher neutral densities, however, the ion production and elastic collisions are no longer negligible, and the discharge undergoes a mode transition to coherent rotating spokes. A similar transition has been observed in PIC simulations [108] of magnetron discharges. Increasing the neutral density results in a non-monotonic variation of the potential, which presents a maximum before decreasing again at large values of n_n; nevertheless, a local maximum of ϕ is always observed in the injection region in the presence of spokes, both at 50 and 100 G. An analysis conducted on the case at 100 G and $n_n = 10^{20}$ m^{-3}, showed that the spokes move with a velocity close to the ion acoustic speed; this is confirmed by the 2D FFT of E_y which closely follows the ion acoustic dispersion relation. As a result, the CIV theory does not seem to be a driver of the ro-

tating spoke. A distinct onset of the instability has been observed between the cases $n_n = 10^{20}$ m^{-3} and $n_n = 10^{21}$ m^{-3}, even though similar rotating spokes are present in the saturated regime; in the case of lower neutral density, the instability appears to originate from a diocotron-like perturbation while in the latter case short-wavelength oscillations form around the beam injection.

The square domain Penning discharge is analysed. In analogy with the plasma layer case, the limit of pure electron plasma is analysed. In this condition, the discharge reaches a quasi-steady state where a large electron blob is confined at the centre of the domain. At its centre, fast fluctuations of density can be observed, although without developing into any coherent structure. When n_n is increased, the central blob periodically destabilises outwards, originating a swirling vortex that rotates following the lateral walls. This behaviour is reflected in the current collected at the walls, which presents periodic bursts at 65 kHz; a further increase in the neutral density results in a larger frequency.

In analogy with the plasma layer, at $n_n \simeq 10^{20}$m^{-3} the discharge undergoes a mode transition and a constant long-wavelength $m = 1$ rotating structure is recovered. The $m = 1$ rotating spoke in Penning discharges is particularly difficult to obtain with fluid models, and to the authors' knowledge, this is the first occurrence in the literature. The single spoke, rotating at 83.9 kHz, presents some differences with respect to the PIC solutions in the literature. In particular, the spoke is always led by a recirculation region, more evident than in PIC simulations, and it is followed by the periodic detachment of blobs. Such differences may be due to the more diffusive nature of fluid algorithms, differences in the beam injection or to the selection of discharge parameters. Short-wavelength structures can be observed in the leading edge of the spoke. The time-averaged profiles of the discharge show that in the central part of the discharge, the modified Simon-Hoh instability criterion is met, although no origin mechanism is proposed.

Finally, although a continuous mode transition to the short-wavelength $m > 1$ mode could not be obtained, a slight variation of the square Penning configuration is presented. By assuming a current free injection with a Gaussian profile, the discharge recovers the short-wavelength $m > 1$ spiral structure, highlighting the capabilities of the presented fluid model to resolve relevant instabilities in $E \times B$ plasmas in a large variety of regimes.

Acknowledgments

This work has been supported by the R&D project HEEP (PID2022-140035OB-I00) funded by MCIN/AEI/10.13039/ 501100011033 and by "ERDF A way of making Europe". The authors would like to acknowledge Dr Gerjan Hagelaar for the guidance throughout the research exchange at Laplace laboratory, Toulouse, from which this work took inspiration, and Matteo Ripoli for the invaluable discussion on the onset of instabilities.

Appendices

5.A. 1D gas-vacuum expansion

This appendix presents an illustrative test case of the vacuum scheme, as explained in Section 5.2.3, and compares it to standard methods. Equation 5.16 reports the initial state of a 1D gas-vacuum expansion Riemann problem [123], for which an adiabatic index of $5/3$ is considered. The 2D code is here reduced to quasi-1D by imposing normalised periodic boundaries on the y direction.

$$[n, u_z, u_y, p] = \begin{cases} [1,0,0,2.5], & \text{if } z \leq 0.3, \\ [0,0,0,0], & \text{if } z > 0.3. \end{cases} \tag{5.16}$$

As stated before, if such problem is integrated assuming a low density to mimic the vacuum state, a strong shock appears at the front of the expansion, as it can be observed in Fig. 5.A.1(b) where the dashed line represents the solution obtained with a (relative) background density of 10^{-4}: at smaller background densities the magnitude of the shock increases, eventually contributing to the failure of the simulation. On the other hand, the vacuum scheme (solid line) smoothly transitions to the vacuum state. By comparing the two solutions, it seems that the vacuum scheme slightly overestimates the vacuum front velocity and thus the front position. Munz has already observed this defect in his sub-cell front-tracking algorithm, and it can be attributed to the difficulty in numerically evaluating the vanishing pressure and density (and their quotient), thus overestimating the sound velocity by taking the value on the interface immediately before the vacuum state. Nevertheless, for the applications presented here, the exact position of the vacuum front is not of great importance since the scheme is used to preserve positive energy and density in localised regions (usually close to the walls) in a regime far from free expansion.

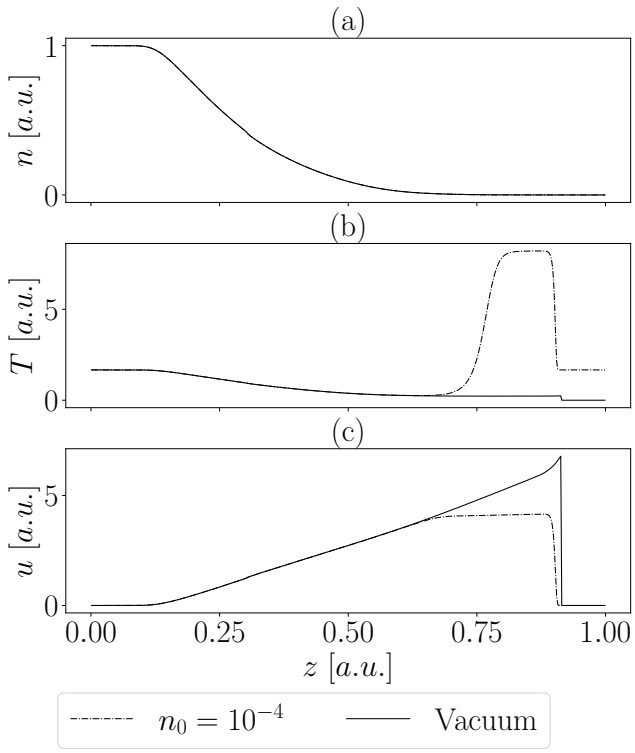

Figure 5.A.1: Numerical solution of the 1D free expansion problem. The plots represent density, temperature and velocity for the classic scheme with a low background density (dashed) and the vacuum algorithm (solid). The problem has been normalised to obtain classic units for fluid dynamic test cases.

CHAPTER 6

Towards Full-fluid Modelling of the Axial-azimuthal Hall Thruster Discharge

This chapter reproduces the contents presented by the author at the 39th International Electric Propulsion Conference in London, manuscript 341, 14-20 September 2025. The typography has been adapted to the style of this thesis.

Abstract

Theoretical studies and axial-azimuthal kinetic simulations have demonstrated the significant contribution of plasma instabilities to electron cross-field transport. However, the intrinsic complexity of the Hall thruster discharge and the kinetic nature of PIC simulations can make the interpretation of the results challenging. As a result, it remains unclear how to model the anomalous transport, leading to the absence of practical predictive models for the Hall effect discharge. Here, the problem is approached using a fluid formalism, which, albeit lacking kinetic effects, can provide insightful results by dealing with more tangible macroscopic quantities. A 3-fluid, 2D2V model of the axial-azimuthal Hall thruster discharge is presented. The discharge is self-consistently sustained without including any empirical anomalous transport in the model. The discharge appears rich in instabilities, exhibiting the onset of short and long-wavelength azimuthal oscillations, coupled with axial ionisation and ion transit time instabilities.

6.1. Introduction

Despite the increasing number of in-orbit Hall Effect Thrusters (HET), there is a well-known fundamental lack of understanding of the main processes regarding the anomalous electron transport. Today, it is widely accepted that the onset of plasma instabilities in the azimuthal direction is the primary contributor to cross-field transport. As a result, the community is devoted to the analysis of the instabilities developing in the plasma discharge of HETs and other $E \times B$ devices [3], [19]. The contribution of plasma instabilities to the anomalous transport has been theoretically analysed in the kinetic [142] and fluid formulations [34], [143], [144], and confirmed by particle in cell (PIC) [21]–[23], [145], [146], hybrid [147], [148] and non-linear fluid simulations [149]–[151]. The majority of full axial-azimuthal Hall thruster simulations (i.e. not considering reduced models) are performed using PIC models. These simulations have demonstrated the onset of a short-wavelength azimuthal instability, known as the electron cyclotron drift instability (ECDI), triggered by the large azimuthal drift of the electrons. The ECDI has been identified as a major contributor to the enhanced electron cross-field transport. Moreover, the simulations have revealed a complex picture of the discharge, with the coexistence and interaction of azimuthal and axial instabilities, such as the breathing mode (BM) and the ion transit time (ITT) instability. However, within the context of the complex HET discharge, the kinetic nature of PIC models and their ability to resolve a large number of physical effects can make the interpretation of the results challenging. For these reasons, it remains unclear how to properly model the anomalous transport, leading to the absence of practical predictive models for Hall effect thrusters. On the other hand, fluid models deal directly with more tangible macroscopic quantities at the cost of relying on stronger assumptions than PIC, such as a quasi-Maxwellian velocity distribution functions (VDFs), finite Larmor radius effects, and approximate closures of the set of equations. Nevertheless, fluid models are known to capture many types of instabilities [24], [25] and have demonstrated the capability to capture instability-induced cross-field transport [149], [150]. Cross-field transport has been observed using hybrid models (i.e. assuming PIC heavy species and fluid electrons) by Lam et al. [147] and Kawashima and Komurasaki [148]. However, the quasi-neutral drift-diffusion approximation of the electron fluid assumed by these models results in the lack of inertial and non-neutral effects, which can be important for the saturation of instabilities [151]. Finally, Lam et al. [152] and Sadouni [151] have approached the problem with full-fluid quasi-neutral models, although limited to very short simulation times and suffering from the same modelling limitations of the hybrid approach (due to quasi neutrality). Here, to the authors' knowledge, the first full-fluid 2D axial-azimuthal non-neutral simulation of the Hall thruster discharge accounting for electron inertia is presented, along with a preliminary analysis of the results.

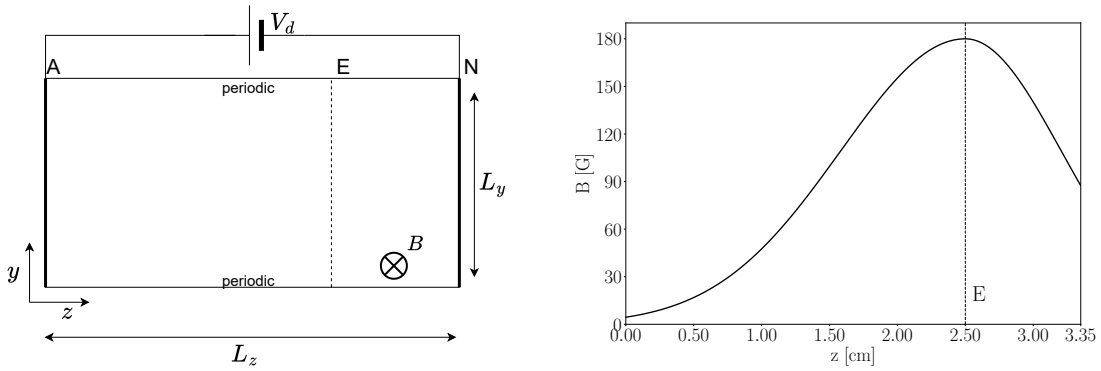

Figure 6.1: (Left) Computational domain of the $z-y$ plane of the Hall thruster. Points A,E,N represent the anode, channel exit and cathode plane, respectively. (Right) Magnetic field profile, the vertical dashed line represents the channel exit E.

6.2. Model equations and code description

A full-fluid 2D-2V Cartesian model is used to simulate the axial-azimuthal plane of the HET discharge. The model describes the time evolution of continuity, energy and momentum equations for the three fluid populations: electrons, ions and neutrals, denoted by the subscripts e,i,n, respectively. A sketch of the computational domain, which extends from the anode A to the planar cathode N, is reported in Fig. 6.1(left). Only the radial component (perpendicular to the computational domain) of the magnetic field $\boldsymbol{B}$ is considered. The axial profile of the magnetic field is shown in Fig. 6.1(right), and it is expressed as

$$\boldsymbol{B}(z) = \mathbf{1}_r\, B_m \exp\left[-(z-z_m)^2/\ell_m^2\right], \quad \ell_m = \begin{cases} \ell_{m1} & \text{if } z < z_m, \\ \ell_{m2} & \text{if } z \geq z_m, \end{cases} \tag{6.1}$$

where B_m is the maximum magnetic field, z_m its location and $\ell_{m1,2}$ the decay lengths.

The system of equations for the three species in conservation form is expressed as:

(Electrons)

$$\frac{\partial n_e}{\partial t} + \nabla\cdot(n_e\boldsymbol{u}_e) = S_p - S_w, \tag{6.2}$$

$$\frac{\partial n_e\boldsymbol{u}_e}{\partial t} + \nabla\cdot(n_e\boldsymbol{u}_e\boldsymbol{u}_e) = \frac{en_e}{m_e}(\nabla\phi - \boldsymbol{u}_e\times\boldsymbol{B}) - \frac{\nabla p_e}{m_e} - n_e\boldsymbol{u}_e\nu_e, \tag{6.3}$$

$$\frac{\partial \mathscr{E}_e}{\partial t} + \nabla\cdot[(\mathscr{E}_e + p_e)\boldsymbol{u}_e] = e\nabla\phi\cdot n_e\boldsymbol{u}_e - S_w\mathscr{E}_{ew} - S_p\mathscr{E}_{inel}, \tag{6.4}$$

(Ions)

$$\frac{\partial n_i}{\partial t} + \nabla\cdot(n_i\boldsymbol{u}_i) = S_p - S_w, \tag{6.5}$$

$$\frac{\partial n_i\boldsymbol{u}_i}{\partial t} + \nabla\cdot(n_i\boldsymbol{u}_i\boldsymbol{u}_i) = -\frac{\nabla p_i}{m_i} - \frac{en_i}{m_i}\nabla\phi - \boldsymbol{u}_iS_w + S_p\boldsymbol{u}_n, \tag{6.6}$$

$$\frac{\partial \mathscr{E}_i}{\partial t} + \nabla \cdot [(\mathscr{E}_i + p_i)\boldsymbol{u}_i] = -e\nabla\phi \cdot n_i \boldsymbol{u}_i - S_w \mathscr{E}_i + S_p \mathscr{E}_n, \tag{6.7}$$

(Neutrals)

$$\frac{\partial n_n}{\partial t} + \nabla \cdot (n_n \boldsymbol{u}_n) = -S_p + S_w, \tag{6.8}$$

$$\frac{\partial n_n \boldsymbol{u}_n}{\partial t} + \nabla \cdot (n_n \boldsymbol{u}_n \boldsymbol{u}_n) = -\frac{\nabla p_n}{m_n} - S_p \boldsymbol{u}_n, \tag{6.9}$$

$$\frac{\partial \mathscr{E}_n}{\partial t} + \nabla \cdot [(\mathscr{E}_n + p_n)\boldsymbol{u}_n] = -S_p \mathscr{E}_n, \tag{6.10}$$

(Electrostatic Potential)

$$\nabla^2 \phi = \frac{e}{\varepsilon}(n_e - n_i), \tag{6.11}$$

where $S_p = n_e n_n R_p(T_e)$ is the production rate due to ionisation and $S_w = n_e \nu_w(T_e)$ the lateral wall losses expressed analytically as a function of the local electron temperature [26]. For all the species, the total energy equation is used, the isotropic scalar pressure $p_j, j = e,i,n$ is considered, and the conductive heat flux is neglected $\boldsymbol{q}_j = 0, j = e,i,n$. In general, the heat flux is known to be important for electrons in the Hall thruster source and should be included. However, the classic Fourier-like closure employed in fluid models [30]

$$\boldsymbol{q}_e + \frac{\omega_{ce}}{\nu_e}(\boldsymbol{q}_e \times \boldsymbol{B}) = -\frac{5 e n_e T_e}{2 m_e \nu_e} \nabla T_e, \tag{6.12}$$

is obtained from the steady-state, stationary ($\boldsymbol{u}_e = 0$) approximation of the complete heat flux transport equation [74], which for the present model is not justified: large electron fluid velocities are found due to the self-consistent anode sheath and the $E \times B$ drift. As a result, inclusion of Eq. (6.12) in the present model is unstable unless an implicit treatment (in time) or a more suitable description of the heat flux (i.e the full transport equation) is used, hence the choice of considering $\boldsymbol{q}_e = 0$ until a more appropriate model can be derived.

The total electron collision frequency ν_e in the momentum equation is expressed as:

$$\nu_e = \nu_{en} + \nu_{ei} + \nu_{wm}, \tag{6.13}$$

thus accounting for electron-ion and electron-neutral collisions, as well as momentum loss due to wall interactions. In the electron energy equation, $\mathscr{E}_{ew}$ and $\mathscr{E}_{inel}$ represent the energy loss due to wall interaction and inelastic collisions, respectively. Ion recombination at the lateral walls has been included in the neutral continuity equation, although assuming perfect accommodation and cold walls (i.e. not contributing to neutral momentum and energy equations). A complete description of the collision frequency expression is reported in appendix 6.A.

In this work, no additional anomalous or turbulent collisionality is considered. As customary in axial-azimuthal HET simulations, artificially augmented vacuum permittivity $\varepsilon = f_d^2 \varepsilon_0$ with $f_d^2 = 64$ is used to ease the computational cost.

6.2.1. Boundary conditions

This section describes the boundary conditions imposed for the three species and the Poisson equation. Boundary conditions are applied at the point A (anode) and N(neutraliser).

Anode The anode is characterised by the presence of an electron-repelling (in normal conditions) sheath. The resolution of plasma sheaths in fluid models is known to be cumbersome due to the kinetic nature of the plasma-wall interaction [29], [90]. Among the various approaches, the so-called "kinetic" conditions of Sahu et al. [39] have been used due to their robustness. In such formulation, the drifted Maxwellian velocity distribution function is integrated to recover the mass, momentum and energy fluxes:

$$\Gamma_{1\alpha} = -n_\alpha \frac{\bar{c}_\alpha}{4}\left[\exp(-\tilde{u}_{z\alpha}^2) + \sqrt{\pi}\tilde{u}_{z\alpha}\left(\operatorname{erf}\tilde{u}_{z\alpha} - 1\right)\right], \tag{6.14}$$

$$\Gamma_{2\alpha} = -\frac{n_\alpha T_\alpha}{m_\alpha}\left[\frac{\tilde{u}_{z\alpha}}{\sqrt{\pi}}\exp(-\tilde{u}_{z\alpha}^2) + \left(\frac{1}{2} + \tilde{u}_{z\alpha}^2\right)\left(\operatorname{erf}\tilde{u}_{z\alpha} - 1\right)\right], \tag{6.15}$$

$$\Gamma_{3\alpha} = u_{y\alpha}\Gamma_{1\alpha}, \tag{6.16}$$

$$\Gamma_{4\alpha} = -n_\alpha \frac{\bar{c}_\alpha}{4} T_\alpha\left[\left(\tilde{u}_{z\alpha}^2 + \tilde{u}_{y\alpha}^2 + 2\right)\exp(-\tilde{u}_{z\alpha}^2) + \left(\tilde{u}_{z\alpha}^2 + \tilde{u}_{y\alpha}^2 + \frac{5}{2}\right)\sqrt{\pi}\tilde{u}_{z\alpha}\left(\operatorname{erf}\tilde{u}_{z\alpha} - 1\right)\right], \tag{6.17}$$

where $u_{z\alpha}, u_{y\alpha}$ are the axial and azimuthal velocities at the wall, $\tilde{u}_{z\alpha} = u_{z\alpha}(2T_\alpha/m_\alpha)^{-0.5}$ is the normalised velocity (the same holds for $\tilde{u}_{y\alpha}$), and $\bar{c}_\alpha = (8T_\alpha/\pi m_\alpha)^{0.5}$ the thermal speed. The fluxes are computed for both charged species $\alpha = i, e$. At each iteration of the algorithm, the boundary fluxes are imposed directly in the finite volume scheme.

The boundary condition for the neutral fluid assumes supersonic injection, allowing for the imposition of the mass flow rate, injection velocity and energy, taking into account full ion recombination at the anode.

For the Poisson equation, a Dirichlet condition $\phi_A = 0$ is imposed at the anode cell interface.

Cathode At the cathode, ions and neutrals are supersonic, so that no external boundary condition is imposed, and the numerical values are extrapolated from the domain.

The electron population cathode boundary condition is notoriously the most complicated to impose, even for PIC codes [23], [146]. Here, the main difficulty lies in the fact that the cathode boundary is close to the channel exit and in a region where the flow is not fully developed but rather rich in instabilities. Moreover, the small mass of electrons makes them very responsive to the Lorentz force, which in a "turbulent" region ends up dominating the dynamics of electrons, complicating the imposition of boundary conditions according to the hyperbolic (without external forces) Euler-like equations. In the assumption of a planar cathode, the boundary for electrons is a subsonic inlet, thus allowing to impose 3 conditions, where a flux $\Gamma_{eN} = (\Gamma_{iA} - \Gamma_{eA}) - \Gamma_{iN}$ corresponding to

the difference between the discharge and ion beam current, should be injected. However, such a boundary condition results in unstable behaviour, which inevitably leads to the failure of the simulation. Instead, the imposed condition approximates a quasi-neutral cathode, often employed in PIC simulations, where the following values are imposed in the ghost-cells at N:

$$\begin{bmatrix} n_e \\ nu_{ze} \\ nu_{ye} \\ \mathscr{E}_e \end{bmatrix}_N^{ghost} = \begin{bmatrix} n_i \\ 0 \\ 0 \\ \mathscr{E}_c \end{bmatrix}, \tag{6.18}$$

where $\mathscr{E}_c = \frac{3}{2} n_e^{ghost} T_c$ is the assumed electron energy at the cathode. Even though this boundary condition is ill-posed (it over-constraints the system by not respecting the characteristics of the hyperbolic problem and imposes $u_{ze} = 0$), it results in a numerically stable simulation. In the rest of this work, this boundary condition is used, fully acknowledging the inconsistency it might generate. The development of a more suited boundary condition will be addressed in future works.

As for the anode, a Dirichlet condition $\phi_N = -300V$ is imposed at the cathode interface for the electric potential.

6.2.2. 2D FVM code

The system of hyperbolic equations is solved using a 2D Cartesian Finite Volume Method (FVM). The spatial discretisation is performed with a 2nd order MUSCL scheme with minmod slope limiter using primitive variable reconstruction. The numerical flux is computed with the HLLC approximate Riemann solver [83] for the charged species, and with the Rusanov solver for the neutral fluid. The electron and ion systems are treated separately but coupled through the Poisson equation. To satisfy the stability criterion of the Euler-Poisson system [89], [90], the equations cannot be trivially advanced in time explicitly, as the system is unconditionally unstable. To overcome this issue, a fractional step method is used to advance separately the homogeneous and the source part of the balance laws. In particular, the second-order accurate Simpler [92] splitting scheme is used, computing the new potential between the convective and source term steps. The temporal integration is performed with the 3rd order Strong-Stability-Preserving Runge-Kutta (SPP-RK3) [93] and the Poisson equation is solved using a 5-point finite-difference stencil with the direct solver MUMPS [95]. The algorithm uses an adaptive time-step, meaning that in every iteration, the time-step is computed to satisfy the convective CFL constraint dictated by the largest eigenvalue of the electron system

$$\Delta t_c = \mathrm{CFL} \times \min\left(\frac{\Delta z}{\max_\Omega(\rho_z)}, \frac{\Delta y}{\max_\Omega(\rho_y)} \right), \tag{6.19}$$

with Ω the computational domain, $\Delta z, \Delta y$ the mesh size and $\rho_{z,y} = \max\{|\lambda_1|, ..., |\lambda_n|\}$ the spectral radius of the flux Jacobian of the electron system in the two directions. Moreover,

Table 6.1: Main operating (top) and numerical parameters (bottom) used in the simulation.

Parameter	Value	Parameter	Value
$\dot{m}$	$4.75\,\mathrm{mg\,s^{-1}}$	V_d	300 V
T_n	0.06 eV	u_{zn}	$300\,\mathrm{m\,s^{-1}}$
$\tilde{\nu}_w$	0.17	T_c	5 eV
B_m	180 G	z_m	2.5 cm
ℓ_{m1}	1.30 cm	ℓ_{m2}	1 cm
z_E	2.5 cm	A_c	$40\,\mathrm{cm^2}$
Cell z	1107	Cell y	300
L_z	3.35 cm	L_y	1 cm
ε_r	64	CFL	0.7

to ensure plasma stability, the time-step must resolve the upper-hybrid frequency $\omega_{uh} = \sqrt{\omega_{pe}^2 + \omega_{ce}^2}$, with ω_{pe} and ω_{ce} the plasma and electron cyclotron frequency, respectively. The time-step is thus computed according to:

$$\Delta t \leq \min\left(\Delta t_c, 0.2\frac{2\pi}{\omega_{uh}}\right), \tag{6.20}$$

where the factor 0.2 has been introduced to ensure numerical stability; a value of CFL=0.7 is typically used. To further reduce the computational time, the code is parallelised using domain decomposition with the MPI standard.

6.2.3. Simulation initialisation

Due to the discharge setup (i.e. the planar cathode) and the nature of the model, initialising the simulation with uniform densities, as is usually done in PIC simulations, may result in difficult transients that cause the model to fail. For this reason, 1D solutions obtained by the model of Poli et al. [26] are used as an approximate initial guess. The 1D profiles are used in the 2D simulation, considering an azimuthally uniform distribution. Nevertheless, it is important to note that the 1D first guess is found to be quite far from the axial-azimuthal solution with self-consistent cross-field transport, so strong oscillations or deviations from such profiles are expected in the transient.

6.3. Simulation results

In this section, the results obtained by the simulation of the $z-y$ plane of the HET discharge are presented. The operating and the numerical parameters of the simulation are reported in Tab. 6.1. In the following subsections, various aspects of the discharge are analysed. The simulation has been run with 45 CPUs in a single node for a total computational time of 38 days (41k CPU hours) and $\sim$ 62 million timesteps.

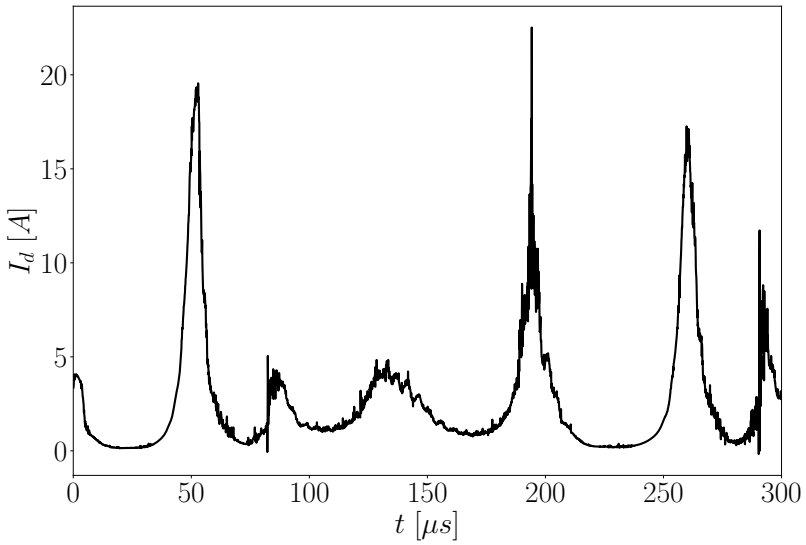

Figure 6.2: Time evolution of the discharge current I_d.

6.3.1. Discharge overview

Here, a global overview of the discharge is presented. As stated before, the simulation is initialised using steady-state 1D profiles, which include empirical anomalous transport and can be far from the actual 2D solution. This discrepancy is reflected in the time evolution of the discharge current, reported in Fig. 6.2, characterised by a strong initial transient where the discharge is almost extinguished. Large oscillations of the discharge current are observed throughout the whole simulation, and can be identified with the onset of the ionisation instability (i.e. breathing mode) at 20 kHz. As expected, the low-frequency oscillations are accompanied by strong fluctuations of plasma density, although never violating the resolution of the Debye length. A high-frequency fluctuation ($f \approx 200$ kHz) can be observed superimposed on the breathing mode, most noticeably on the decay phase of the current fluctuation, commonly associated with the ion transit time instability. A more detailed description of the longitudinal instabilities is provided in Section 6.3.5. Overall, the discharge current profile shows an irregular time evolution of the plasma discharge, suggesting that the simulated 300 µs might not be sufficient to reach the saturated regime of the slow neutral dynamics.

6.3.2. Azimuthal instabilities

Figure 6.3 shows instantaneous snapshots of the electron density n_e, electron temperature T_e and azimuthal electric field E_y at $t = 133$ µs. Although the plots represent the instantaneous profiles of a highly dynamic process, several interesting observations can be made. For instance, the electron density appears to be concentrated in a blob, as opposed to the rather azimuthally uniform (except for the short-wavelength instabilities) distribution of similar PIC simulations. This is a direct consequence of modelling the neutral fluid in the $z-y$ plane, instead of assuming a one-dimensional flow, allowing

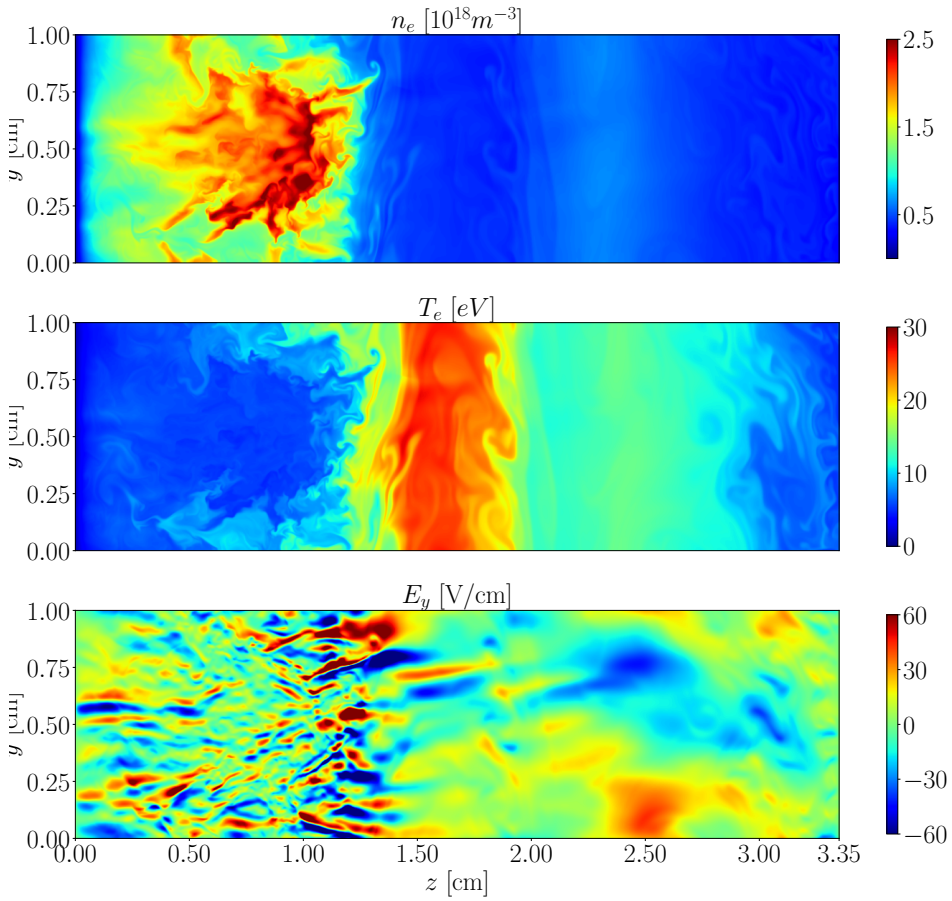

Figure 6.3: Instantaneous distribution of n_e, T_e and E_y at $t = 133\,\mu s$.

for the formation of long-wavelength azimuthal instability (i.e. rotating spokes). Figure 6.4(top) shows the time evolution of the azimuthal fluctuations of neutral density $n_n - \langle n_n \rangle_y$ at $z = 1$ cm, whereas the time evolution of the azimuthal average $\langle n_n \rangle_y$ is shown below. The fluctuations clearly show the onset of a long-wavelength azimuthal instability, identified by coherent diagonal streaks, between $t = 130\,\mu s$ and $t = 175\,\mu s$. The corresponding dip in the average density $\langle n_n \rangle_y$ [Fig. 6.4(bottom)] indicates that the instability develops in correspondence with an axial breathing-mode peak, as it can be observed in the discharge current plot for the same time window. The azimuthal velocity of the rotating structure can be obtained from the slope of the diagonal streaks, and it is found to be $v_y = \Delta y/\Delta t \approx 200\,m\,s^{-1}$ in the $+E \times B$ direction, corresponding to a frequency $f \approx 20\,kHz$. Although similar spoke velocities have been observed experimentally [153], [154], the simulation azimuthal length is too short (compared to the spoke wavelength and the real thruster circumference) to draw any reliable conclusion. Nevertheless, the presence of the rotating spoke visibly affects the 2D distribution of all other discharge properties, as can be observed in the electron temperature and azimuthal electric field maps in Fig. 6.3 (middle and bottom, respectively). This can partially explain the less coherent structures of the azimuthal electric field when compared to PIC simulations. Moreover, it is impor-

tant to keep in mind that the comb-like structure of E_y observed in kinetic simulations is produced by the onset of the electron cyclotron drift instability. The 5-moment fluid model can only capture the first electron resonance, as opposed to the kinetic description, and only the fastest growing mode can be adequately described for sufficiently low T_e, as shown by Wang et al. [150]. For this reason, differences with respect to PIC simulations are expected, especially in regions of high electron temperature. The loss of the short-wavelength structures in the high temperature region is directly reflected in the distribution of the anomalous force, as shown in Section 6.3.4. Finally, a preliminary frequency analysis, limited by the coarse time resolution (data is saved every 0.1 µs), has shown that the short wavelength structures saturate at the ion acoustic wave, with ω_{pi} =2.9 MHz, in agreement with the results in the literature.

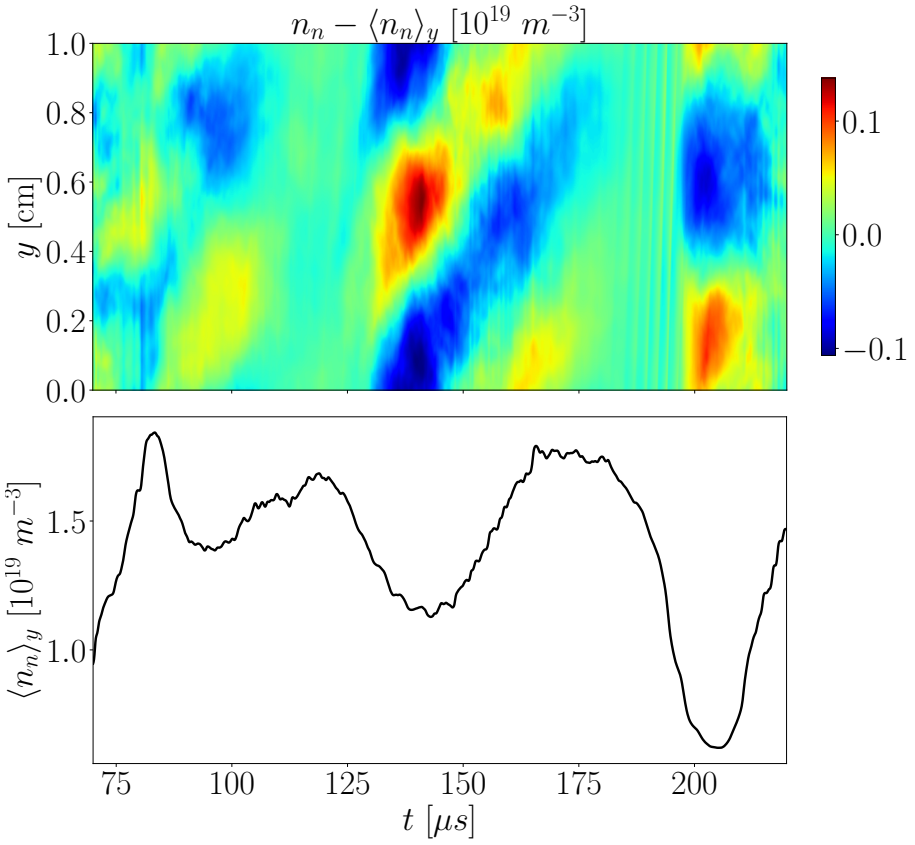

Figure 6.4: (Top) Azimuthal fluctuations of the neutral density in time, sampled at z =1 cm. (Bottom) Azimuthally averaged neutral density at the same axial coordinate.

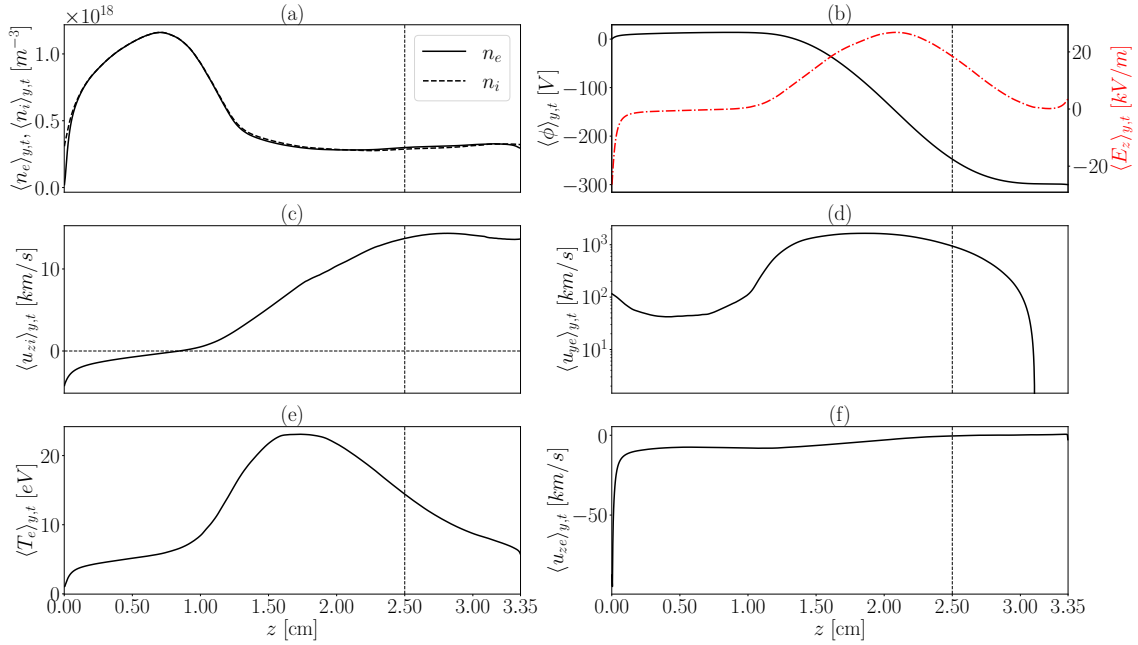

Figure 6.5: Azimuthally and time-averaged profiles of some relevant variables of the discharge. Time averaging is performed over 150 µs (70 to 220 µs), capturing several breathing mode cycles.

6.3.3. Axial structure of the discharge

The azimuthally and time-averaged profiles of some relevant discharge variables are reported in Fig. 6.5. Overall, the 1D structure of the discharge behaves as expected for a conventional Hall thruster, correctly capturing the main features. The plasma is mainly quasi-neutral, as shown in plot (a), where the largest charge separation remains confined in the normal sheath at the anode. As expected, the axial electron velocity [plot (f)] remains negative in the whole domain, with a sharp increase (in magnitude) in the anode sheath, whereas u_{zi} [plot (c)] shows the characteristic ion back-flow region near the anode and the supersonic acceleration towards the channel exit. The onset of the ion transit time instability results in large fluctuations of the ion velocity at the cathode, hence the relatively low average value. The azimuthal electron velocity u_{ye}, shown in plot (d), on average remains quite low in the first part of the channel, followed by a sudden increase to $O(10^6 \mathrm{m\,s^{-1}})$. An excessive electron mobility in the near-anode region can explain this behaviour, as it will be shown later with the momentum balances. As in the case of u_{zi}, the electron temperature [plot (e)] presents strong fluctuations with the axial instabilities, with the maximum oscillating from 15 to 35 eV and displacing axially, hence the rather low average maximum value and broad profile. Finally, the electric potential profile [plot (b)] shows how, on average, the acceleration region is quite broad and slightly upstream of the maximum magnetic field located at $z = 2.5$ cm, as confirmed by the axial electric field [dashed red line]. Once again, the ion transit time instability alters significantly the electric field distribution, both in magnitude and shape, as it can be observed in Fig. 6.9.

6.3.4. Electron Momentum Balances

Here, the electron momentum balance equation is analysed. After re-writing Eq. (6.3) along the two components z and y, and taking the azimuthal and time averages, we have

$$0 = \underbrace{-\langle\frac{\partial}{\partial z}\left(n_e u_{ze}^2 m_e\right)\rangle_{y,t}}_{\bar{F}_{in,z}} \underbrace{-\langle\frac{\partial p_e}{\partial z}\rangle_{y,t}}_{\bar{F}_{pr,z}} + \underbrace{\langle en_e\frac{\partial \phi}{\partial z}\rangle_{y,t}}_{\bar{F}_{el,z}} + \underbrace{\langle n_e u_{ye} eB\rangle_{y,t}}_{\bar{F}_{mg,z}} \underbrace{-\langle n_e u_{ze}\nu_e m_e\rangle_{y,t}}_{\bar{F}_{co,z}}, \quad (6.21)$$

$$0 = \underbrace{-\langle\frac{\partial}{\partial z}\left(n_e u_{ye} u_{ze} m_e\right)\rangle_{y,t}}_{\bar{F}_{in,y}} + \underbrace{\langle en_e\frac{\partial \phi}{\partial y}\rangle_{y,t}}_{\bar{F}_{el,y}} \underbrace{-\langle n_e u_{ze} eB\rangle_{y,t}}_{\bar{F}_{mg,y}} \underbrace{-\langle n_e u_{ye}\nu_e m_e\rangle_{y,t}}_{\bar{F}_{co,y}}. \quad (6.22)$$

These equations represent the axial balance of the forces in the z and y directions, respectively, in the slow dynamics of the electron fluid. In particular, the term $\langle en_e\frac{\partial\phi}{\partial y}\rangle_{y,t}$ is the electrostatic force in the azimuthal direction, and it is commonly identified as the main contributor to the anomalous transport. When the high-frequency oscillations of the density and of the azimuthal electric field are correlated, the anomalous force is non-zero and enhances the electron transport [155]. Figure 6.6 shows the axial distribution of all the terms of equations (6.21) and (6.22), and their sum (black dashed line) averaged over 150 µs. It must be noted that the convection part of the inertia in equations (6.21) and (6.22) is computed a posteriori using the cell-centred variables saved by the code, and it inevitably differs from the HLLC numerical flux employed by the code at the cell interface. Hence, some discrepancies are expected in the balance computation. As expected for normal HET operation, the axial momentum balance is dominated by the magnetic, electrostatic and pressure forces, whereas the inertial and collisional terms appear negligible. As commented in section 6.3.1, the relatively low average azimuthal electron drift and the low magnetic field at the anode result in a negligible magnetic force for $z < 1.5$ cm. Looking at the azimuthal momentum balance, the same region is characterised by a strong correlation of n_e and $\frac{\partial\phi}{\partial y}$ balancing the magnetic force, indicating a strong contribution to the cross mobility of electrons (the collisional term in this region is indeed negligible). On the other hand, the anomalous electric force seems to vanish for $z > 1.5$ cm, corresponding to the sharp increase in the electron temperature. As a result, no anomalous force is found in regions of higher magnetic field. This result appears in contradiction with PIC simulations [22], where the maximum anomalous force is located close to the channel exit, and thus in the region of maximum magnetic field. PIC simulations [23] have shown how the anomalous force is strongly influenced by the azimuthal dimension and the scaling parameter of the vacuum permittivity f_d^2. In particular, a much smaller force is observed for small computational domains (along y) and large scaling parameters, consistent with a reduction of the ECDI growth rate [22]. Here, a small domain ($L_y = 1$ cm) and a scaling parameter $\varepsilon_r = 64$ are coupled with a crude approximation of the electron-neutral collision frequency $\nu_{en} \propto \sqrt{T_e}$, resulting in the over-estimation of the collisional term which balances the relatively low magnetic force. Moreover, as previously commented, the 5-moment fluid model's capability to capture the fastest-growing mode of

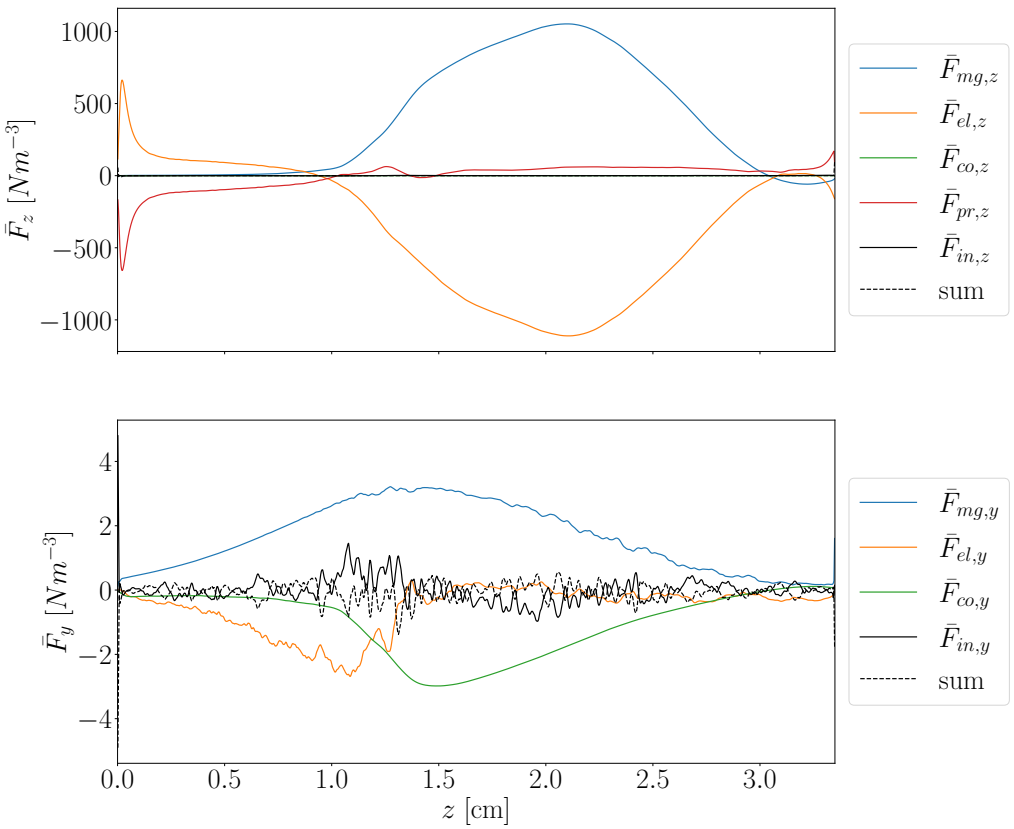

Figure 6.6: Axial and azimuthal electron momentum balance. The forces are azimuthally and time averaged over 150 µs (70 to 220 µs), capturing several breathing mode cycles.

the ECDI deteriorates at large electron temperatures [150], as found in this region of the domain. Nevertheless, even though this could cause a reduction of the anomalous force for $z > 1.5$ cm, it does not explain the large contribution close to the anode. To address these questions, a more detailed analysis is needed and will be performed in future works.

The anomalous force is strongly modulated by the axial ionisation instability, as shown in Fig. 6.7(left), where the anomalous and collisional forces, represented by solid and dashed lines, respectively, are shown at different moments of the breathing mode oscillation. Each one of the coloured lines corresponds to an averaging window of 5 µs, as shown by the respective vertical bands overlayed on the discharge current (right). However, the force per particle (middle), obtained by normalising by the averaged density to remove the fluctuation associated with the oscillations of the density in the breathing mode period, appears fairly constant throughout the cycle. This suggests that the fluctuations of the anomalous force are mainly due to the increase in plasma density and not a substantial change in the origin of the force. It is worth noting that both the anomalous and collisional forces are much higher with respect to Fig. 6.6, where the large time-averaging window includes periods of very low density. Finally, it can be observed how the anomalous force always dominates in the near-anode region, whereas the sharp decrease observed in Fig. 6.6 persists in the high temperature region.

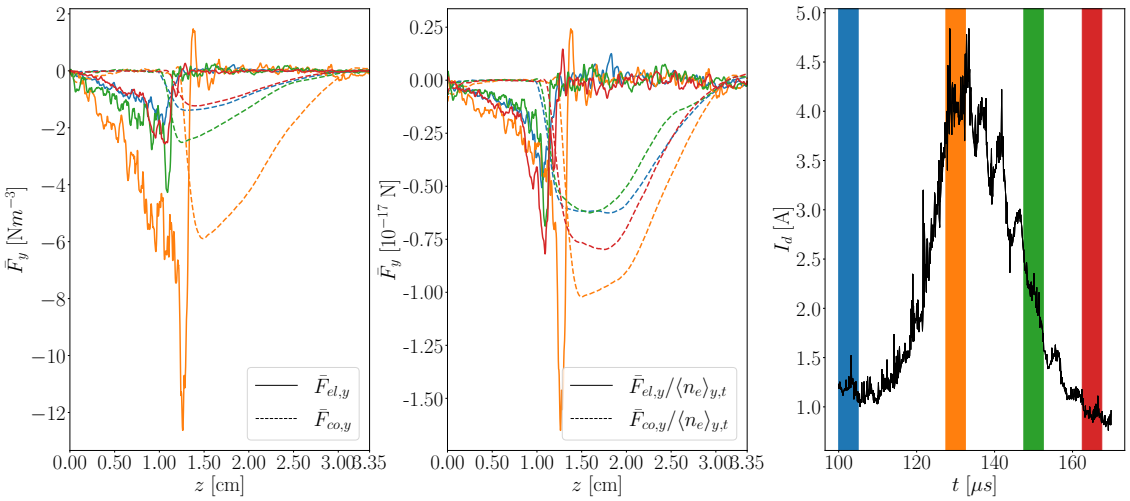

Figure 6.7: (Left) Time variation of the anomalous (solid) and collisional (dashed) forces in different moments of the breathing mode cycle. (Middle) Time variation of the forces per particle. (Right) Discharge current and corresponding 5 µs averaging time windows for computing those forces.

6.3.5. Axial instabilities

In agreement with experimental evidence and axial-azimuthal PIC simulations in the literature, the discharge is characterised by the onset of axial instabilities, as it can be observed in the time evolution of the discharge current [Fig. 6.2]. The most prominent features in the time evolution of I_d can be associated with a strong ionisation instability, or breathing-mode, which results in large fluctuations of neutral and plasma density. Figure 6.8 reports the time evolution of the azimuthally averaged neutral density (top) and electron density (bottom), where the characteristic breathing mode pattern can be observed. The irregularity of the instability in both the discharge current and density evolution suggests that the slow neutral dynamics has not reached the final (or saturated) regime in the simulated time. High-frequency fluctuations at 200 kHz can be observed superimposed on the ionisation instability. This fast axial perturbation has been observed in several PIC and fluid simulations, and it is associated with the ITTI. The most prominent feature of the ITTI consists in the production of a population of slow ions, leading to a double-peaked velocity distribution function and a consequent increase in the ion temperature and ion density [22], [23], [146]. The present 5-moment fluid model does not capture a non-Maxwellian VDF, and the ITTI manifests itself as a shock-like structure in the ion flow, decreasing u_{zi} and increasing T_i and n_i. Figure 6.9 shows the time evolution of $\langle u_{zi}\rangle_y, \langle n_i\rangle_y$ and $\langle E_z\rangle_y$ over a period of the ion transit time instability in the decreasing part of the breathing mode peak at $t = 140$ µs. Each of the variables is normalised with its maximum value in space and time across the snapshots. The perturbation develops in the acceleration region, resulting in the formation of a wave which undergoes wave-steepening until a sharp discontinuity is observed at $t = 144$ µs in all the variables. The shock-like structure is then convected out of the domain in the following microseconds,

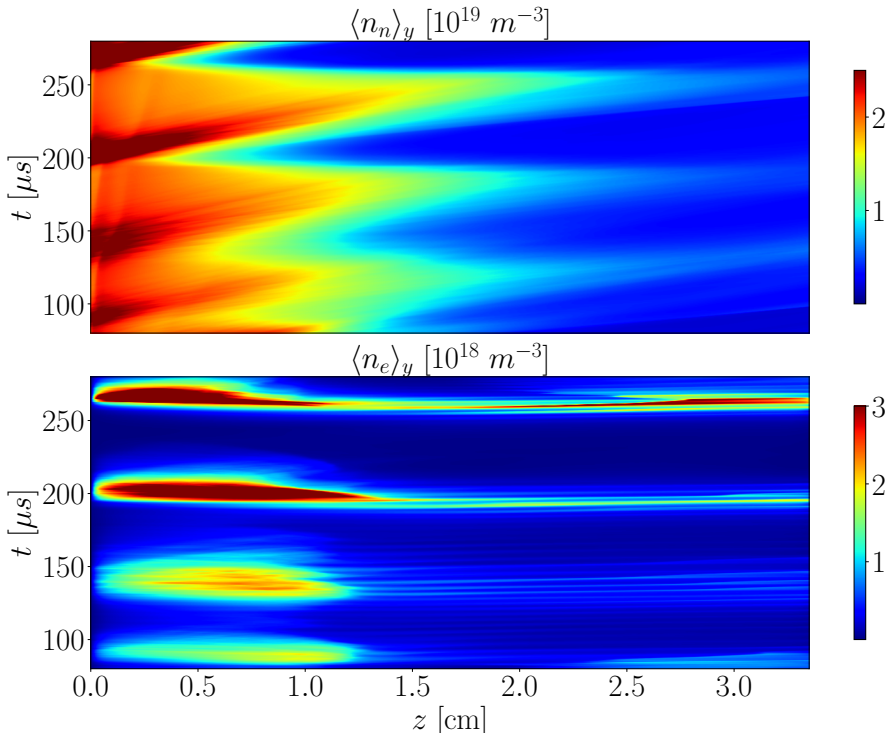

Figure 6.8: Time evolution of the azimuthally averaged neutral density (top) and electron density (bottom).

until the process starts again. The same qualitative behaviour has been observed in axial-azimuthal PIC [22], [23], [146] and axial-radial hybrid [156] simulations, although the perturbation does not appear as a shock-like structure, but rather as a softer decrease of u_{zi}. Analogous shock-like structures have been observed in 1D fluid models [157], and numerical experiments with the model of Poli et al. [26], [29] (both quasi-neutral and non-neutral) have recovered the same behaviour when the anomalous transport coefficient is reduced (consistently with Fife [156], who observed the disappearance of ITTI for large anomalous transport coefficients in axial-radial hybrid simulations). The last observation seems to be in line with the findings of Charoy et al. [23], for which a stronger ITTI is associated with a lower anomalous force. Currently, the reason behind the formation of the shock-like structure in fluid models compared to the smoother PIC solution remains unclear. However, it is worth mentioning that the methods and approximations used to solve the fluid formalism rely on the solution of hyperbolic Euler-like equations, which admit shocks by neglecting viscosity and heat conduction, the latter of which is intrinsically resolved by the PIC formulation.

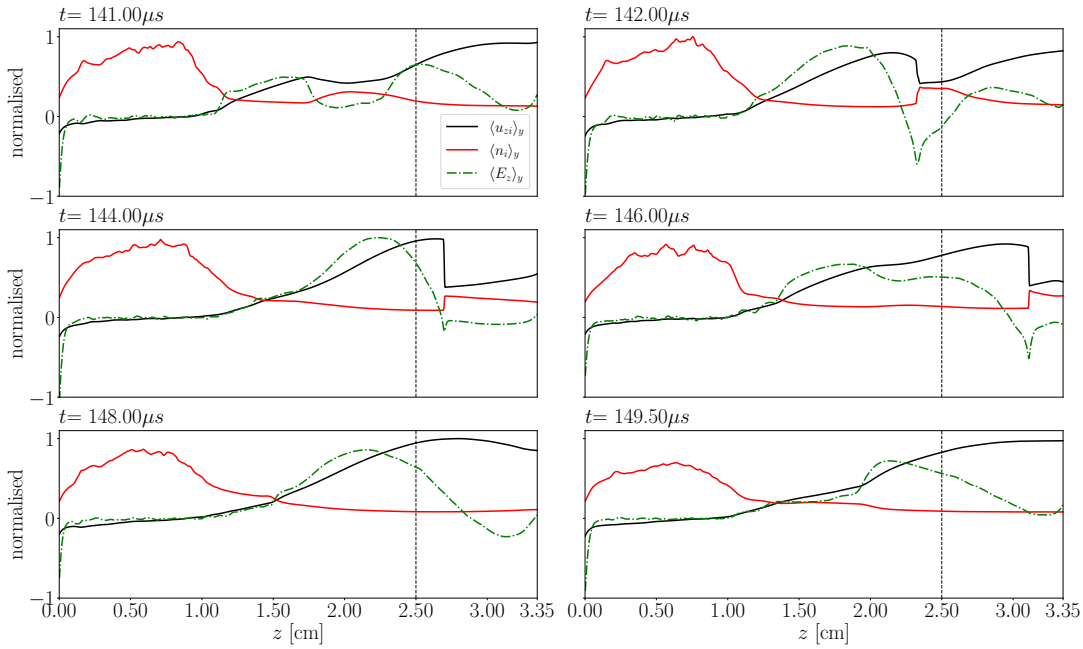

Figure 6.9: Time evolution of the instantaneous normalised profiles of $\langle u_{zi}\rangle_y, \langle n_i\rangle_y$ and $\langle E_z\rangle_y$ during a period of ion transit time instability. The vertical dashed line represents the channel exit (and the maximum of the magnetic field).

6.4. Conclusion

A 2D2V fluid axial-azimuthal simulation of the Hall effect discharge has been presented. The standard 5-moment fluid formulation has been applied to the electron, ion and neutral populations to obtain a self-consistent description of the plasma discharge, without the use of additional anomalous cross-field electron transport. The system of equations is integrated with a MUSCL-based finite volume approach, using the HLLC flux for the charged populations and the Rusanov flux for the neutrals; time integration is performed with a third-order Runge-Kutta scheme and the Simpler splitting method. The equations are solved in a Cartesian domain which extends from the anode to the cathode, representing a section of the circumference of a Hall thruster. Periodic boundary conditions are imposed in the azimuthal directions, whereas a sheath condition is considered at the anode for the charge species; the gas propellant is injected supersonically. A quasi-neutral cathode boundary condition is assumed for the electrons, which, albeit overconstraining the electron fluid, is in line with PIC simulations. Further analysis on the effects of such boundary condition on the dynamics of the discharge is reserved for future work.

A total time of 300 µs has been simulated, depicting a complex picture of the discharge. In the azimuthal direction, the onset of both short and long-wavelength instabilities is observed. In particular, the first ones are responsible for the generation of an anomalous azimuthal force, contributing to the (axial) cross-field transport of electrons. The coupling with the low-frequency mode, which appears to be related to the 2D modelling of the Xenon gas (i.e. rotating spokes), and the limitation of fluid models

in predicting the electron cyclotron drift instability, result in non-negligible differences with respect to PIC simulations. For instance, the highly coherent comb-shaped structure of the ECDI is not found, and the anomalous force is localised in the first 1.5 cm of the channel. This is in contrast with PIC results in the literature, for which the maximum anomalous force is located at the maximum of the radial magnetic field. A possible explanation for this discrepancy can be found in the degraded capability of fluid models to predict the fastest growing mode of ECDI at larger electron temperature, localised in this area of the discharge. Other factors, such as the large scaling factor of ε_0, coupled with a short azimuthal domain and an excessive electron-neutral collision frequency, can inhibit the formation of instabilities. The origin of these differences will be the focus of future works.

Nevertheless, the discharge is capable of sustaining self-consistently, correctly capturing the axial structure of the discharge, albeit with anomalously low prediction of the average azimuthal velocity close to the anode. This effect can be related to the excessive transport observed in this region, where the electrostatic force in the azimuthal momentum balance is maximum.

The discharge is subject to strong axial instabilities, identified as the low-frequency ionisation instability and the high-frequency ion transit time instability. The ionisation instability appears as the dominant axial mode in the discharge, persisting throughout the whole simulation. The fluctuations of the discharge current associated with the instability appear very irregular, suggesting that the saturated regime of the neutral fluid has not been reached in the simulated time. The onset of the ion transit time instability is observed superimposed on the low-frequency oscillations, manifesting itself as a periodic shock-like structure in the ion dynamics and affecting all the main variables of the discharge (e.g. electric field, electron temperature, etc.). The appearance of the ITTI is consistent with PIC simulations, where it generates a population of slow ions in the velocity distribution function. At the present moment, it is not clear why, in fluid models (both 1D and 2D), the formation of a shock-like structure is observed, and a deeper analysis will be carried out in the future.

This preliminary work highlights the capabilities and limitations of axial-azimuthal fluid models in reproducing a self-consistent simulation of the Hall effect thruster discharge. This paves the way for deeper analysis and comparison with kinetic results to better understand the nature of cross-field transport.

Acknowledgments

This work has been supported by the R&D project HEEP (PID2022-140035OB-I00) funded by MCIN/AEI/ 10.13039/501100011033 and by “ERDF A way of making Europe”.

Appendices

6.A. Collision Frequencies

This appendix briefly summarises the analytical formulation of the collisional processes and wall interaction used in the model. The expressions are consistent with the ones reported in Poli et al. [26] for the 1D model of the HET discharge. Some of the constants hereby reported are specific to Xenon.

Plasma production is given by $S_p = n_e \nu_p$, with the ionisation (or production) frequency expressed as

$$\nu_p = n_n \bar{c}_e \sigma_{ion0} \left[1 + \frac{T_e E_{ion}}{(T_e + E_{ion})^2}\right] \exp\left(-\frac{E_{ion}}{T_e}\right), \tag{6.23}$$

with $E_{ion} = 12.1\text{eV}$ the first ionization energy and σ_{ion0} =$5 \times 10^{20}\,\text{m}^{-2}$. The effective inelastic energy loss $\mathscr{E}_{inel}$ accounts for both ionisation and excitation and is expressed as a fit to the expression derived by Dugan et al. [122] proposed by Fife [58]:

$$\mathscr{E}_{inel} = \left(2 + 0.25\exp\left(0.667\frac{E_{ion}}{T_e}\right)\right) E_{ion}. \tag{6.24}$$

The elastic electron-neutral collision frequency is modelled as $\nu_{en} = n_n \bar{c}_e \sigma_{en}$ with σ_{en} =$27 \times 10^{-20}\,\text{m}^{-2}$, whereas the elastic electron-ion collision frequency is given by

$$\nu_{ei} = n_i R_{ei}, \quad \frac{R_{ei}}{10^{-12} m^3/s} = 2.9 \cdot \left(\frac{1eV}{T_e}\right)^{3/2} \ln\Lambda,$$
$$\ln\Lambda \approx 9 + \frac{1}{2}\ln\left[\left(\frac{10^{18} m^{-3}}{n_e}\right)\left(\frac{T_e}{1eV}\right)^3\right]. \tag{6.25}$$

Finally, the lateral wall interaction is modelled as Ahedo et al.[32]. The sheath potential falls in a dielectric wall satisfies

$$\Delta\phi_w = \frac{T_e}{e}\ln\left(\sqrt{\frac{m_i}{2\pi m_e}}(1 - \delta_s)\right). \tag{6.26}$$

Here, δ_s is the effective SEE yield, modelled as

$$\delta_s = \begin{cases} \sqrt{T_e/T_1}, & \text{if } T_e < T_1 \delta_s^{\star 2}, \\ \delta_s^{\star}, & \text{if } T_e \geq T_1 \delta_s^{\star 2}, \end{cases} \tag{6.27}$$

with T_1 material-dependent and $\delta_s^{\star}$ the emission yield corresponding to the space-charge saturation limit:

$$\delta_s^{\star} = 1 - 3.32 \sqrt{2\pi m_e/m_i}, \tag{6.28}$$

representing the classical Hobbs-Wesson result[52]. In this work T_1 =36.77 eV. The wall-loss term in the continuity equations is expressed as $S_w = n_e \nu_w$, with

$$\nu_w = \tilde{\nu}_w \sqrt{T_e/m_i}, \tag{6.29}$$

and $\tilde{\nu}_w$ a fitting parameter, constant inside the source and decreasing to zero downstream the cathode. The wall-collisionality for electron momentum follows

$$\nu_{wm} = \nu_w \delta_s/(1-\delta_s), \tag{6.30}$$

and the effective energy loss per electron is

$$\mathscr{E}_{ew} = \left(5.62 + \frac{1.65}{1-\delta_s}\right) T_e, \tag{6.31}$$

for xenon.

CHAPTER 7

Conclusions and future works

In this Chapter, the main results of the Thesis are summarised, and possible future works are proposed.

7.1. Summary and main results

The Thesis provides a comprehensive application of fluid models to $E \times B$ discharges, with particular focus on Hall Effect thrusters. This has been made possible by the development of two main tools, namely the 1D and 2D codes, and their application to specific problems.

1D Modelling of Hall Effect Thruster discharges A 1D time-dependent quasi-neutral drift-diffusion model of the HET discharge has been developed, extending the capabilities of the previously developed stationary models in the group [28] by allowing for the resolution of the discharge dynamics. The model differs from other time-dependent models available in the literature for the inclusion of the far-plume region, complete characterisation of heavy species dynamics and azimuthal electron inertia.

These additions have non-negligible effects on the stationary and dynamical behaviour of the discharge, further confirming the importance of the correct resolution of neutral dynamics and the role of electron inertia. The latter one plays an important role in the near anode region in conditions of reduced electron mobility, both in the stationary and dynamic regimes, confirming the findings of previous stationary models [47], [28]. Moreover, the analysis of the dynamic behaviour of the thruster discharge revealed the high susceptibility of the breathing mode instability to the discharge parameters and the level of modelled physics. In particular, a dramatic effect of the neutral dynamics, most often

neglected, has been observed, as well as a strong dependency on plasma-wall interaction processes.

This suggests the limitations of 1D modelling of HET, which, in the Author's opinion, cannot be used to isolate the onset mechanism of the breathing mode instability due to the abundance of uncertainties and free parameters. On the other hand, 1D models are particularly indicated for fast parametric analysis and preliminary performance evaluations.

As a natural extension of the quasi-neutral model, a non-neutral 1D model of the HET discharge with full-electron inertia has been developed (as part of the same code). Direct comparison of the two models (quasi-neutral drift-diffusion and non-neutral) confirms the applicability of quasi-neutrality and of the drift-diffusion approximation to the Hall Effect discharge in the normal operating regime of the thruster.

On the other hand, in certain operating conditions, characterised by strongly reduced electron mobility at the anode or low propellant mass-flow-rate, a transition of the anode sheath from electron-repelling to electron-attracting has been observed. This is in line with the experimental observations [57], [73], [16]. Finally, although no stable solution with an electron-attracting sheath could be found, the model showed the existence of a regime characterised by strong breathing mode oscillations resulting in a periodic transition of the sheath.

2D Modelling of $E \times B$ discharges A 2D full-fluid model has been developed to analyse more fundamental aspects of $E \times B$ plasmas. The code solves the 3-fluid 5-moment approximation of a plasma using a finite volume method parallelised on MPI. The inclusion of a vacuum-tracking algorithm allows for the resolution of near-vacuum states, which can form in low-pressure $E \times B$ discharges.

The vacuum-tracking capabilities enabled the simulation of Penning-like geometries otherwise impossible to address with standard fluid methods. A wide range of regimes has been explored, down to the limit of pure electron plasmas where the onset of diocotron modes has been observed. The numerical simulations are in line with experimental observations of such a phenomenon. A distinct mode transition is observed by increasing the background neutral density, which results in the formation of $m > 1$ rotating spokes, in line with kinetic simulations of a similar device [108] and the abundant experimental literature on the subject.

Moreover, the model has demonstrated the unprecedented capability of the fluid formalism to resolve the $m = 1$ long-wavelength rotating spoke characteristic of Penning discharges, showing remarkable similarities with PIC simulations available in the literature.

This, within the intrinsic limitations of the 5-moment approximation, proves the applicability of fluid modelling to the simulation of $E \times B$ plasmas and their instabilities, bridging the gap with the kinetic approach.

Following this line, the 2D code has been used to simulate, for the first time, a section of the axial-azimuthal plane of the Hall Effect thruster discharge to self-consistently resolve the anomalous cross-field transport. The discharge has been simulated for 300 µs, being able to self-sustain without the inclusion of any empirical anomalous transport, and exhibiting a rich variety of instabilities, both axial and azimuthal. The interaction of the different modes highlights the complexity of the plasma dynamics in these devices.

The simulation has demonstrated the capability of the fluid model of capturing the axial structure of the discharge and of resolving breathing mode, ion-transit time, rotating spokes, and most importantly, a short-wavelength azimuthal instability responsible for cross-field transport of electrons. The resulting anomalous force dominates the transport of electrons in the near-anode region. Even though the location of this high-frequency instability differs from similar kinetic simulations, these results represent the first step into self-consistent full-fluid simulations of the problem.

Overall, the Thesis demonstrates the applicability of fluid modelling to $E \times B$ plasmas, both for preliminary assessment and theoretical analysis of the discharge.

7.2. Future developments

Here, a collection of future developments of the subjects of this Thesis is proposed, following the same structure as the previous section.

1D Modelling of Hall Effect Thruster discharges The 1D model, both in its quasi-neutral and non-neutral formulations, proved to be an extremely versatile tool. Recently, the models have been improved by adding the possibility of using different propellants and experimental cross-sections for the collisional rates. Nevertheless, there is room for development to improve the current capabilities, expand them further and perform new analyses. Some ideas consist of:

- Improving the model for the radial wall losses. The current model relies on an empirically defined parameter $\tilde{\nu}_w$, which does not provide an accurate estimation of the particle and energy losses. The problem is inherently bi-dimensional, and a 1D reduction can be difficult to obtain. A possibility is to use a kinetic-informed formulation based on the results of the in-house developed hybrid axial-radial code HYPHEN.
- Including a second neutral population to differentiate the slow injected neutrals and the fast wall-born neutrals. This work has demonstrated the importance of neutral dynamics in the stationary and oscillatory behaviour of the thruster. Nevertheless, the difference in velocity between the injected and wall-born neutrals should result in a double-peaked VDF that cannot be captured by the current model. A second population would help analyse the effects of the neutral dynamics with more accuracy.

- Analogously to the previous point, the extension of the model to multiple heavy species populations would enable the inclusion of doubly-charged ions and account for charge-exchange collisions (resulting in the formation of slow ions and fast neutrals). In certain conditions, these effects are known to be important in the performance assessment of HETs.

- Including a volumetric cathode and the near-plume in the non-neutral formulation. This would result in a more realistic treatment of the cathode boundary condition, in the limit of 1D modelling. This analysis would also be beneficial for the 2D model in view of a more suitable downstream boundary condition.

- Improving the model for the power supply, including a more advanced cathode model and an external circuit. This would allow for a more realistic description of the oscillatory regime of the thruster.

2D Modelling of $E \times B$ discharges This Thesis contributed to proving the applicability of fluid models to study instabilities in $E \times B$ plasmas. However, the final goal of applying both the fluid and kinetic formulation to characterise the anomalous cross-field transport remains a topic for future studies. Moreover, before venturing in that direction, some open points need to be addressed:

- Obtain a suitable closure for the electron heat flux vector $\boldsymbol{q}_e$. As explained throughout the Thesis, the heat flux can have a strong impact on the behaviour of the plasma discharge, and the standard Fourier-like closure is not applicable. While the most obvious solution would be to solve for higher moments of the VDF, simulations such as the HET discharge might become too complex and computationally expensive. Hence, a trade-off between accuracy and complexity needs to be formulated.

- Obtain a more suitable cathode boundary condition for the HET simulation. As stated in Chapter 6, the boundary condition is currently over-constraining the system, due to the difficulties in obtaining a stable, well-posed formulation. On the other hand, the inclusion of a volumetric cathode, as for the non-neutral 1D model, results in an unstable operation. Hence, it is important to first assess the effects of the current condition on the dynamics of the discharge, and then to understand the origin of the boundary instability and extend the domain into the near-plume region.

- Improve the parallelisation and performance of the code. In view of more realistic simulations of the HET discharge, the already large computational burden will increase. This requires the use of HPC facilities, for which the code needs to be properly adapted. As an alternative to CPU-based HPC, the code can be ported to GPU parallelisation, although this would require a complete rewrite.

Bibliography

[1] S. N. Abolmasov, "Physics and engineering of crossed-field discharge devices," *Plasma Sources Science and Technology*, vol. 21, no. 3, p. 035 006, May 2012. DOI: 10.1088/0963-0252/21/3/035006. [Online]. Available: https://dx.doi.org/10.1088/0963-0252/21/3/035006.

[2] I. D. Kaganovich *et al.*, "Perspectives on physics of E×B discharges relevant to plasma propulsion and similar technologies," *Physics of Plasmas*, vol. 27, no. 12, pp. 120–601, 2020. DOI: 10.1063/5.0010135.

[3] J.-P. Boeuf and A. Smolyakov, "Physics and instabilities of low-temperature E x B plasmas for spacecraft propulsion and other applications," *Physics of Plasmas*, vol. 30, no. 5, p. 050 901, 2023.

[4] C. E. S. Phillips and W. Crookes, "The action of magnetised electrodes upon electrical discharge phenomena in rarefied gases. preliminary note," *Proceedings of the Royal Society of London*, vol. 64, no. 402-411, pp. 172–176, 1899. DOI: 10.1098/rspl.1898.0088. [Online]. Available: https://royalsocietypublishing.org/doi/abs/10.1098/rspl.1898.0088.

[5] R. J. Strutt, "A peculiar form of low potential discharge in the highest vacua," *Proceedings of the Royal Society of London. Series A, Containing Papers of a Mathematical and Physical Character*, vol. 89, no. 607, pp. 68–74, 1913. [Online]. Available: http://www.jstor.org/stable/93459 (visited on 05/28/2025).

[6] M. Wehrli, "Funkenpotentiale im transversalen magnetfelde," *Annalen der Physik*, vol. 374, no. 20, pp. 285–314, 1922.

[7] F. Penning, "Ein neues manometer für niedrige gasdrucke, insbesondere zwischen $10e-3$ und $10e-5$ mm," *Physica*, vol. 4, no. 2, pp. 71–75, 1937. DOI: https://doi.org/10.1016/S0031-8914(37)80123-8. [Online]. Available: https://www.sciencedirect.com/science/article/pii/S0031891437801238.

[8] E. Hooper, "A review of reflex and penning discharges," in *Advances in Electronics and Electron Physics*, vol. 27, Elsevier, 1970, pp. 295–343. DOI: 10.1016/S0065-2539(08)60040-2. [Online]. Available: https://linkinghub.elsevier.com/retrieve/pii/S0065253908600402 (visited on 06/10/2025).

[9] P. Redhead, "Instabilities in crossed-field discharges at low pressures," *Vacuum*, vol. 38, pp. 901–906, 1988. [Online]. Available: https://api.semanticscholar.org/CorpusID:93820290.

[10] K. I. Thomassen, "Turbulent diffusion in a penning-type discharge," *The Physics of Fluids*, vol. 9, no. 9, pp. 1836–1842, Sep. 1966. DOI: 10.1063/1.1761940. eprint: https://pubs.aip.org/aip/pfl/article-pdf/9/9/1836/12464147/1836_1_online.pdf. [Online]. Available: https://doi.org/10.1063/1.1761940.

[11] E. Choueiri, "A critical history of electric propulsion: The first 50 years (1906-1956)," *Journal of Propulsion and Power*, vol. 20, no. 2, pp. 193–203, 2004.

[12] H. Oberth, *Wege zur Raumschiffahrt*. Berlin, Boston: Oldenbourg Wissenschaftsverlag, 1929. DOI: doi:10.1515/9783486760521. [Online]. Available: https://doi.org/10.1515/9783486760521.

[13] R. Jahn, *Physics of Electric Propulsion*. Dover, 2006.

[14] M. Andrenucci, "Magnetoplasmadynamic thrusters," *Encyclopedia of Aerospace Engineering*, 2010.

[15] V. Kim *et al.*, "Electric propulsion activity in russia," in *27th International Electric Propulsion Conference, Pasadena, CA, USA*, ser. IEPC 01-05, 2001.

[16] V. Zhurin, H. Kaufman, and R. Robinson, "Physics of closed drift thrusters," *Plasma Sources Science and Technolgy*, vol. 8, p. 1, 1999.

[17] J. Boeuf, "Tutorial: Physics and modeling of Hall thrusters," *J. Applied Physics*, vol. 121, no. 1, p. 011 101, 2017.

[18] I. Levchenko *et al.*, "Recent innovations to advance space electric propulsion technologies," *Progress in Aerospace Sciences*, vol. 152, p. 100 900, 2025. DOI: https://doi.org/10.1016/j.paerosci.2023.100900.

[19] F. Taccogna and L. Garrigues, "Latest progress in Hall thrusters plasma modelling," *Reviews of Modern Plasma Physics*, vol. 3, no. 1, p. 12, 2019.

[20] E. Choueiri, "Plasma oscillations in Hall thrusters," *Physics of Plasmas*, vol. 8, no. 4, pp. 1411–1426, 2001.

[21] J. Adam, A. Herón, and G. Laval, "Study of stationary plasma thrusters using two-dimensional fully kinetic simulations," *Physics of Plasmas*, vol. 11, pp. 295–305, 2004.

[22] P. Coche and L. Garrigues, "A two-dimensional (azimuthal-axial) particle-in-cell model of a hall thruster," *Physics of Plasmas*, vol. 21, p. 023 503, 2014.

[23] T. Charoy, T. Lafleur, A. Alvarez-Laguna, A. Bourdon, and P. Chabert, "The interaction between ion transit-time and electron drift instabilities and their effect on anomalous electron transport in hall thrusters," *Plasma Sources Science and Technology*, 2021.

[24] J. J. Ramos, E. Bello-Benítez, and E. Ahedo, "Local analysis of electrostatic modes in a two-fluid E x B plasma," *Physics of Plasmas*, vol. 28, no. 5, p. 052 115, 2021. DOI: 10.1063/5.0039341. [Online]. Available: https://doi.org/10.1063/5.0039341.

[25] A. Smolyakov *et al.*, "Fluid theory and simulations of instabilities, turbulent transport and coherent structures in partially-magnetized plasmas of ExB discharges," *Plasma Physics and Controlled Fusion*, vol. 59, no. 1, p. 014 041, 2017.

[26] D. Poli, E. Bello-Benítez, P. Fajardo, and E. Ahedo, "Time-dependent axial fluid model of the Hall thruster discharge and its plume," *Journal of Physics D: Applied Physics*, vol. 56, no. 41, p. 415 203, 2023. [Online]. Available: http://iopscience.iop.org/article/10.1088/1361-6463/ace2d0.

[27] E. Ahedo, J. Gallardo, and M. Martínez-Sánchez, "Model of the plasma discharge in a Hall thruster with heat conduction," *Physics of Plasmas*, vol. 9, no. 9, pp. 4061–4070, 2002.

[28] E. Bello-Benítez and E. Ahedo, "Stationary axial model of the Hall thruster plasma discharge: Electron azimuthal inertia and far plume effects," *Plasma Sources Science and Technology*, vol. 32, no. 11, p. 115 011, 2023. DOI: 10.1088/1361-6595/ad066f. [Online]. Available: http://dx.doi.org/10.1088/1361-6595/ad066f.

[29] D. Poli, P. Fajardo, and E. Ahedo, "A non-neutral 1d fluid model of hall thruster discharges: Full electron inertia and anode sheath reversal," *Plasma Sources Science and Technology*, vol. 33, no. 7, p. 075 014, Jul. 2024. DOI: 10.1088/1361-6595/ad6500. [Online]. Available: https://dx.doi.org/10.1088/1361-6595/ad6500.

[30] E. Ahedo, "Using electron fluid models to analyze plasma thruster discharges," *Journal of Electric Propulsion*, vol. 2, no. 1, p. 2, 2023.

[31] E. Ahedo, P. Martínez-Cerezo, and M. Martínez-Sánchez, "One-dimensional model of the plasma flow in a Hall thruster," *Physics of Plasmas*, vol. 8, pp. 3058–3068, 2001.

[32] E. Ahedo, J. Gallardo, and M. Martínez-Sánchez, "Effects of the radial-plasma wall interaction on the axial Hall thruster discharge," *Physics of Plasmas*, vol. 10, no. 8, pp. 3397–3409, 2003.

[33] E. Bello-Benítez and E. Ahedo, "Advances on low-dimensionality fluid modelling of Hall thruster discharges," in *Space Propulsion Conference 2021*, March 17-19: Association Aéronautique et Astronautique de France, 2021.

[34] D. Escobar and E. Ahedo, "Low frequency azimuthal stability of the ionization region of the hall thruster discharge. i. local analysis," *Physics of Plasmas*, vol. 21, no. 4, p. 043 505, 2014.

[35] D. Escobar and E. Ahedo, "Global stability analysis of azimuthal oscillations in hall thrusters," *IEEE Transactions on Plasma Science*, vol. 43, no. 1, pp. 149–157, 2015.

[36] E. Bello-Benítez and E. Ahedo, "Axial-azimuthal, high-frequency modes from global linear-stability model of a Hall thruster," *Plasma Sources Science and Technology*, vol. 30, no. 3, p. 035 003, 2021. DOI: 10.1088/1361-6595/abde21.

[37] V. Giannetti, M. M. Saravia, L. Leporini, S. Camarri, and T. Andreussi, "Numerical and experimental investigation of longitudinal oscillations in hall thrusters," *Aerospace*, vol. 8, p. 148, May 2021. DOI: 10.3390/aerospace8060148.

[38] S. Barral and E. Ahedo, "Low-frequency model of breathing oscillations in Hall discharges," *Physical Review E*, vol. 79, p. 046 401, 2009.

[39] R. Sahu, A. Mansour, and K. Hara, "Full fluid moment model for low temperature magnetized plasmas," *Physics of Plasmas*, vol. 27, no. 11, p. 113 505, 2020. DOI: 10.1063/5.0021474. [Online]. Available: https://doi.org/10.1063/5.0021474.

[40] O. Chapurin, A. I. Smolyakov, G. Hagelaar, J.-P. Boeuf, and Y. Raitses, "Fluid and hybrid simulations of the ionization instabilities in hall thruster," *Journal of Applied Physics*, vol. 132, no. 5, p. 053 301, 2022. DOI: 10.1063/5.0094269. eprint: https://doi.org/10.1063/5.0094269. [Online]. Available: https://doi.org/10.1063/5.0094269.

[41] K. Hara and I. G. Mikellides, "Characterization of low frequency ionization oscillations in hall thrusters using a one-dimensional fluid model," in *2018 Joint Propulsion Conference*, ser. AIAA 2018-4904, Cincinatti, OH, 2018. DOI: 10.2514/6.2018-4904. eprint: https://arc.aiaa.org/doi/pdf/10.2514/6.2018-4904. [Online]. Available: https://arc.aiaa.org/doi/abs/10.2514/6.2018-4904.

[42] T. Lafleur, P. Chabert, and A. Bourdon, "The origin of the breathing mode in Hall thrusters and its stabilisation," *Journal of Applied Physics*, vol. 130, no. 5, p. 053 305, 2021.

[43] K. Hara, "Non-oscillatory quasineutral fluid model of cross-field discharge plasmas," *Physics of Plasmas*, vol. 25, no. 12, p. 123 508,

[44] A. Kurganov and E. Tadmor, "New high-resolution central schemes for nonlinear conservation laws and convection–diffusion equations," *Journal of Computational Physics*, vol. 160, no. 1, pp. 241–282, 2000. DOI: 10.1006/jcph.2000.6459. [Online]. Available: https://www.sciencedirect.com/science/article/pii/S0021999100964593.

[45] P. G. (G. Hill and C. R. Peterson, *Mechanics and thermodynamics of propulsion / Philip G. Hill, Carl R. Peterson.* 2nd ed. Reading, Mass.: Addison-Wesley, 1992.

[46] V. Kim, "Main physical features and processes determining the performance of stationary plasma thrusters," *J. Propulsion Power*, vol. 14, no. 5, pp. 736–743, 1998.

[47] E. Ahedo and J.Rus, "Vanishing of the negative anode sheath in a Hall thruster," *Journal of Applied Physics*, vol. 98, p. 043 306, 2005.

[48] E. Ahedo and D. Escobar, "Two-region model for positive and negative plasma sheaths and its application to Hall thruster metallic anodes," *Physics of Plasmas*, vol. 15, p. 033 504, 2008.

[49] J. Fife, M. Martínez-Sánchez, and J. Szabo, "A numerical study of low-frequency discharge oscillations in Hall thrusters," in *33rd Joint Propulsion Conference, Seattle, WA*, ser. AIAA 97-3052, 1997.

[50] D. Poli, E. Bello-Benítez, P. Fajardo, and E. Ahedo, "Non stationary fluid modelling of plasma discharge in Hall thrusters," in *Space Propulsion Conference 2022*, 2022. [Online]. Available: available%20at%20https://ep2.uc3m.es.

[51] E. Ahedo and D. Escobar, "Influence of design and operation parameters on Hall thruster performances," *Journal of Applied Physics*, vol. 96, no. 2, pp. 983–992, 2004.

[52] G. Hobbs and J. Wesson, "Heat flow through a langmuir sheath in the presence of electron emission," *Plasma Physics*, vol. 9, p. 85, 1967.

[53] A. Domínguez-Vázquez, F. Cichocki, M. Merino, P. Fajardo, and E. Ahedo, "On heavy particle-wall interaction in axisymmetric plasma discharges," *Plasma Sources Science and Technology*, vol. 30, no. 8, p. 085 004, Aug. 2021. DOI: 10.1088/1361-6595/ac1715.

[54] S. Livadiotti *et al.*, "A review of gas-surface interaction models for orbital aerodynamics applications," *Progress in Aerospace Sciences*, vol. 119, p. 100 675, 2020. DOI: 10.1016/j.paerosci.2020.100675. [Online]. Available: https://www.sciencedirect.com/science/article/pii/S0376042120300877.

[55] A. Bishaev and V. Kim, "Local plasma properties in a Hall-current accelerator with and extended acceleration zone," *Sov. Physics-Tech. Physics*, vol. 23, no. 9, pp. 1055–1057, 1978.

[56] L. Dorf, Y. Raitses, N. Fisch, and V. Semenov, "Effect of anode dielectric coating on Hall thruster operation," *Applied Physics Letters*, vol. 84, no. 7, pp. 1070–1072, 2003.

[57] L. Dorf, Y. Raitses, and N. Fisch, "Experimental studies of anode sheath phenomena in a Hall thruster discharge," *Journal of Applied Physics*, vol. 97, p. 103 309, 2005.

[58] J. M. Fife, "Hybrid-PIC modeling and electrostatic probe survey of Hall thrusters," Ph.D. dissertation, Massachusetts Institute of Technology, 1998.

[59] S. Barral, K. Makowski, Z. Peradzynski, N. Gascon, and M. Dudeck, "Wall material effects in stationary plasma thrusters. II. Near-wall and in-wall conductivity," *Phys. Plasmas*, vol. 10, no. 10, pp. 4137–4152, 2003.

[60] S. Yokota, K. Komurasaki, and Y. Arakawa., "Numerical analysis of anode sheath structure transition in an anode-layer type hall thruster," in *30th International Electric Propulsion Conference*, ser. IEPC-2007, Florence, Italy, September 17-20, 2007.

[61] Y. Yamashita, R. Lau, and K. Hara, "Inertial and anisotropic pressure effects on cross-field electron transport in low-temperature magnetized plasmas," *Journal of Physics D: Applied Physics*, 2023.

[62] P. Cagas, A. Hakim, J. Juno, and B. Srinivasan, "Continuum kinetic and multi-fluid simulations of classical sheaths," *Physics of Plasmas*, vol. 24, no. 2, p. 022 118, Feb. 2017. DOI: 10.1063/1.4976544. eprint: https://pubs.aip.org/aip/pop/article-pdf/doi/10.1063/1.4976544/13590097/022118_1_online.pdf. [Online]. Available: https://doi.org/10.1063/1.4976544.

[63] S. Mazouffre, G. Bourgeois, L. Garrigues, and E. Pawelec, "A comprehensive study on the atom flow in the cross-field discharge of a Hall thruster," *Journal of Physics D: Applied Physics*, vol. 44, no. 10, p. 105 203, 2011.

[64] R. Hofer, I. Katz, I. Mikellides, and M. Gamero-Castano, "Heavy particle velocity and electron mobility modeling in hybrid-pic Hall thruster simulations," *AIAA Paper*, vol. 4658, 2006.

[65] G. Bird, *Molecular Gas Dynamics and the Direct Simulation of Gas Flows* (The Oxford Engineering Science Series). Oxford University Press, Oxford, UK, 1994.

[66] S. Gottlieb and C.-W. Shu, "Total variation diminishing runge-kutta schemes.," *Mathematics of Computation*, vol. 67, pp. 73–85, Aug. 1996. DOI: 10.1090/S0025-5718-98-00913-2.

[67] V. Joncquieres, F. Pechereau, A. A. Laguna, A. Bourdon, O. Vermorel, and B. Cuenot, "A 10-moment fluid numerical solver of plasma with sheaths in a hall effect thruster," in *2018 Joint Propulsion Conference*. DOI: 10.2514/6.2018-4905. eprint: https://arc.aiaa.org/doi/pdf/10.2514/6.2018-4905. [Online]. Available: https://arc.aiaa.org/doi/abs/10.2514/6.2018-4905.

[68] G. Hagelaar, F. Hoog, de, and G. Kroesen, "Boundary conditions in fluid models of gas discharges," *Physical Review E: Statistical, Physics, Plasmas, Fluids, and Related Interdisciplinary Topics*, vol. 62, no. 1, pp. 1452–1454, 2000. DOI: 10.1103/PhysRevE.62.1452.

[69] R. J. LeVeque, "Finite volume methods for hyperbolic problems," in (Cambridge Texts in Applied Mathematics), Cambridge Texts in Applied Mathematics. Cambridge University Press, 2002.

[70] I. D. Boyd and E. T. Schwartzentruber, "Nonequilibrium gas dynamics and molecular simulation," in Cambridge University Press, 2017.

[71] A. Marín-Cebrián, E. Bello-Benítez, A. Domínguez-Vázquez, and E. Ahedo, "Non-maxwellian electron effects on the macroscopic response of a hall thruster discharge from an axial–radial kinetic model," *Plasma Sources Science and Technology*, vol. 33, no. 2, p. 025 008, Feb. 2024. DOI: 10.1088/1361-6595/ad227c. [Online]. Available: https://dx.doi.org/10.1088/1361-6595/ad227c.

[72] A. Alvarez-Laguna, T. Magin, M. Massot, A. Bourdon, and P. Chabert, "Plasma-sheath transition in multi-fluid models with inertial terms under low pressure conditions: Comparison with the classical and kinetic theory," *Plasma Sources Science and Technology*, vol. 29, no. 2, p. 025 003, Feb. 2020. DOI: 10.1088/1361-6595/ab6242. [Online]. Available: https://dx.doi.org/10.1088/1361-6595/ab6242.

[73] L. Dorf, Y. Raitses, and N. Fisch, "Effect of magnetic field profile on the anode fall in a Hall-effect thruster discharge," *Physics of Plasmas*, vol. 13, p. 057 104, 2006.

[74] J. Bittencourt, *Fundamentals of plasma physics*. Springer, Berlin, Germany, 2004.

[75] C. Hirsch, *Numerical computation of internal and external flows. Volume 1, Fundamentals of numerical discretization* (Wiley series in numerical methods in engineering). Chichester: Wiley, 1989 - 1988.

[76] R. J. LeVeque, *Finite Volume Methods for Hyperbolic Problems* (Cambridge Texts in Applied Mathematics). Cambridge University Press, 2002.

[77] E. F. Toro, *Riemann Solvers and Numerical Methods for Fluid Dynamics*. Heidelberg: Springer Berlin, 2009.

[78] A. Harten, "High resolution schemes for hyperbolic conservation laws," *Journal of Computational Physics*, vol. 49, no. 3, pp. 357–393, 1983. DOI: https://doi.org/10.1016/0021-9991(83)90136-5. [Online]. Available: https://www.sciencedirect.com/science/article/pii/0021999183901365.

[79] A. Kurganov and D. Levy, "A third-order semidiscrete central scheme for conservation laws and convection-diffusion equations," *SIAM Journal on Scientific Computing*, vol. 22, no. 4, pp. 1461–1488, 2000. DOI: 10.1137/S1064827599360236. eprint: https://doi.org/10.1137/S1064827599360236. [Online]. Available: https://doi.org/10.1137/S1064827599360236.

[80] V. Rusanov, "The calculation of the interaction of non-stationary shock waves and obstacles," *USSR Computational Mathematics and Mathematical Physics*, vol. 1, no. 2, pp. 304–320, 1962. DOI: 10.1016/0041-5553(62)90062-9. [Online]. Available: https://www.sciencedirect.com/science/article/pii/0041555362900629.

[81] B. Einfeldt, "On godunov-type methods for gas dynamics," *SIAM Journal on Numerical Analysis*, vol. 25, no. 2, pp. 294–318, 1988. DOI: 10.1137/0725021. eprint: https://doi.org/10.1137/0725021. [Online]. Available: https://doi.org/10.1137/0725021.

[82] B. Einfeldt, C. Munz, P. Roe, and B. Sjögreen, "On godunov-type methods near low densities," *Journal of Computational Physics*, vol. 92, no. 2, pp. 273–295, 1991. DOI: https://doi.org/10.1016/0021-9991(91)90211-3. [Online]. Available: https://www.sciencedirect.com/science/article/pii/0021999191902113.

[83] E. Toro, "The hllc riemann solver," *Shock Waves*, vol. 29, Nov. 2019. DOI: 10.1007/s00193-019-00912-4.

[84] P. Roe, "Approximate riemann solvers, parameter vectors, and difference schemes," *Journal of Computational Physics*, vol. 43, no. 2, pp. 357–372, 1981. DOI: https://doi.org/10.1016/0021-9991(81)90128-5. [Online]. Available: https://www.sciencedirect.com/science/article/pii/0021999181901285.

[85] A. Harten and J. M. Hyman, "Self adjusting grid methods for one-dimensional hyperbolic conservation laws," *Journal of Computational Physics*, vol. 50, no. 2, pp. 235–269, 1983. DOI: https://doi.org/10.1016/0021-9991(83)90066-9. [Online]. Available: https://www.sciencedirect.com/science/article/pii/0021999183900669.

[86] S. F. Davis, "Simplified second-order godunov-type methods," *SIAM Journal on Scientific and Statistical Computing*, vol. 9, no. 3, pp. 445–473, 1988. DOI: 10.1137/0909030. eprint: https://doi.org/10.1137/0909030. [Online]. Available: https://doi.org/10.1137/0909030.

[87] P. Batten, N. Clarke, C. Lambert, and D. M. Causon, "On the choice of wavespeeds for the hllc riemann solver," *SIAM Journal on Scientific Computing*, vol. 18, no. 6, pp. 1553–1570, 1997. DOI: 10.1137/S1064827593260140. eprint: https://doi.org/10.1137/S1064827593260140. [Online]. Available: https://doi.org/10.1137/S1064827593260140.

[88] V. Subramaniam and L. L. Raja, "A plasma–vacuum interface tracking algorithm for magnetohydrodynamic simulations of coaxial plasma accelerators," *Journal of Computational Physics*, vol. 366, pp. 207–225, 2018. DOI: https://doi.org/10.1016/j.jcp.2018.03.041. [Online]. Available: https://www.sciencedirect.com/science/article/pii/S0021999118302079.

[89] S. Fabre, "Stability analysis of the euler-poisson equations," *Journal of Computational Physics*, vol. 101, no. 2, pp. 445–451, 1992. DOI: https://doi.org/10.1016/0021-9991(92)90020-Y. [Online]. Available: https://www.sciencedirect.com/science/article/pii/002199919290020Y.

[90] L. Reboul, M. Massot, and A. A. Laguna, "Numerical challenges in the simulation of 1D bounded low-temperature plasmas with charge separation in various collisional regimes," *AIP Conference Proceedings*, vol. 2996, no. 1, p. 190 004, Feb. 2024. DOI: 10.1063/5.0187483. eprint: https://pubs.aip.org/aip/acp/article-pdf/doi/10.1063/5.0187483/19583651/190004_1_5.0187483.pdf. [Online]. Available: https://doi.org/10.1063/5.0187483.

[91] G. Strang, "On the construction and comparison of difference schemes," *SIAM Journal on Numerical Analysis*, vol. 5, no. 3, pp. 506–517, 1968. DOI: 10.1137/0705041. eprint: https://doi.org/10.1137/0705041. [Online]. Available: https://doi.org/10.1137/0705041.

[92] H. Wu, P. C. Ma, and M. Ihme, "Efficient time-stepping techniques for simulating turbulent reactive flows with stiff chemistry," *Computer Physics Communications*, vol. 243, pp. 81–96, 2019. DOI: https://doi.org/10.1016/j.cpc.2019.04.016. [Online]. Available: https://www.sciencedirect.com/science/article/pii/S001046551930133X.

[93] S. Gottlieb, C.-W. Shu, and E. Tadmor, "Strong stability-preserving high-order time discretization methods," *SIAM Review*, vol. 43, May 2001. DOI: 10.1137/S003614450036757X.

[94] E. Hairer and G. Wanner, *Solving Ordinary Differential Equations II. Stiff and Differential-Algebraic Problems*. Jan. 1996, vol. 14, pp. 31–36. DOI: 10.1007/978-3-662-09947-6.

[95] P. Amestoy, A. Buttari, J.-Y. L'Excellent, and T. Mary, "Performance and Scalability of the Block Low-Rank Multifrontal Factorization on Multicore Architectures," *ACM Transactions on Mathematical Software*, vol. 45, 2:1–2:26, 1 2019.

[96] R. Liska and B. Wendroff, "Comparison of several difference schemes on 1d and 2d test problems for the euler equations," *SIAM Journal on Scientific Computing*, vol. 25, no. 3, pp. 995–1017, 2003. DOI: 10.1137/S1064827502402120. eprint: https://doi.org/10.1137/S1064827502402120. [Online]. Available: https://doi.org/10.1137/S1064827502402120.

[97] C. W. Schulz-Rinne, J. P. Collins, and H. M. Glaz, "Numerical solution of the riemann problem for two-dimensional gas dynamics," *SIAM Journal on Scientific Computing*, vol. 14, no. 6, pp. 1394–1414, 1993. DOI: 10.1137/0914082. eprint: https://doi.org/10.1137/0914082. [Online]. Available: https://doi.org/10.1137/0914082.

[98] E. F. Toro, *NUMERICA: A Library of Source Codes for Teaching, Research and Applications*. Numeritek Ltd, 1999.

[99] J. J. Quirk, "A contribution to the great riemann solver debate," *International Journal for Numerical Methods in Fluids*, vol. 18, no. 6, pp. 555–574, 1994. DOI: https://doi.org/10.1002/fld.1650180603. eprint: https://onlinelibrary.wiley.com/doi/pdf/10.1002/fld.1650180603. [Online]. Available: https://onlinelibrary.wiley.com/doi/abs/10.1002/fld.1650180603.

[100] H. Nishikawa and K. Kitamura, "Very simple, carbuncle-free, boundary-layer-resolving, rotated-hybrid riemann solvers," *Journal of Computational Physics*, vol. 227, no. 4, pp. 2560–2581, 2008. DOI: https://doi.org/10.1016/j.jcp.2007.11.003. [Online]. Available: https://www.sciencedirect.com/science/article/pii/S0021999107004822.

[101] N. Fleischmann, S. Adami, and N. A. Adams, "A shock-stable modification of the hllc riemann solver with reduced numerical dissipation," *Journal of Computational Physics*, vol. 423, p. 109 762, 2020. DOI: https://doi.org/10.1016/j.jcp.2020.109762. [Online]. Available: https://www.sciencedirect.com/science/article/pii/S0021999120305362.

[102] S. Chen, B. Lin, Y. Li, and C. Yan, "Hllc+: Low-mach shock-stable hllc-type riemann solver for all-speed flows," *SIAM Journal on Scientific Computing*, vol. 42, no. 4, B921–B950, 2020. DOI: 10.1137/18M119032X. eprint: https://doi.org/10.1137/18M119032X. [Online]. Available: https://doi.org/10.1137/18M119032X.

[103] A. Morozov and V. Savelyev, "Fundamentals of stationary plasma thruster theory," in *Reviews of Plasma Physics, Vol. 21*, New York: Kluwer Academic, 2000.

[104] F. C. Hoh, "Instability of Penning-type discharges," *The Physics of Fluids*, vol. 6, no. 8, pp. 1184–1191, 1963. DOI: 10.1063/1.1706878.

[105] K. I. Thomassen, "Rotational instability in a penning-type discharge," *Phys. Rev. Lett.*, vol. 14, pp. 587–589, 15 Apr. 1965. DOI: 10.1103/PhysRevLett.14.587. [Online]. Available: https://link.aps.org/doi/10.1103/PhysRevLett.14.587.

[106] L. Xu, D. Eremin, and R. P. Brinkmann, "Direct evidence of gradient drift instability being the origin of a rotating spoke in a crossed field plasma," *Plasma Sources Science and Technology*, vol. 30, no. 7, p. 075 013, 2021.

[107] J. P. Boeuf, "Spoke formation in low temperature E x B plasmas: Transition from gradient-drift instability to ionization wave," *Physics of Plasmas*, vol. 30, no. 2, p. 022 112, Feb. 2023. DOI: 10.1063/5.0136888. eprint: https://pubs.aip.org/aip/pop/article-pdf/doi/10.1063/5.0136888/19821993/022112_1_online.pdf. [Online]. Available: https://doi.org/10.1063/5.0136888.

[108] J.-P. Boeuf, "Rotating structures in low temperature magnetized plasmas—insight from particle simulations," *Frontiers in Physics*, vol. 2, p. 74, 2014.

[109] J. Carlsson, I. Kaganovich, A. Powis, Y. Raitses, I. Romadanov, and A. Smolyakov, "Particle-in-cell simulations of anomalous transport in a Penning discharge," *Physics of Plasmas*, vol. 25, no. 6, 2018. DOI: 10.1063/1.5017467. [Online]. Available: https://doi.org/10.1063/1.5017467.

[110] A. Powis, J. Carlsson, I. Kaganovich, Y. Raitses, and A. Smolyakov, "Scaling of spoke rotation frequency within a penning discharge," *Physics of Plasmas*, vol. 25, no. 7, p. 072 110, 2018. DOI: 10.1063/1.5038733. [Online]. Available: https://doi.org/10.1063/1.5038733.

[111] M. Tyushev *et al.*, "Azimuthal structures and turbulent transport in penning discharge," *Physics of Plasmas*, vol. 30, no. 3, p. 033 506, Mar. 2023. DOI: 10.1063/5.0129804. eprint: https://pubs.aip.org/aip/pop/article-pdf/doi/10.1063/5.0129804/16796916/033506_1_online.pdf. [Online]. Available: https://doi.org/10.1063/5.0129804.

[112] R. Lucken, A. Bourdon, M. A. Lieberman, and P. Chabert, "Instability-enhanced transport in low temperature magnetized plasma," *Physics of Plasmas*, vol. 26, no. 7, p. 070 702, Jul. 2019. DOI: 10.1063/1.5094422. eprint: https://pubs.aip.org/aip/pop/article-pdf/doi/10.1063/1.5094422/19753566/070702_1_online.pdf. [Online]. Available: https://doi.org/10.1063/1.5094422.

[113] R. Lucken, A. Tavant, A. Bourdon, M. A. Lieberman, and P. Chabert, "Saturation of the magnetic confinement in weakly ionized plasma," *Plasma Sources Science and Technology*, vol. 29, no. 6, p. 065 014, Jun. 2020. DOI: 10.1088/1361-6595/ab38b2. [Online]. Available: https://dx.doi.org/10.1088/1361-6595/ab38b2.

[114] M. Tyushev *et al.*, "Mode transitions and spoke structures in $E \times B$ penning discharge," *Physics of Plasmas*, vol. 32, no. 1, p. 013 511, Jan. 2025. DOI: 10.1063/5.0238577. eprint: https://pubs.aip.org/aip/pop/article-pdf/doi/10.1063/5.0238577/20370580/013511_1_5.0238577.pdf. [Online]. Available: https://doi.org/10.1063/5.0238577.

[115] Y. Sakawa, C. Joshi, P. Kaw, F. Chen, and V. Jain, "Excitation of the modified Simon–Hoh instability in an electron beam produced plasma," *Physics of Fluids B: Plasma Physics*, vol. 5, no. 6, pp. 1681–1694, 1993.

[116] A. R. Mansour and K. Hara, "Full fluid moment modeling of rotating spokes in penning-type configuration," *Plasma Sources Science and Technology*, vol. 31, no. 5, p. 055 012, May 2022. DOI: 10.1088/1361-6595/ac6a73. [Online]. Available: https://dx.doi.org/10.1088/1361-6595/ac6a73.

[117] A. J. Peurrung and J. Fajans, "Experimental dynamics of an annulus of vorticity in a pure electron plasma," *Physics of Fluids A: Fluid Dynamics*, vol. 5, no. 2, pp. 493–499, Feb. 1993. DOI: 10.1063/1.858872. [Online]. Available: https:

//pubs.aip.org/pof/article/5/2/493/940338/Experimental-dynamics-of-an-annulus-of-vorticity (visited on 06/10/2025).

[118] C. C. Cutler, "Instability in hollow and strip electron beams," *Journal of Applied Physics*, vol. 27, no. 9, pp. 1028–1029, Sep. 1956. DOI: 10.1063/1.1722535. eprint: https://pubs.aip.org/aip/jap/article-pdf/27/9/1028/18315932/1028_1_online.pdf. [Online]. Available: https://doi.org/10.1063/1.1722535.

[119] E. Carbone *et al.*, "Data needs for modeling low-temperature non-equilibrium plasmas: The lxcat project, history, perspectives and a tutorial," *Atoms*, vol. 9, no. 1, 2021. DOI: 10.3390/atoms9010016. [Online]. Available: https://www.mdpi.com/2218-2004/9/1/16.

[120] R. P. McEachran and A. D. Stauffer, "Momentum transfer cross sections for the heavy noble gases," *The European Physical Journal D*, vol. 68, no. 6, p. 153, Jun. 2014. DOI: 10.1140/epjd/e2014-50166-7. [Online]. Available: https://doi.org/10.1140/epjd/e2014-50166-7.

[121] S. Sakabe and Y. Izawa, "Simple formula for the cross sections of resonant charge transfer between atoms and their positive ions at low impact velocity," *Physical Review A*, vol. 45, no. 3, p. 2086, 1992.

[122] J. Dugan and R. Sovie, "Volume ion production costs in tenuous plasmas: A general atom theory and detailed results for helium, argon, and cesium," Tech. Rep., 1967.

[123] C.-D. Munz, "A tracking method for gas flow into vacuum based on the vacuum riemann problem," *Mathematical Methods in the Applied Sciences*, vol. 17, no. 8, pp. 597–612, 1994. DOI: https://doi.org/10.1002/mma.1670170803. eprint: https://onlinelibrary.wiley.com/doi/pdf/10.1002/mma.1670170803. [Online]. Available: https://onlinelibrary.wiley.com/doi/abs/10.1002/mma.1670170803.

[124] D. Poli, P. Fajardo, E. Ahedo, and G. Hagelaar, "Comparison of two fluid codes for modelling 2d instabilities in exb plasmas," in 38^{th} *International Electric Propulsion Conference*, Toulouse, France, June 23-28: Electric Rocket Propulsion Society, 2024.

[125] H. F. Webster, "Structure in magnetically confined electron beams," *Journal of Applied Physics*, vol. 28, no. 12, pp. 1388–1397, Dec. 1957. DOI: 10.1063/1.1722665. eprint: https://pubs.aip.org/aip/jap/article-pdf/28/12/1388/18317429/1388_1_online.pdf. [Online]. Available: https://doi.org/10.1063/1.1722665.

[126] H. F. Webster, "Some additional observations of the vortex instability in electron beams," *Physics of Plasmas*, vol. 7, no. 1, pp. 84–88, Jan. 2000. DOI: 10.1063/1.873783. eprint: https://pubs.aip.org/aip/pop/article-pdf/7/1/84/19113177/84_1_online.pdf. [Online]. Available: https://doi.org/10.1063/1.873783.

[127] R. Kyhl and H. Webster, "Breakup of hollow cylindrical electron beams," *IRE Transactions on Electron Devices*, vol. 3, no. 4, pp. 172–183, 1956. DOI: 10.1109/T-ED.1956.14185.

[128] R. W. Gould, "Space charge effects in beam-type magnetrons," *Journal of Applied Physics*, vol. 28, no. 5, pp. 599–605, May 1957. DOI: 10.1063/1.1722810. eprint: https://pubs.aip.org/aip/jap/article-pdf/28/5/599/18316679/599_1_online.pdf. [Online]. Available: https://doi.org/10.1063/1.1722810.

[129] W. Knauer, "Diocotron instability in plasmas and gas discharges," *Journal of Applied Physics*, vol. 37, no. 2, pp. 602–611, Feb. 1966. DOI: 10.1063/1.1708223. eprint: https://pubs.aip.org/aip/jap/article-pdf/37/2/602/18336915/602_1_online.pdf. [Online]. Available: https://doi.org/10.1063/1.1708223.

[130] J. Pierce, "Instability of hollow beams," *IRE Transactions on Electron Devices*, vol. 3, no. 4, pp. 183–189, 1956. DOI: 10.1109/T-ED.1956.14186.

[131] N. A. Kervalishvili, "Formation and Dynamics of Vortex Structures in Pure and Gas-Discharge Nonneutral Collisionless Electron Plasmas,"

[132] N. Kervalishvili, "Electron vortices in a nonneutral plasma in crossed $E \times H$ fields," *Physics Letters A*, vol. 157, no. 6, pp. 391–394, 1991. DOI: https://doi.org/10.1016/0375-9601(91)90875-9. [Online]. Available: https://www.sciencedirect.com/science/article/pii/0375960191908759.

[133] K. S. Fine, C. F. Driscoll, J. H. Malmberg, and T. B. Mitchell, "Measurements of symmetric vortex merger," *Physical Review Letters*, vol. 67, no. 5, pp. 588–591, Jul. 1991. DOI: 10.1103/PhysRevLett.67.588. [Online]. Available: https://link.aps.org/doi/10.1103/PhysRevLett.67.588 (visited on 06/10/2025).

[134] R. H. Levy, "Diocotron instability in a cylindrical geometry," *The Physics of Fluids*, vol. 8, no. 7, pp. 1288–1295, Jul. 1965. DOI: 10.1063/1.1761400. eprint: https://pubs.aip.org/aip/pfl/article-pdf/8/7/1288/12617137/1288_1_online.pdf. [Online]. Available: https://doi.org/10.1063/1.1761400.

[135] J. Sommeria, C. Staquet, and R. Robert, "Final equilibrium state of a two-dimensional shear layer," *Journal of Fluid Mechanics*, vol. 233, pp. 661–689, 1991. DOI: 10.1017/S0022112091000642.

[136] P. S. Marcus, "Vortex dynamics in a shearing zonal flow," *Journal of Fluid Mechanics*, vol. 215, pp. 393–430, 1990. DOI: 10.1017/S0022112090002695.

[137] P. Tabeling, "Two-dimensional turbulence: A physicist approach," *Physics Reports*, vol. 362, no. 1, pp. 1–62, 2002. DOI: https://doi.org/10.1016/S0370-1573(01)00064-3. [Online]. Available: https://www.sciencedirect.com/science/article/pii/S0370157301000643.

[138] T. Lafleur, S. Baalrud, and P. Chabert, "Theory for the anomalous electron transport in hall effect thrusters. i. insights from particle-in-cell simulations," *Physics of Plasmas*, vol. 23, p. 053 502, 2016.

[139] N. Brenning, "Review of the civ phenomenon," *Space Science Reviews*, vol. 59, no. 3, pp. 209–314, Feb. 1992. DOI: 10.1007/BF00242088. [Online]. Available: https://doi.org/10.1007/BF00242088.

[140] A. Piel, "Review of laboratory experiments on alfven's critical ionization velocity," *Advances in Space Research*, vol. 10, no. 7, pp. 7–16, 1990. DOI: https://doi.org/10.1016/0273-1177(90)90267-4. [Online]. Available: https://www.sciencedirect.com/science/article/pii/0273117790902674.

[141] G. Fubiani *et al.*, "Impact of the radial electric field on plasma instabilities in a penning discharge: Insights from a 3d particle-in-cell model," *Physics of Plasmas*, vol. 32, no. 8, p. 080 704, Aug. 2025. DOI: 10.1063/5.0271375. eprint: https://pubs.aip.org/aip/pop/article-pdf/doi/10.1063/5.0271375/20667777/080704_1_5.0271375.pdf. [Online]. Available: https://doi.org/10.1063/5.0271375.

[142] A. Ducrocq, J. Adam, A. Héron, and G. Laval, "High-frequency electron drift instability in the cross-field configuration of Hall thrusters," *Physics of Plasmas*, vol. 13, p. 102 111, 2006.

[143] A. Morozov, Y. Esipchuk, A. Kapulkin, V. Nevrovskii, and V. Smirnov, "Effect of the magnetic field on a closed-electron-drift accelerator," *Sov. Phys.-Tech. Phys.*, vol. 17, no. 3, pp. 482–7, 1972.

[144] W. Frias, A. Smolyakov, I. Kaganovich, and Y. Raitses, "Long wavelength gradient drift instability in Hall plasma devices. I. Fluid theory," *Physics of Plasmas*, vol. 19, no. 7, p. 072 112, 2012.

[145] T. Charoy, "Numerical study of electron transport in hall thrusters," PhD Thesis, École Polytechnique de Paris, 2020.

[146] T. Chernysev and D. Krivoruchko, "On a force balance role of cathode plasma in hall effect thrusters," *Plasma Sources Science and Technology*, vol. 31, no. 1, p. 05 001, 2022.

[147] C. M. Lam, E. Fernandez, and M. A. Cappelli, "A 2-D hybrid Hall thruster simulation that resolves the ExB electron drift direction," *IEEE Transactions on Plasma Science*, vol. 43, pp. 86–94, 2015.

[148] R. Kawashima and K. Komurasaki, "Two-dimensional hybrid model of gradient drift instability and enhanced electron transport in a hall thruster," *Physics of Plasmas*, vol. 28, no. 6, 2021.

[149] O. Koshkarov, A. Smolyakov, Y. Raitses, and I. Kaganovich, "Self-organization, structures, and anomalous transport in turbulent partially magnetized plasmas with crossed electric and magnetic fields," *Physical review letters*, vol. 122, no. 18, p. 185 001, 2019.

[150] L. Wang, A. Hakim, J. Juno, and B. Srinivasan, "Electron cyclotron drift instability and anomalous transport: Two-fluid moment theory and modeling," *Plasma Sources Science and Technology*, vol. 31, no. 10, p. 105 001, Sep. 2022. DOI: 10.1088/1361-6595/ac90e7. [Online]. Available: https://dx.doi.org/10.1088/1361-6595/ac90e7.

[151] S. Sadouni, "Fluid modeling of transport and instabilities in magnetized low-temperature plasma sources," PhD Thesis, Université Paul Sabatier - Toulouse III, Feb. 2020. [Online]. Available: https://theses.hal.science/tel-02978476.

[152] C. M. Lam, A. Knoll, M. A. Cappelli, and E. Fernandez, "Two-Dimensional (z-θ) Simulations of Hall Thruster Anomalous Transport," in 31st *International Electric Propulsion Conference*, ser. IEPC-2009-102, Ann Harbor, Michigan, September 20-24: Electric Rocket Propulsion Society, Fairview Park, OH, 2009.

[153] M. S. McDonald and A. D. Gallimore, "Rotating spoke instabilities in Hall thrusters," *IEEE Transactions on Plasma Science*, vol. 39, no. 11, pp. 2952–2953, 2011.

[154] M. S. McDonald and A. D. Gallimore, "Comparison of breathing and spoke mode strength in the h6 hall thruster using high speed imaging," in 33rd *International Electric Propulsion Conference*, Washington D.C., USA, October 6-10: Electric Rocket Propulsion Society, 2013.

[155] T. Lafleur, R. Martorelli, P. Chabert, and A. Bourdon, "Anomalous electron transport in hall-effect thrusters: Comparison between quasi-linear kinetic theory and particle-in-cell simulations," *Physics of Plasmas*, vol. 25, no. 6, 2018.

[156] J. Fife and M. Martínez-Sánchez, "Two-dimensional hybrid particle-in-cell (pic) modelling of Hall thrusters," in *24th International Electric Propulsion Conference, Moscow, Russia*, ser. IEPC 95-240, 1995.

[157] A. Morozov and V. Savel'ev, "One-dimensional hydrodynamic model of the atom and ion dynamics in a stationary plasma thruster," *Plasma Physics Reports*, vol. 26, no. 3, pp. 219–224, 2000.